Influence of Cross-Section Details on Vortex-Induced Vibrations of Bridge Decks: Experiments and Modeling

Dissertation

submitted to the

Faculty of Architecture, Civil Engineering and Environmental Sciences
Technische Universität Braunschweig

and the

Department of Civil and Environmental Engineering
University of Florence

in candidacy for the degree of a
Doktor-Ingenieur (Dr.-Ing.) /
Dottore di Ricerca Civil and Environmental Engineering *)

by

Bernardo Nicese
born 21.09.1988
from Fiesole (FI), Italy

Professorial advisors
Dr. Claudio Mannini
Dr. Antonino Maria Marra
Prof. Gianni Bartoli
Prof. Klaus Thiele

2021

*) Either the German or the Italian form of the title may be used.

Abstract

Vortex-induced vibrations represent a potentially critical phenomenon for bridges in a multitude of cases. The increasing optimization of modern bridge structures is giving rise to long spans and slender decks particularly sensitive to vortex shedding, which may generate deck oscillations unacceptable for the comfort of the users even for relatively low wind velocities. At the same time, the variety of geometric details characterizing bridge deck cross sections and the marked influence of an even limited variation of the flow angle of incidence add further difficulties to the prediction of bridge deck VIV response without an accurate and extended experimental campaign. In this context, VIV mathematical modeling represents a challenging but also an attractive issue for bridge decks, not only from a scientific point of view, but hopefully with the practical purpose of developing a mathematical approach able to support or at least partially reduce the amount of wind tunnel tests needed during the design phase.

The present dissertation deals with the critical effect of significant cross-section geometric details and flow angle of attack on bridge deck VIV response and these factors are included in an extended study about two mathematical approaches for VIV response prediction applied to different configurations of a realistic bridge section. An overview of representative and meaningful studies provided by scientific literature about the influence of geometric details and angle of attack is firstly proposed, along with a description of mathematical modeling attempts developed over the years for VIV modeling of elongated cylinders with a constant cross section. The variability given by geometric features combined with angle of attack variation over a realistic range of values can be remarkable. This should be preferably taken into account by VIV mathematical modeling, usually developed, on the other hand, for simplified section geometries at zero angle of attack. In this work, a wake-oscillator model, derived from Tamura and Matsui's one, and a modified version of harmonic model are deeply discussed and employed for a realistic cross-section geometry.

For the purpose of exploring the influence of geometric details at different wind angles of incidence, calibrating both models and assessing their performances, wind tunnel tests were performed on a bridge deck sectional model. The modification of bridge section lower corners, the addition of two lateral barrier typologies and the investigation of different angles of attack gave rise to a large amount of tested section layouts. Aerodynamic force measurements were firstly performed on the stationary body and

results were employed for mathematical model calibration and to formulate qualitative suppositions about the expected dynamic behavior of different cross-section layouts. Then, aeroelastic tests were carried out, with the model elastically suspended and free to vibrate. Response curves for different values of wind velocity were determined for each geometric layout. They were employed to complete wake-oscillator model calibration and compared to the predictions of both mathematical approaches. A critical effect of lateral barriers installed on the deck was observed, along with marked effects, even unexpected in some cases, produced by limited angle of attack variations. In addition, an estimation of the aerodynamic damping was conducted through free-decay tests.

In the last part of the dissertation, VIV response mathematical modeling is addressed specifically. According to what previously stated, a Tamura-type wake-oscillator model and a modified harmonic model were investigated. The first one is a physically based two-degree-of-freedom approach, while the second one is a one-degree-of-freedom simplified model aiming to a quick and relatively easy prediction of the peak response at lock-in. A mathematical connection between the models was explored and both approaches were studied and applied preliminarily for a 4:1 rectangular cylinder and then for the bridge deck geometric configurations experimentally tested at different angles of attack. The modified harmonic model was calibrated only through results of static force measurements, while for the wake oscillator model, in absence of further static tests like flow visualizations, the response curves obtained at low Scruton number were employed to calibrate a part of model parameters.

Virtues and limitations of both models are discussed. In particular, the necessity of adapting the wake oscillator design of the Tamura-type model for elongated cross sections, like a 4:1 rectangle or a bridge deck, was observed. Speculations about wake lamina geometry modification were formulated, with the purpose of achieving, for elongated sections, the appropriate values of model parameters without losing their physical origin. On the other hand, wake-oscillator model equations of motion were found able to reproduce a large variety of experimental response curve shapes, while limitations in peak response amplitude prediction were frequently observed, as well as for the modified harmonic model, especially where a considerable oscillation amplitude was found. Such limitations were attributed to the spanwise correlation increase of the vortex-shedding force with the oscillation amplitude; full correlation at lock-in was proposed as upper bound condition for the fluctuating force acting on the body.

Pressure measurements for correlation effect quantification and further study about the wake oscillator structure for elongated sections, including the addition of a degree of freedom, are finally proposed as main possible advancements to improve the present work.

List of Figures

List of Tables

Contents

1. Introduction

1.1. General introduction to the work topic

The construction of light and slender bridge structures, characterized by limited mass per unit length and low frequencies of oscillation, is currently becoming more and more common. Cable-stayed bridges, suspension bridges or modern footbridges built with particular materials and geometries can exhibit considerable interaction with the wind in several instances. In some cases, due to the continuous attempt to reach a higher length of the main span, the wind action can become the main issue to address for the success of the structure design.

Even if the earliest interest in wind action on bridge structures dates back to the nineteenth century, the event that established the origin of the aerodynamic bridge design is probably the failure of the Tacoma Narrows suspension bridge in 1940, caused by torsional flutter. This is probably the most evocative example of bridge collapse due to the wind action and gave rise to a series of studies aimed to consider bridge aerodynamics as a potentially crucial element during the design phase.

The interaction between the structure and the incoming wind gives rise to three main categories of effects:

- Static deformation caused by the mean value of the wind velocity;
- Response to the fluctuating part of the wind velocity, for the turbulence of the boundary layer;
- Aeroelastic phenomena due to the mutual interaction between the flow and the motion of the structure.

where the last category includes heaving and torsional instabilities and vortex-induced vibrations (VIV) of bridge decks, as well as dynamic effects on structural elements like bridge cables. The present work deals with the phenomenon of vortex-induced vibrations, which is a relatively common problem affecting a potentially large variety of bridge decks.

Bridge vortex-induced vibrations occur because of the alternate detachment of vortices from the surface of the deck, which is subjected to a dynamic across-wind force fluctuating at the same frequency of the vortex shedding. As better described in the following chapter, the phenomenon can be incompatible with the use of the bridge especially in case of lock-in, which is a condition of synchronization between the structure

motion and the vortex-shedding force leading to a magnification of deck oscillations. The relatively common occurrence of this phenomenon is due to the quite low wind speed values at which it is usually observed and the potentially wide range of velocity over which it can continue. Vortex-induced oscillations can arise in terms of both heaving and torsional motion of a bridge deck, with possible consequent great discomfort for the users and/or fatigue damage accumulation on some structural elements caused by the oscillation cycles.

Last decades provided several examples of bridge decks suffering because of VIV, which leaded to search for different solutions for this kind of problem. A famous case of VIV concerned the Storebælt Bridge, Denmark (Larsen et al., 2000; Frandsen, 2001), a suspension bridge with a main span of 1624 m, which showed low-frequency vertical oscillations of the main girder, considered unacceptable with respect to the comfort of the bridge users (Figure 1.1). Low-frequency vibrations were observed during the last phase of deck erection and roadway surfacing at moderate wind speeds of approximately 5-10 m/s, indicative of vortex-induced motion. To mitigate the vortex-induced oscillations, appropriate aerodynamic appendices (guide vanes) had to be installed.

Another famous example is the case of the Trans-Tokyo Bay Crossing Bridge, Japan (Fujino and Yoshida, 2002). This is a ten-span continuous steel box-girder bridge with a main span of 240 m and variable cross-section height; the vibration amplitude exceeded 50 cm, occurring for the first vertical mode in the wind speed range 13-18 m/s (Figure 1.2). A large amount of experimental tests was performed to develop the best solution to suppress vibrations sufficiently and, even if several aerodynamic additions were tested, finally the installation of TMDs along the bridge girder was necessary.

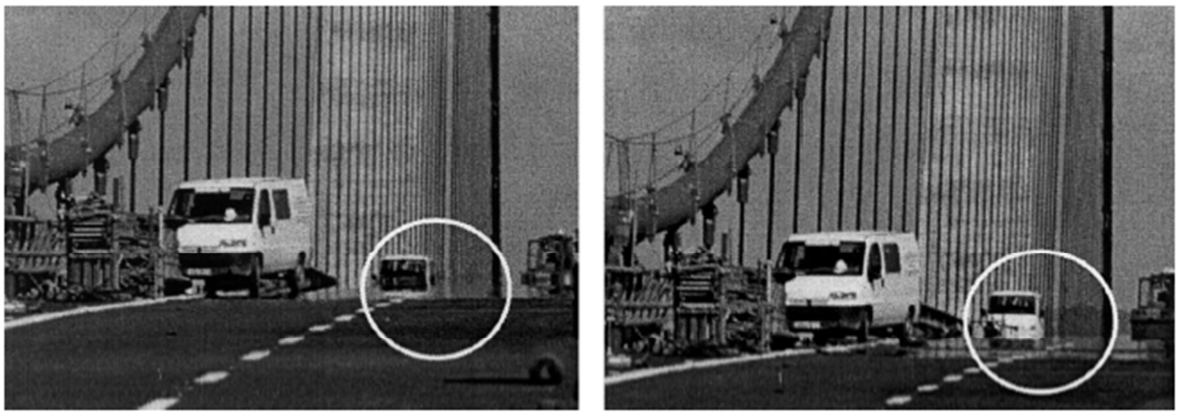

Figure 1.1. View along the deck of Storebælt Bridge at crest (left) and trough (right) of a large amplitude vertical (Larsen et al., 2000).

Figure 1.2. Video photos of vortex-induced first mode vibration of the Trans-Tokyo Bay Crossing Bridge at two instants of time (Fujino and Yoshida, 2002).

A well-known and recent case of VIV is represented by the Volgograd Bridge, Russia, which showed large vertical vibrations in May 2010 with a maximum peak-to-peak amplitude of almost 80 cm (Figure 1.3). The bridge had been opened to traffic few months earlier, in October 2009, and it was closed for such a VIV event, becoming an attraction on the web too. According to meteorological data, average wind speeds between about 11 m/s and 15 m/s were recorded when large oscillations were observed; the match between the frequency of oscillation and the natural frequency of the structure for the vertical vibration indicated the presumable synchronization between deck motion and vortex shedding. The bridge is characterized by a main span of 155 m with a steel deck and a trapezoidal box girder cross section with lateral cantilevers. To suppress the wind-induced oscillations, semi-active TMDs were designed and installed inside the girder (Weber et al., 2013).

The cases reported above represent only a part of the available examples and point out how appropriate and potentially complex and expensive countermeasures have to be taken. In addition, both the two latter examples demonstrate the possibility of significant VIV response not only for cable-supported bridges and, in the case of the Volgograd Bridge, even for relatively limited span length.

Bridge deck aerodynamics and, in particular, sensitivity to vortex shedding are determined by the interaction between the body and the incoming flow. The flow pattern is primarily influenced by the shape of the deck cross section. Its geometry is the result of both the basic shape, composed by structural elements, and other geometric details, such as sharpness of the edges, lateral screens or traffic barriers characterized not only by their dimensions but also by the amount and the distribution of the openings along their surface, fairings, aerodynamic devices (e.g. guide vanes) for VIV suppression.

Figure 1.3. Views of the Volgograd bridge (top) and of its deck during the VIV phenomenon observed in 2010 (bottom) (Corriols and Morgenthal, 2012).

Figure 1.4. View of the structure (top) and of the deck (bottom) of the Humen Bridge. In the deck view, the lateral walls applied temporarily are indicated.

A brand new example of bridge deck aerodynamics modified by local additions is represented by the Humen Pearl River Bridge, located in Guangdong province, China, which exhibited violent vibrations caused by the wind on 5th May 2020. Local authorities described this occurrence as probably caused by lateral retaining walls applied to the deck for maintenance operations, with a consequent bridge aerodynamics modification (Figure 1.4).

The relative frequency of VIV occurrence and the difficult predictability of bridge VIV response intensity make this phenomenon important to be considered even during the design phase of a bridge, because of the considerable difficulty to solve it later. The usual procedure to correctly assess vortex-induced oscillation of a deck is to perform aeroelastic wind tunnel tests on a bridge model. The performance of such tests may present some difficulties and issues, possibly deriving also from the specific bridge deck investigated, and requires a non-negligible amount of time and money.

Different procedures for VIV response prediction were developed over the years. Recently, the use of computational fluid dynamics (CFD) to perform numerical simulations on bridge decks is assuming more and more importance. A remarkable amount of promising results is provided by literature for the determination of aerodynamic forces and pressures on stationary decks. Nevertheless, CFD simulations in case of oscillating bodies and aeroelastic phenomena like VIV are certainly more complex.

The prediction of the VIV response of a bridge and, in general, of a bluff body has been pursued over last about fifty years from the mathematical point of view too. Several mathematical models available in the scientific literature were formulated for VIV response estimation of elongated bodies with a reasonably constant cross section, such as cylinders. In this context, simplified and representative cross-section geometries were originally studied, like circle, square or rectangles, also with the purpose of extending the results to a practical use for bodies like chimneys, cables or bridges. In particular, the variety of bridge cross-section shapes is certainly considerable, due to the possible different geometries of the deck and to non-structural elements possibly installed on it, leading the mathematical prediction of VIV response to be extremely challenging for bridge decks. Nevertheless, the scientific interest generated by such a topic and the potential practical usefulness of a suitable approach able to support or replace, even partially, wind tunnel tests during the bridge design phase make the investigation of such issue attractive.

Finally, indications provided by standards and codes have to be mentioned. The wind action has to be considered by a bridge designer according to regulations and some approaches are provided to evaluate the VIV response of a structure. As an example, the Eurocode (EN 1991-1-4, 2005) provides two different approaches to estimate the peak value of the VIV response amplitude of a structure. Nevertheless, they did not exhibit a sufficient suitability for bridge decks in general.

Consequently, bridge deck VIV response prediction is a still open challenge, which is worth investigating both from the scientific point of view and with a possible practical purpose for bridge design.

1.2. Motivation and outline of the work

The present work aims to investigate the influence of non-structural cross-section geometric details on the vortex-induced vibration of a bridge deck, over a realistic range of wind angle of attack, from the point of view of the deck response experimentally observed and with regard to the mathematical modeling of the phenomenon.

A systematic investigation of the combined effects of sectional details and angle of attack variation is certainly meaningful from the point of view of bridge deck VIV response. Indeed, scientific literature provides several studies in which VIV response is assessed in presence of local geometric modifications or additions to the deck section (screens, barriers, fairings, guide vanes), and, at the same time, the aerodynamic investigation of a certain section geometry or local elements added to the deck should be preferably performed over a realistic range of flow angle of incidence. In addition, the inclusion of such factors in the assessment of mathematical model performances may certainly increase the substance and the practical interest of the modeling work.

In the present work, static and dynamic wind tunnel tests were conducted on a realistic bridge deck cross section progressively altered through local geometric changes: a first modification of the sharpness of deck lower corners, then a much more remarkable change obtained by installing a lateral traffic barrier quite transparent to the flow, finally the addition of a second barrier, very similar to the first one in terms of cross-flow dimension but with a lower degree of transparency. The geometric layouts so obtained were all tested over an appropriate range of angle of attack values. A large VIV response variety due to the combined effect of even relatively limited variations of cross-section

details, like barrier openings, and of the wind angle of attack was found during aeroelastic tests.

The variability of VIV response and its sensitivity to several factors remark the potentially large amount of wind tunnel tests necessary for the aerodynamic description of a bridge deck during the design phase of a structure. Any tool able to support the process of bridge deck oscillation assessment can be certainly useful. In particular, a mathematical approach able to provide even an approximate estimation or a qualitative prediction of the deck VIV behavior could be useful to optimize the wind tunnel test campaign and/or to obtain information about the most critical configurations to investigate.

In this context, firstly, qualitative suppositions about sensitivity to vortex shedding and VIV response were formulated, based on results of static wind tunnel tests. The different cross-section layouts were compared and supposed to be differently prone to vortex-induced oscillation on the basis of aerodynamic force measurements, including the aerodynamic damping estimation according to the quasi-steady theory. In this context, an experimental estimation of aerodynamic damping through free-decay tests was also carried out for different values of wind velocity.

Finally, two mathematical models for VIV response prediction were studied and their performances were extensively assessed. In particular, a non-linear wake oscillator model derived from Tamura's model (Tamura and Matsui, 1979) and a very simplified single-degree-of-freedom approach for peak response estimation were studied and applied to the investigated bridge deck for all the configurations tested. Wind tunnel test results were employed to calibrate the models and to assess the quality of their performances. The variety of VIV response typologies produced by cross-section details and flow angle of attack variation provided a large amount of tested cases, which allowed to assess the main qualities and limitations of the mathematical models with considerable comprehensiveness.

2. Literature review

2.1. Introduction

Accurate analyses and investigations of the vortex-induced vibrations of bridge decks require a basic knowledge about a more general topic: vortex shedding from a bluff body immersed in a fluid flow. As a matter of fact, a bridge deck cross section can be usually regarded as equivalent to a bluff body, due to the flow separation generated over a considerable portion of its surface by the interaction with a fluid stream.

Vortices are shed first from one side of the body and then from the other one, giving rise to a staggered vortex distribution in the wake, and a consequent non-symmetric variation of pressures is generated around the body. The lack of symmetry of such phenomenon generates oscillating pressures imposed on the structure, causing non-negligible vibrations if the structure is able to oscillate, usually named vortex-induced vibrations (VIV).

The phenomenon of vortex-induced vibrations has been widely investigated over the years in different ways, with particular attention to its effects on buildings and structural elements. The scientific and practical interest in this phenomenon led to develop different procedures for VIV response prediction, including experimental tests, numerical simulations and a variety of mathematical models.

The content of the present dissertation requires to introduce specifically some aspects of the investigated topic, along with meaningful and explanatory works available in scientific literature. Such main aspects are herein listed:

- Vortex shedding from stationary bluff bodies;
- Vortex shedding from oscillating bluff bodies, giving rise to vortex-induced vibrations (VIV);
- Vortex-induced vibrations of bridge decks;
- Effects of cross-section details on bridge deck VIV response at different flow angles of attack;
- Mathematical modeling of VIV response.

2.2. Vortex shedding and VIV

2.2.1. Vortex shedding from stationary bluff bodies

The occurrence of a vortex wake behind a body has been largely observed and studied over decades, since ancient times. Going back to the fifteenth century, Leonardo da Vinci sketched a row of vortices generated in the wake behind a pile in a river flow (Lugt, 1983). In 1878, Strouhal noticed that tones generated by a taut wire put into an air flow were proportional to the wind velocity divided by the wire thickness. In addition, he also observed a great sound magnification when the natural tones of the wire coincided with the wind-generated Aeolian tones. In the same period, in 1879, Lord Rayleigh observed a violin string vibrating primarily in the across-wind direction, rather than along the flow. Some years later, the periodicity of a cylinder wake was related to vortex generation by Bernard, in 1908, and to the formation of a stable row of staggered vortices by von Karman, in 1912 (Blevins, 2001). As reported by Buresti (1998), von Karman carried out an estimation of stability of a vortex within two parallel rows of ideal inviscid vortices of opposite sign, observing that the configuration was stable uniquely for a particular anti-symmetric configuration with a critical spacing ratio l/h, where l is the distance between consecutive vortices and h the separation between the two rows (Figure 2.1).

A large amount of scientific publications about vortex shedding from fixed bluff bodies has been published over the years and several review works are also available about this topic (Wille, 1960; Marris, 1964; Morkovin, 1964; Berger and Wille, 1972; Sarpkaya, 1979; Oertel, 1990; Williamson, 1996; Zdravkovich, 1996; Buresti, 1998; Matsumoto, 1999; Blevins, 2001).

In line with the content of the present work, infinitely long and rigid cylinders are here specifically considered. Such ideal condition is approximately reproduced in wind tunnel by a sectional model, a cylinder characterized by high stiffness, sufficient length compared to its cross-section dimensions (aspect ratio), appropriate end conditions, limited blockage. These conditions are particularly suitable to reproduce the behavior of elongated and slender structures like bridge decks.

Assuming an infinitely long cylinder allows to consider the problem from a two-dimensional point of view: the elongated body is geometrically defined uniquely by its cross section. The main cross-section parameter for vortex-shedding investigation is certainly the Strouhal number (St), defined as follows (Strouhal law):

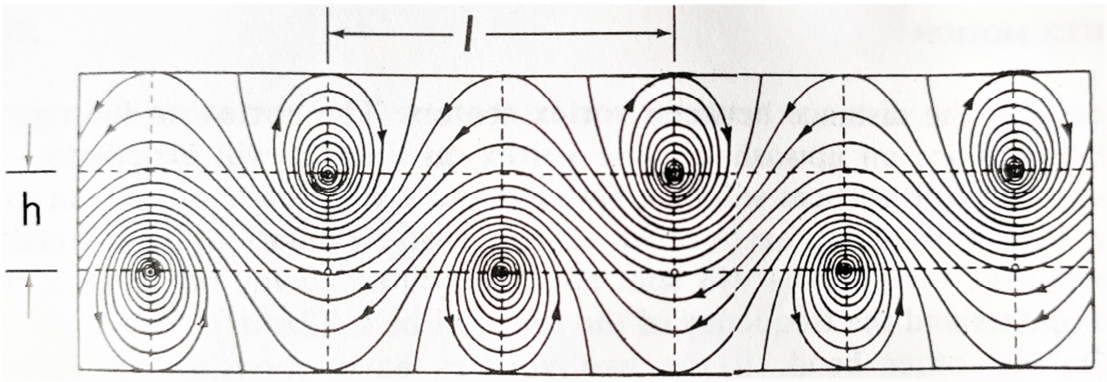

Figure 2.1. Von Karman's ideal vortex street, $h/l = 0.281$ (Blevins, 2001).

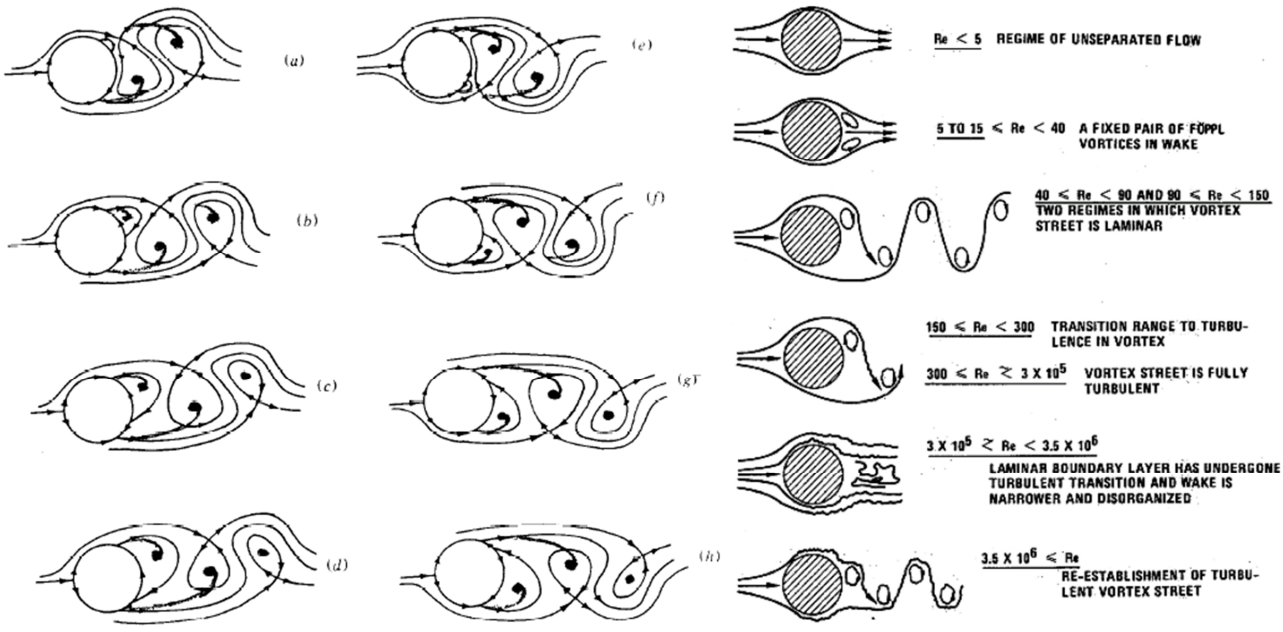

a) b)

Figure 2.2. Simplified vortex-shedding model (a) (Perry et al., 1982). Major Reynolds number regimes of vortex shedding from a smooth circular cylinder (b) (Lienhard, 1966).

$$St = n_s \cdot \frac{D}{U} \tag{2.1}$$

where n_s is the frequency of vortex shedding from the body, D is a reference dimension of the cross section and U is the mean velocity of the incoming flow. The Strouhal number depends on the cross-section geometry and it is actually a non-dimensional expression of vortex-shedding frequency for an elongated body.

The two-dimensional circular cylinder has been probably the most frequently investigated geometry over the years. As a matter of fact, a large part of reviews available in literature about this topic deal with vortex shedding from elongated circular cylinders. The circular cylinder is characterized by an axisymmetric cross section and a completely round surface; if the cylinder exhibits a smooth surface too, with negligible effects given by roughness, a classical vortex street can be observed behind the body. A simplified vortex-shedding outline, derived from Perry et al. (1982), is reported in Figure 2.2(a). Vortex shedding from a smooth, circular cylinder is a function of Reynolds number (*Re*), defined as follows:

$$Re = \frac{UD}{\nu} \tag{2.2}$$

where U is the free stream velocity, D is the diameter of the cylinder and ν is the kinematic viscosity of the fluid. *Re* is decisive for the location of separation points on the body surface and for the vortex-shedding frequency value: a “critical” Reynolds number range leads to a reduction of wake width and increase of the Strouhal number. Figure 2.2(b) reports an outline of main Reynolds number regimes of vortex shedding as summarized by Lienhard in 1966. A detailed description of all regimes for a circular cylinder was provided by Roshko (1993) and Williamson (1996).

A substantial difference is observable in case of a cylinder cross section with sharp edges forcing the separation of boundary layers. In this case, the flow separation is fixed by the shape of the body regardless Reynolds number value. For bodies with fixed separation, value and direction of the velocity outside the boundary layer in the separation region, and thus the amount of shed vorticity and the width of the wake, are crucially determined by the shape of the forebody, or rather the portion of body surface located before flow separation (Buresti, 1998).

The most widely investigated sharp edged cross section is probably the rectangular one. A large amount of scientific works have been published over the years about vortex shedding from rectangular cylinders with different ratio between along-wind and across-flow dimensions (side ratio). Rectangular cylinder side ratio determines the portion of body surface located downstream of flow separation, usually named afterbody, which may drastically affect the vortex-shedding process and the geometry of the wake behind the body. This can be appreciated by considering cylindrical bodies with a rectangular cross section, having a fixed cross-flow dimension (D) and increasing along-wind length (B). For a very limited side ratio B/D, the vortex-shedding frequency is not significantly different from that of a flat plate normal to the flow ($St \simeq 0.145$) and it does not depend on Reynolds number. When a certain geometric condition occurs ($B/D \simeq 0.6$), the increasing interference between the separated shear layers and the downstream corners of the rectangle significantly modifies the shedding process, and the consequent mean and fluctuating forces.

For a certain side ratio range, the situation may become considerably complicated, since the vortex-shedding frequency is affected by Re despite the fixed flow separation. Okajima (1982) found significant Reynolds number dependence of the Strouhal number for rectangular cylinders with $B/D = 2$ and $B/D = 3$, while such dependence was observed to be much weaker for a square cylinder and disappeared almost completely for $B/D = 4$ (Figure 2.3).

In 1990, Knisely provided a comprehensive review on Strouhal numbers for rectangular cylinders with different B/D value (Figure 2.4(a)). In such a work, a large amount of new data was reported to show the effect of the flow angle of attack (α) on St for several side ratios, introducing another important factor; an example is reported in Figure 2.4(b). The flow angle of incidence may affect drastically the vortex-shedding frequency, as well as pressures and forces generated on the body, since rectangular sections are not axisymmetric as the circular one.

Vortex shedding from rectangular cylinders has been introduced with care, for the closeness of such geometry to bridge deck cross sections. Among simple geometric shapes, indeed, the rectangular ones exhibit some similarities with typical bridge deck cross sections, from the point of view of both side ratio and flow separation. As a matter of fact, bridge decks are usually characterized by an elongated section and sharp edges fixing flow separation, especially on the upper side due to the usual presence of screens or barriers. For

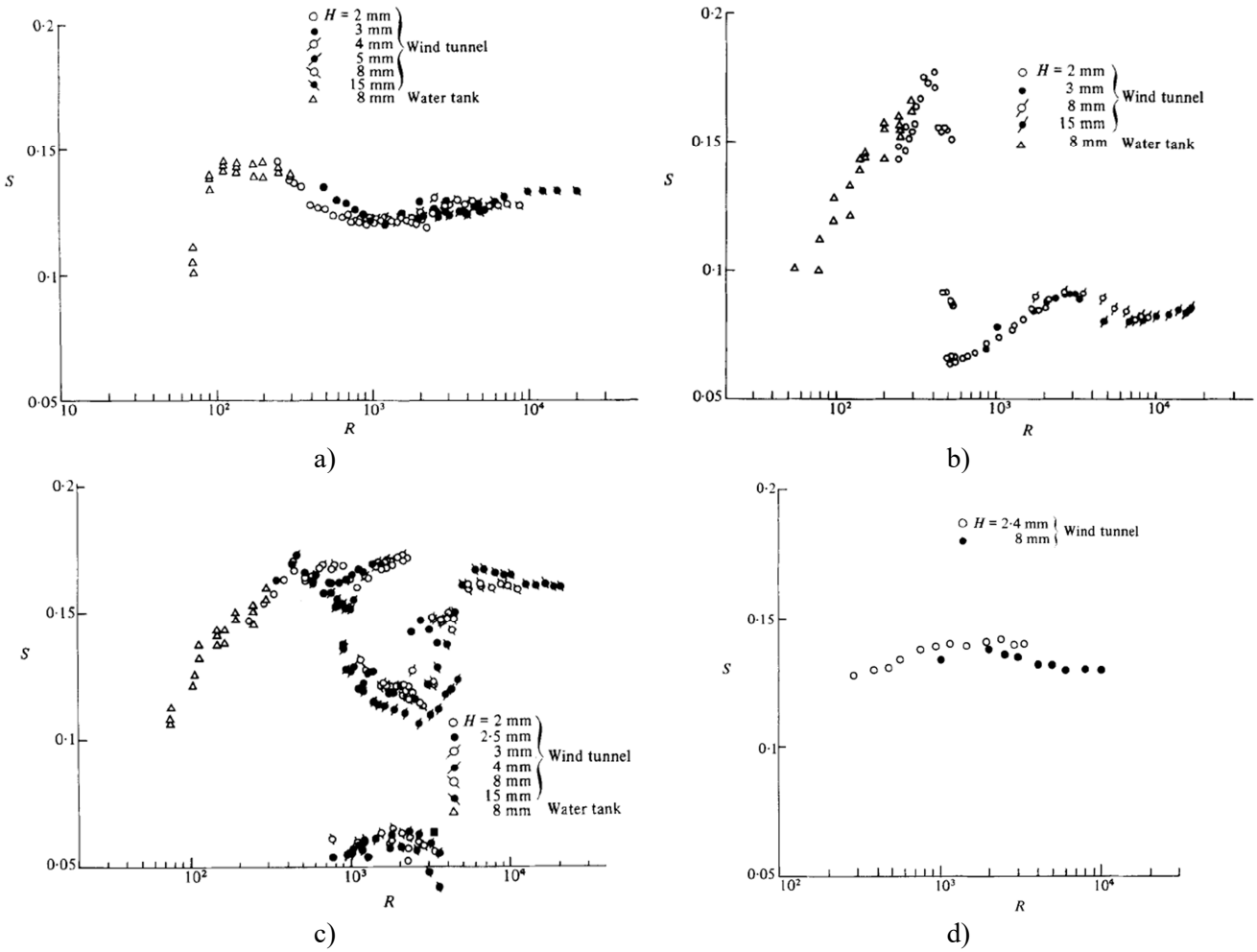

Figure 2.3. Variation of Strouhal number with Reynolds number for rectangular cylinders with side ratio $B/D = 1$ (a), $B/D = 2$ (b), $B/D = 3$ (c), $B/D = 4$ (d) (Okajima, 1982).

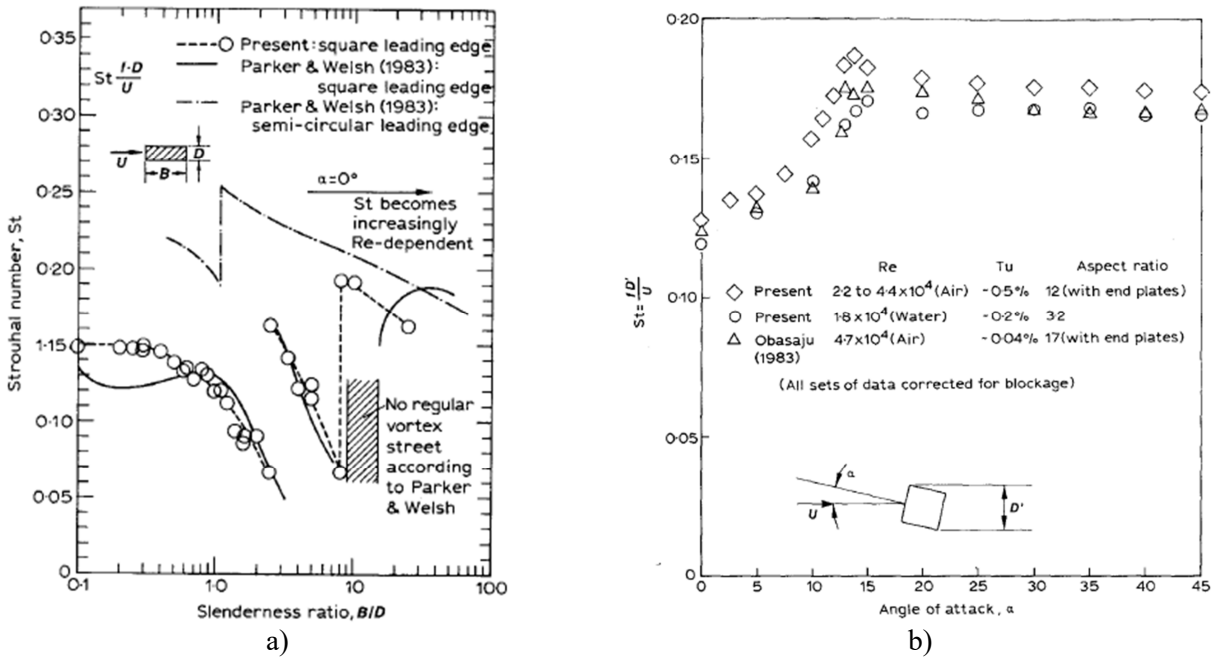

Figure 2.4. Strouhal number for rectangular cylinders for different side ratio at zero angle of attack (a) and for $B/D = 1$ at different values of α (b) (Knisely, 1990).

this reason, possible similarities in terms of vortex-shedding behavior between bridge decks and rectangles are suggested. On the other hand, most of times a bridge deck cross section is perfectly or almost symmetric with respect to the vertical direction, while upper and lower side are markedly different; on the contrary, rectangles exhibit a double axial symmetry. From this point of view, the flow angle of attack variation may be expected to produce even more remarkable effects on Strouhal number and pressure distribution for bridge decks, making the study of flow incidence effects particularly meaningful.

2.2.2. Vortex-induced vibrations of bluff bodies

The occurrence of vortex shedding, described so far for a stationary body, may give rise to further effects in case of a body able to oscillate. The flow pattern can be dramatically modified in case of both imposed vibrations and body free to oscillate under the action of the vortex-shedding fluctuating force.

On the basis of experience and knowledge about VIV, a body free to vibrate subjected to vortex shedding exhibits a self-excited and self-limited oscillation, varying with the incoming flow speed and, hence, with the vortex-shedding frequency according to the Strouhal law (Eq. (2.1)) As reported by Bearman (1984), probably the two most remarkable effects are:

- The match between vortex shedding and oscillating body frequencies over a certain range of flow velocity (Figure 2.5(a));
- The marked increase of the correlation length observed when the vortex-shedding frequency coincides with the body frequency (Figure 2.5(b)).

The two occurrences above mentioned can be observed in case of lock-in condition: when the vortex-shedding frequency is close to the natural one of the structure, a magnification of across-wind oscillation is usually observed, and the Strouhal law is violated for a certain range of wind velocity. The lock-in is actually a synchronization condition where the motion of the body controls the vortex-shedding process.

A clear example of lock-in is reported in Figure 2.5(a), where results obtained by Feng in 1968 for a freely vibrating circular cylinder are shown, in terms of ratio between vortex shedding and natural frequencies against reduced velocities (U_{red}), obtained by

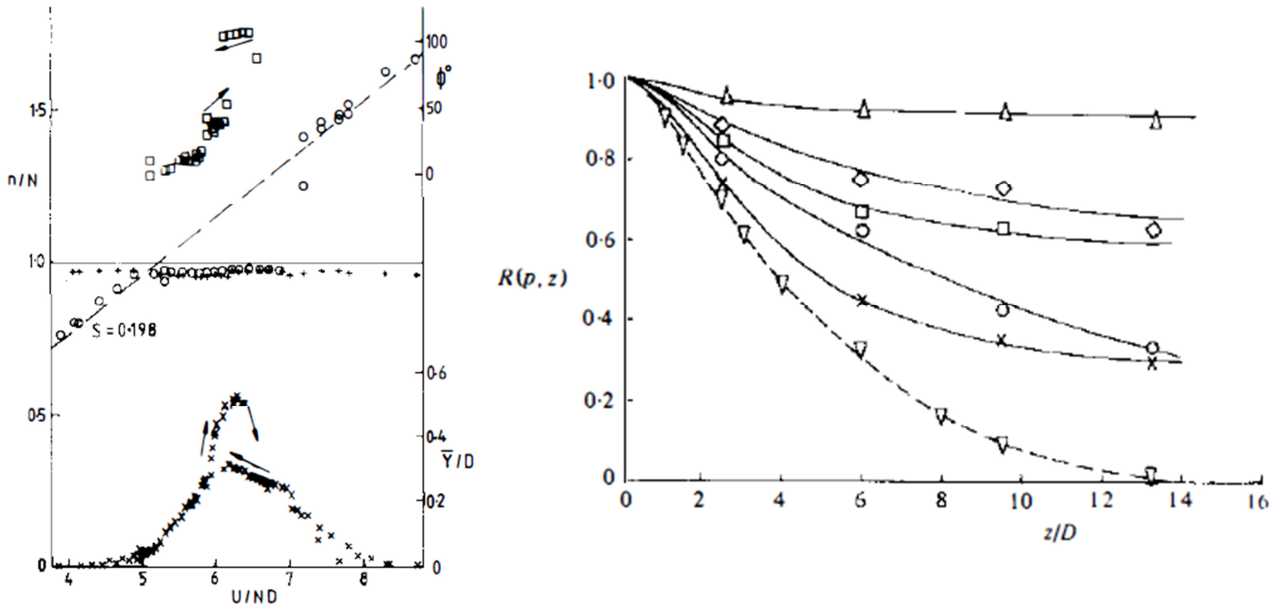

a) b)

Figure 2.5. Ratio between vortex shedding (n) and body (N) frequencies for different reduced wind velocities ($U_{red} = U/ND$) for a freely vibrating circular cylinder (a) (Feng, 1968). Correlation of surface pressures ($R(p, z)$) against spanwise separation (z/D) for a square cylinder from stationary (∇) to oscillating condition at lock-in (Δ) with amplitude $\overline{Y}/D = 0.1$ (b) (Bearman and Obasaju, 1982).

dividing the incoming flow speed U by frequency and diameter of the oscillating cylinder. The two frequencies are substantially equal over a reduced flow speed range between about 5 and 7 (lock-in range) with a consequent Strouhal law violation. The vibration amplitude $\overline{Y}/D$ reaches its maximum value inside the lock-in range for increasing wind velocity, while for reducing velocity a lower peak value of $\overline{Y}/D$ was found, giving rise to a hysteresis effect, quite typical in case of remarkably large lock-in curves.

The peak amplitude at lock-in is dependent on the Scruton number (Sc) of the vibrating system: the higher is Sc, the lower is $\overline{Y}/D$ maximum value. Such quantity depends on mass and mechanical damping of the system and it is usually defined in the following way:

$$Sc = \frac{4\pi m \zeta_0}{\rho D^2} \tag{2.3}$$

where m is the mass per unit length of the oscillating body, ζ_0 is the mechanical damping ratio of the system, ρ is the air density and D is a body reference length. In case of an elongated cylindrical body with a constant cross section, D is usually the cross-flow sectional dimension. For rectangular cross sections or other geometries with marked

difference between cross-flow (D) and along-wind (B) dimensions, as for bridge decks, the Scruton number may be expressed in the following way in several cases:

$$Sc = \frac{4\pi m \zeta_0}{\rho B D} \tag{2.4}$$

Due to its influence on the response amplitude, *Sc* value also affects the lock-in range extension, which was found to be connected with the vibration amplitude exhibited by the body. As a matter of fact, forced vibration experiments provided wider synchronization ranges for higher oscillation amplitudes (Bearman, 1984).

As said before, the lock-in occurs in case of vortex-shedding frequency close to body natural frequency. According to the Strouhal law (Eq. (2.1)), the theoretical vortex-resonance flow speed corresponds to a vortex-shedding frequency equal to the natural one. The location of such a velocity value over the lock-in range can be extremely variable for different cross-section geometries. An example is reported in Figure 2.6, where the lock-in curves for a circular and a D-shaped cylinder are shown (Feng, 1968), with the resonant point highlighted. In the former case (Figure 2.6(a)) the resonant point coincides approximately with the onset lock-in velocity, while in the latter (Figure 2.6(b)) it is very close to the upper bound of the range. In this context, further observations are provided by scientific literature: as an example, Shiraishi and Matsumoto (1983) distinguished some cross-section typologies with different VIV response also including observations about the resonant point position over the lock-in range.

With regards to the increase of vortex-shedding correlation along the body, it was associated with a magnification of the fluctuating lift force at lock-in. In particular, the motion of the body gives rise to a synchronization of vortex shedding along the body in the longitudinal direction. This provides an increase of the correlation length with the amplitude of vortex-induced oscillation, with a consequent growth of the fluctuating lift force acting on the body.

Figure 2.5(b) reports correlation of surface pressure for a square cylinder (Feng, 1968) in case of stationary body and in case of body oscillating at a fixed amplitude for different reduced flow velocities. An increasing correlation starting from the stationary condition up to the oscillation inside the lock-in range is clearly observable.

The effect of correlation growth on VIV response can certainly be significant and it is included in different ways also in mathematical approaches for VIV modeling. In

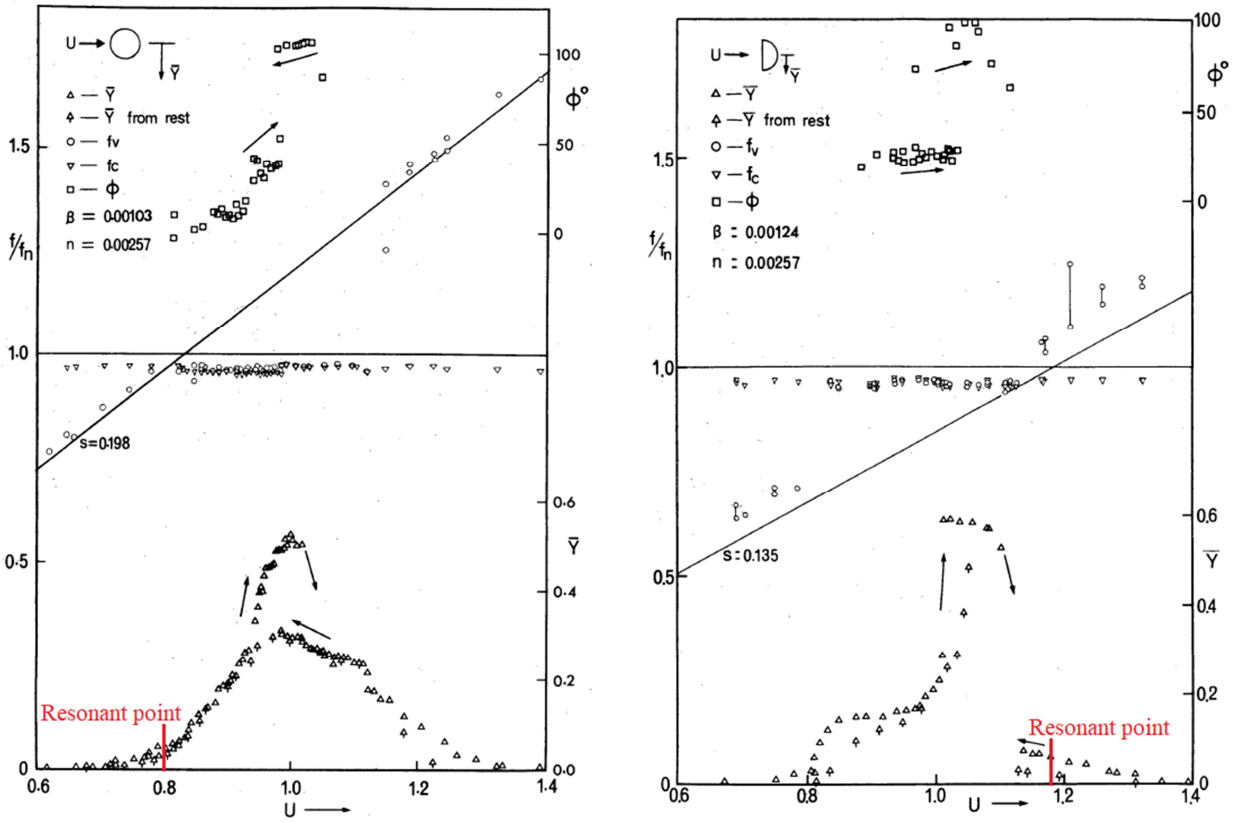

a) b)

Figure 2.6. VIV response of cylinders with circular (a) and D-shaped (b) cross section (Feng, 1968). The theoretical vortex-resonance flow speed is highlighted (red line).

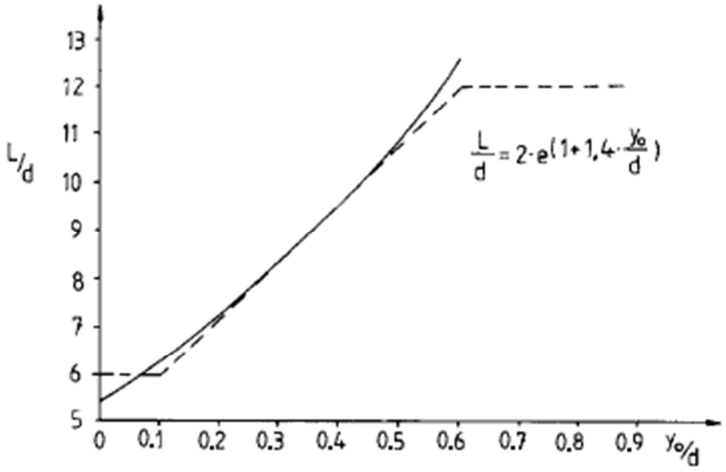

Figure 2.7. Dimensionless correlation length (L/d) against dimensionless response amplitude (y_0/D) (Ruscheweyh, 1990).

particular, Ruscheweyh's model (Ruscheweyh, 1990) is probably the best-known mathematical model especially based on the vortex-shedding force spanwise correlation. In such a work, a linear approximation for the spanwise correlation length increase was proposed for three different ranges of response amplitude, as shown by the dashed line in Figure 2.7. The correlation increase is directly included in the response amplitude expression through an appropriate factor depending on the correlation length. It is worth to highlight that the linear approximation proposed by Ruscheweyh is constant for a vibration amplitude lower than 10 % of the body reference length (Figure 2.7), which is a typical range of interest for vortex-induced oscillations of a multitude of structures. For this reason, such approach is particularly simple but it could not be suitable in case of a significant correlation increase over this range of amplitude. Nevertheless, Ruscheweyh's work encourages to take into account the role played by vortex-shedding spanwise correlation as critical for VIV response evaluation.

On the other hand, other models provided by scientific literature (e.g. Hartlen and Currie, 1970; Skop and Griffin, 1973) assume a different value for the amplitude of the fluctuating lift coefficient due to vortex shedding in case of stationary and oscillating body. This is consistent with a growth of the lift force when the body is vibrating due to vortex-shedding correlation increase.

2.2.3. Vortex-induced vibrations of bridge decks

The history of bridge design over the years, starting in particular from the second half of nineteenth century, has been always characterized by the need to face the action of wind on bridge structures. As reported by Holmes (2001), most of the early interest in this field was about drag force and along-wind actions (Baker, 1884; Kernot, 1893). However, the famous American builder of suspension bridges, John Augustus Roebling, was already aware of some dynamic effects of wind in 1855 (Steinman and Watson, 1957). Nevertheless the dynamic wind actions on bridge decks, in particular vertical across-flow forces and torsional moments, were deeply considered and investigated only after the failure of Tacoma Narrows suspension bridge (1940). In the present work, the focus is on vortex-induced vibration (VIV) of bridge decks, a phenomenon which usually does not lead to structure failure but whose occurrence is relatively frequent and may cause problems for bridge users.

The construction of flexible and weakly damped bridge structures became more and more common over last decades. This is consistent with an extension to new limits of bridge deck span length, especially in case of long-span suspension and cable-stayed bridges, from the end of twentieth century (Ehsan and Scanlan, 1990; Holmes, 2001). The reduction of weight and the design of streamlined deck cross section to improve aerodynamic performances leaded to slender and flexible structures. Nevertheless, in some cases, these features may also cause a considerable proneness to vortex-induced oscillation. Due to the self-limitation of VIV response, this phenomenon usually does not lead to the failure of a structure, as said above, but the problems for serviceability can be great. An additional problem is represented by the relatively low wind velocities related to lock-in condition in several cases and the potentially wide lock-in range extension for certain cross sections.

The limitation or suppression of remarkable vortex-induced oscillation for a given cross-section geometry can be obtained by increasing the Scruton number of the system. In particular, additional mechanical damping is provided in some cases by installing appropriate dampers, similarly to the case of Volgograd Bridge deck (Weber et al., 2013). Such a process is not simple and can also be expensive in terms of money and time. For these reasons, acting on the mechanical damping of the structure for VIV suppression is generally considered as a last resort, while the prevention of the phenomenon during the design phase is generally preferred.

The other way to act on VIV response of bridge decks is working on the cross-section shape and its geometric details. The intensity of vortex-shedding process and the extension of the synchronization range are determined by the flow pattern around the cross section, which is a consequence of its geometry. The geometry can be assumed as composed by the basic structural shape of the deck and by possible non-structural details and additions, which can also have an aerodynamic purpose. So, cross-section shape factors influencing the bridge deck response, not only in case of VIV but also in presence of other aeroelastic phenomena, can be summarized as follows:

- Basic cross-section geometry: global shape given by structural elements, side ratio, spacing and dimension of girders in case of multi-box girder bridge deck, shape of leading and trailing edges (Shiraishi and Matsumoto, 1983; Ehsan and Scanlan, 1990; Brancaleoni and Diana, 1993; Larsen, 1993; Kubo et al., 2002; Diana et al., 2006; Larsen and Wall, 2012; Yang et al., 2015);

- Fairings, guide vanes, baffles for aerodynamic performance improvement (Larsen, 1993; Kubo et al., 1993; Larsen et al., 2000; Macdonald et al., 2002; Sarwar and Ishihara, 2010; Yu et al., 2015);
- Screens. traffic barriers, railings: location on the bridge deck, dimension, transparency to the flow (Honda et al., 1992; Jones et al., 1995; Ricciardelli and Hangan, 2001; Bruno and Mancini, 2002; Kubo et al., 2002; Bai et al., 2020);
- Flaps, airfoils and other equivalent aerodynamic devices mounted on appropriate supports and/or on barriers, screens or railings (Brancaleoni and Diana, 1993; Sarwar and Ishihara, 2010).

In addition to geometric factors, a very important role is similarly played by the angle of attack of the incident flow. The variation of the wind direction can change drastically the VIV response of a bridge deck. Given the relative rotation between the wind and the body, such occurrence actually modifies the perception of the cross section by the incoming flow. Consequently, angle of attack variations are usually comparable to modification of the cross-section geometry from the point of view of the effects produced.

Scientific literature provides studies about effects produced on VIV response of cylinders with different geometries, such as square or rectangles with different side ratios, by angle of attack variation over a wide range of values (Carassale et al., 2013; Massai et al., 2018). In addition, a large part of publications cited above for cross-section geometric details provide results obtained for different angles of attack too. From the point of view of bridge deck VIV, realistic values potentially assumed by the flow angle of incidence are relatively limited, usually between about -5°/-4° and +4°/+5°. A remarkable VIV response indeed is usually related to a regular incoming flow and such a condition requires a particular orography to occur at high values of angle of attack. Nevertheless, scientific literature provides examples showing how even limited variations of the angle of attack can be related to strong effects on bridge deck VIV response, as also confirmed by the present work in Chapter 5.

Such a large amount of factors which can potentially influence the VIV response of a bridge deck makes wind tunnel tests necessary during the structure design phase in several cases. The prediction of VIV response can be actually crucial for the successful realization of a bridge. For this reason, along with wind tunnel tests usually performed, the development of suitable mathematical approaches for VIV response modeling is a challenging but attractive issue.

Mathematical modeling possibilities have been explored in the present work, taking into account the influence of both section details and angle of attack on the VIV response.

2.3. Effects of cross-section geometric details and angle of attack

A variety of works in scientific literature deals with the effects produced by cross-section geometric details on bridge deck aerodynamics and, in particular, on VIV response. The cross-section shape is the result of a primary geometry given by the structural components and a certain multitude and variety of additions, which contribute to define the flow pattern around the deck.

On the other hand, the influence of the wind angle of attack variation is assessed in several cases, usually along with the presence of certain elements installed on the deck, with the purpose of evaluating the combined effect of the two factors. As a matter of fact, a different wind incidence may change considerably the interaction between the deck and the flow, acting equivalently to an alteration of the body shape. Equivalently, the same geometric modification may produce markedly different effects for different values of the wind angle of attack.

In the present section, an overview about studies available in scientific literature is reported. Some works considered particularly meaningful and explicatory from the point of view of cross-section detail effects at different angles of attack were selected and described. For the purpose of defining a sort of classification for cross-section details, the list of geometric peculiarities and additions previously reported was reformulated with a more general terminology and three main macro-categories of elements were defined, as indicated in the outline in Figure 2.8:

- Elements composing bare deck geometry: structural components and other non-structural elements installed on the lower side or applied to the ends of the deck, like fairings, guide vanes, or baffles;
- Vertical elements rising up from the upper side of the deck, like screens, traffic barriers or railings;
- Aerodynamic devices and appendices installed on appropriate supports or on vertical elements on the upper side of the deck: flaps, airfoils, spoilers or other equivalent aerodynamic devices.

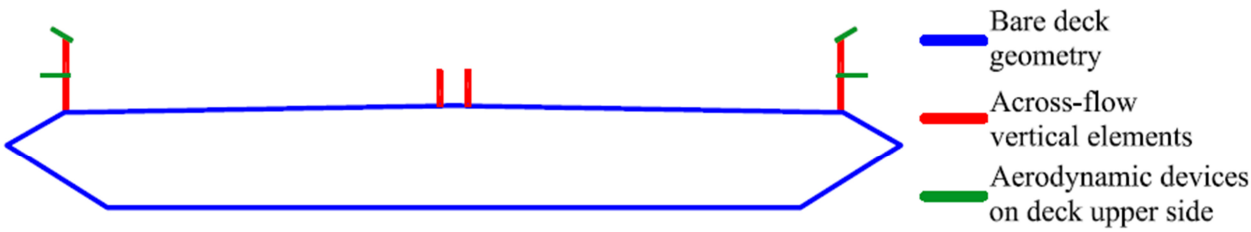

Figure 2.8. Outline of a generic section with different categories of geometric details highlighted: bare deck geometry defined by structural and non-structural elements (blue), vertical elements rising up from the deck like screens or barriers (red), aerodynamic devices installed on deck upper side (green).

Even though the present work deals with bridge deck VIV response, the selection of works reported below includes also studies aimed to address other problems, like torsional stability or aerodynamic pressure distribution, potentially meaningful and interesting from a vortex-induced oscillation perspective too.

2.3.1. Bare deck geometry

The bare deck shape, primarily determined by structural elements, is the very first geometric factor affecting the VIV response of a bridge. The ratio between along-wind and across-flow dimensions, namely the side ratio, the distance between the girders, the single or multiple box-girder design, the shape of lateral ends are the main factors deriving from the bridge deck structural design and affecting the aerodynamic behavior.

On the other hand, different typologies of fairings can be applied to the cross-section, at the ends or to its lower side, with an aesthetic and/or an aerodynamic purpose. Similarly, guide vanes or baffles can also be installed, usually on the deck lower side, in order to improve the aerodynamics of the structure. Fairings, guide vanes and baffles are fixed to deck structural elements, modifying the bare deck geometry and, consequently, the VIV response of a bridge.

A first extended study about bare deck cross-section geometry was proposed by Shiraishi and Matsumoto (1983). In their work, the problem of vortex-induced oscillations of bridges is widely addressed, from the point of view of both heaving (y) and torsional (φ) displacement, and related to the geometry of the deck cross-section. Firstly, three macro-categories of cross-sections (Group 1, Group 2, Group 3) were defined and distinguished, basing on VIV response typology (Figure 2.9(a)), flow pattern around the body (Figure 2.9(b)) and frequency of flow fluctuations in the wake (Figure 2.9(c)). Such distinctions

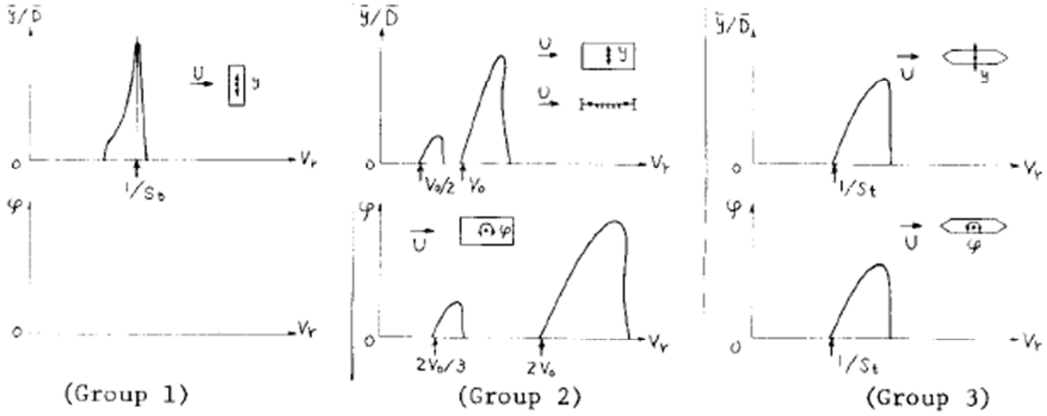

a)

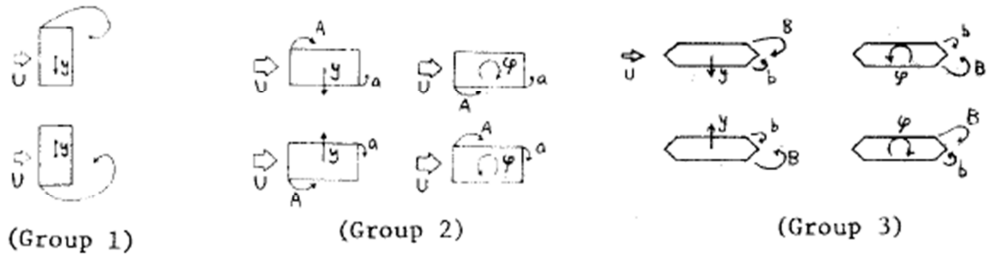

b)

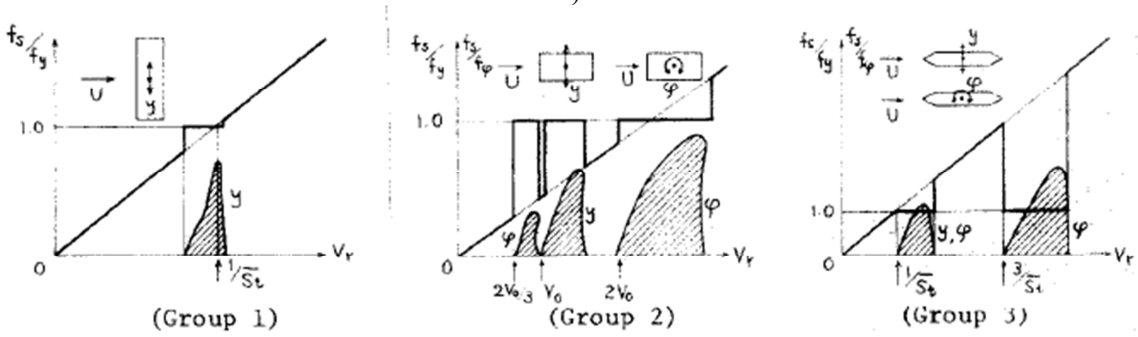

c)

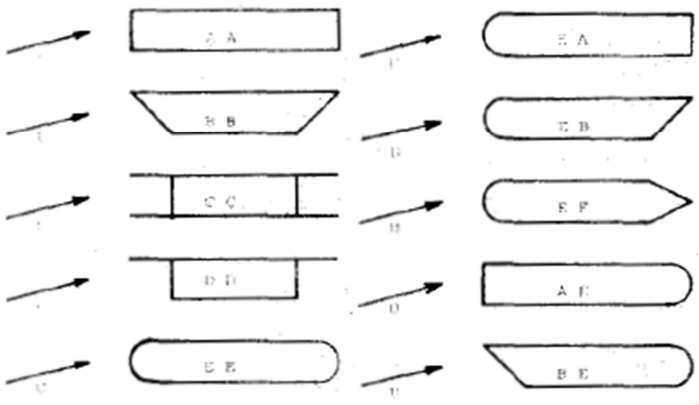

d)

Figure 2.9. Three cross-section typologies distinguished basing on VIV response amplitude (a), flow pattern (b) and velocity fluctuations in wake (c); simplified bridge deck cross-section differently elongated with different upstream and downstream end geometry at +7° angle of attack (d) (Shiraishi and Matsumoto, 1983).

were based on different typologies of heaving and torsional vortex-induced vibrations observed. Particular attention was paid to Group 2, because of the similarity of VIV response observed for many bridges to the one exhibited by this group, and several typologies of simplified potential bridge deck cross-section were obtained by starting from an elongated rectangular shape and modifying its upstream and/or downstream end in different ways (Figure 2.9(d)). Some solutions were found to be more optimized than the others for VIV control and suppression, by acting on vortex generation from the leading edge and on flow control in the wake near the trailing edge, through different geometries of both ends. The geometries shown by Figure 2.9(d) may correspond to bridge decks differently designed from the structural point of view, but also, in some cases, to the same section equipped with different fairing typologies. This is consistent with the common elongated rectangular origin of most of the sections reported by Figure 2.9(d), whose differences are local and confined to the ends.

Some years later, Ehsan and Scanlan (1990) considered two simplified outlines coming from realistic bridge cross sections (Figure 2.10(a)) and compared them to a 4:1 rectangular cylinder in terms of VIV response (Figure 2.10(b)). In such a work, which represents a milestone for the research about VIV, the main focus is the mathematical modeling of the phenomenon. In the second part of the paper, wind tunnel test results for the three sectional models are presented. The side ratios of the three tested sections are quite similar to each other, and the two bridge deck shapes differ only partially. Nevertheless, the response curves at lock-in obtained are strongly different from each other, as observable in Figure 2.10(b), from several points of view: shape of the curve,

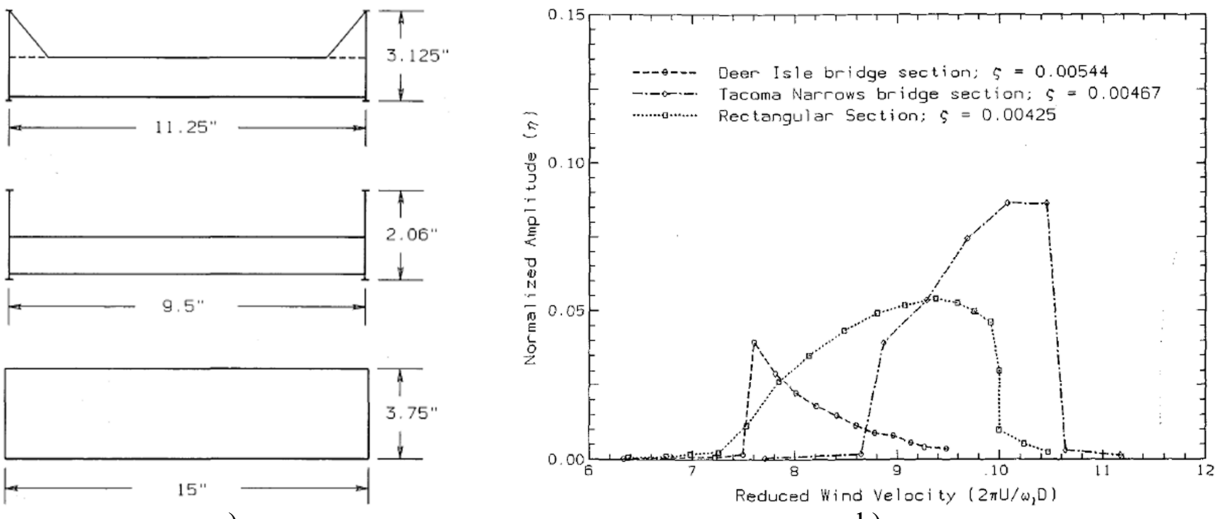

a) b)

Figure 2.10. Cross-sections tested in wind tunnel (a). Comparison of response curves at lock-in for the three sectional models tested (b) (Ehsan and Scanlan, 1990).

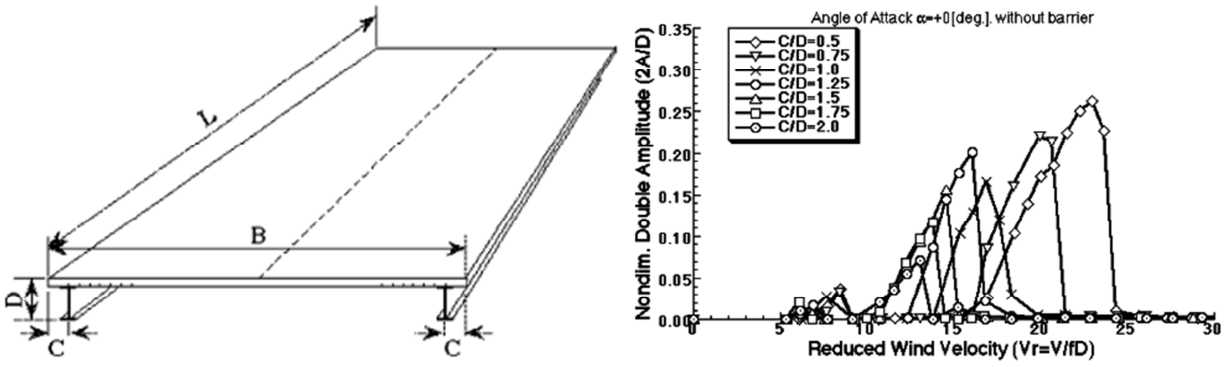

a) b)

Figure 2.11. Studied π-shaped cross-section with longitudinal main girders at variable distance from deck edges (a); heaving response curves (b) for different positions of the girders (Kubo et al., 2001)

lock-in range, peak response amplitude.

The works carried out by Shiraishi and Matsumoto (1983) and by Ehsan and Scanlan (1990) represent points of reference for the study of bridge deck vortex-induced oscillation. Nevertheless, the former provides results for simplified and not much detailed bridge sections, while the second one considers deck geometries derived from real bridges, but without focusing with particular attention on specific geometric feature effects. Literature provides several studies more specifically focused on the cross-section geometry optimization from the point of view of structural elements.

As an example, Kubo et al. (2001) carried out an optimization study about a π-shaped open bridge cross section (Figure 2.11). The section was optimized by changing the distance between the two vertical plate girders, aiming to combine structural and aerodynamic bridge deck design. Figure 2.11(a) shows the cross section of the model used to perform wind tunnel tests. The position of the two main longitudinal girders was varied by adjusting the distance *C* from the lateral ends. Dynamic test results are reported in Figure 2.11(b), where the heaving response curves for different positions of the girders are shown. As observable, both the peak response amplitude and the lock-in range are markedly influenced by the distance *C*. In particular, the decrease of *C* leads to a higher onset wind velocity, but also to a growth of the peak response.

A bridge deck typology providing meaningful examples of interaction between structural and aerodynamic design is represented by multi-box girder decks. The number, the dimension, the distance and the geometry of the box girders, in several cases, can be adjusted to optimize the deck behavior in terms of aerodynamic forces and VIV.

In this context, the extended work carried out for the design of Messina Strait Bridge

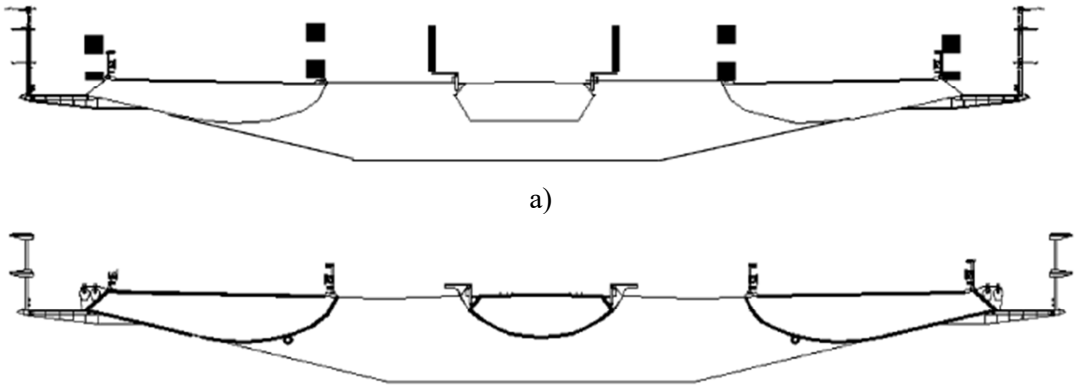

a)

b)

Figure 2.12. Optimization of Messina Strait Bridge: optimized section (a) and section affected by considerable vortex-induced vibrations (b) (Diana et al., 2006).

is certainly an evocative example. The design phase of this suspension bridge gave rise to a wide series of scientific works about the aerodynamics of the cross-section, due to the extremely long span making the wind action crucial for the behavior of the structure. Brancaleoni and Diana (1993) published a study about the cross-section optimization, highlighting the main reasons of the final choice of a three-box girder configuration. In particular, the results obtained for multi-box and single-box solutions were compared and the former was selected based on the higher flutter velocity value, which was more than two times the one obtained for the single-box configuration for the same span length.

Later, another work published by Diana et al. (2006) provided an extended investigation about the vortex-shedding action on Messina Strait Bridge, with the purpose of developing a numerical model to reproduce the vortex-shedding force. In the first part of the paper, an optimization procedure proposed in a previous work (Diana et al., 2003) is mentioned and a comparison between two different solutions differently prone to VIV is presented (Figure 2.12). Such optimization work was carried out balancing as well as possible the bridge deck behavior in terms of limiting VIV response and avoiding aerodynamic instability. The three-box geometry was selected and the most of the study was conducted on the sharpness/roundness of the lower part of the girders and on screens and barriers on the upper side, equipped with appropriate aerodynamic appendices. In particular, the central box girder shape, combined with appropriate aerodynamic devices, was found to be important for the cross-section optimization: a sharp-edged lower side of the central box girder (Figure 2.12(a)) exhibited better performances compared to the round lower side solution (Figure 2.12(b)).

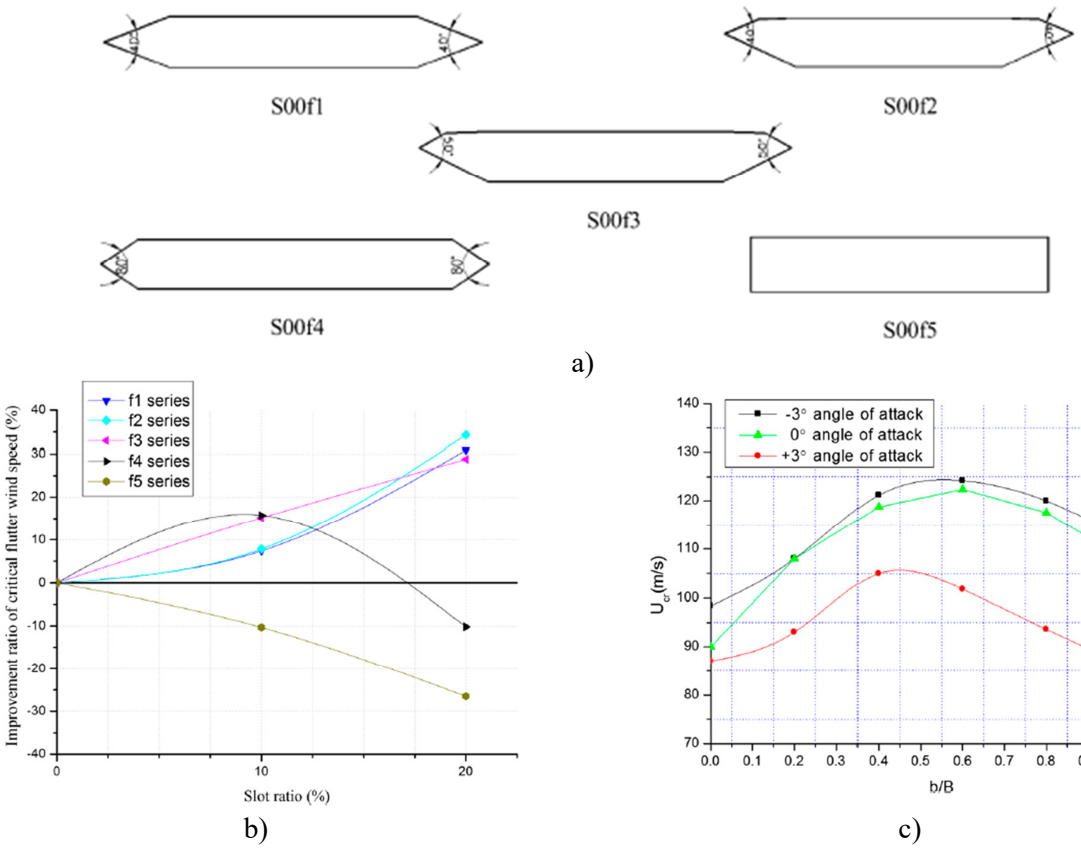

Figure 2.13. Outline of five cross-section configurations with same side ratio and different shape of edges (a). Flutter velocity variation from single box girder to twin-box solutions with different ratio between central empty slot and total width (b/B) (b). Angle of attack effect and slot ratio on flutter velocity for configuration S00f3 (c) (Yang et al., 2015).

The empty space between multiple box girders can also be assumed as a further geometric parameter for aerodynamic optimization. As an example, Yang et al. (2015) addressed the problem of aerodynamic stabilization of a twin-box girder with particular attention to the central gap dimension. The work deals with torsional stability, including both cross-section geometry and wind angle of attack effects. A variety of geometric solutions are considered: five box-girders with the same side ratio and different end shape (Figure 2.13(a)) are defined and each of them assumed in single-box and twin-box version, with a variable gap width (b) in the central part of the deck. The ratio between b and the total width B is named slot ratio and flutter velocity values are reported for each section geometry and different slot ratios (Figure 2.13(b)). Such section feature revealed to be potentially crucial, since in some cases a slot ratio increase was found to lead to a reduction of torsional stability. From this point of view, the effect of the flow angle of attack was studied for one of the sections and the combination of slot ratio and angle of attack variation was found to be potentially cause of reduced stability too (Figure 2.13(c)).

Finally, the inner gap of a multi-box girder can also be used to install appropriate devices for aerodynamic performance improvement. Laima et al. (2013) compared five different VIV mitigation systems located in the central gap of a twin-box girder deck, obtaining a considerable reduction of heaving vibration compared to empty gap configuration (Figure 2.14).

Concerning local non-structural additions modifying the bare deck geometry, like fairings, guide vanes or baffles, a variety of studies is also available in scientific literature. Similarly to the work published by Shiraishi and Matsumoto (1983), Kubo et al. (1993) conducted an accurate study about the influence of different shapes of cross-section ends. They were gradually altered by installing lateral fairings on a closed box girder (Figure 2.15(a)) and on an open deck section (Figure 2.15(b)). In this case, all the modifications were applied to the same two primary cross sections, so that the effect of local alteration produced by such geometric details was isolated and observed specifically. Heaving and torsional aerodynamic stability and VIV response were indeed assessed for the two basic cross-sections with different solutions for the geometry of the ends (Figure 2.16). The variety of results is large: aerodynamic behaviors caused by details include possible instability in some cases and different VIV response curves. In this work, the effect of the angle of attack variation is also carefully considered. The open cross section was tested for different values of the angle of attack, so that the effects produced by the modification of lateral fairings and by the flow incidence interact with each other, giving rise to a

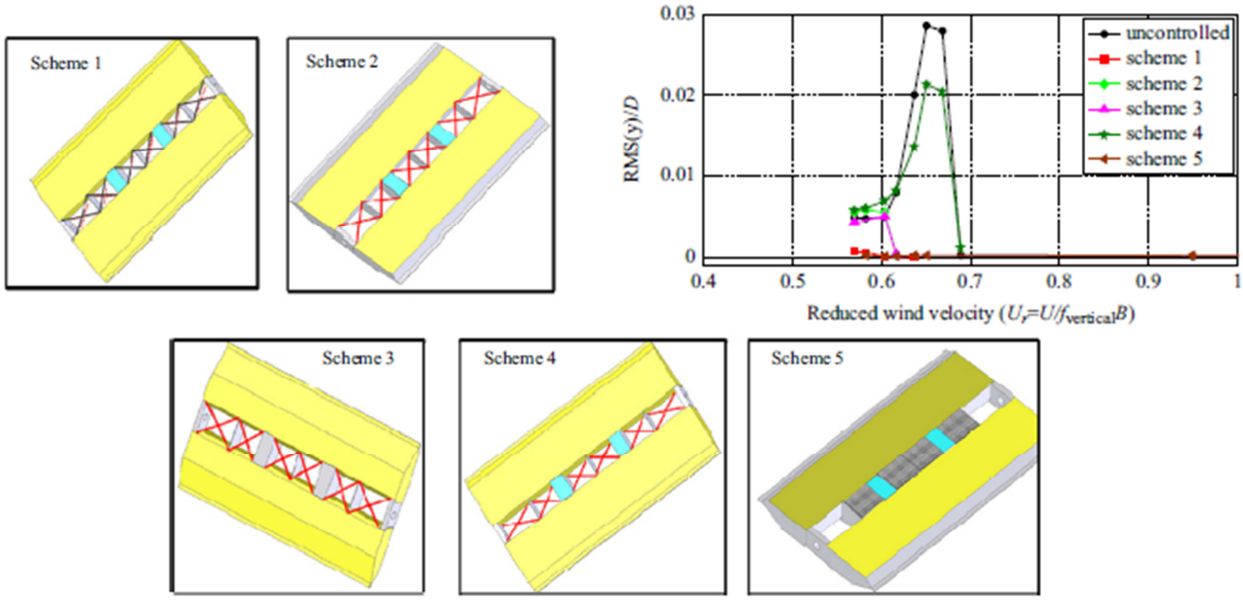

Figure 2.14. VIV mitigation systems installed inside the gap between box girders and response curves obtained for each solution (Laima et al., 2013).

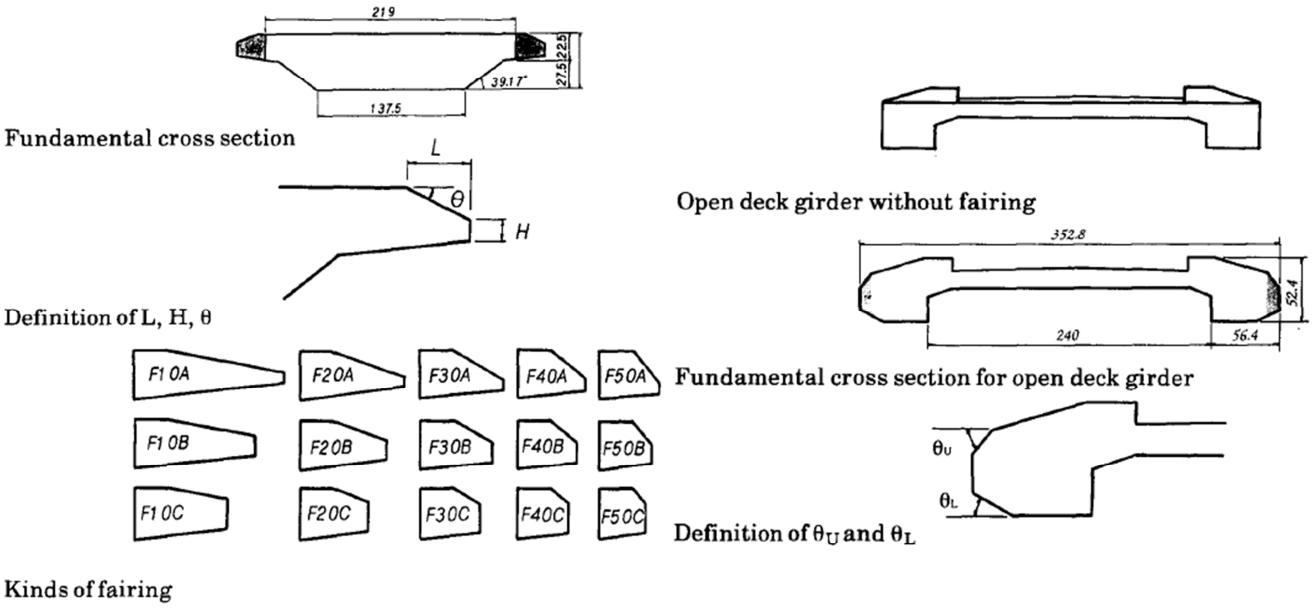

a) b)

Figure 2.15. Closed box girder altered though lateral fairings (a) and open deck section with local modification of lateral tips (b) (Kubo et al., 1993).

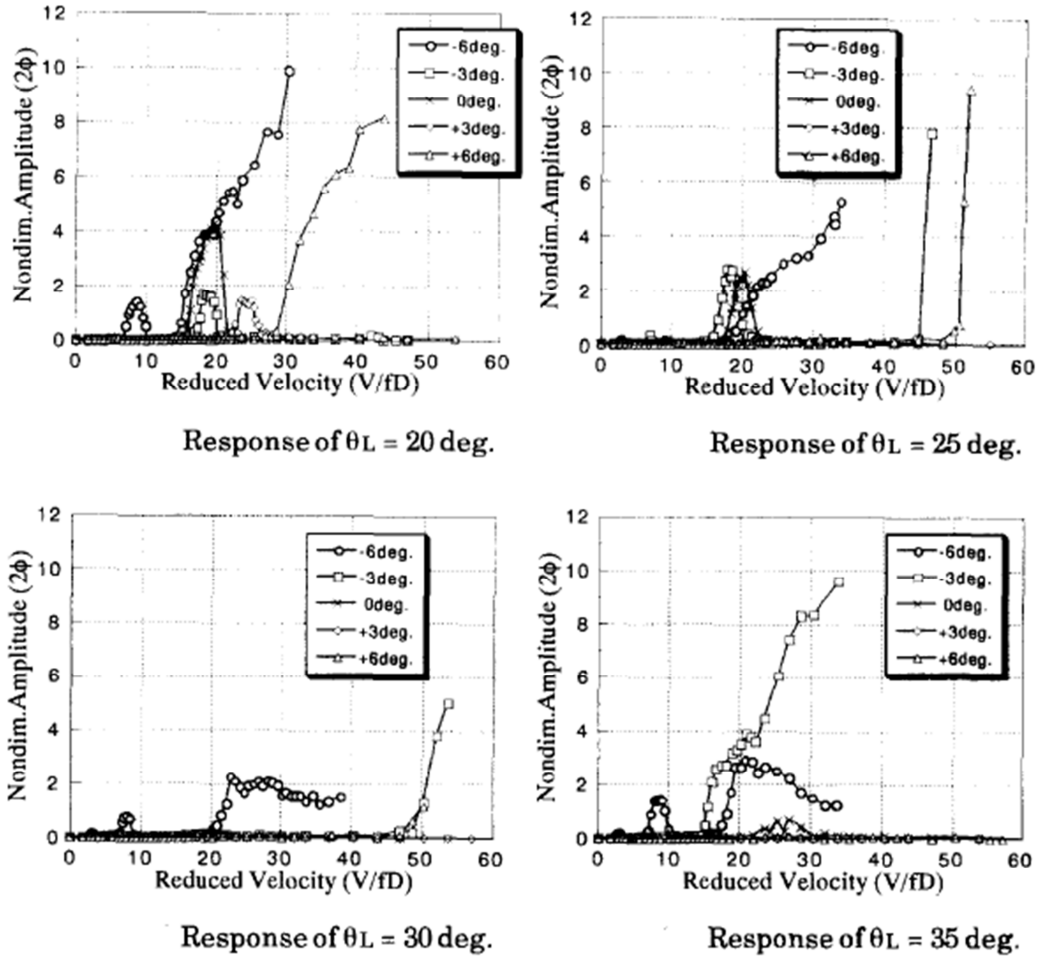

Figure 2.16. Response curves for torsional displacement for open cross-section; different values of the slope of lateral tips walls and of the angle of attack are tested (Kubo et al., 1993)

high variability of results, as reported by Figure 2.16.

A very famous example of bridge exhibiting vortex-induced oscillation is represented by the Storebælt Bridge, which suffered of considerable vertical vibrations noticed during the last phase of the erection. Larsen et al. (2000) provided an accurate study about this case and proposed a mitigation system for VIV response through guide vanes installed on the lower side of the deck (Figure 2.17(a)). The suppression of vortex-induced oscillation was excellent, as shown by Figure 2.17(b), proving the very strong effect that such local detail can have on a geometry sufficiently streamlined like the Storebælt one.

An accurate study about the VIV response of the Second Severn Crossing cable-stayed bridge was proposed by Macdonald et al. in 2002. Both full-scale and wind tunnel measurements were performed on the bridge deck. The bare deck cross-section is elongated and relatively streamlined, nevertheless it is equipped with lateral wind barriers with limited transparency to the flow (Figure 2.18(a)). The section proved to be quite sensitive to heaving VIV response, from both full-scale measurements and wind tunnel tests. To mitigate the VIV transverse displacement several solutions were considered and the installation of baffles on the lower side of the deck was considered as a viable solution (Figure 2.18(a)), preferable to mechanical devices such as tuned mass dampers. The effect of such local modification on the cross-section was a strong reduction of the sensitivity of the deck to vortex-shedding, as observable in Figure 2.18(b), where VIV response curves before and after baffle installation are reported.

2.3.2. Across-flow vertical elements on deck upper side

The second category assumed for cross-section geometric details is represented by vertical screens, traffic barriers and railings, usually installed on bridge decks. Such elements stand vertically from the upper side of the deck and they are generally decisive in terms of structure aerodynamic behavior, due to their considerable across-flow size and, in several cases, their even limited transparency to the flow. As a matter of fact, in addition to the height of the vertical elements installed, the quantity and the distribution of openings may affect crucially the aerodynamic forces and the aeroelastic behavior of a deck. In this context, even a very streamlined bare deck geometry can be indeed markedly frustrated by installing vertical elements considerably solid to the flow. For this reason, a variety of

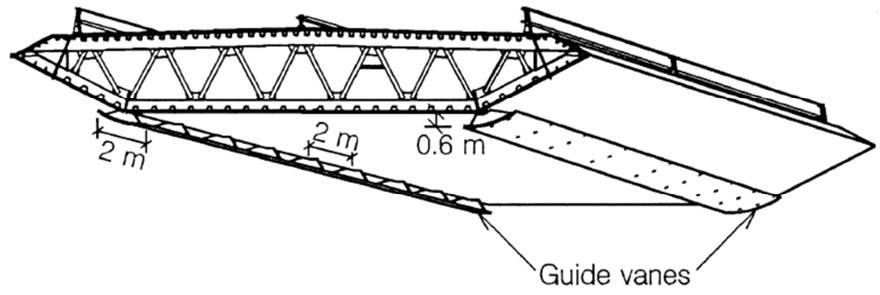

a)

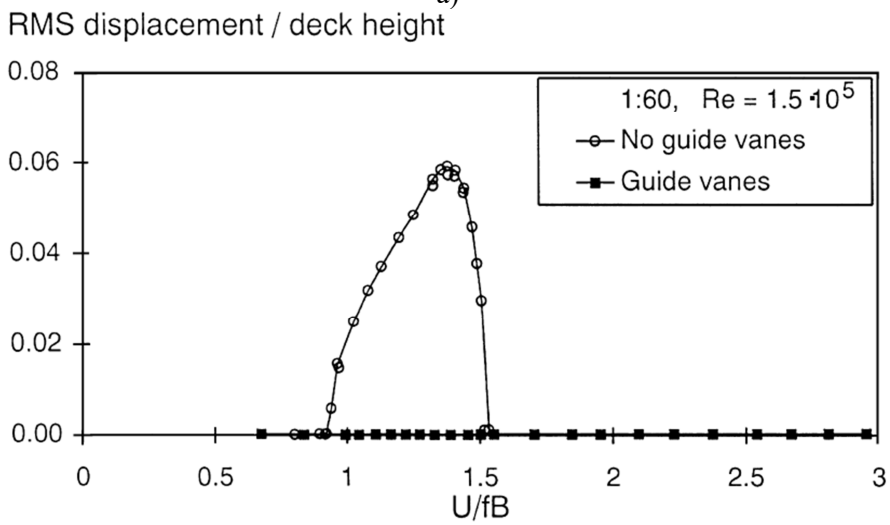

b)

Figure 2.17. Guide vanes installed on the lower side of the bridge (a) and response curves before and after such local geometric modification (b) (Larsen et al., 2000).

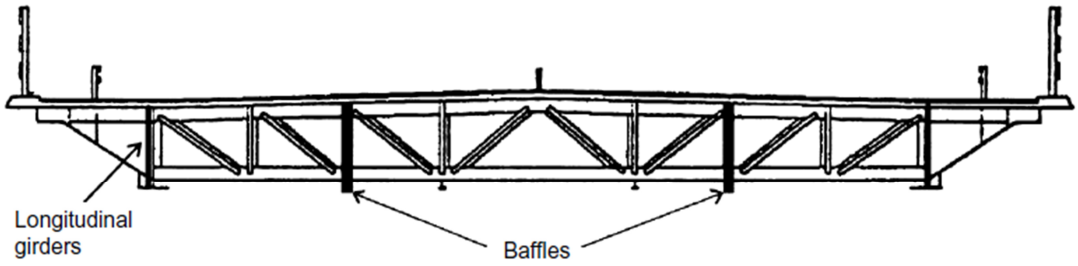

a)

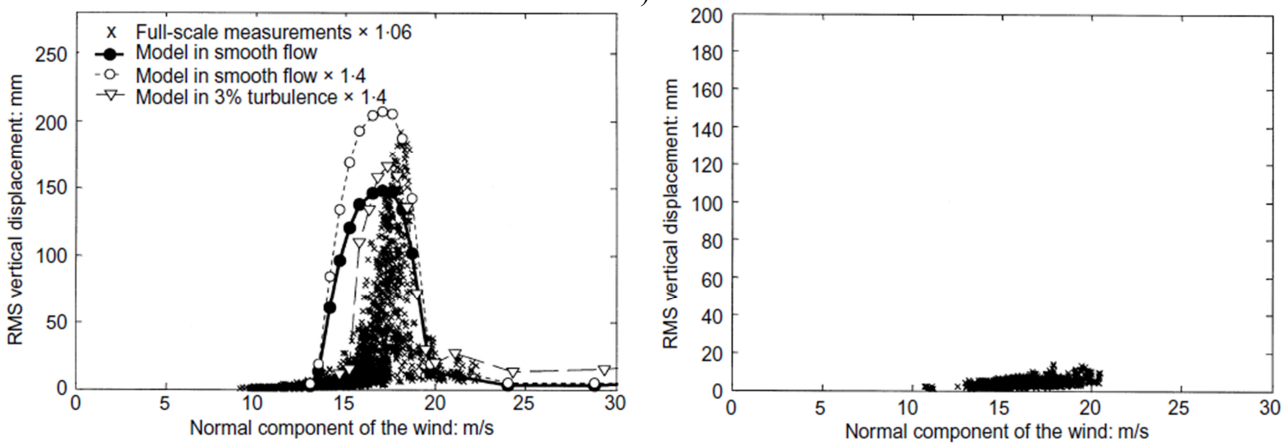

b)

Figure 2.18. Bridge cross-section with baffles installed on the lower side indicated (a). Comparison between heaving VIV response (b) without (left) and with (right) baffles (Macdonald et al., 2002).

studies about different solutions for screens, barriers and railings were conducted over the years.

An accurate work on the effects produced by noise barriers on the aerodynamic behavior of a cable-stayed bridge deck was conducted by Honda et al. (1992). This is one of the first examples focused on the influence of this typology of details on VIV response. The study includes also a vortex generator as possible method for reduction of the bridge VIV response. Nevertheless, it is shown that even simply moving noise barriers outwards on both sides and bending their top and bottom inwards (Figure 2.19(b)) to reduce the width of the wake was sufficient to reduce considerably both heaving and torsional oscillation amplitudes caused by vortex shedding. In addition, the role of the angle of attack is strongly involved, since the comparison between different solutions for lateral barriers is reported for a wide range of flow incidence. The results reported in Figure 2.19 show indeed how different solutions for lateral barriers can work better for certain angle of attack values and worse for others, emphasizing the importance of a global overview about the problem.

One year later, in 1993, Sakai et al. focused on the improvement of aerodynamic behavior and response to aeroelastic phenomena given by local details located at cross-section edges. In particular, in such work plate appendices are installed at both ends of two open cross-sections with different side ratio. Figure 2.20 reports a part of the results, showing clear changes in aeroelastic behavior in terms of bending and torsional vortex-induced oscillation and torsional stability. It is worth to notice that for cross-section configurations from type 2 to type 6 (Figure 2.20) the aerodynamic improvement through edge plates is assessed with lateral railings installed. The addition of lateral across-flow elements as railings, traffic barriers or screens is here considered as potentially decisive, so that aerodynamic appendices are calibrated not only on the bare deck cross section but also on the presence of lateral across-flow elements. Finally, the angle of attack was also taken into account, providing results for different values (-5°, 0°, +5°). It can be observed how a markedly positive value of the angle of attack (+5°) causes the most noticeable effects in terms of both VIV and flutter instability.

The study by Kubo et al. (2001) mentioned in the previous section, with reference to the aerodynamic optimization of a π-shaped deck structure, was extended from the point of view of non-structural geometric details. In particular, effects produced by the addition of solid lateral barriers on VIV response were investigated for different wind angle of attack

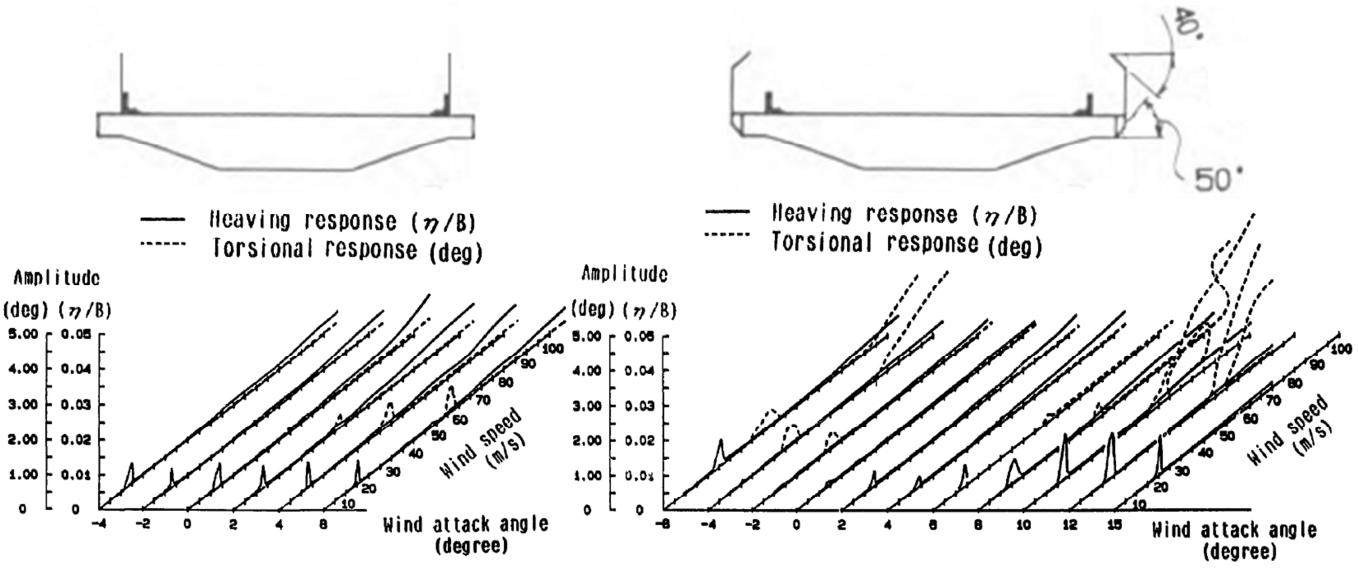

Figure 2.19. Heaving and torsional response for the cross-section for two different geometric configurations of lateral noise barriers: without (a) and with (b) top and bottom bent inwards (Honda et al., 1992)

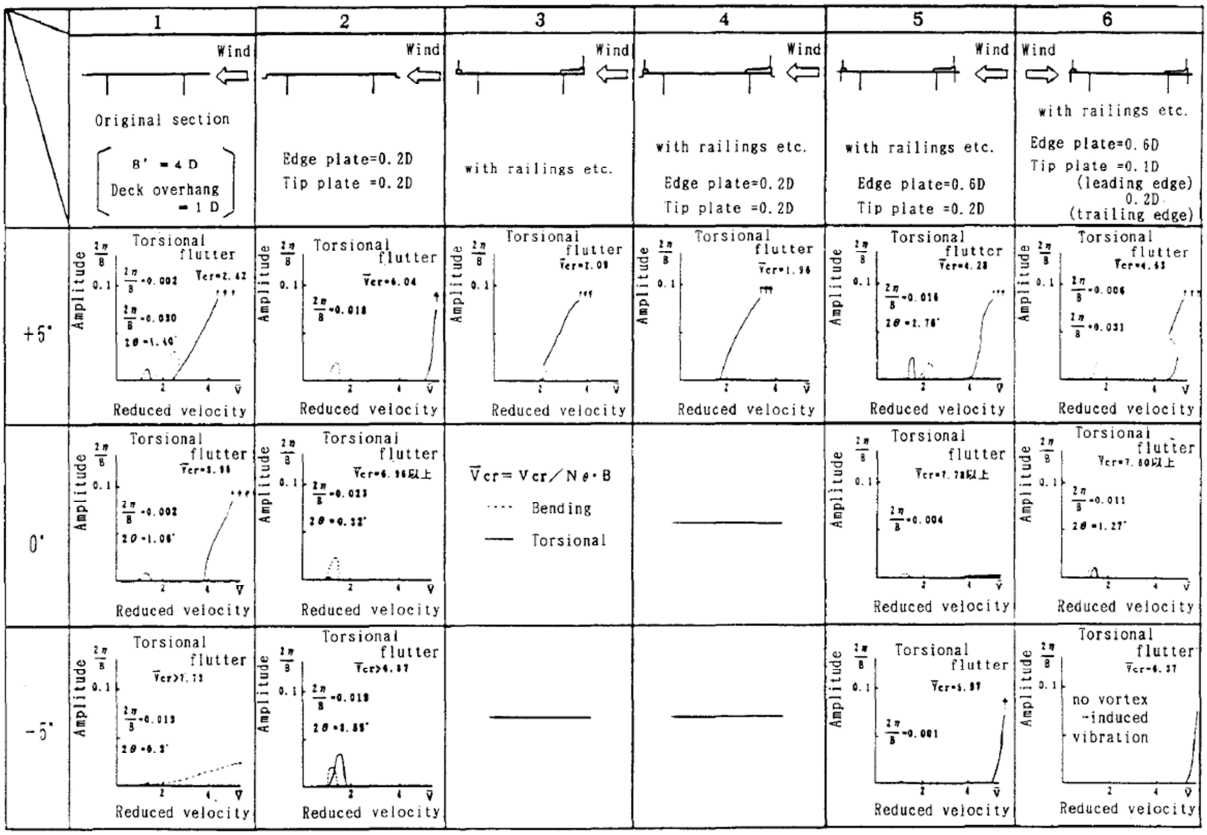

Figure 2.20 Effects on bending and torsional vibrations of progressive modification of cross-section edges by installing edge and tip plates. The presence of lateral railings is also considered (Sakai et al., 1993).

values (Figure 2.21). The influence of barriers on heaving and torsional VIV response was assessed for different positions of the elements, by varying their distance from deck edges (Figure 2.21(a)). A large amount of results is reported, including the variation of the wind angle of attack over a wide range, from -6° to +6°. In this case, heaving oscillations were found to be more sensitive to the angle of attack value than to the presence or absence of barriers, with large vibration amplitude observed for +6° flow incidence (Figure 2.21(b)). On the other hand, torsional vibrations and stability were found to be strongly affected by the presence of lateral solid barriers.

In the wake of vortex-induced oscillation observed for two suspension bridges in the Northern Europe, Storebælt Bridge in Denmark and Osterøy Bridge in Norway, a deep study about VIV suppression through box girder shaping with and without railings (Figure 2.22) was conducted by Larsen and Wall in 2012. Peculiarity of this work is the proposal to adopt an appropriate shape of the box girder to suppress VIV caused by railings, so that the bare deck geometry is adapted to the effects caused by such non-structural elements. The considerable VIV response increase caused by railings and the very satisfying suppression achievable through cross-section geometry is clearly observable from the response curves compared in Figure 2.22(b).

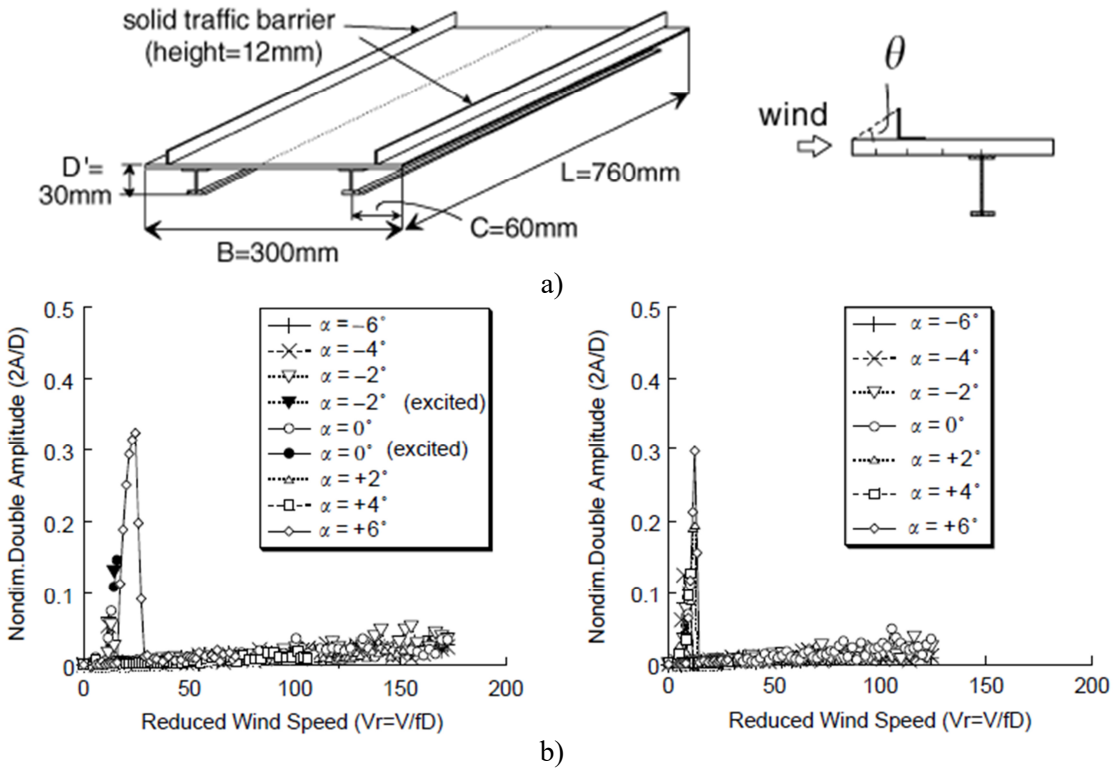

Figure 2.21. Studied π-shaped cross-section with lateral barriers at variable distance from deck edges (a); heaving response curves (b) without (left) and with barriers (right) (Kubo et al., 2002)

Another example of effects produced by cross-section details like lateral screens or barriers along with angle of attack variation was provided by Chen et al. (2017). The Jianghai Channel Bridge, an across-sea cable-stayed bridge (Figure 2.23(a)), was investigated in wind tunnel through tests on sectional models with different scale factors. The study included the effect produced by lateral windbreak barriers on heaving and torsional VIV response of the deck and the measurements were repeated for an exhaustive range of angle of attack values, between -5° and +5°. As observable in Figure 2.23(b), the positive angles of attack tested were found to be critical in terms of transverse vortex-induced oscillation. In addition, the presence of windbreak produced a magnification of lock-in condition at +3° flow incidence, from the point of view of both peak response amplitude and synchronization range extension.

Similarly to the work of Chen et al. described above, Bai et al. (2020) investigated

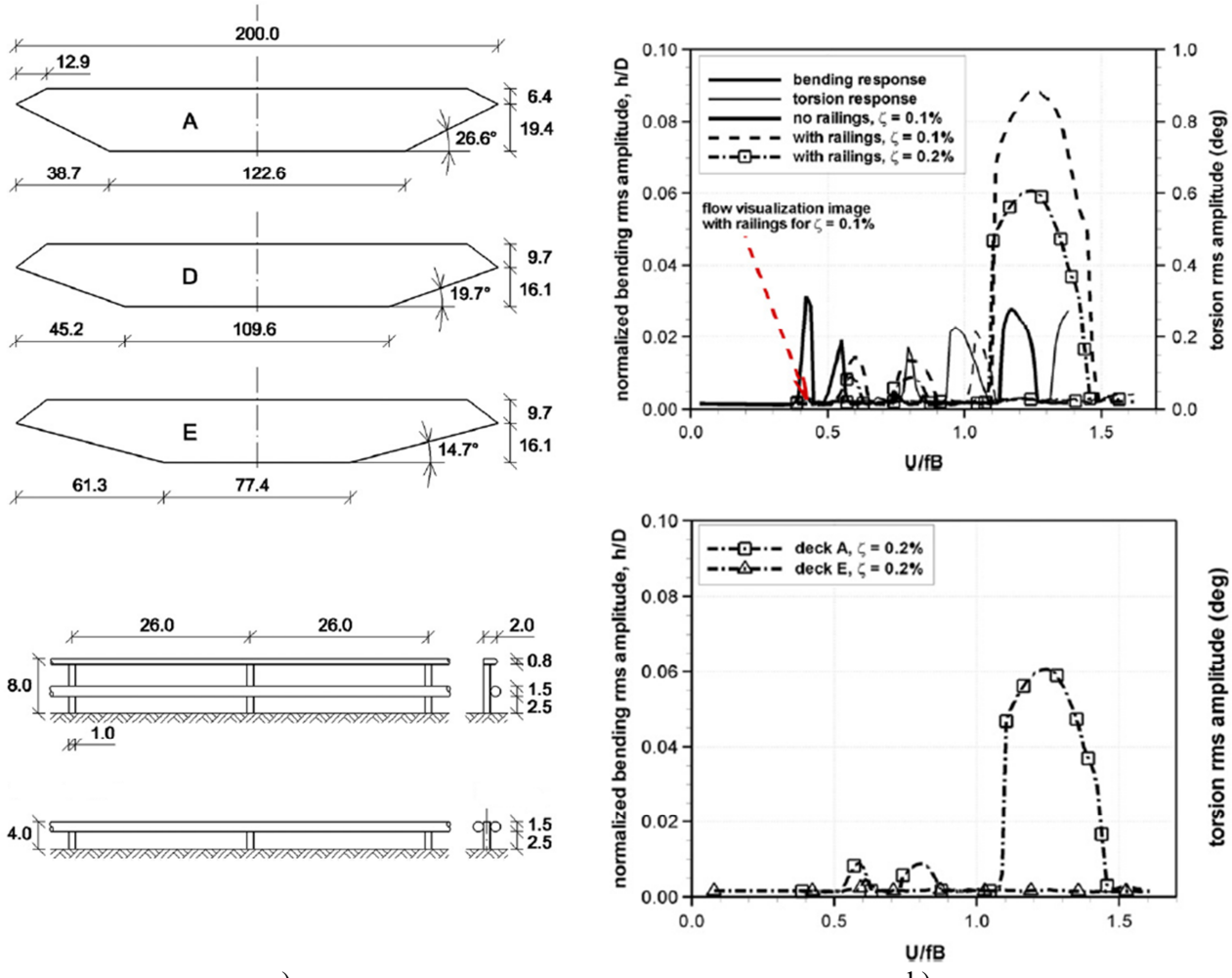

a) b)

Figure 2.22. Geometric outlines (a): box-girder cross-sections (top), lateral railings and median divider (bottom). Comparison between heaving and torsional VIV response curves (b): with and without railings for the same cross-section (top) and with railings installed on different sections (bottom) (Larsen and Wall, 2012).

the effect of partially sealed traffic barriers for VIV suppression, at different values of the angle of attack and for three long-span bridges. Both heaving and torsional dynamic tests were conducted in wind tunnel on sectional models, firstly with traditional traffic barriers and then with possible solutions of partial cladding to mitigate the effect of vortex-shedding (Figure 2.24(a)). The flow angle of incidence was also accurately considered: the bridge decks equipped with the original not sealed traffic barriers were firstly studied for different wind angles of attack, which were found to produce marked effects on the VIV response. Then, the same angles were tested with barriers sealed in different ways. The results obtained for one of the three bridges tested, the Hong Kong-Zhuhai-Macao Bridge, are reported in Figure 2.24(b, c). The effect of different opening distribution on the same typology of barrier is clear: the first solution was able to limit heaving vibrations, while with the second one torsional vibrations were suppressed too.

Finally, two works not specifically dealing with vortex-induced oscillations but meaningful in terms of barrier effects are reported: Jones et al. (1995) and Ricciardelli and Hangan (2001). In 1995 Jones et al. assessed the possible crucial effect of cross-section

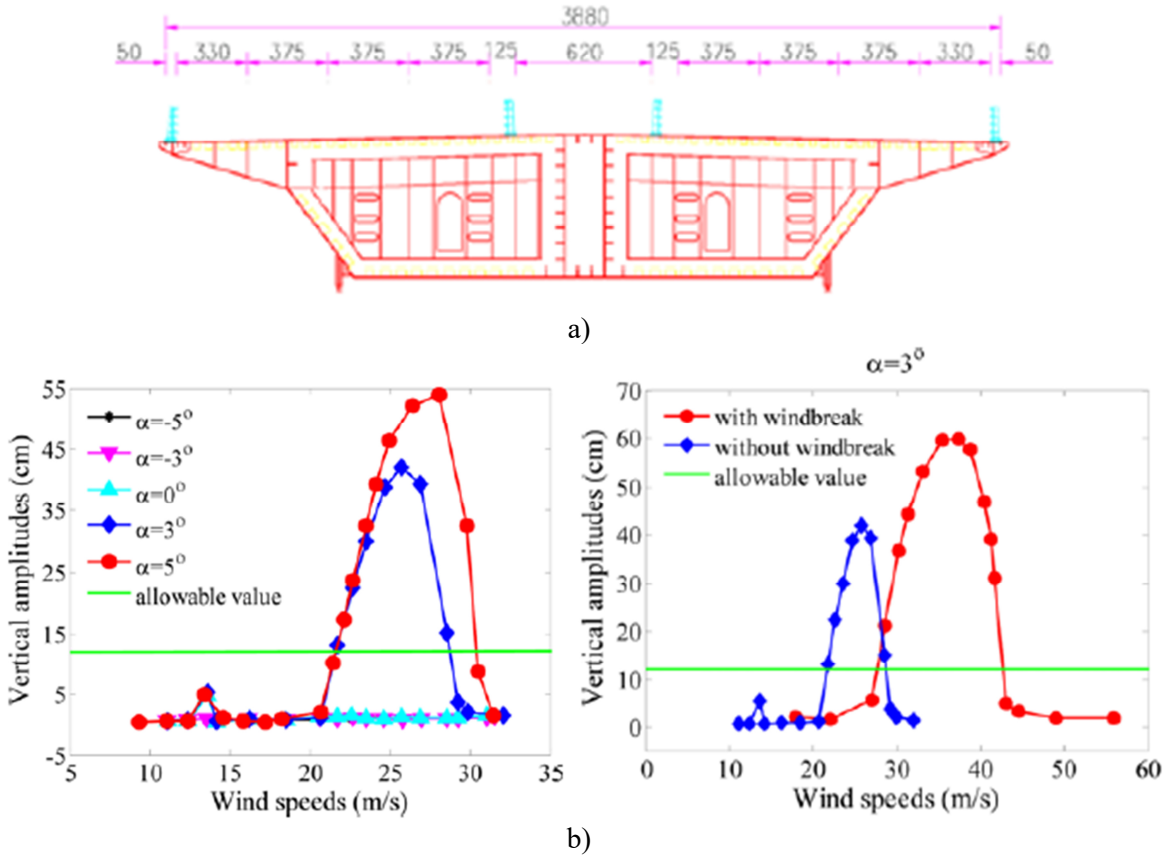

Figure 2.23. Bridge cross-section tested in wind tunnel (a). Heaving and torsional response amplitude curves (b) at different wind angle of attack values (left) and with and without windbreak (right) (Chen et al., 2017).

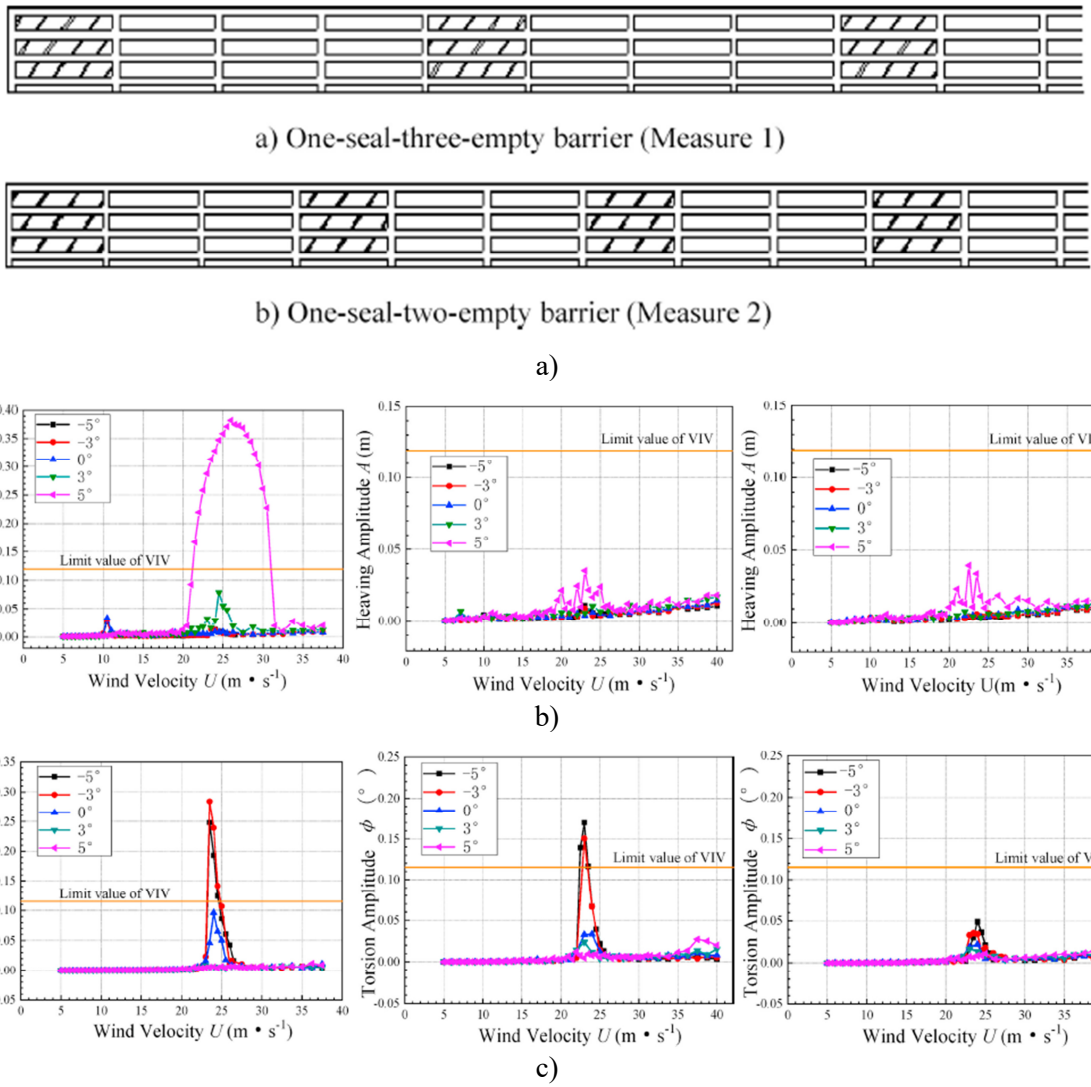

Figure 2.24. Two different solutions for partially sealed barriers (a). Heaving (b) and torsional (c) VIV response curves with not sealed (left) and sealed barriers according to Measure 1 (center) and Measure 2 (right) outlines (Bai et al., 2020).

details on the value of aeroelastic parameters. In particular, the work focuses on the role played by minor details like railings on the response of a box-girder bridge deck (Figure 2.25(a)). Different configurations were tested: bare deck without railings, deck with open railings transparent to the flow and deck with sealed railings. The effect of such modifications was found to be remarkable, especially in case of sealed railings: bare deck and deck with railings transparent to the flow were found to be aerodynamically stable, while sealing the railings led to a change in the sign of flutter derivative A_2^* and a consequent potential torsional instability (Figure 2.25(b)).

In 2001, Ricciardelli and Hangan published a study about a sectional model

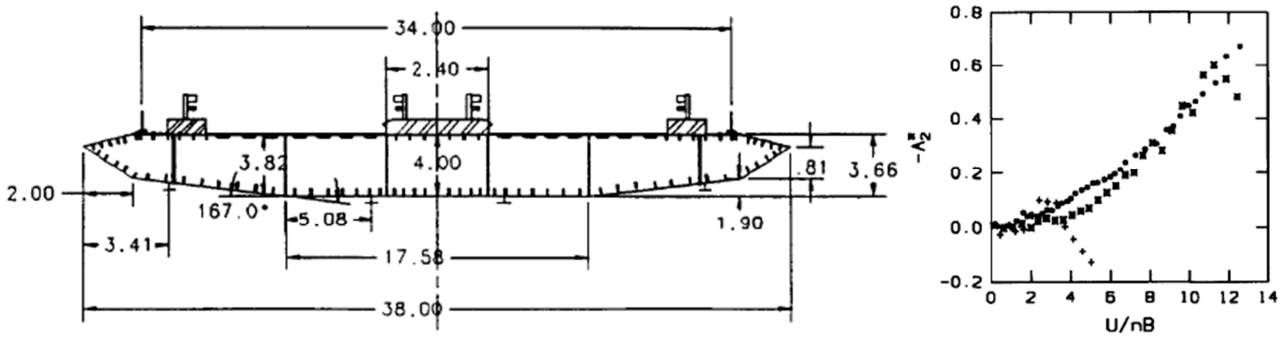

a) b)

Figure 2.25. Cross-section of the bridge deck investigated (a) and flutter derivative A_2^* for bare deck, open railings and sealed railings (b) (Jones et al., 1995).

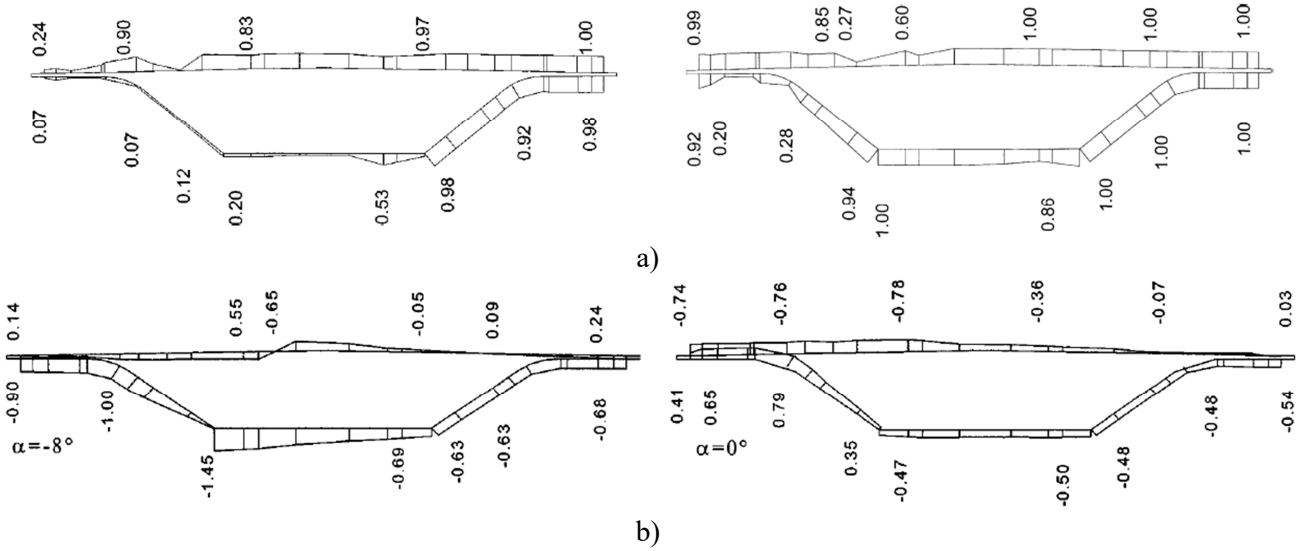

Figure 2.26. Values of coherence function of local pressures and torque at the shedding frequency (a) at zero angle of attack for bare deck (left) and deck with barriers (right); mean pressures at different angle of attack for deck with New Jersey barriers (b) (Ricciardelli and Hangan, 2001).

reproducing the Sunshine Skyway Bridge deck. Aerodynamic force and pressure measurements were performed on the stationary model, with and without New Jersey traffic barriers at different angles of attack. Pressure and force measurements showed that the addition of the barriers produced a global modification of section aerodynamics, rather than a local alteration of the flow close to the barriers, emphasizing how an element modifying locally the geometry of the cross section can give rise to a different overall behavior. From this perspective, Figure 2.26(a) shows a marked increase of coherence function values of local pressures and torque at the vortex-shedding frequency with barriers installed, indicating a more efficient mechanism of excitation given by the presence of barriers. The angle of attack variation is also considered, especially in terms of effect of traffic barriers installed on the deck at different flow angles of incidence. In Figure 2.26(b) a comparison between pressure distributions obtained for two different angles of attack of the wind is reported.

2.3.3. Aerodynamic devices installed on deck upper side and on vertical elements

A final category of cross-section aerodynamic details was considered: flaps, airfoils and spoilers installed on appropriate supports, rising up from the upper side of the deck, or on vertical elements like screens, barriers or railings. Such elements represent passive or active aerodynamic appendices aiming to improve the aerodynamics of bridge decks. With reference to the scientific works mentioned so far, the optimization study conducted for the Messina Strait Bridge by Diana et al. (2006) included airfoils installed on deck edges (Figure 2.12).

As a further example, Sarwar and Ishihara (2010) provided a CFD study about a bridge deck cross-section geometry inspired to the Trans-Tokyo Bay Bridge, which suffered from vortex-induced oscillations, and on VIV response suppression through aerodynamic countermeasures. The performances of the numerical model were assessed by comparing the results to previous studies, both for the investigated bridge deck geometry and for a rectangular geometry with 4:1 side ratio. Two different typologies of aerodynamic countermeasures were selected: lateral fairings and double flaps, both installed on cross-section edges (Figure 2.27(a, b)). As observable in Figure 2.27(c), the response amplitude obtained in presence of double flaps is drastically lower not only than the case without aerodynamic countermeasures, but also than in case of lateral fairings applied to the deck.

In 2018, Hu et al. published a paper dealing with vortex-induced vibration of a streamlined closed box girder (Figure 2.28(a)). The main focus of the study is represented by time-frequency evolutionary characteristics of aerodynamic forces. In the first part of the work, the effect produced by the installation of inclined spoilers on the top part of lateral railings (Figure 2.28(b)) is shown. Figure 2.28(c) reports the response curves obtained with and without spoilers installed on lateral railings and the improvement in terms of vortex-induced oscillations of the deck is clearly observable: the spoilers are able to almost suppress the VIV response, which is reduced from about 7% to less than 1% of the deck across-flow dimension *D*.

2.3.4. Remarks about main aerodynamic effects

The works mentioned in the last three sections represent only a part of the studies conducted over the years. The effects produced by cross-section details and angle of attack are various and, in several cases, decisive for the aerodynamic behavior of a bridge deck. In this context, identifying a clear pattern in terms of input variation against output is not easy. Nevertheless, some effects generally produced by certain geometric details or angle of attack variations can be observed.

Fairings and other equivalent elements determining the bare deck geometry do not seem to exhibit an influence on aerodynamic performances systematically associated with specific geometric features, like slope of the walls or sharpness of the corners. A more streamlined geometry, obtained by applying such elements to the deck, generally improves bridge behavior in terms of VIV response, but a quantitative connection between fairing geometric details and deck aerodynamic performance is hardly recognizable. A similar deduction can be formulated for sections with multiple box girder in terms of shape of the girders and gap between them.

Aerodynamic devices like guide vanes, baffles, airfoils, spoilers reduce the VIV response in terms of both lock-in extension and peak response amplitude. On the other hand, screens and barriers are particularly critical for aerodynamics of a cross-section. In particular, the amount of openings and their distribution seem to play a key role: for the same cross-flow size of the element, a sealed barrier may lead to an extremely stronger VIV response and/or torsional instability compared to a more transparent one. Nevertheless, an appropriate partial cladding of barriers may be useful to improve the VIV

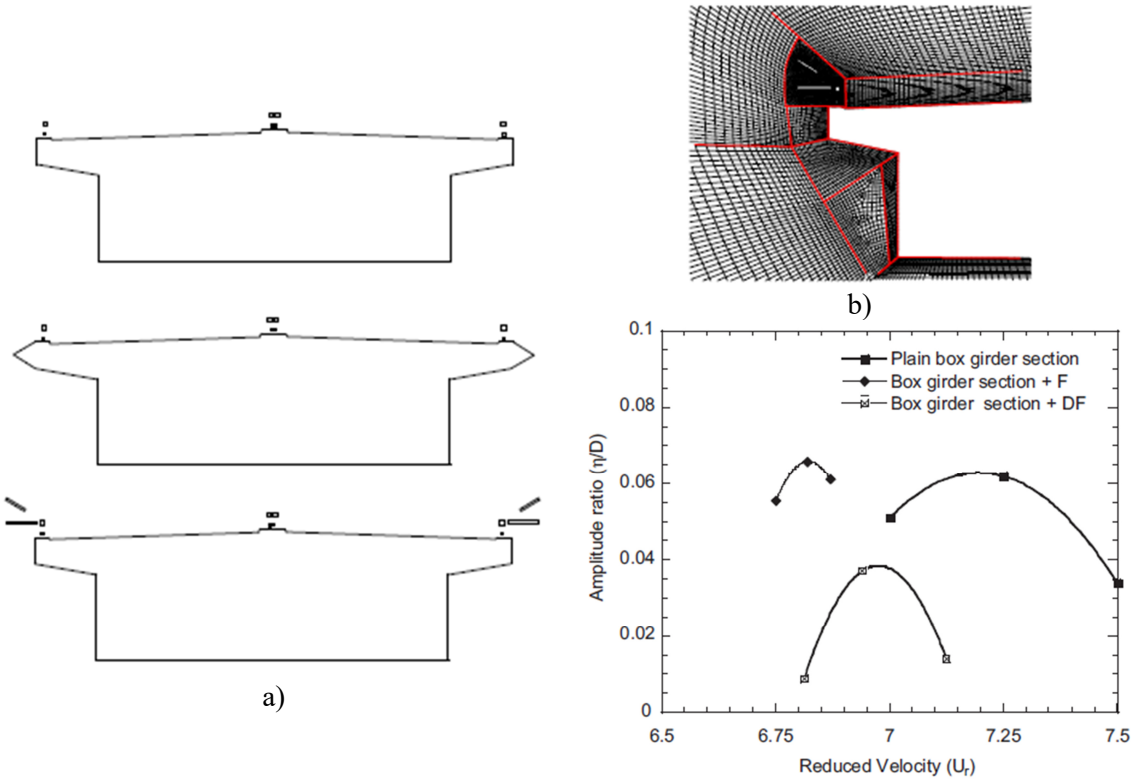

Figure 2.27. Bridge deck cross-section with and without aerodynamic countermeasures (a): plain section, section with fairings and with double flaps. Close-up of the meshing scheme on the leading edge for section with flaps (b). VIV response curves for each case (Sarwar and Ishihara, 2010).

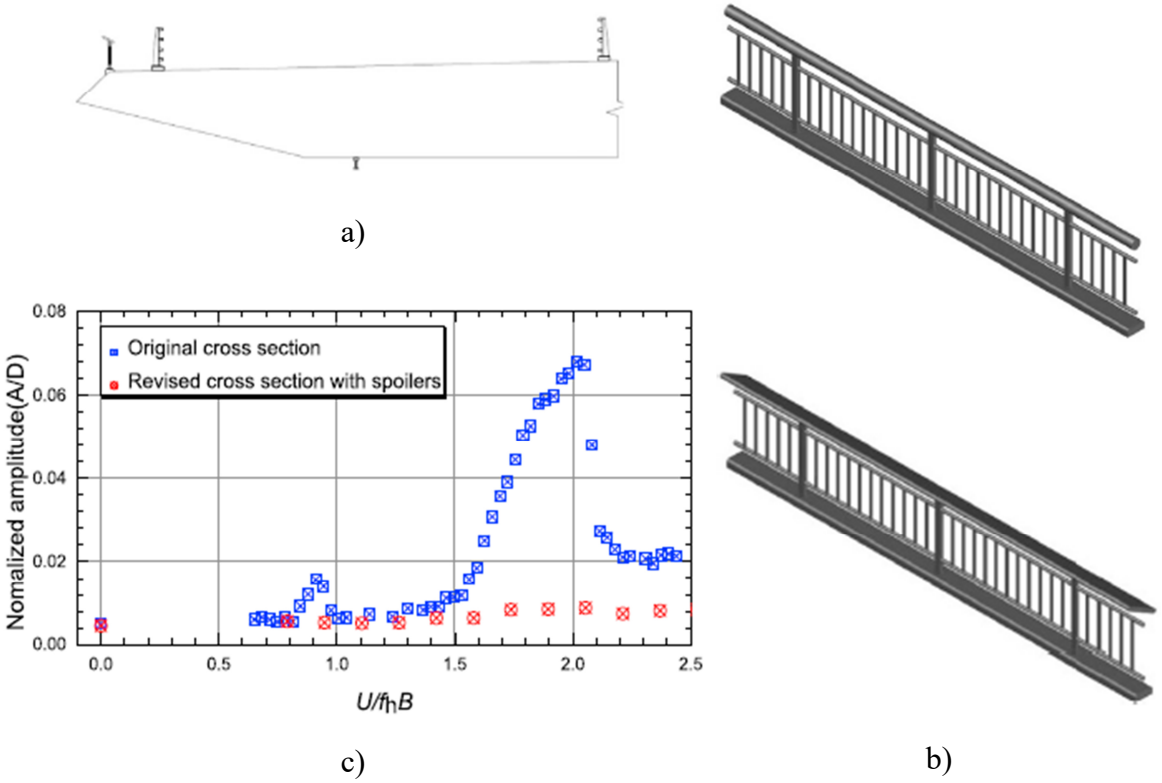

Figure 2.28. Bridge cross-section outline (a). Lateral railings (b) without (top) and with (bottom) inclined spoilers. Heaving response curves before and after spoiler installation (c) (Hu et al., 2018)

response (Figure 2.24), possibly by reducing vortex-shedding correlation along the deck. An adequate cladding along with the installation of aerodynamic devices on screens or barriers can make such elements much more compatible with acceptable deck oscillation amplitudes, despite the general negative effect produced by this typology of non-structural additions.

With regards to the incoming flow incidence, a positive value of the angle of attack generally seems to promote vortex-induced oscillation, both in terms of vibration amplitude and lock-in range, and to reduce aerodynamic stability. From this perspective, the correct evaluation of the flow incidence range to investigate for bridge design may be decisive, considering that a geometric configuration considerably optimized close to zero angle of attack could exhibit unsatisfactory performances especially for positive angles.

2.4. Mathematical modeling for VIV response prediction

The present work focuses particularly on the mathematical modeling of bridge deck VIV response. This is a very challenging issue, for a multitude of reasons. The difficulty of modeling a complex phenomenon like vortex-induced vibrations and predict its results is certainly remarkable in itself. The dependence of such phenomenon on the flow pattern around a body and, indeed, on the shape of the body has to be taken into account too. From this point of view, bridge deck cross-sections exhibit a wide variety of different geometries, differing for their basic shape, firstly for their side ratio, and also for a multitude of possible local details. As reported in the previous section, the influence of such details can be so crucial that the whole flow pattern can be modified by a local cross-section alteration. Finally, the angle of attack can also play a key role and act equivalently to a cross-section geometry modification in terms of flow pattern around the body.

Over decades, different mathematical approaches have been developed and proposed in several works available from scientific literature. Starting from basic bluff-body geometries, first of all circular cylinders, modeling possibilities were assessed for different shapes, such as square or rectangles with different side ratio, up to more articulate cases, like a bridge deck cross-section. Mathematical models differ for several main features: underlying concept, parameters appearing in their formulation, number of degrees of freedom, linearity or nonlinearity of the equations. An overview of the main model categories available in literature is reported below, and particular attention is paid to the ones relating to the content of the present work.

2.4.1. Mathematical model typologies

The knowledge achieved over the years about vortex-induced oscillation led to different formulations for the mathematical modeling of the phenomenon. They are based on different assumptions and present different formulations and, based on such aspects, they can be distinguished and classified in a few main categories. A complete and overview about models can be found in Marra (2011). In the present work, different typologies of models for VIV response prediction of cylindrical bodies are mentioned, but only the ones actually employed or significant for the present work are described.

All of existing models include at least an equation of motion representing the oscillation of a body under the action of the fluctuating vortex-shedding force, such as a chimney, a cable, a bridge deck. If the body oscillates elastically, its motion is described by the classical linear expression and a forcing term acting on the system:

$$m\left(\ddot{y}+2\zeta_0\omega_0\dot{y}+\omega_0^2 y\right)=F\left(y,\dot{y},\ddot{y},U,t\right) \tag{2.5}$$

where the term F is the aeroelastic function representing the vortex-induced force per unit length. If the only mechanical oscillator equation is present, a single-degree-of-freedom model is defined. For such a typology, the vortex-induced force expression includes a series of aeroelastic parameters estimated through free-vibration tests (negative damping models) or forced-vibration tests (forced-coefficient data models) in wind tunnel (Billah, 1989; Marra, 2011).

Consequently, three macro-categories of single-degree-of-freedom approaches can be defined:

- Single-degree-of-freedom linear negative damping models (Scruton, 1963; Scanlan, 1981; Scanlan, 1998);
- Single-degree-of-freedom non-linear negative damping models (Scanlan, 1981; Vickery and Basu, 1983; Goswami, 1991; Larsen, 1993; D'Asdia et al., 2003);
- Single-degree-of-freedom forced-coefficient data models (Sarpkaya, 1978; Staubli, 1983; Iwan and Botelho, 1985).

It is worth to notice that probably the most simple one-degree-of-freedom approach is represented by harmonic model. Such a model is based on the approximation of the fluctuating lift force generated by vortex-shedding with a harmonic function. The harmonic

approach will be better reported in Section 2.4.4, where a simplified VIV modeling is derived from it and discussed.

Along with one-degree-of-freedom models, scientific literature provides also two-degree-of-freedom approaches. They are conceived by including a non-linear equation of motion representing the fluctuating vortex-shedding force. This second oscillator is usually called wake oscillator, which is coupled with the mechanical oscillator, representing the vibrating body, to reproduce the interaction between flow and body.

Wake oscillator models can be distinguished in two main typologies: the ones assuming a non-linear wake oscillator without any physical description and the ones assuming an oscillating fluid lamina whose motion generates the vortex-induced force (Marra, 2011). The former group is based on Bishop-Hassan concept (Bishop and Hassam, 1964) while the second one on the swinging wake concept proposed by Birkhoff (1953). Both model typologies propose a wake oscillator equation in agreement with the main evidences related to VIV: self-excitation and self-limitation. So, two-degrees-of-freedom models can be classified as follows:

- Non-linear wake oscillator without any physical description (Hartlen and Currie, 1970; Skop and Griffin, 1973; Iwan and Blevins, 1974; Landl, 1975; Dowell, 1981; Benaroya and Lepore, 1983; Krenk and Nielsen, 1999; Facchinetti et al., 2004; Diana et al., 2006);
- Non-linear wake oscillator based on fluid lamina oscillating behind the body (Funakawa, 1969; Nakamura, 1969; Tamura and Matsui, 1979; Tamura and Shimada, 1987; Mannini et al, 2018).

Tamura and Shimada (1987) and Mannini et al. (2018) are actually derived from the model proposed by Tamura and Matsui (1979), through some appropriate modifications. The structure of these three models is accurately described in Section 2.4.3 and a study about Tamura-type modeling is presented and discussed in Chapter 6.

2.4.2. Close-up on wake-oscillator models

In this section some mathematical approaches among those cited above are described more specifically. The following models have been selected for a more accurate

description because of their relevance or meaningfulness with respect to the content of the present work and, in particular, to the study presented in Chapter 6.

Hartlen and Currie (1970)

One of the first most significant works about VIV mathematical modeling is certainly the approach proposed by Hartlen and Currie, in 1970. The model is described and applied for a vibrating circular cylinder. The basic idea is to formulate two equations, for the body and for the vortex-shedding lift force, with the wake oscillator equation characterized by three primary conditions to be satisfied:

- Self-excitation and self-limitation;
- Lift oscillator frequency proportional to free-stream velocity according to Strouhal law, in absence of cylinder motion;
- Interaction with the mechanical oscillator through some kind of forcing term, so that the coupling between the two motions is guaranteed.

The final expressions of the equations of motion are here reported:

$$m\left(\ddot{y}+2\zeta_n\omega_n\dot{y}+\omega_n^2 y\right)=\frac{1}{2}\rho U^2 D C_L \tag{2.6}$$

$$\ddot{C}_L-\alpha\omega_s\dot{C}_L+\frac{\gamma}{\omega_s}\dot{C}_L^3+\omega_s^2 C_L=\frac{b\omega_n}{D}\dot{y} \tag{2.7}$$

where ω_n and ω_s are, respectively, the circular frequency of the mechanical oscillator and the vortex-shedding circular frequency and α, γ and b are unknown quantities that have to be determined.

In the wake oscillator equation, the non-linear behavior is obtained through a Rayleigh-oscillator-type expression, while the interaction with the vibrating body is guaranteed by a single coupling forcing term, linear with respect to the velocity of the body.

It is worth to remark the difference between fluctuating lift force values in case of stationary and elastically mounted cylinder close to the resonance condition. For the former condition, the lift coefficient amplitude is defined as C_{L0}:

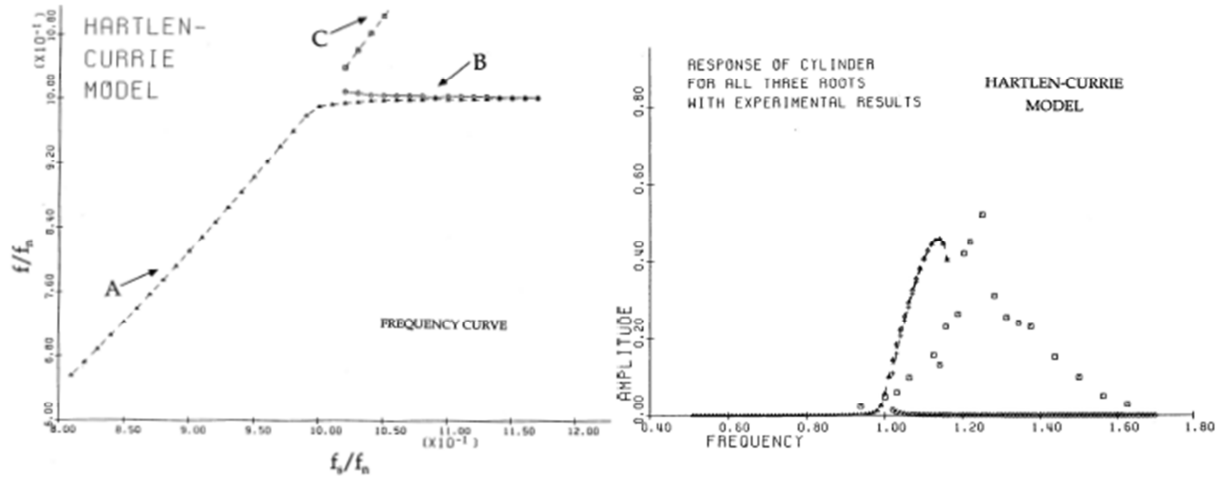

a) b)

Figure 2.29. Frequency curve (a) and response curve (b) against reduced vortex-shedding frequency (f_s/f_n) obtained by Hartlen and Currie (Billah, 1989).

$$C_{L0} = \sqrt{\frac{4\alpha}{3\gamma}} \tag{2.8}$$

which is measured experimentally and defines the ratio between unknown parameters α and γ. In case of vibrating cylinder close to resonance condition, both motions are approximated to sinusoidal functions, with a lift coefficient amplitude named C_L.

In Figure 2.29 results obtained by Hartlen and Currie, and reported by Billah (1989), are presented. Figure 2.29(a) shows the frequency curve, where non-dimensional cylinder frequency (f/f_n) is plotted against non-dimensional vortex-shedding frequency (f_s/f_n), while Figure 2.29(b) shows the response amplitude of the cylinder, obtained through the model and experimentally, against f/f_n.

Skop and Griffin (1973)

In the wake of the work proposed by Hartlen and Currie, Skop and Griffin, in 1973, proposed another modeling solution for vortex-excited resonant response of bluff cylinders. To this purpose, a modified van der Pol equation was proposed to model the fluctuating lift coefficient acting on the body and the two equation of the model can be expressed as follows:

$$m\left(\ddot{y} + 2\zeta_n \omega_n \dot{y} + \omega_n^2 y\right) = \frac{1}{2}\rho U^2 D C_L \tag{2.9}$$

$$\ddot{C}_L - \omega_s G\left[C_{L0}{}^2 - \frac{4}{3}\left(\frac{\dot{C}_L}{\omega_s}\right)^2\right]\dot{C}_L + \omega_s{}^2\left(1 - \frac{4}{3}HC_L{}^2\right)C_L = \omega_s F\frac{\dot{y}}{D} \tag{2.10}$$

where five quantities have to be determined: ω_s, which is the circular vortex-shedding frequency, C_{L0}, the amplitude of the dimensionless fluctuating lift force on a stationary cylinder, and the parameters G, H and F. Such an approach exhibited good performances in case of circular cylinders (Figure 2.30). It is worth to highlight that the procedure for the estimation of empirical constants was conceived especially for the circular cross-section. Regardless qualities and limits of this approach, similarities with Hartlen and Currie work are easily observable in Skop and Griffin model: the basic assumptions for the wake oscillator equation are similar and the coupling with the body motion is achieved through a forcing term linearly dependent on the velocity of the mechanical oscillator.

It is worth to report the approximate solutions for the cylinder oscillation and the lift coefficient fluctuation in the steady or entrained state, that is, the state in which the vortex-shedding and structural vibration circular frequencies are locked together at the common value ω:

$$\frac{y}{D} = aC_{L0}\sin(\omega t) \tag{2.11}$$

$$C_L = AC_{L0}\sin(\omega t + \varphi) \tag{2.12}$$

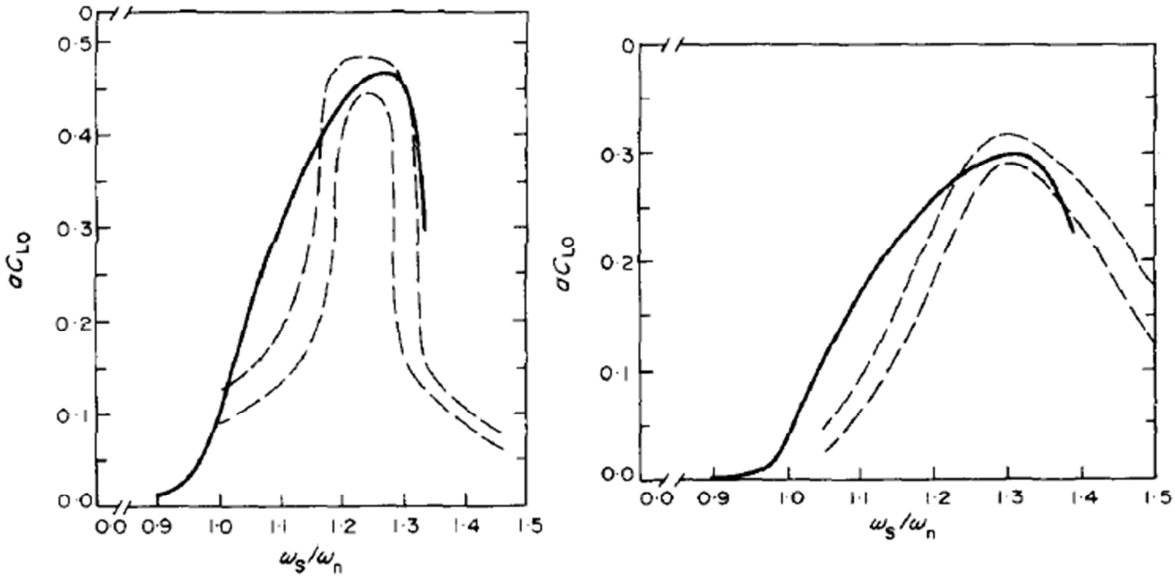

a) b)

Figure 2.30. Resonant response curves, for mathematical model (solid line) and experimental results (dashed line), for two vortex-excited vibration systems with circular cylinder (Skop and Griffin, 1973).

where both cylinder motion and lift fluctuation are approximated as a harmonic process at lock-in. Both amplitudes are defined as linearly dependent on C_{L0}, as observable from the expressions above, through appropriate scale factors: a and A. A scale factor A for the fluctuating lift amplitude between stationary and oscillating cylinder is indeed assumed.

Facchinetti, de Langre, Biolley (2004)

An interesting study about the interaction between vibrating cylinder and wake oscillator was provided by Facchinetti et al. in 2004. The VIV response of an elastically oscillating circular cylinder was addressed by considering different possibilities for the forcing term in the wake oscillator equation.

The equations of motion in terms of dimensionless time and dimensionless displacement are expressed as follows:

$$\ddot{y} + \left(2\zeta \frac{\omega_n}{\omega_s} + \frac{\gamma}{\mu} \right) \dot{y} + \left(\frac{\omega_n}{\omega_s} \right)^2 y = s \tag{2.13}$$

$$\ddot{q} + \varepsilon \left(q^2 - 1 \right) \dot{q} + q = f \tag{2.14}$$

where the dimensionless wake variable q may be associated with a fluctuating lift coefficient, as for several other models. The wake oscillator exhibits a Van der Pol-type formulation, and the coupling between the two motions is guaranteed by appropriate forcing terms $s = s(q)$ and $f = f(y)$.

It is worth to focus on the coupling term f, which introduces in the wake oscillator the interaction with the mechanical oscillator. Three possibilities of linear coupling with the motion of the body are proposed:

- Displacement coupling: $f = Ay$;
- Velocity coupling: $f = A\dot{y}$;
- Acceleration coupling: $f = A\ddot{y}$.

and the VIV response prediction was evaluated through all of them. In Figure 2.31, amplitude response curves for cylinder vibration (y_0) and wake variable fluctuation (q_0) are reported.

The displacement coupling was found to be not suitable for VIV response modeling, since it exhibited a decrease of the wake oscillation amplitude along with the increase of the cylinder oscillation at lock-in, so that the lift magnification is not achieved and the obtained cylinder vibration is very weak too, compared to other cases. On the other hand, both velocity and acceleration couplings provided potentially satisfying results and, in this case, the best match with experimental results came from the acceleration coupling.

Regardless the performances of these two coupling possibilities, it is interesting to note that the lock-in curves obtained are quite similar from the point of view of peak oscillation amplitude, but different in terms of synchronization range and, above all, in terms of shape of the curve (Figure 2.31(a)). The curve obtained through the velocity coupling is markedly asymmetric and triangle-shaped, reaching its peak value at the very end of a wide lock-in range, while the acceleration coupling gives rise to a rounder and more symmetric curve. In addition, for decreasing reduced velocity a large hysteresis is observable in case of velocity coupling, while for acceleration coupling this phenomenon is more limited.

So, the choice of a certain typology of coupling between wake and mechanical oscillator may indeed be crucial to obtain a satisfying match with experimental results. It is reasonable to suppose that the flow pattern associated with a certain cross-section geometry may require a specific typology of coupling term: with velocity, acceleration or both.

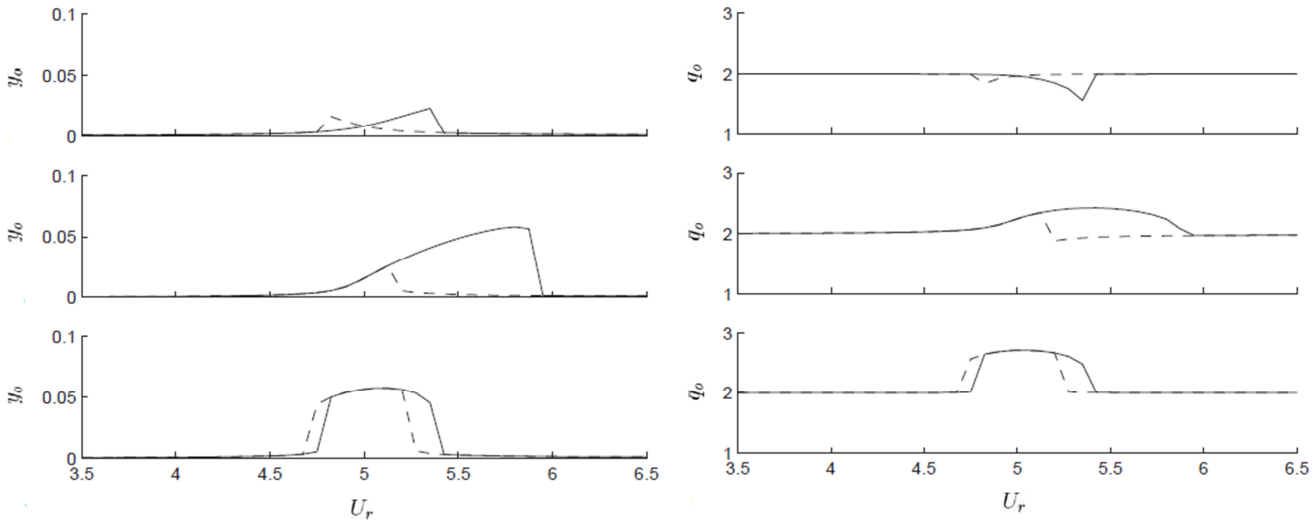

a) b)

Figure 2.31. Response curves in terms of amplitude of cylinder displacement (a) and wake variable (b) for increasing (solid) and decreasing (dashed) reduced flow speed U_r in case of displacement (top), velocity (middle) and acceleration (bottom) coupling (Facchinetti et al., 2004).

2.4.3. Tamura-type wake-oscillator models

Tamura and Matsui (1979) - Tamura and Shimada (1987)

A very important contribution to the VIV response modeling was given by the approach proposed by Tamura and Matsui in 1979. This model was conceived for the VIV response of a circular cylinder and differs from the ones described previously, since it is based on Birkhoff's physical assumption: the vortex-shedding lift force is generated by the angular oscillation (ϑ) of a fluid plate, located behind the vibrating body (y), around a pivot point (Figure 2.32(a)).

The fluctuating lift coefficient value (C_L) is defined proportionally to the effective angular displacement of the fluid plate behind the body:

$$C_L = f\left(\vartheta - \frac{\dot{y}}{U}\right) \tag{2.15}$$

and it fluctuates with the vortex-shedding frequency (n_s) according to the Strouhal law (Eq. (2.1)) for a stationary cylinder. In Eq (2.15), the parameter f is the proportionality constant between C_L and the wake angular displacement, calculated as difference between the fluid plate rotation ϑ and the relative angle of attack $\dot{y}/U$, due to the transverse motion of the body and, hence, of the wake pivot point. $\dot{y}$ is the velocity of the oscillating body, where the dot indicates the derivative with respect to the time t, and U is the mean incoming flow speed. The value f = 1.16 is assumed by Tamura and Matsui in analogy with the relationship experimentally observed between Magnus-effect transverse force and wake angular displacement for a rotating circular cylinder. The model can be described defined by the following equations, in a non-dimensional formulation:

$$Y'' + \left[2\zeta_0 + \left(f + C_D\right)\frac{U_{red}}{2\pi m^*}\right]Y' + Y = \frac{{U_{red}}^2}{4\pi^2 m^*} f\vartheta \tag{2.16}$$

$$\vartheta'' - 2\beta\upsilon\vartheta'\left(1 - \frac{4f^2}{C_{L0}^2}\vartheta^2\right) + \upsilon^2\vartheta = \lambda Y'' + \upsilon^2\frac{2\pi Y'}{U_{red}} \tag{2.17}$$

where the dimensionless body transverse displacement Y and the wake rotation ϑ are derived with respect to a dimensionless time $\tau = \omega_0 t$, where ω_0 is the circular natural frequency of the cylinder. The other symbols appearing in the two equations of motion are here reported:

- ζ_0 is the mechanical damping ratio of the mechanical oscillator;
- $U_{red} = U/n_0D$ is the reduced flow speed, where U is the incoming wind velocity, n_0 is the natural frequency of the mechanical oscillator and D is diameter of the circular cross section;
- $m^* = 2m/\rho D^2$ is a dimensionless mass ratio, where m is the equivalent mass per unit length of the system and ρ is the density of the air;
- f is the ratio between the fluctuating lift coefficient and the effective wake angular displacement, calculated as difference between the fluid lamina rotation for a stationary body and the apparent angle of attack, given by the motion of the body. It is actually the parameter connecting the motion of the wake with the vortex-shedding force on the mechanical oscillator;
- C_D is the circular cylinder drag coefficient;
- C_{L0} is the amplitude of the fluctuating lift coefficient for the stationary cylinder;
- β is a sort of negative linear damping ratio of the wake oscillator. It is also a crucial parameter for the amount of nonlinearity in the wake oscillator behavior;
- $\upsilon = U_{red}/(1/St) = n_s/n_0$ is the ratio between the reduced wind speed and the vortex-resonance reduced speed, where St is the Strouhal number of the cross section and n_s is the vortex-shedding frequency calculated according to the Strouhal law;
- λ is a parameter which defines the coupling forcing term for the wake oscillator coming from the acceleration of the mechanical oscillator.

The model formulation and the parameters are physically based. According to scientific literature, it is known that vortex-shedding force modeling has to satisfy two main conditions: the lift oscillator has to be self-excited and self-limited. These two conditions are usually satisfied by assuming an appropriate expression for the damping term, usually leading to a Van der Pol-type formulation of the wake oscillator. Peculiarity of Tamura's approach is the achievement of this kind of expression from the deformation of the wake lamina during its motion (Figure 2.32(b)). In particular, the first-order effect of the length fluctuation of the wake behind the body, due to the alternate detachment of vortices on both sides, is included, giving rise to a non-linear contribution to the restoring moment acting on the fluid lamina. This results in a Van der Pol-type equation of motion with a non-linear damping term, which is not empirically assumed but physically derived.

As observable in Eq. (2.17), the wake oscillator is coupled with both acceleration and

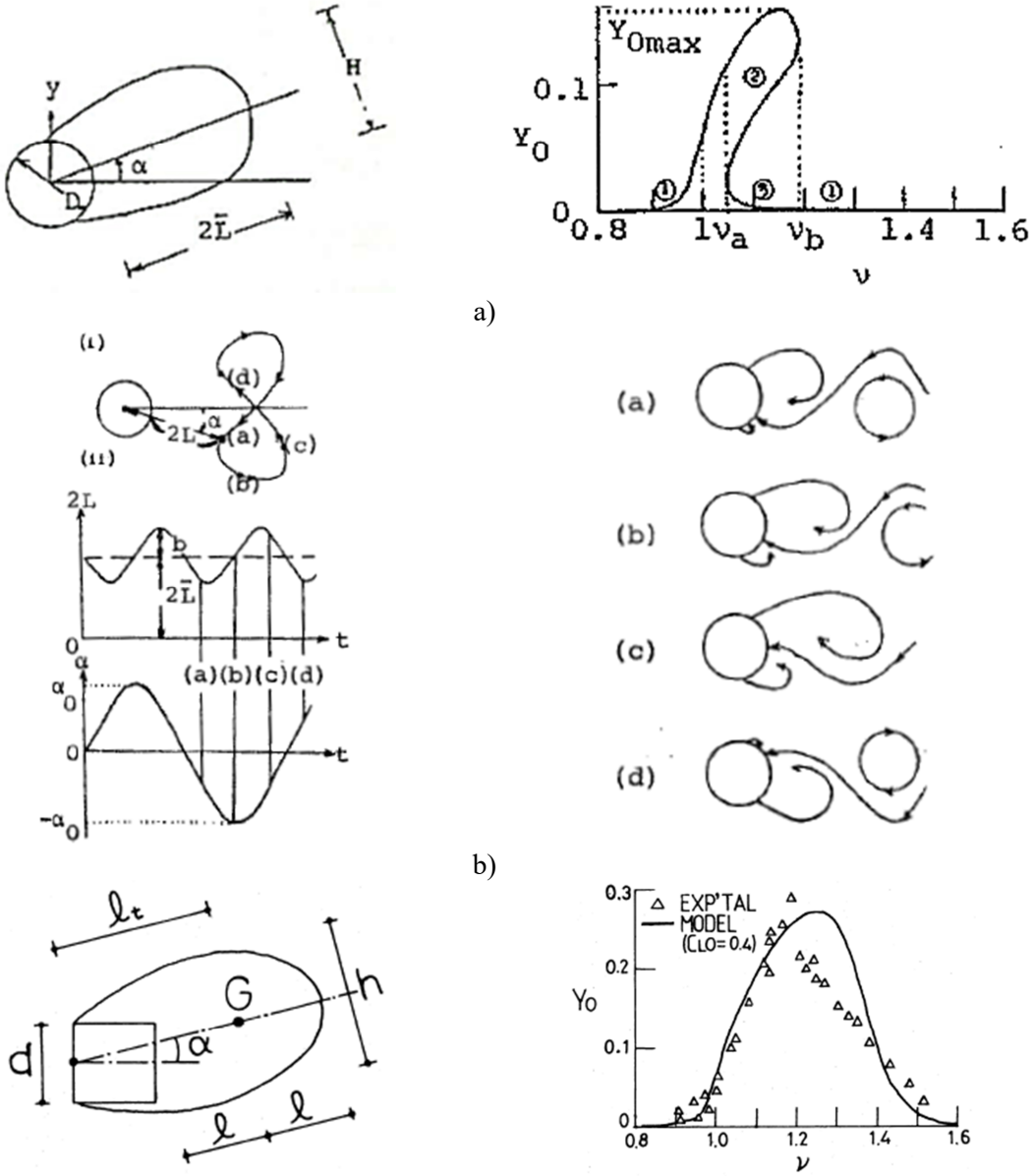

Figure 2.32. From Tamura and Matsui (1979): outline of the wake oscillator model physical design (left) and oscillation amplitude response curve (right) (a); length fluctuation and angular displacement of the wake lamina during a half-period of vortex shedding behind the cylinder (b). From Tamura and Shimada (1987): outline of the wake oscillator model (left) and response curve (right) (c).

velocity of the vibrating cylinder. According to Tamura and Matsui's work, both coupling terms are introduced on the basis of physical assumptions. The acceleration coupling comes from the analogy between the rotating lamina and a pendulum with an oscillating pivot point, whose acceleration generates a moment acting on the equivalent wake lamina. The velocity coupling originates from the substitution of the rotation ϑ in the wake-oscillator equation with the difference between ϑ and the apparent flow angle of attack given by the velocity of the cylinder. Due to the presence of two different coupling terms, the model is expected to reproduce a variety of lock-in response curve typologies.

Finally, model parameters are physically defined and they are function of the wake lamina geometry. The outline reported by Figure 2.33 represents the wake-oscillator model design assumed by Tamura and Matsui for modeling circular cylinder VIV response. The half-length l and the width h of the rotating fluid lamina can be respectively expressed in a non-dimensional way as $l^* = l/D$ and $h^* = h/D$. The following expressions mutually connecting l^*, h^*, f, β and λ are derived:

$$h^* = \frac{1}{4\pi St^2\left(0.5 + l^*\right)} \tag{2.18}$$

$$\beta = \frac{f}{2\sqrt{2}\pi^2 l^*} \tag{2.19}$$

$$\lambda = 4\pi St^2 h^* \tag{2.20}$$

Eqs (2.18), (2.19) and (2.20) come from the physical assumptions which Tamura's model is based on and they are influenced by the design of the rotating fluid plate. In particular, the rotational inertia I of the equivalent wake lamina and the moment per unit rotation K generated by the restoring force F_L are defined starting from the geometric structure assumed for the wake oscillator. According to the scheme in Figure 2.33, I and F_L defined by Tamura and Matsui can be expressed as follows:

$$I = 2\rho hl\left(D/2 + l\right)^2 \tag{2.21}$$

$$F_L = \frac{1}{2}\rho U^2 \cdot 2l \cdot 2\pi\vartheta \tag{2.22}$$

The restoring force F_L, applied at one half of the chord of the wake lamina, can be written as function of the restoring moment per unit of rotation K, as $F_L = (K\vartheta)/(D/2 + l)$,

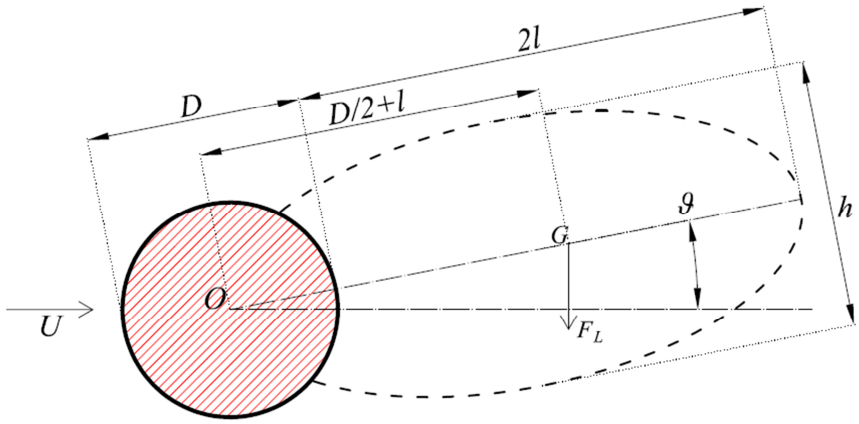

Figure 2.33. Reference outline of the non-linear wake oscillator model for circular cylinder (Tamura and Matsui, 1979).

so that K is defined in the following way:

$$K = 2\pi\rho U^2 l\left(D/2 + l\right) \tag{2.23}$$

I and K are included in the calculations coming from the physics of the model, leading to the final expressions reported by Eqs (2.18), (2.19) and (2.20). The expression of h^* as function of l^* comes directly from the Strouhal law. The vortex-shedding frequency n_s can be expressed as function of I and K:

$$n_s = \frac{1}{2\pi}\sqrt{\frac{K}{I}} \tag{2.24}$$

leading to the following expression of the Strouhal number:

$$St = \frac{1}{2\pi}\sqrt{\frac{K}{I}}\frac{D}{U} \tag{2.25}$$

The connection between the dimensionless quantities h^* and l^* reported by Eq. (2.18) is obtained by replacing I and K with Eqs. (2.21) and (2.23) in Eq. (2.25).

The parameter β is the coefficient of the damping term in the van der Pol-type equation and it can be seen as a negative linear damping ratio of the wake oscillator. According to original Tamura and Matsui's formulation, it comes from the equivalence between the work done by the viscous damping force and the work done by the transverse force R due to the vortices discharging behind the body (Eq. (2.26)), calculated according to Kutta-Joukowsky's theorem (Eq. (2.27)):

$$\pi C\left(\frac{C_{L0}}{f}\right)^2 \omega_s = 2\sqrt{2}\frac{C_{L0}}{f}\left(D/2+l\right)R \tag{2.26}$$

$$R = \rho U \Gamma_v \tag{2.27}$$

where the circulation Γ_v represents the vortex intensity behind the wake oscillator. The term C is the opposite of the equivalent damping coefficient of the wake oscillator, achievable from Eq. (2.26), whose relationship with the corresponding damping ratio β is expressed as follows:

$$\beta = \frac{C}{2\omega_s I} \tag{2.28}$$

By approximating the transverse force R with the amplitude of the lift force acting on the stationary cylinder produced by the vortex shedding (Eq. 2.29), the parameter β can be defined as reported by Eq. (2.30):

$$R = \frac{1}{2}\rho U^2 D C_{L0} \tag{2.29}$$

$$\beta = \frac{1}{2}\rho U^2 \frac{\sqrt{2}\left(D/2+l\right)Df}{\pi K} \tag{2.30}$$

which leads to the expression of β reported by Eq. (2.19), by including Eq. (2.23) in Eq. (2.30).

Finally, the parameter λ is defined starting from the acceleration of the oscillating body acting on the rotating wake lamina. The dimensional acceleration $\ddot{y}$ can be expressed as function of the non-dimensional displacement Y derived with respect to the non-dimensional time τ: $\ddot{y} = Y''\omega_0^2 D$. Such acceleration generates a force on the wake oscillator, calculated as the product between $\ddot{y}$ and the mass per unit length of the fluid lamina. In analogy with the pendulum concept, the force applied at the midpoint of the wake lamina generates a moment per unit length (M_{acc}) around the pivot point:

$$M_{acc} = Y''\omega_0^2 D \cdot 2\rho h l \cdot \left(D/2+l\right) \tag{2.31}$$

To obtain the final wake oscillator equation (Eq. (2.17)), all the terms are divided by the inertia I and by ω_0^2, so that the coefficient λ of the dimensionless body acceleration is:

$$\lambda = \frac{2\rho h l \left(D/2 + l \right) D}{I} \tag{2.32}$$

leading to $\lambda = 1/(0.5 + l^*)$ by substituting Eq (2.21) in Eq (2.32) and, finally, to the expression of λ reported by Eq. (2.20) by including Eq. (2.18).

Finally, it is worth to remark that the forcing terms coupling the wake oscillator with the body motion include both velocity and acceleration coupling. For this reason, the model is expected to reproduce a variety of lock-in response curve typologies potentially.

Tamura and Matsui's model provided good results for circular cylinder VIV response modeling, from both a qualitative and a quantitative point of view (Figure 2.32(a)). Then, in 1987, Tamura and Shimada extended the model to the case of a square cylinder, with some slight adaptations in the oscillating fluid lamina design and in the terms of the equations of motion (Figure 2.32(c)). In particular, the wake oscillator pivot point was moved to the midpoint of the upstream transverse side of the square and the contribution of the lift coefficient was added to the term coming from the transverse component of the quasi-steady drag, as a consequence of the non-axisymmetric square geometry compared to the circular one.

Mannini, Massai, Marra (2018)

The wake oscillator model proposed by Mannini et al. in 2018 is the result of a further modification of Tamura and Matsui's approach. This version was formulated to model the response of an elongated cylinder with a constant 3:2 rectangular cross-section, providing good results from both a qualitative and a quantitative point of view.

In the present work, such modified version of Tamura's model was specifically considered and, hence, it is described with particular care. The wake lamina description (Figure 2.34) exhibits similarities and differences with Tamura's approaches for circular and square cylinders:

- Wake lamina pivot point is located in the center of the body cross-section;
- The wake lamina starts from the center of the body, so that its upstream end is coincident with the pivot point O;
- The restoring lift force (F_L) acting on the lamina, defined by Birkhoff following

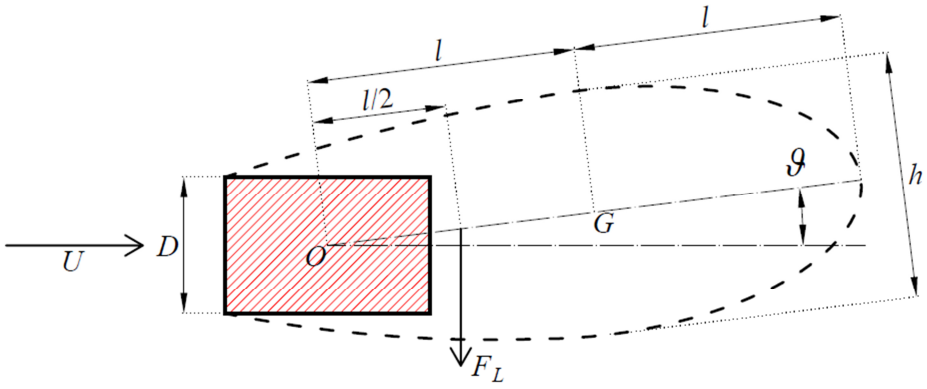

Figure 2.34. Reference outline of the non-linear wake oscillator model for 3:2 rectangular cylinder (Mannini et al., 2018).

the Kutta-Joukowsky's theory for small wake oscillations, is applied at one fourth of the chord of the lamina and calculated according to Eq. (2.22)

The first point denotes a similarity with Tamura and Matsui's model for a circular cylinder and a difference from Tamura and Shimada's model for a square cylinder. On the other hand, both last two points represent differences compared to Tamura's previous formulations. As a matter of fact, both of them assumed the wake lamina starting from the rear end of the body and the restoring force applied at the middle point of the lamina. Modifications in the wake lamina geometry cause some differences in the definition of model parameters, while the structure of the equations and the model basic physical assumptions remain unchanged compared to Tamura's work.

The mathematical model is expressed by the two equations of motion here reported:

$$Y''+2\zeta_0 Y'+Y=\frac{U_{red}^{\ 2}}{4\pi^2 m^*}f\left(\vartheta-\frac{2\pi Y'}{U_{red}}\right)+\frac{U_{red}^{\ 2}}{4\pi^2 m^*}C_{Fy} \tag{2.33}$$

$$\vartheta''-2\beta\upsilon\vartheta'\left(1-\frac{4f^2}{C_{L0}^2}\vartheta^2\right)+\upsilon^2\vartheta=\lambda Y''+\upsilon^2\frac{2\pi Y'}{U_{red}} \tag{2.34}$$

As for Tamura and Matsui's model, the equations are expressed in a non-dimensional formulation. The quasi-steady drag C_D is here substituted by the quasi-steady transverse force coefficient C_{Fy}, because of the non-axisymmetric rectangular geometry. C_{Fy} is defined starting from the lift (C_L) and drag (C_D) force coefficient measured for the stationary body:

$$C_{Fy} = -\sec(\alpha)\left[C_L(\alpha) + C_D(\alpha)\tan(\alpha)\right] \tag{2.35}$$

The modifications adopted for the equivalent wake lamina geometry and for the position of the restoring force F_L lead to new expressions for I and K:

$$I = 2\rho h l^3 \tag{2.36}$$

$$K = \pi\rho U^2 l^2 \tag{2.37}$$

and, consequently, to a modification of the expressions connecting l^*, h^*, f, β and λ:

$$l^* = \frac{1}{8\pi St^2 h^*} \tag{2.38}$$

$$\beta = \frac{4\sqrt{2}}{\pi} St^2 h^* f \tag{2.39}$$

$$\lambda = 8\pi St^2 h^* \tag{2.40}$$

Assuming a certain position for the pivot point O and the restoring force F_L, the values of l^*, β and λ depend on the values of the wake lamina width h^* and of the lift coefficient per unit rotation f. Both of them should be determined through appropriate flow visualizations on the stationary body and, for the parameter f, such visualizations should be performed along with the synchronous lift force measurement. So, once defined the location of O and F_L, the values of model parameters could be theoretically determined only through static wind tunnel tests.

The modified version of Tamura's approach proposed by Mannini et al. (2018) was able to model the VIV response of a 3:2 rectangular cylinder both qualitatively and, to a certain extent, quantitatively, over an extended range of the Scruton number of the system (Figure 2.35). In particular, the model exhibited satisfying performances in matching both the experimental response curve (Figure 2.35(a)) and the peak amplitude observed at lock-in condition (Figure 2.35(b)). Flow visualizations were not performed and the wake width was assumed $h^* = 1.8$ according to the visualizations performed by Shimada and Ishihara (2002). On the other hand, the most important role was played by the choice of the parameter f. It was varied over a large range of values, comparing the model response curve to the experimental one. Such a calibration procedure was carried out only for a relatively high Scruton number of the system. The results reported in Figure 2.35(a) were

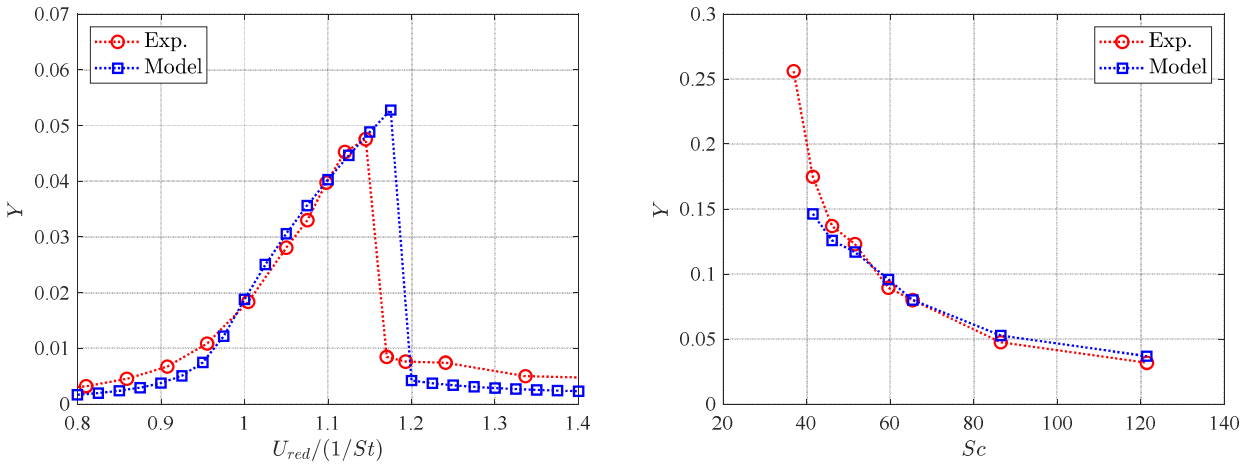

Figure 2.35. Response curves for Sc = 86 (a) and Griffin plot (b) comparison between mathematical models and experiments for 3:2 rectangular cylinder (Mannini et al., 2018).

obtained with f = 9. It was indeed observed that f = 1.16 assumed both by Tamura and Matsui (1979) and by Tamura and Shimada (1987), in analogy with Magnus-effect for a circular cylinder, was not appropriate to reproduce the behavior observed for the 3:2 rectangular cylinder.

2.4.4. Modified harmonic model

Given that vortex-shedding is a quasi-harmonic process, a harmonic formulation can be considered for modeling its action. The harmonic model is a single-degree-of-freedom approach with a linear formulation, so it can be used to predict the VIV response of an oscillating body only in terms of vibration amplitude without any information about the lock-in range or the response curve shape.

With this approach, a cylinder elastically suspended and forced by vortex shedding exhibits a linear resonance when the oscillation frequency of the body (n_0) matches the vortex-shedding frequency (n_s). The equation of motion can be written as follows:

$$m\left(\ddot{Y}+2\zeta_0\omega_0\dot{Y}+\omega_0{}^2Y\right)=\frac{1}{2}\rho U^2\bar{C}_L\,sin\left(\omega_s t\right) \tag{2.41}$$

where $\omega_0 = 2\pi n_0$ and $\omega_s = 2\pi n_s$ are the angular frequencies, respectively, of the vibrating body and of the vortex-shedding force and m is the mass per unit length of the oscillating system. The fluctuating lift coefficient is expressed as a harmonic process with amplitude

$\bar{C}_L$ and circular frequency ω_s, defined according to the Strouhal law. Y is the body non-dimensional transverse displacement and dots indicate derivatives with respect to time t. When resonance condition occurs, the response amplitude grows up to its maximum value Y_{peak}, which can be approximately expressed in the following way:

$$Y_{peak} = \bar{C}_L \cdot \frac{\rho D^2}{16\pi^2 St^2 m\zeta_0} \tag{2.42}$$

where ρ is the fluid density, D is a reference length, St is the Strouhal number of the cylinder cross section and ζ_0 is the mechanical damping ratio of the system.

The harmonic model is a linear approach and cannot take into account the non-linearity deriving from the synchronization between the body and the vortex-shedding process. Generally, it is indeed not suitable for the prediction of bridge deck VIV response amplitude at lock-in.

A modified version of harmonic model was proposed by Marra et al. (2017). In particular, a single-degree-of-freedom model was obtained by modifying the damping term in the harmonic model expression and assuming the amplitude of the fluctuating lift coefficient $\bar{C}_L$ equal to C_{L0}, which is the fluctuating lift coefficient due to vortex-shedding action on the stationary body. The model equation of motion can be written in this way:

$$m\left[\ddot{Y} + 2\left(\zeta_0 + \zeta_{aero}^{QS}\right)\omega_0\dot{Y} + {\omega_0}^2 Y\right] = \frac{1}{2}\rho U^2 C_{L0}\sin\left(\omega_s t\right) \tag{2.43}$$

The term ζ_{aero}^{QS} indicates an aerodynamic damping ratio added to the mechanical one and calculated according to the quasi-steady theory in the following way:

$$\zeta_{aero}^{QS} = -\frac{\rho D^2 U_{red}}{8\pi m} \cdot \frac{dC_{Fy}}{d\alpha} \tag{2.44}$$

where:

- D is a reference length for the cross section of the cylinder, usually the across-flow dimension;
- $U_{red} = U/n_0 D$ is the reduced flow speed, where U is the incoming wind velocity;
- C_{Fy} is the mean quasi-steady transverse force coefficient;
- α is the angle of attack of the incident flow

The quasi-steady aerodynamic damping calculation requires static force and/or pressure measurements, since it depends on the transverse force coefficient C_{Fy} (Eq. (2.35)) with a linear proportionality between ζ_{aero}^{QS} and $dC_{Fy}/d\alpha$. The addition of such quantity to ζ_0 can be directly included in the peak response amplitude Y_{peak}, which can be expressed in the following way:

$$Y_{peak} = C_{L0} \cdot \frac{\rho D^2}{16\pi^2 St^2 m\left(\zeta_0 + \zeta_{aero}^{QS}\right)} \tag{2.45}$$

The main features of this modified version of the harmonic model can be summarized as follows:

- The model output is the peak response amplitude at lock-in.
- Extreme simplicity of mathematical formulation and output calculation;
- Relatively simple static tests are needed to determine model parameters;

The approach was proposed by Marra et al. in 2017 and applied to a 4:1 rectangular cylinder. Then, it was also applied by Mannini et al. (2018) to a 3:2 rectangular cylinder in the same work including the modified Tamura's model described previously and the results obtained by both models were compared to each other and to the experimental results (Figure 2.36). As observable in Figure 2.36(b), the modified harmonic model provided promising results in predicting the peak response amplitude over a wide range of Scruton number values, especially in case of response amplitude not extremely large, within about

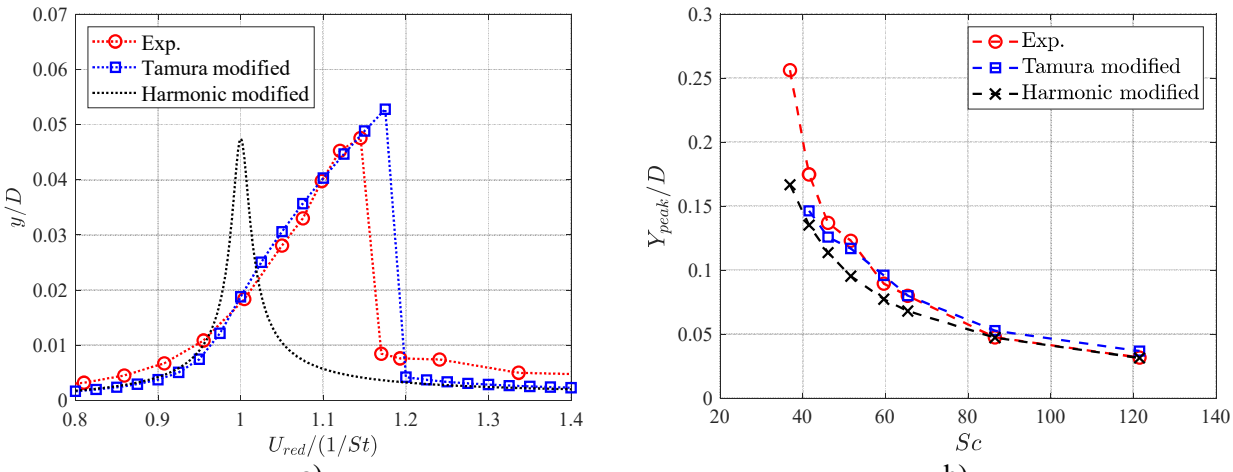

Figure 2.36. Response curves for Sc = 86 (a) and Griffin plot (b) comparison between mathematical models and experiments for 3:2 rectangular cylinder (Mannini et al., 2018).

10% of the cylinder cross-flow dimension. This simplified approach also exhibited a good agreement, in terms of peak response prediction, with the results provided by modified Tamura's approach described in the previous section (Figure 2.36).

A kind of connection between the two models was found from the mathematical point of view, leading to suppose that the modified harmonic model might be seen as a sort of simplified version of Tamura-type wake oscillator model. For the purpose of highlighting the mentioned connection, some simplifications and approximations have to be done in the mechanical oscillator equation of modified Tamura's model (Eq. (2.18)):

- Wake angular displacement ϑ approximated with a harmonic process: $\vartheta = \vartheta_0 \sin(\upsilon\tau)$, with $\vartheta_0 = C_{L0}/f$ and $\upsilon = \omega_s/\omega_0$;
- C_{Fy} linearized close to the incoming flow angle of incidence $\alpha = \alpha_0$: $C_{Fy} = C_{Fy}(\alpha_0) + \left.\frac{\mathrm{d}C_{Fy}}{\mathrm{d}\alpha}\right|_{\alpha=\alpha_0}$.

According to these approximations, the equation of motion of Tamura's mechanical oscillator can be written in the following way:

$$Y'' + 2\left[\zeta_0 - \frac{\rho D^2 L U_{red}}{8\pi M}\cdot\left(\frac{dC_{Fy}}{d\alpha} - f\right)\right]Y' + Y = \frac{U_{red}^{\ 2}}{4\pi^2 m^*}\left[C_{L0} sin(\upsilon\tau) + C_{Fy}(\alpha_0)\right] \quad (2.46)$$

On the other hand, the modified harmonic model equation (Eq. (2.38)) expressed in terms of non-dimensional time $\tau = \omega_0 t$ can be written as follows:

$$Y'' + 2\left[\zeta_0 - \frac{\rho D^2 L U_{red}}{8\pi M}\cdot\frac{dC_{Fy}}{d\alpha}\right]Y' + Y = \frac{U_{red}^{\ 2}}{4\pi^2 m^*} C_{L0}\, sin(\upsilon\tau) \quad (2.47)$$

Eqs (2.46) and (2.47) exhibit the same formulation, except for the presence of terms $-f$ and $C_{Fy}(\alpha_0)$ in the first one. The term $C_{Fy}(\alpha_0)$ is a constant value, so, from the point of view of peak oscillation amplitude Y_{peak}, the difference between the two equations is actually represented only by the value $-f$ included in the damping term of Eq (2.46). For this reason, the role played by the parameter f in the comparison between the two models has to be specifically considered.

In addition, the derivation of modified harmonic model from Tamura's approach should consider the wake oscillator equation too (Eq. (2.34)) and, in particular, the

influence of the coupling terms $\lambda Y''$ and $\upsilon^2 \frac{2\pi Y'}{U_{red}}$. The effects of parameter f and of the coupling of the wake oscillator with the mechanical one have been studied and the results obtained are reported in Section 6.3. The potential connection observed between the two models may suggest a physical origin for the modified harmonic model, since it can be possibly derived from a more complex approach based on clear physical assumptions.

2.5. Final remarks

The overview about the main topics addressed in the present work gave rise to some observations. The VIV response of an elongated body with a bluff cross-section is certainly a complicated topic, for the variety of behaviors potentially observed due to different flow patterns around the oscillating body, caused by its geometry and the flow angle of incidence.

Bridge decks may exhibit a large variety of cross-section shapes, usually relatively elongated. The addition of aerodynamic devices may lead bridge sections to behave like a quasi-streamlined body, nevertheless this can be in contrast, in many cases, with the effect produced by lateral screens or barriers, which can lead to a behavior much closer to a bluff geometry. The variation of the wind angle of attack introduces another element of complexity, since the same geometry can exhibit a strongly different response for different directions of the incoming flow.

Predicting, even approximately, how certain variations in cross-section details and angle of attack affect bridge deck VIV response is extremely difficult without an accurate experimental campaign. Nevertheless, such topic might be reasonably deepened by assessing the VIV response of a deck section progressively altered in a systematic way. The addition of fairings with slope of the walls or shape of the corners varying in a certain range, the installation of barriers of the same type but with different height or characterized by the same height and variable distribution of the openings are examples of progressive modifications of the section which could better isolate the effect of a specific geometric alteration. On the other hand, a certain cross-section detail should be tested for zero, positive and negative angle of attack, with the purpose of better describe possible patterns in effects produced by local changes in deck geometry. A clearer overview about potential effects of various cross-section details for different flow angles of incidence could be certainly useful for qualitative considerations during the design phase of a bridge.

On the other hand, the modeling of bridge deck vortex-induced oscillation is still an open issue. From the scientific point of view, the development of an accurate mathematical prediction would be certainly very interesting. In addition, an efficient model could be practically useful, by integrating experimental results and/or reducing, even partially, the amount of wind tunnel tests performed during the design phase of a bridge. From this perspective, the potential usefulness is emphasized by the previously mentioned variety of aeroelastic behaviors possibly exhibited by a bridge deck in presence of local additions or modifications and for different angle of attack values. Finally, the practical efficiency and suitability of a model is determined not only by its accuracy, but also by computational cost and difficulty of the calibration procedure.

The two approaches specifically explored in the present work, a modified Tamura's model and a modified harmonic model, exhibited interesting results for different rectangular cylinders. Both approaches are based on parameters achievable through static wind tunnel tests; in particular, a considerable part of modified Tamura's model parameters and all the parameters required by modified harmonic model can be estimated through relatively simple static wind tunnel tests. Finally, the clear physical origin of Tamura-type formulation represents certainly an interesting feature of the model. On the other hand, the possibility of assuming the modified harmonic model as a simplified and quick version of a physically based wake oscillator model might be attractive, so that the connection between the two models could be worthily deepened.

3. Experimental facilities and methods

3.1. Introduction

The present work includes a large amount of experiments: wind tunnel tests on an aluminum sectional model, whose cross section aims to reproduce a realistic bridge deck geometry. The sectional model is characterized by a constant cross section along the longitudinal direction, aiming to reproduce a portion of a real bridge deck, to conduct a two-dimensional study about it.

Two main typologies of experiments were carried out on the sectional model in wind tunnel: static and aeroelastic tests. The first ones consisted of measurements of aerodynamic forces on the stationary model for several values of the flow angle of incidence. This typology of experiments is generally preliminary to any aeroelastic test campaign, in order to achieve information about the aerodynamics of the investigated body and to better understand and discuss the VIV response of the body when it is free to oscillate. In the present work, static force measurements were specifically carried out to formulate qualitative suppositions about the expected VIV response of the sectional model and to calibrate the mathematical models presented in Sections 2.4.3 and 2.4.4.

During aeroelastic tests, the model was left free to oscillate elastically through an appropriate setup and its displacements along the across-flow direction were monitored, while any motion in the other degrees of freedom was restrained. These tests were performed to assess the actual VIV response of the investigated bridge deck and the performances of the mathematical modeling. With regard to the wake-oscillator model (Section 2.4.3), test results were also employed for model calibration. Aeroelastic tests were carried out in two different ways: firstly, the system was left free to vibrate from a rest condition, with the motion excited by flow-induced forces acting on the sectional model, while then the oscillating system started its motion from a certain initial condition of displacement through an appropriate procedure described in Section 5.5.

3.2. Wind tunnel

Wind tunnel tests were carried out in the CRIACIV Boundary Layer Wind Tunnel (Figure 3.1 and Figure 3.2) in Prato, Italy. The open circuit wind tunnel has a total length

Figure 3.1. View of the CRIACIV Boundary Layer Wind Tunnel (Prato, Italy).

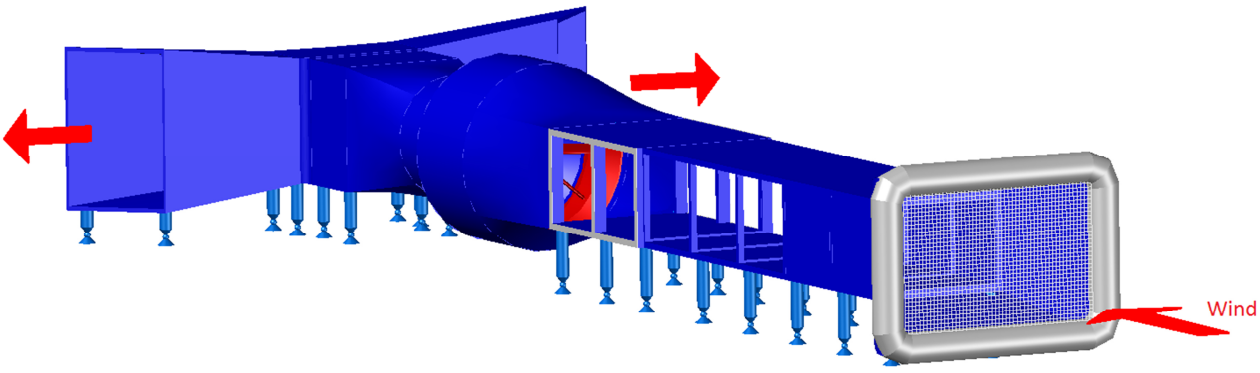

Figure 3.2. 3D rendering of CRIACIV wind tunnel with incoming and outgoing flow indicated.

of about 22 m, and a test section of 2.40 m × 1.65 m with an upstream fetch of about 8 m. A small longitudinal variability of the tunnel width allows the formation of floor, ceiling and wall boundary layers, thus keeping the static pressure almost constant along the tunnel length. The target wind speed, in the range from 0 to approximately 30 m/s, is obtained by adjusting both the fan rotation speed and the pitch of its 10 blades. The free-stream turbulence intensity is below 1%, while other turbulence values can be obtained by using appropriate grids installed at different positions along the wind tunnel or wood panels with a certain level of roughness fixed to the floor. In the present experimental work, all tests were carried out in smooth flow condition, since it usually represents the most meaningful condition for the assessment of bridge deck VIV response.

3.3. Instrumentations

The main technical instruments used during the experimental tests are herein listed:

- Pitot tube
- High frequency force balances
- Laser transducers

The mean flow speed was monitored through a Pitot tube placed upstream of the model and connected to an ASL Setra AccuSense sensor. The wind velocity at the position where the model is located is impossible to be measured during the test performance because of the presence of the model itself. For this reason, the upstream Pitot tube was calibrated through another Pitot tube placed at the midpoint of the model axis before wind tunnel tests: the ratio between the wind speed measured by the upstream tube and by the one located at the position of the model is calculated, to determine the actual mean speed of the incoming flow during the experiments.

The aerodynamic forces at various angles of attack (angle between the cross section of the sectional model and the oncoming flow) have been measured by means of two ATI FT-Delta SI-165-15 high frequency six-components strain-gauges force balances (Figure 3.3(a)) placed at the ends of the model. The HFFBs use a Multi-Axis Force/Torque Sensor (F/T) system that allows to measure six components of force and moment (F_x, F_y, F_z, T_x, T_y, T_z) through a monolithic sensor instrumented. The sensor F/T uses six silica

a) b)

Figure 3.3. High frequency force balance (a) and laser transducer (b) used, respectively, for static and dynamic tests.

strain-gauges to minimize the level of noise in the signal. The signals are amplified in the sensor, conditioned, scanned and converted into digital by means of the same A/D converter USB cDAQ-9172 National Instruments. HFFB technical specifications are listed in Table 3.1.

Two non-contact optical laser transducers (Figure 3.3(b)) OptoNCDT 1605,produced by Micro-epsilon, were used to determine model displacements during the tests. They are characterized by a semiconductor with 675 nm wavelength and a maximum output power of 1 mW and their functioning principle is based on triangulation. The output voltage range is ± 10 V, which corresponds to a working displacement range of about ± 100 mm. The lasers are connected to a card (National Instruments AT-MIO 16XE50) and then logged through a PC. The characteristics of the lasers are reported in Table 3.2.

3.4. Set-up for static wind tunnel tests

Aerodynamic force measurements were performed by connecting the sectional model, with the high frequency force balances at both its ends, to an appropriate support system. The model was connected to the balances in a perfectly rigid way, through a couple of cylindrical steel clamps, while two joints blocking just translational and torsional degrees of freedom were placed between the balances and the external support system. This kind of connection was realized with the purpose of reducing as much as possible forces and moments generated by the locking of the clamps around sectional model ends, to be sure that in presence of additional loads produced by the wind the balances did not reach their full-scale limit.

Table 3.1. Main technical characteristics of the high frequency force balances used for static tests.

Sensor type	FT – Delta HFFB
Model	SI – 165 – 15
Range of measurements F_x, F_y	± 165 N
Range of measurements F_z	± 495
Range of measurements M_x, M_y, M_z	± 15 Nm
Resolution F_x, F_y	± 1/128 N
Resolution F_z	± 1/64 N
Resolution M_x, M_y, M_z	± 1/2112 Nm
Repeatability	± 0.03% FS
Full scale error F_x, F_y	± 0.06% FS
Full scale error F_z	± 0.10% FS
Full scale error M_x, M_y, M_z	± 0.01% FS
Resonance frequency	1.7 kHz
Operating temperature range	0 ÷ 70 °C

Table 3.2. Main technical characteristics of the laser transducers used for dynamic tests.

Sensor type		Laser sensor
Model		LD 1605
Type		200
Measuring range		± 100 mm
Stand-off midrange		340 mm
Non-linearity ≤ ± 0.3% d. M.		600 µm
Resolution (noise) static		60 µm
Measuring spot dia. Midrange		2 mm
Light source		Laser 1 mW, wavelength: red 675 nm
Sampling frequency		40 kHz
Laser class		2
Analogical output	Displacement	± 10 V
	Output impedance	Approx. 0 Ohm (10 mA max.)
	Angle dependence	Approx. 0.5% when turning ± 30° about long axis
	Rise time	0.1/0.2/2 or .20 msec selectable
	Frequency response	10 kHz, 3 kHz, 250 Hz or 25 Hz
	Temperature stability	0.03 %/°K
	Intensity of reflecting light	1 V bis 10 V/max. : 0 V bis + 13 V
Permissible ambient light		2000 Lux
Life time		50000 h for laser-diode
Insulation		200 VDC, 0 V against housing
Max. vibration		10 g to 1 kHz
Operation temperature		0 ÷ 50 °C

The external support represents the system allowing to fix the sectional model inside the wind tunnel. During the experimental work, two different support systems for static tests were used, named in the following way:

- Manual static test set-up
- Automated static test set-up

The manual static test set-up (Figure 3.4) consists of two vertical steel uprights rigidly fixed to the floor and to the ceil of the wind tunnel. Two horizontal C-shaped steel elements, starting from the uprights, compose the support which force balances and sectional model were connected to. The wind angle of attack can be appropriately modified by rotating manually the model around its longitudinal axis. The automated static test set-up (Figure 3.5) consists of two steel columns fixed to the floor of the wind tunnel, and directly connected to the model and the balances. The upper part of both columns is equipped with an electric motor that allows to rotate automatically the sectional model around its axis to obtain different angles of attack of the incident flow.

The main difference between the two systems mentioned is represented by the much lower time needed to perform the same amount of measurements with the automated setup. They provide substantially the same level of accuracy in terms of force measurement, since they are equipped with the same force balances described in the previous section. Nevertheless, a slight improvement form the point of view of the accuracy is also reached through the automated setup, since varying and setting the flow angle of attack is certainly more correct in this case than with a manual rotation and adjustment of the model.

In case of manual rotation of the model the angle was indeed set by checking the correct position through a digital inclinometer each time. On the other hand, the automated system allowed to check only the very first angle through the inclinometer, while the others were automatically adjusted by the system. Both manual and automated procedures were found to be accurate, but the precision of the second one can be reasonably considered slightly higher.

3.5. Set-up for aeroelastic wind tunnel tests

Dynamic aeroelastic wind tunnel tests were performed by suspending the sectional

Figure 3.4. Static wind tunnel setup with manual rotation system, used for the first set of force measurements on the sectional model

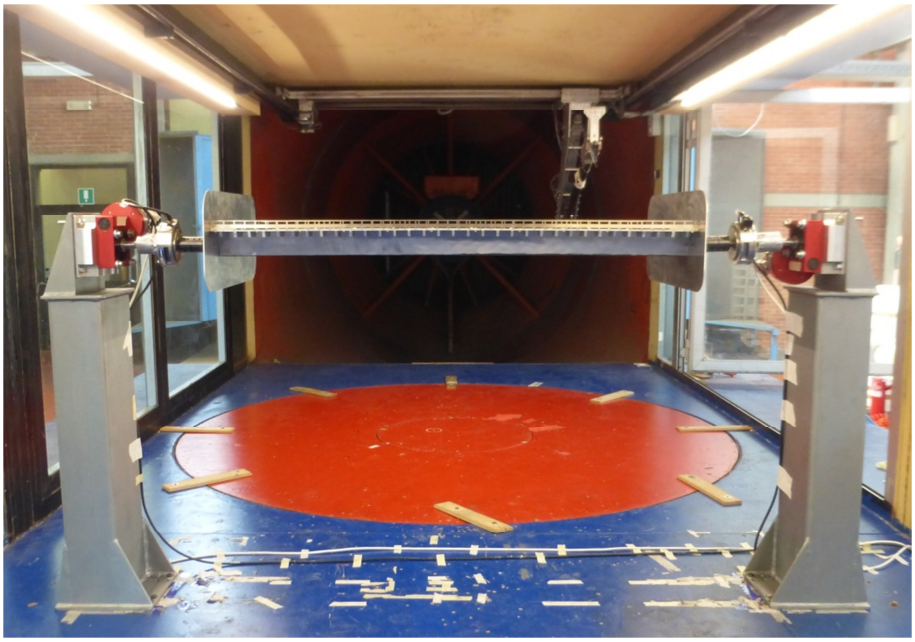

Figure 3.5. Static wind tunnel setup with automated rotation system, used for second, third and fourth sets of measurements.

model through two steel shear-type frames, connecting them to the model at both ends. The frames were fixed to the two steel uprights described above for the manual static test set-up (Figure 3.6(a, b)) and only the vertical translation of the sectional model was allowed. Vertical displacements were measured through the laser transducers described in Section 0.

This kind of setup provides a single-degree-of-freedom oscillating system, which can be used to reproduce the response of a real bridge deck in terms of vibration in the across-wind direction. It is a quite typical procedure to evaluate bridge deck VIV response during the design phase of the structure; to this purpose, the equivalent mass of the real structure related to the transverse oscillation degree of freedom has to be determined to correctly evaluate the response through the single-degree-of-freedom system in wind tunnel.

The dynamic characteristics of the oscillating system were determined by the couple of laminas of each frame sticking out from the upright for an adjustable length. The flow angle of attack was manually set by regulating the inclination of the sectional model around its longitudinal axes in this kind of set-up too. The linearity of the oscillating system in a sufficiently wide range of displacement of the sectional model was checked through an appropriate procedure described in Section 5.3.

This set-up also allowed to change the Scruton number of the vibrating system through an additional contribution to the mechanical damping. This additional damping was obtained by employing two couples of permanent magnets attached to the ceil of the wind tunnel (Figure 3.6(c)), exactly above the shear-type frames, and two aluminum plates fixed to the frames in order to oscillate inside the regions between the two couples of magnets. The so obtained damping mechanism is based on the electromagnetic induction phenomenon: the movement of the aluminum plate perpendicular to the magnetic flux generates an eddy current which produces a force opposite to the plate movement and proportional to its velocity (viscous force). The intensity of this viscous force depends on the intensity of the magnetic flux, which is determined by the distance between the two magnets of each couple. The damping of the system was therefore regulated by increasing and reducing the distance between the magnets.

3.6. Sectional model

The sectional model used for wind tunnel tests, as previously mentioned, has a

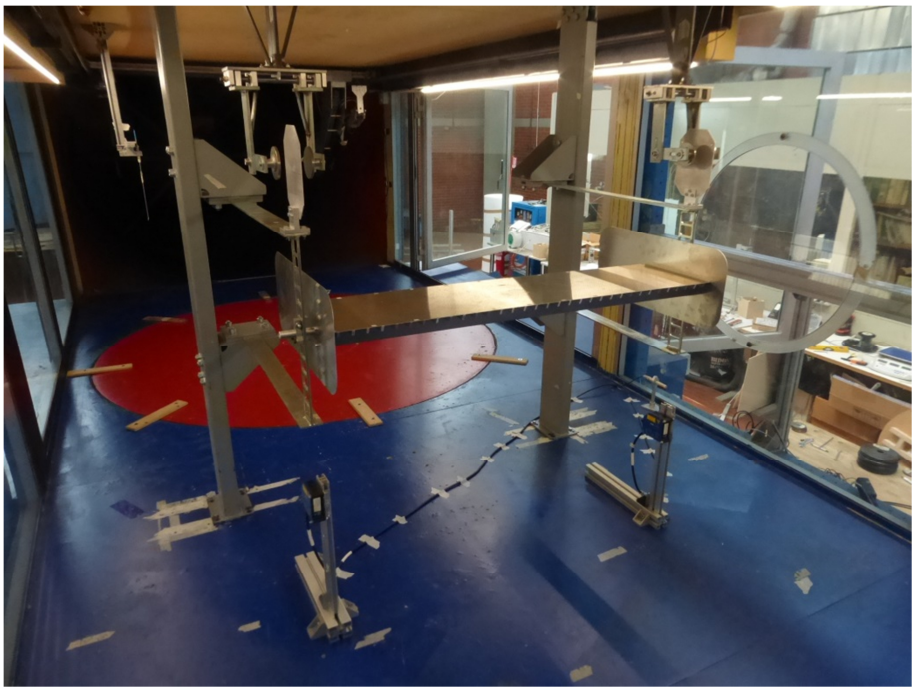

a)

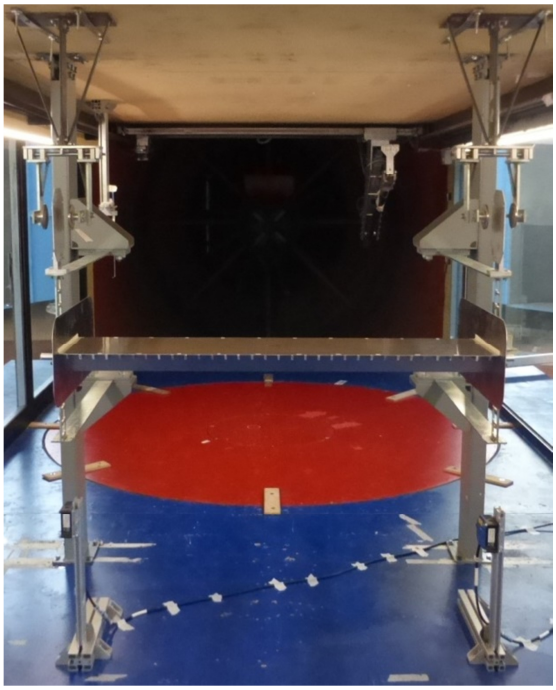

b)

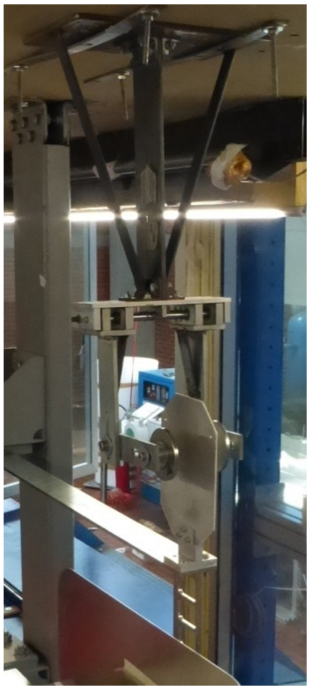

c)

Figure 3.6. Views of the sectional model fixed to the wind tunnel setup for aeroelastic tests (a, b); close-up of the tool used to introduce additional mechanical damping to the oscillating system.

constant cross section (Figure 3.7), aiming to reproduce a quite realistic bridge deck geometry. The shape of the cross section is inspired to the Volgograd Bridge deck, with a scale factor of approximately 1:70 compared to the real structure. The choice of such a cross-section geometry comes from the will to have a strong similarity with a realistic bridge deck that has already shown serious problems due to VIV. As a matter of fact, in 2010 this bridge over the Volga River was closed to traffic because of large vortex-induced oscillations (up to 80 cm of peak-to-peak amplitude), as also reported in works achievable from scientific literature (Corriols and Morghental, 2012; Weber et al., 2013). In addition, the Volgograd Bridge exhibits a quite typical cross-section geometry, a trapezoidal box girder with lateral cantilevers, and a main span about 155 m long, demonstrating how VIV response may represent a considerable problem also in case of relatively limited span length.

Figure 3.7 shows main model cross-section dimensions: B = 246 mm is the total width, while D = 53 mm is the height of the model, which is one meter long (L = 1000 mm). As said before, these dimensions originate from an approximate scaling process of Volgograd Bridge cross-section geometry with a factor of 1:70, whose choice came from limitations given by the blockage ratio, kept below 5% of test section height with the model at zero angle of attack.

In Figure 3.7, a scheme of the aerodynamic forces generated by the wind action and acting on the body is also reported: U is the mean speed of the incoming flow, while F_L, F_D and M are, respectively, drag, lift and torque generated by the wind action. In addition, the

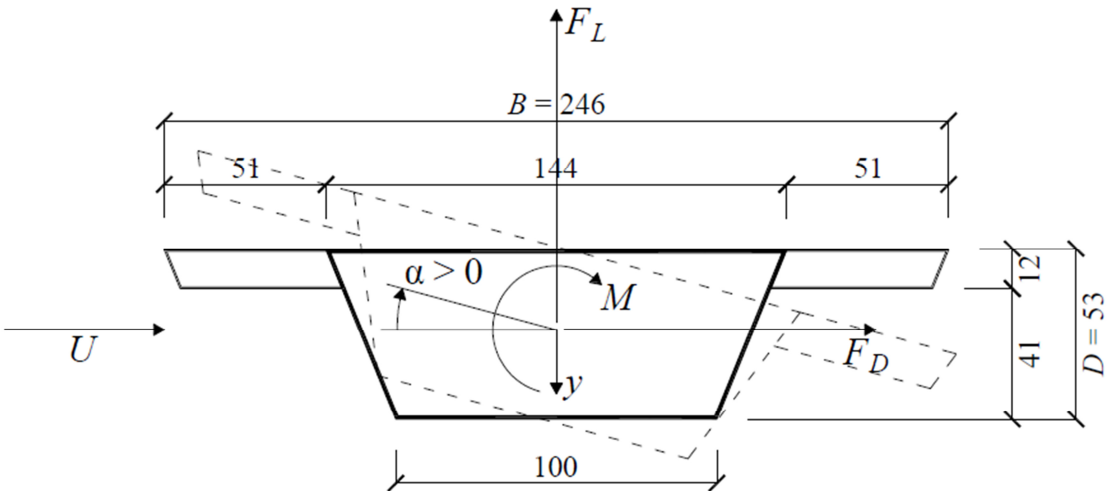

Figure 3.7. Outline of the model cross-section with main dimensions reported in mm. Generic drag, lift and torque are indicated, as well as the positive rotation of the sectional model around its longitudinal axis (α).

angle of attack of the wind (α) is indicated as rotation of the sectional model around the longitudinal axis, since this is the usual procedure to change the flow angle of incidence during wind tunnel tests. The angle α is positive when the model exhibits nose-up rotation. Finally, y indicates the model direction of motion, along which the body oscillates during wind tunnel tests.

Figure 3.8 shows views of the upper (Figure 3.8(a)) and lower side (Figure 3.8(b)) of the sectional model. As observable in Figure 3.8(b), the model was equipped with end-plates fixed at both ends of the body. These large rectangular plates (500 mm × 210 mm, 2 mm thick for static tests and 1 mm thick for dynamic tests) aim to confine the flow and promote the two-dimensional condition required by a study on a sectional model. The end-plates were made of aluminum and their dimensions were chosen complying with ESDU prescriptions (Cowdrey, 1963; Obasaju, 1979).

A large part of the work is focused on the effects produced by cross-section geometric details. To this purpose, the model cross section was progressively altered through some modifications and additions, reported in Figure 3.9. First of all, the lower

a)

b)

Figure 3.8. Views of the sectional model used for wind tunnel tests: sectional model without end-plates installed (a) and view of the lower side of the model (b) with end-plates and fixed to the experimental setup.

corners of the model were modified to make them sharper, by applying and modeling an appropriate adhesive paste on the original quite rounded edges of the girder (Figure 3.9(a, b)). Then, the geometry was more considerably altered by adding two different typologies of lateral barriers (Figure 3.9(g)), named Barrier 1 (Figure 3.9(c, e)) and Barrier 2 (d, f).

These two bridge deck lateral barriers were selected from several typologies achievable from commercial producers (Figure 3.9(c, d)). In particular, Barrier 1 and Barrier 2 are characterized by a very similar height (about 40% of bare deck cross-flow dimension D), while their degree of transparency to the flow and opening distribution are very different from each other. In particular, Barrier 1 degree of transparency is about 51%, while the one of Barrier 2 is about 23%. It is worth to notice that the second typology exhibits a totally close portion in its lower part, completely impermeable to the flow. The height of this part of Barrier 2 is almost equal to 30% of D, so that in presence of this second lateral barrier the cross-flow dimension is increased by 30% continuously along the model. Both barriers were made of aluminum and fixed to the model with screws (Figure 3.9(e, f)).

The modification of the lower edges and the addition of lateral barriers gave rise to four different geometric configurations of the cross section to investigate:

- Bare deck with round lower corners;
- Bare deck with sharp lower corners;
- Deck with sharp lower corners and Barrier 1 installed;
- Deck with sharp lower corners and Barrier 2 installed.

The mentioned geometric layouts were tested and deeply studied for different values of wind velocity and angle of attack, both in static and in dynamic condition. A considerable amount of results was achieved and a large variety of aerodynamic and, above all, aeroelastic behaviors were observed, as described in Chapter 4 and Chapter 5.

The results obtained from such an experimental campaign were finally used in the study about VIV response mathematical modeling, reported in Chapter 6. The two mathematical models introduced in Chapter 2 were calibrated by employing the results of wind tunnel tests. At the same time, the main features of the two mathematical approaches were accurately discussed and their performances were assessed by comparing mathematical predictions to wind tunnel test results.

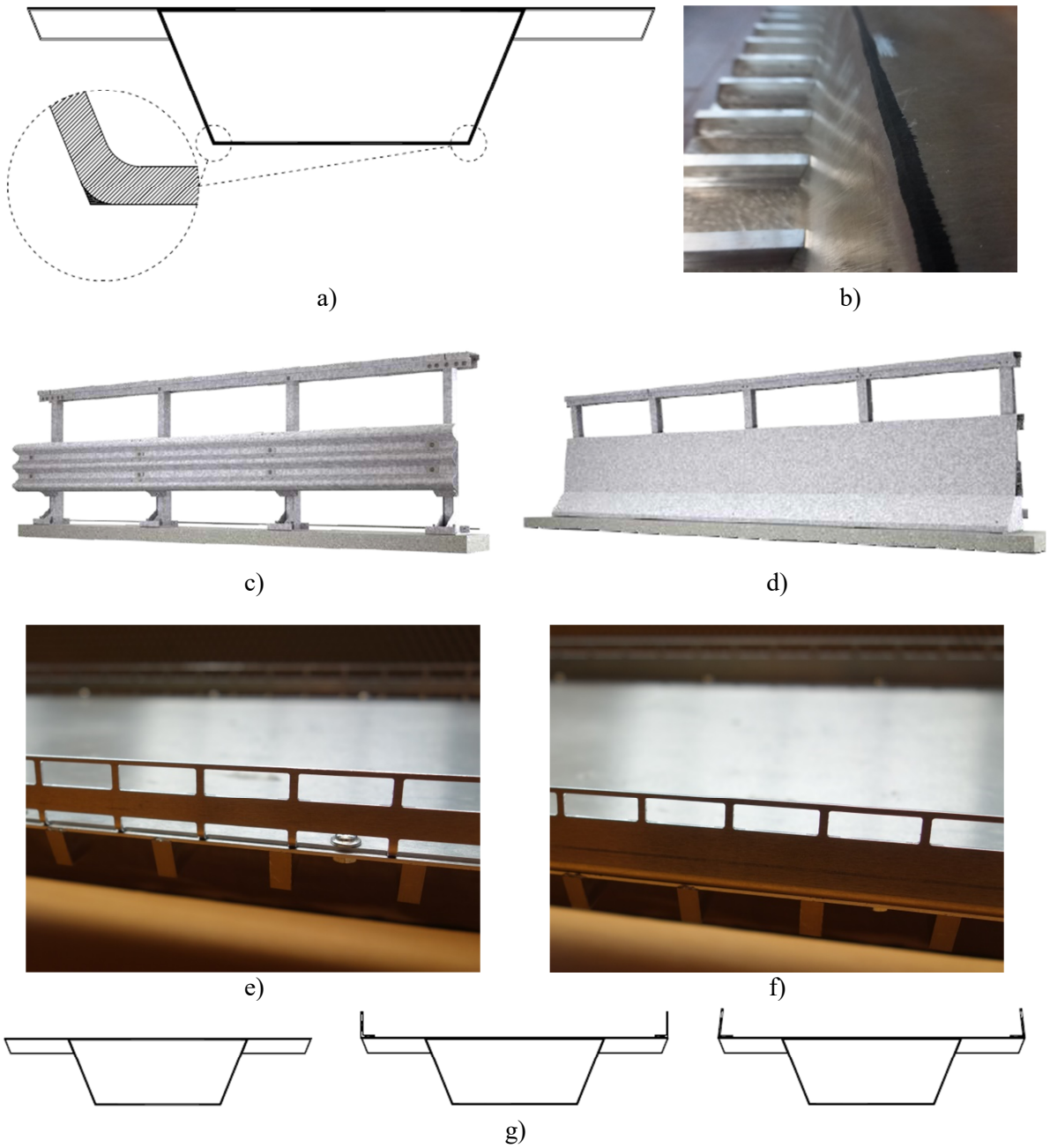

Figure 3.9. Overview of cross-section alteration through geometric details: modification of lower corners of the girder (a, b) and addition of Barrier 1 (c, e) and Barrier 2 (d, f) to the bridge deck sectional model. Comparison between section layouts (g) without barriers (left), with Barrier 1 (center) and with Barrier 2 (right)

4. Results of static wind tunnel tests

4.1. Introduction

In the first phase of the wind tunnel experimental campaign, static tests were performed on the sectional model. These experiments were carried out to describe the aerodynamics of the sectional model cross section for different configurations and determine parameters necessary for the mathematical modeling. Aerodynamic force measurements were carried for each investigated geometric layout at different angles of attack (α), in smooth flow condition. Both mean and fluctuating values of aerodynamic forces generated by the incoming flow on the stationary body were determined. Such tests were performed with two main purposes:

- Formulating qualitative suppositions about dynamic behavior of the investigated cross section for different configurations, including quasi-steady considerations based on static tests results;
- Determining aerodynamic parameters for the calibration of the two mathematical approaches for VIV response modeling investigated in the present work.

In this chapter, the overall idea is to explore as deeply as possible the amount of information about bridge deck VIV response achievable from static force measurements, actually the easiest test typology of wind tunnel tests to perform, for different cross-section geometric configurations and flow angles of incidence.

Mean aerodynamic force coefficients (C_D, C_L, C_M) were determined and used to formulate qualitative predictions about VIV response based on aerodynamic damping definition according to quasi-steady theory (ζ_{aero}^{QS}). In particular, such damping ratio is a function of the quasi-steady transverse force coefficient slope $dC_{Fy}/d\alpha$, as observable in the expression reported by Eq (2.44).

The expression of C_{Fy} as function of α, C_D and C_L is reported by Eq. (2.35), while suppositions about VIV response based on $dC_{Fy}/d\alpha$ value are introduced in Section 4.2.6 and discussed in Section 4.5.2. In addition, ζ_{aero}^{QS} is also crucial for the study about the modified harmonic model introduced in Section 2.4.4 and to explore the relationship with the Tamura-type wake oscillator model described in 2.4.3.

On the other hand, the fluctuating lift force was measured and observed with special care. In particular, the contribution to the lift fluctuation coming from vortex shedding was determined and employed to evaluate cross-section Strouhal number (St) and amplitude of the fluctuating dimensionless lift force (C_{L0}). They were used to formulate additional qualitative hypothesis about bridge deck VIV response, introduced in Sections 4.3 and 4.4 and discussed in Section 4.5.2. In addition, these two to quantities are part of the aerodynamic parameters needed for the two mathematical models above mentioned, since they are necessary for modeling the fluctuating vortex-shedding force acting on the body.

4.2. Mean aerodynamic force coefficients

With the purpose of determining all of the quantities mentioned in the previous section, the time histories of lift and drag forces and torsional moment were recorded for many values of the flow angle of attack for each cross-section geometric layout. Each time history was 60 seconds long and measurements were repeated for at least two different values of the wind velocity.

The lower speed value was set approximately between 5 and 6 m/s, chosen as a value compatible with a sufficient reliability of the instrumentation and, at the same time, close to the vortex-resonance flow velocities expected during dynamic tests described in Chapter 5. In addition, low speed measures were collected with the purpose of appropriately describing force fluctuations, in particular the fluctuating transverse lift force. On the other hand, the higher wind velocity considered was about between 28 and 30 m/s, the maximum value achievable in CRIACIV wind tunnel, since the instruments employed at high flow speed are more accurate, especially in terms of mean values of aerodynamic forces measured, and allow to describe more correctly the aerodynamics of the investigated cross section. In addition, the comparison between low and high velocity results was able to highlight possible changes in the aerodynamic behavior due to Reynolds number Re (Reynolds effects), defined according to Eq. (2.2).

For the first investigated configuration, bare deck with round lower corners, the tests were carried out through the manual static test set-up described Chapter 3, while for the three sharp corner configurations, with and without barriers, the automated static test set-up was used.

The aerodynamic coefficients represent the non-dimensional expression of aerodynamic forces and moments. The mean values of these coefficients were obtained

from the mean values of drag, lift and torque time histories (F_D, F_L, M) through a normalization procedure as follows:

$$C_D = \frac{F_D(\alpha)}{\frac{1}{2}\rho U^2 DL} \tag{4.1}$$

$$C_L = \frac{F_L(\alpha)}{\frac{1}{2}\rho U^2 DL} \tag{4.2}$$

$$C_M = \frac{M(\alpha)}{\frac{1}{2}\rho U^2 BDL} \tag{4.3}$$

The mean values of drag and lift force coefficients were used to evaluate the quasi-steady transverse force coefficient C_{Fy}, which was calculated according to the expression reported by Eq (2.35).

The aerodynamic coefficients were evaluated for the four geometric configurations in a relatively wide range of the flow angle of attack α. Figure 4.1 shows the force coefficient curves against α, between approximately -17° and +17°, for high Reynolds number value. In this figure, C_D, C_L and C_M curves are compared to each other for every geometric layout of the cross section. The drag curves exhibited a relatively flat shape, increasing for strongly positive and negative values of the flow angle of incidence. Both lift and torque coefficients increased with the angle of attack up to a peak value, after which a decrement was observed. The slope of increasing and decreasing trend and the position of the peak were found to be markedly affected by the geometric layout of the cross section.

4.2.1. Bare deck configurations

Firstly, the two bare deck configurations, with round and sharp corners, were compared, to point out aerodynamic effects produced by the modification of model lower edges. In Figure 4.2, aerodynamic coefficients before and after corner alteration are compared. Such geometric variation did not produce extreme changes in force coefficient curves, nevertheless some limited effects are observable. The basic shape of the two drag plots (Figure 4.2(a)) does not change after the applied modification, but in case of sharp

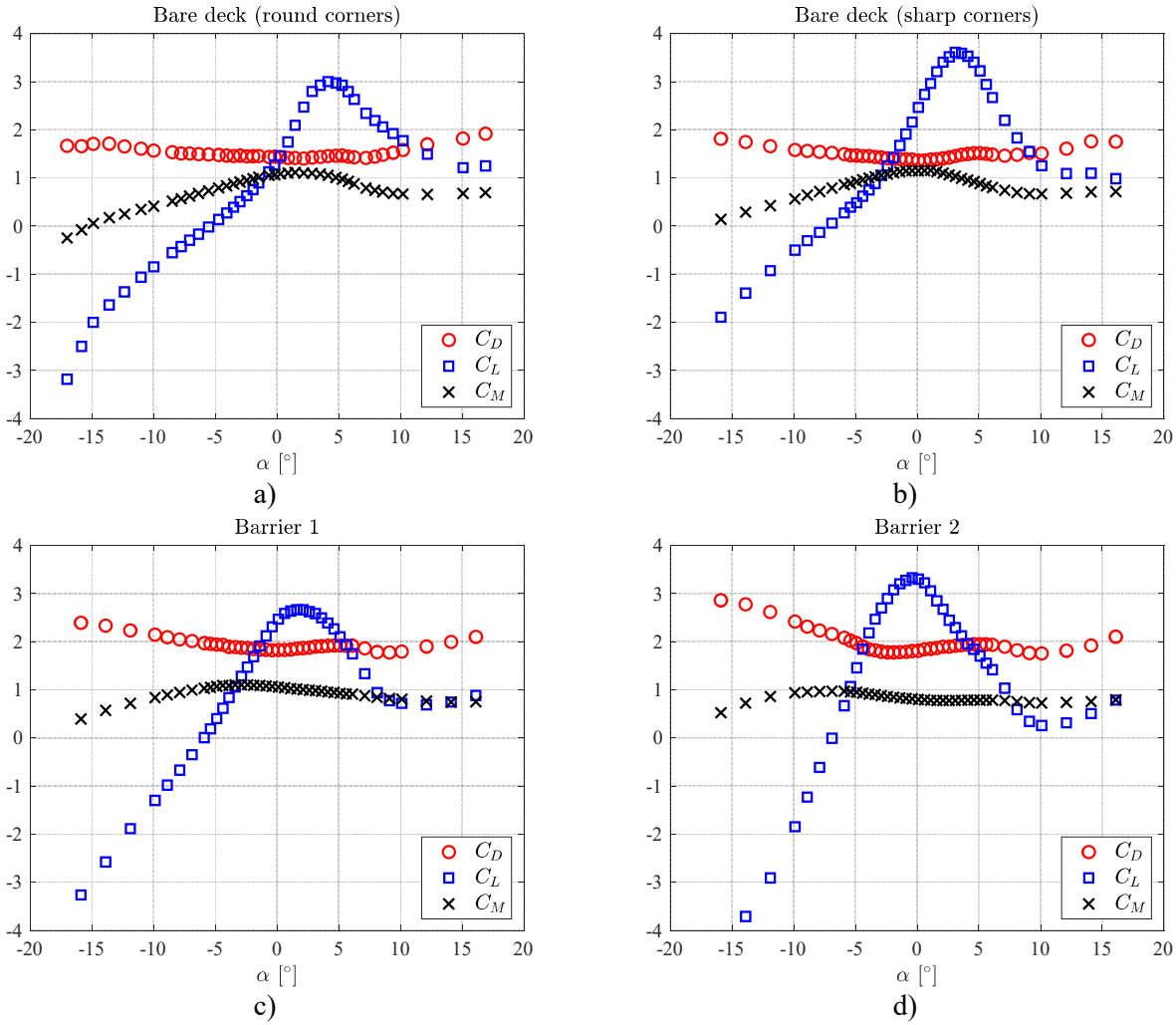

Figure 4.1. Drag, lift and torque coefficient for different values of the angle of attack for each investigated configuration ($Re \simeq 100000$).

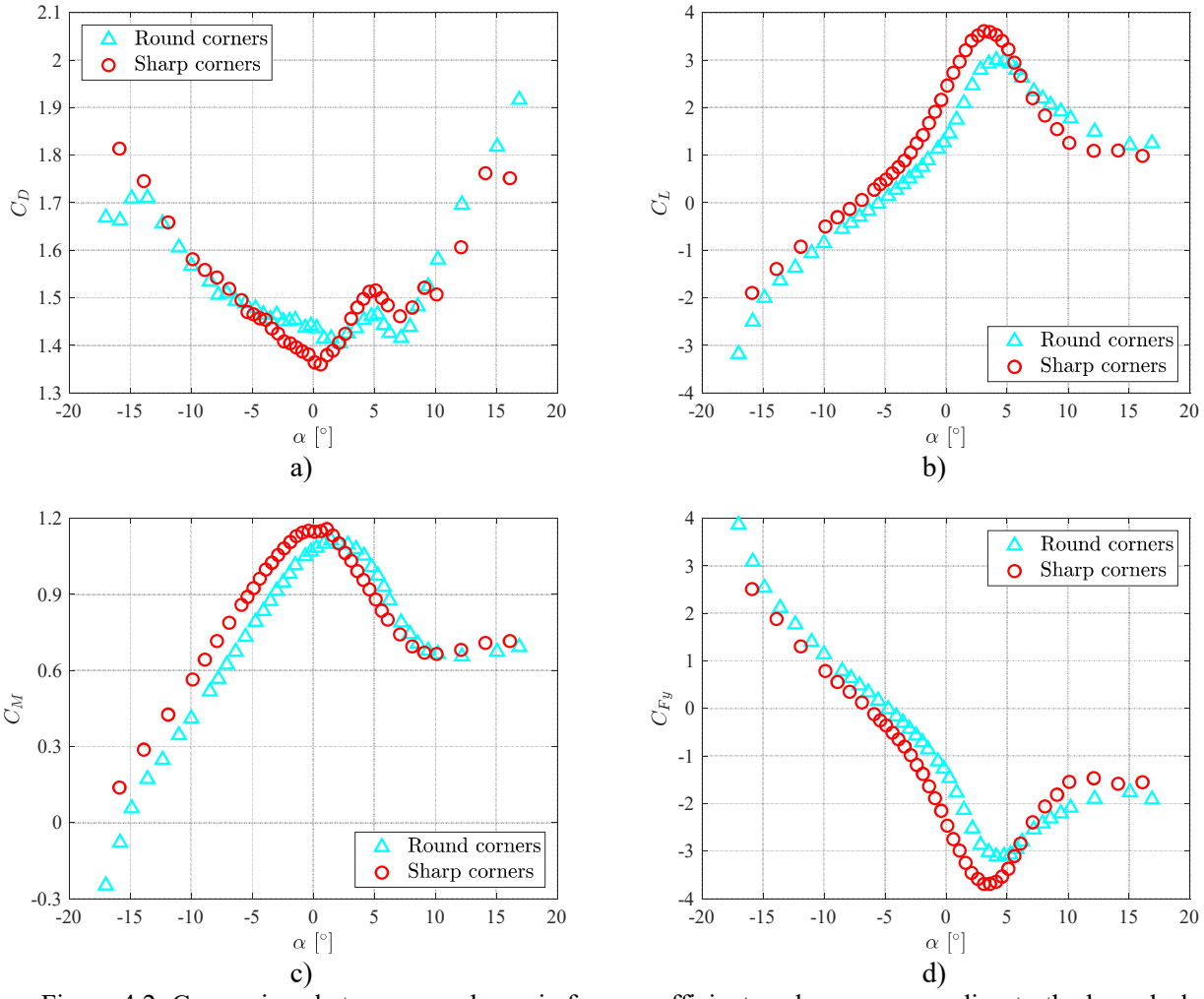

Figure 4.2. Comparison between aerodynamic force coefficients values corresponding to the bare deck configurations, with round and sharp lower corners ($Re \simeq 100000$).

edges the peculiar trend between-5° and +10°, described in Section 4.2.4, is emphasized, as shown also in the close-up in Figure 4.5.

With regard to the lift coefficient curve (Figure 4.2(b)), the increasing of lower edge sharpness produces a slight shift of the peak towards lower angles of attack and a higher slope of the curve before and after the peak itself. In addition, the values of the lift coefficient found in case of sharp corners are greater than in case of round corners before the peak point, where the slope of the curve is positive. Such mean lift growth could be caused by the more marked flow separation on the lower side of the body due to sharper edges, with the consequent reduction of the suction on the lower side of the sectional model.

The plot of the torque coefficient C_M (Figure 4.2(c)) shows the maximum peak shifted towards lower values of α for sharp corner configuration, similarly to what observed for C_L, while the slope of the curve seem not to be affected by corner sharpness far from the peak.

Finally, the transverse force coefficient C_{Fy} (Figure 4.2 (d)) is altered by the shape of the corners very similarly, with opposite sign, to what observed for C_L: minimum peak reduced and shifted towards lower α, with the slope of the curve increased before and after the peak.

4.2.2. Bare deck vs lateral barriers

The two selected typologies of lateral barriers produced much more remarkable effects on all the aerodynamic force coefficients when installed on the sectional model. The drag curve (Figure 4.3(a)) is strongly shifted up to higher values, as expectable, while its shape seems not to be markedly affected by the addition of barriers. Moreover, the drag coefficient does not exhibit any notable differences depending on the typology of lateral barrier installed, except for strongly negative angle of attack values. For about $\alpha < -5°$, the drag values related to Barrier 2 are indeed higher and higher than the ones found for Barrier 1. This suggested that the mean drag coefficient for the configurations with lateral barriers installed could be mainly influenced by the geometry of the deck and the total height of the two tested barriers, very similar to each other, for $\alpha > -5°$, while the amount and the distribution of the openings could markedly affect C_D only for $\alpha < -5°$.

On the other hand, lift and torque coefficient values (Figure 4.3(b, c)) are strongly

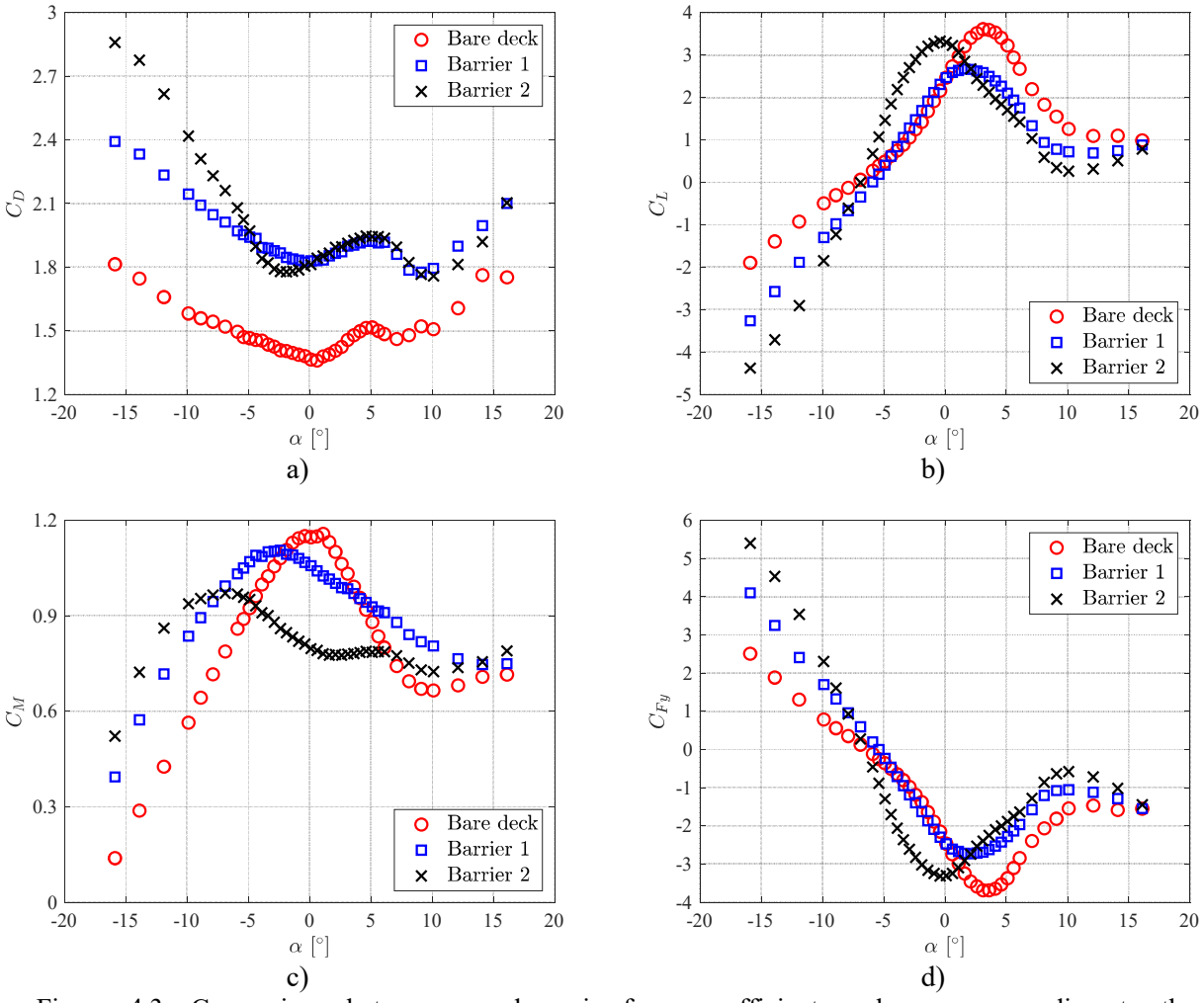

Figure 4.3. Comparison between aerodynamic force coefficients values corresponding to the configurations with sharp corners, with and without lateral barriers ($Re \simeq 100000$).

affected both by the presence and the typology of lateral barriers. Both of them show a shift of the peak towards lower angles of attack. Torque coefficient maximum value becomes lower and lower from bare deck configuration to Barrier 1 and Barrier 2 (Figure 4.3(c)), while the lift peak decreases from bare deck to Barrier 1 and then increases again with Barrier 2 (Figure 4.3(b)).

The slope of C_L curves was found to be higher with the addition of lateral barriers before the peak point, while it does not exhibit any remarkable changes after, as shown in Figure 4.3(b). On the contrary, C_M curve slope seems not to change before the peak with different geometric configurations.

As observed in case of bare deck with round and sharp corners, C_{Fy} curve exhibits a variation due to barrier addition similar to what observed for C_L with opposite sign (Figure 4.3(d))

4.2.3. Force measurements for high and low *Re*

The force coefficients reported in the above mentioned figures relate to the measurements performed at the highest Reynolds number tested, about Re = 100000, as specified in the figure captions. Some comments about the measurements at high and low *Re* are appropriate.

The results are affected by a certain level of uncertainty which is usually greater at lower wind velocities, due to limitations of the instruments in terms of accuracy, especially with regard to the mean coefficient values. According to the experience and the observations achieved during the wind tunnel campaign, even if the reliability of the mean force coefficients measured could be more limited at low Reynolds number, increasing or decreasing trends of the curves with angle of attack variation were generally caught quite well both at high and low flow speed. For this reason, it is worth to make comparison between aerodynamic coefficient values at high and low Reynolds number especially in terms of slope and shape of the curves. Such consideration, indeed, is compatible with static tests main goal, since, as specified in the introduction, suppositions about the VIV response based on force measurements and model calibration procedure are closely connected to trend and slope of the transverse force coefficient ($dC_{Fy}/d\alpha$).

Comparison between transverse force coefficient C_{Fy} at high and low Reynolds number is pointed out in Figure 4.4. Each investigated configuration exhibits a shift of the

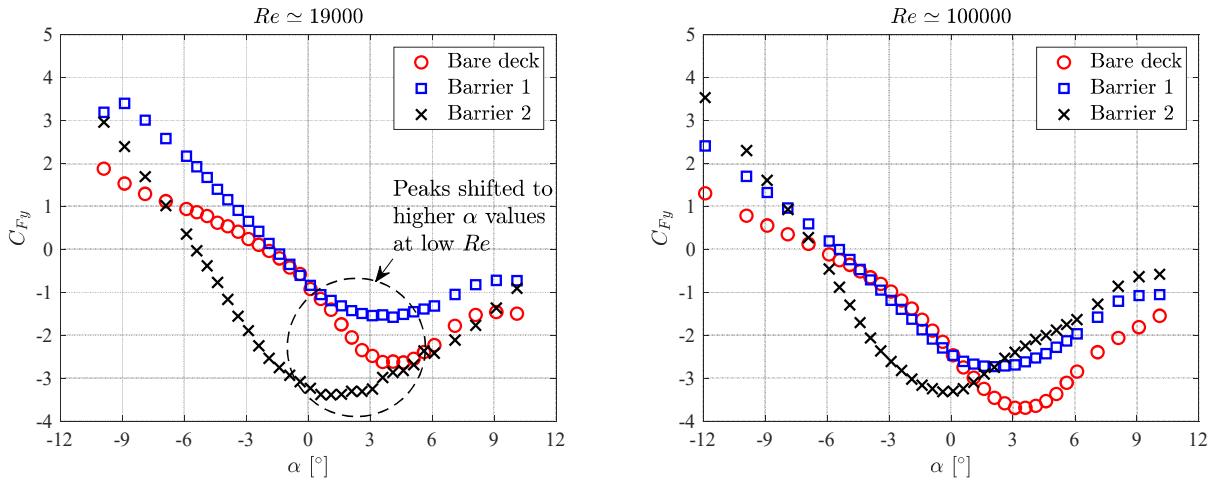

Figure 4.4. Transverse force coefficient curves at low (a) and high (b) Reynolds number.

minimum peak point of the C_{Fy} curve towards higher values of α in case of lower Re results (Figure 4.4(a)) comparing to the higher Re ones. This suggested a greater stability to transverse oscillation based on C_{Fy} slope ($dC_{Fy}/d\alpha$) from a quasi-steady point of view in case of lower wind speed for the studied cross-section regardless of the configuration considered, as described more specifically in Section 4.2.6.

The latter considerations about Reynolds effects on C_{Fy} curve are significant with respect to the expected behavior of the cross-section layouts during dynamic tests, performed generally at relatively low flow speed as reported in Chapter 5.

4.2.4. Flow pattern estimation through wool wires

It is worth to notice the peculiar shape of the drag coefficient curve in the range of angle of incidence between -5° and +12.5° (Figure 4.5). In such a range, the drag curve appearance was found to be approximately the same for each investigated configuration, regardless of presence or absence of the barriers, suggesting that it could be mainly related to the geometry of the lower part of the model cross section. To better understand the flow topology and the evolution of the flow separation some qualitative flow visualizations were performed by applying wool wires on the upper and the lower part of the sectional model during force measurements on the bare deck with round corners (Figure 4.6).

These visualizations are really rough, but they can be useful to obtain, even approximately, a qualitative outlook on the body aerodynamics and the flow pattern. In particular, at zero angle of attack the flow appeared fully separated on the lower side,

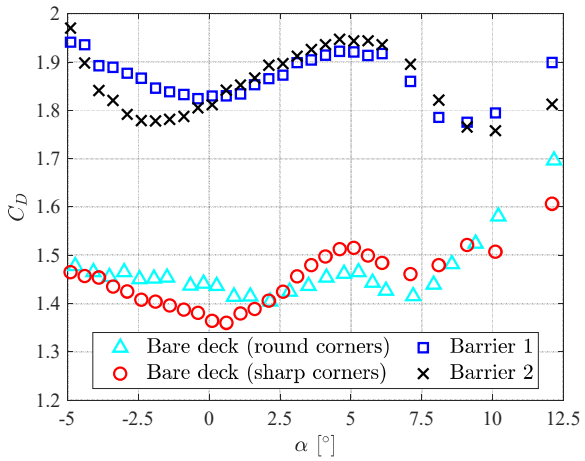

Figure 4.5. Close-up of the drag coefficient curves in angle of attack interval between -5° and 12.5° for all geometric configurations ($Re \simeq 100000$).

while on the upper side the separation seems to occur at the leading edge, followed by reattachment with formation of a separation bubble. The increase of the positive angle of attack leads to a growing separation of the flow on the upper side, while on the lower side the wool wires suggest a sort of reattachment around α = +7°, as shown in Figure 4.6(f), where downstream wires appear adherent to the model wall. It is meaningful that the local decrement observed in drag coefficient and shown in Figure 4.5 seems to be connected to the mentioned flow reattachment.

Based on the latter observations, the evolution of the flow pattern in the range of α between about 0° and +10° was supposed. It is approximately represented by the sketches in Figure 4.7.

4.2.5. Check about end-plates dimension

A quite simple but useful check about the size of the lateral end-plates of the sectional model was carried out too. Two large wood panels were attached to the original aluminum end-plates of the model (Figure 4.8(a)) and force measurements were performed for several values of α, to check the presence of any equalization effects due to a possible not sufficient size of the aluminum plates, in particular concerning the drag force.

For this purpose, the drag coefficients obtained with original and enlarged end-plates were compared (Figure 4.8(b)) in terms of C_D divided by C_D at α = 0° to exclude the additional drag given by the flow action on the new plates. As observable, the results are in very good agreement between about -3° and +7°, while a shift is observed for markedly

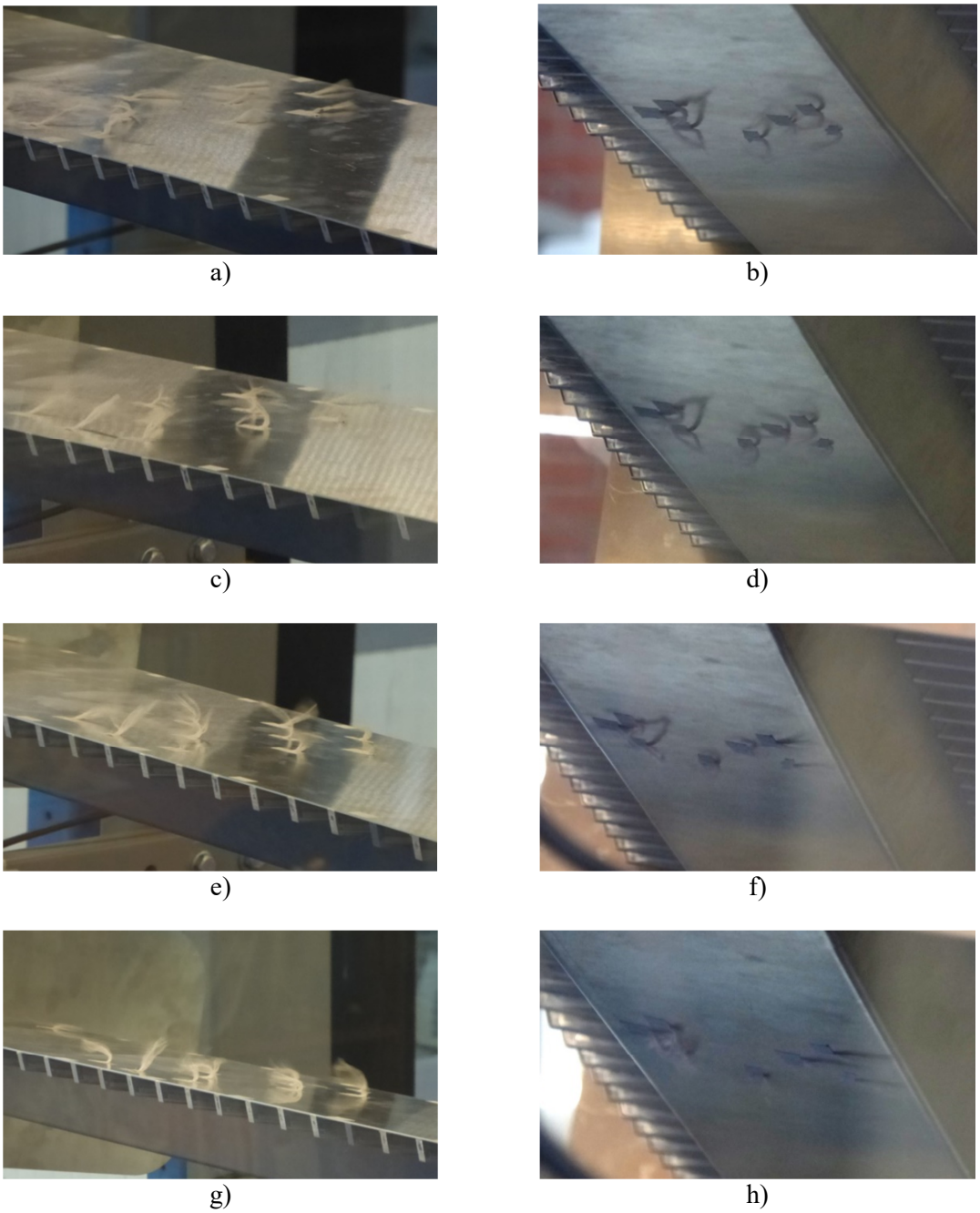

Figure 4.6. Wool wires fixed on upper and lower side of the model for the bare deck at different values of the angle of attack: 0° (a, b), 5° (c, d), 7° (e, f) and 10° (g, h).

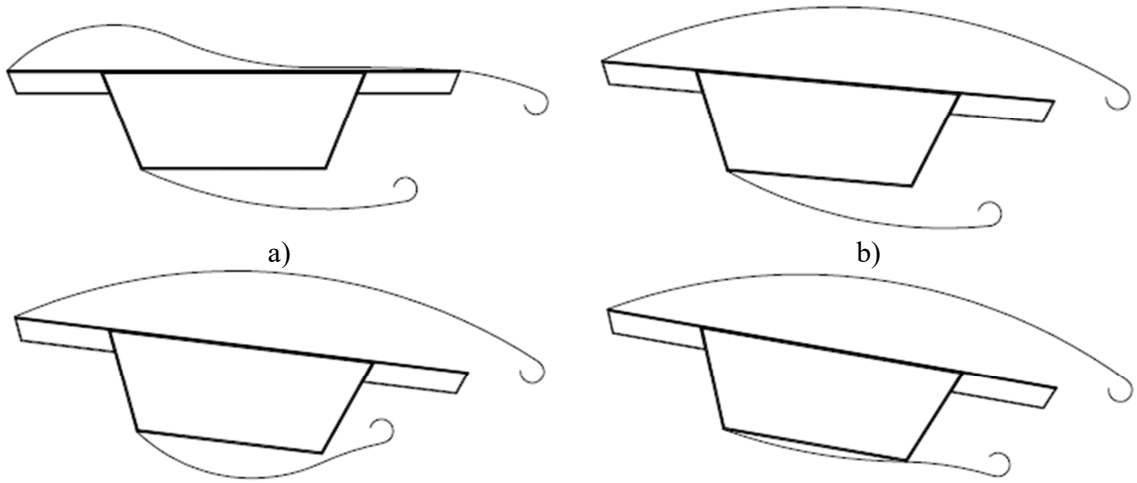

a) b) c) d)

Figure 4.7. Qualitative sketches of flow pattern observed through wool wires for the bare deck at different values of the angle of attack: 0° (a), 5° (b), 7° (c) and 10° (d).

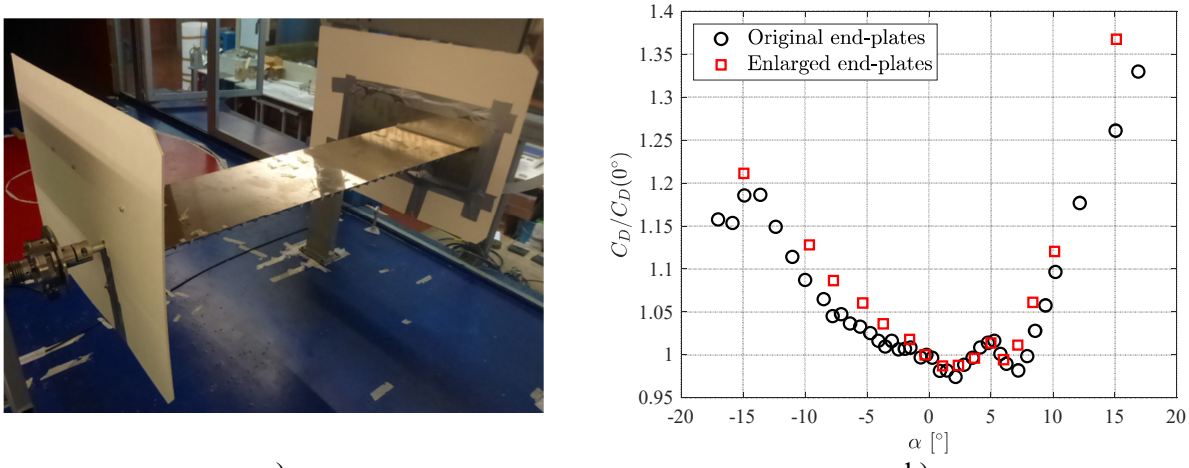

a) b)

Figure 4.8. Picture of enlargement system for end-plates (a) and comparison between drag normalized drag coefficient values (b)

negative and positive angles, which are not indeed so significant or realistic for a bridge deck study.

4.2.6. Slope of the transverse force coefficient curve

As mentioned in the introduction and in Section 4.2.3, special attention was paid to the slope of the transverse force coefficient curve ($dC_{Fy}(\alpha)/d\alpha$). This quantity, through ζ_{aero}^{QS} expression, determines stability or instability of a certain cross-section geometry to the transverse oscillation according to quasi-steady theory. The quasi-steady assumption is expected to be more reliable in case of a high reduced flow speed ($U_{red} = U/n_0D$), obtained dividing the wind velocity (U) by the natural frequency of the oscillating body (n_0) and a reference length (D). For this reason, the quasi-steady theory is generally employed to predict possible galloping condition, according to Den Hartog's criterion (1932) which provides a condition necessary for transverse instability ($dC_{Fy}/d\alpha > 0$), since such a phenomenon is usually observed at higher flow speed compared to VIV.

In case of slender structures with low natural frequency lock-in is usually observed at limited wind velocity and, consequently, quasi-steady approaches are not generally expected to be suitable in such cases. Nevertheless, a qualitative connection between quasi-steady transverse coefficient slope and proneness to vortex-induced oscillation can be searched for.

So, the value assumed by $dC_{Fy}/d\alpha$ was considered meaningful to qualitatively estimate how a certain cross-section configuration could be prone to VIV. In particular, three specific angles of attack were considered for all geometric layouts: 0°, -3° and +3°.

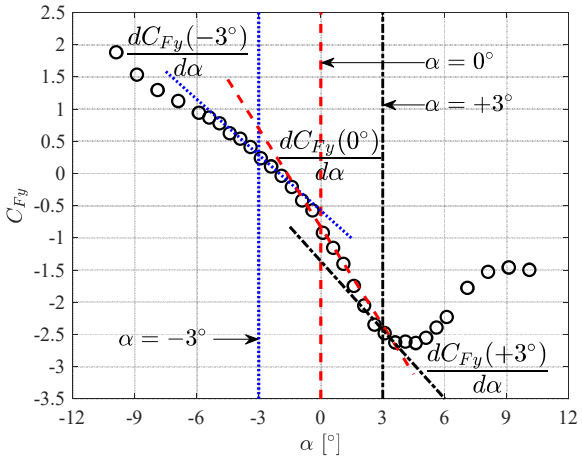

Figure 4.9. Example of C_{Fy} curve slope estimation for different values of the angle of attack.

Table 4.1. Summary of $dC_{Fy}/d\alpha$ values (Re < 20000) for all cross-section geometric layouts at 0°, -3° and +3° angle of attack. For bare deck layouts an additional angle (+8.5°) is specified.

Geometric configuration	α [deg]	$dC_{Fy}/d\alpha$ [-]
Bare deck (round corners)	0	-21.2
	-3	-15.8
	+3	-28.4
	+8.5	+6.4
Bare deck (sharp corners)	0	-29.2
	-3	-15.9
	+3	-18.9
	+8.5	+7.5
Barrier 1	0	-25.8
	-3	-28.2
	+3	-4.2
Barrier 2	0	-15.3
	-3	-40.7
	+3	+13.8

These values are quite typical and reasonable in case of bridge deck studies, since they represent possible real wind directions and cover a meaningful and realistic range of cases.

The slope of C_{Fy} curve was evaluated for all geometric configurations at the three mentioned angles of attack (Figure 4.9). The obtained values of $dC_{Fy}/d\alpha$ are reported in Table 4.1. For bare deck configurations, values corresponding to α = +8.5° are reported too, since this angle was also tested during dynamic tests, as described in Chapter 5. Finally, $dC_{Fy}/d\alpha$ values reported in Table 4.1 correspond to the transverse force coefficient evaluated at the lowest Reynolds number at which force measurements were performed ($Re \simeq 19000$). C_{Fy} slope evaluated for Re closer to the one expected during aeroelastic tests was considered more appropriate to formulate suppositions about the dynamic behavior of each configuration.

4.3. Strouhal number

Static force measurements were performed to evaluate also the Strouhal number (St) of the cross section for each investigated configuration (Figure 4.11, Figure 4.12, Figure 4.13). The Strouhal number was evaluated through the study of the power spectral density (PSD) of the lift force. Vortex shedding is a reasonably narrow band process and, in several cases, the lift power spectral density graphic shows a peak corresponding to the vortex-shedding frequency.

Strouhal number is calculated, according to the Strouhal law (Eq. 2.1) through the evaluation of the vortex-shedding frequency n_s from the lift spectrum at a certain value of the mean flow speed U and assuming a reference length D equal to the cross-flow dimension of the bare deck at zero angle of attack.

This process was carried out for each configuration, repeated for different flow angles of attack and for many values of wind velocity, so that possible variations of the Strouhal number due to Reynolds effects were taken into account too.

An example of Strouhal number evaluation from the power spectral density of the lift coefficient is reported in Figure 4.10. The frequency values on the horizontal axis were multiplied by D/U, so that the dependence of n_s on the wind velocity was removed. In this way, when spectral graphics were compared for different values of flow speed and Reynolds number, the Strouhal number could be easily identified. The Strouhal peak is highlighted in Figure 4.10, as well as a second-order super harmonic observable both at low (Figure 4.10(a)) and high (Figure 4.10(b)) flow speed.

As for the aerodynamic coefficients, the Strouhal number estimation was carried out for a wide range of angle of attack for each configuration. Figure 4.11 shows and compares *St* curves to each other and effects of cross-section geometry alteration along with angle variation can be observed. For the bare deck, the sharpness of the corners seems not to produce any effects on *St* for $\alpha < -3°$, while for $\alpha > 3°$ the sharp edge curve is slightly lower than the round edge one, with an approximately constant shift. In addition, both bare deck curves exhibit a peak value reached between about -3° and 0°.

With lateral barriers installed, the Strouhal number decreased in the whole range of angle of attack values considered. From strongly negative angles of attack up to about 3°, the Strouhal number reduction with Barrier 2 was found to be markedly stronger than with Barrier 1, while for $\alpha > 3°$ the two curves became much closer to each other. The peak point reached by *St* with both barriers is located between 0° and 3°, shifted towards higher values of α compared to bare deck. The angles of attack ranging from -3° to 3° exhibit meaningful effects due to geometric cross-section details. As for the slope of the transverse force coefficient curve in the previous section, the cases $\alpha = 0°$, $\alpha = -3°$ and $\alpha = +3°$ were investigated with special care for all geometric configurations.

The Strouhal number is displayed against the Reynolds number in Figure 4.12 and Figure 4.13: the former highlights the effects produced by each geometric layout at a certain angle of attack on *St* for several values of *Re*, while the latter compares results at

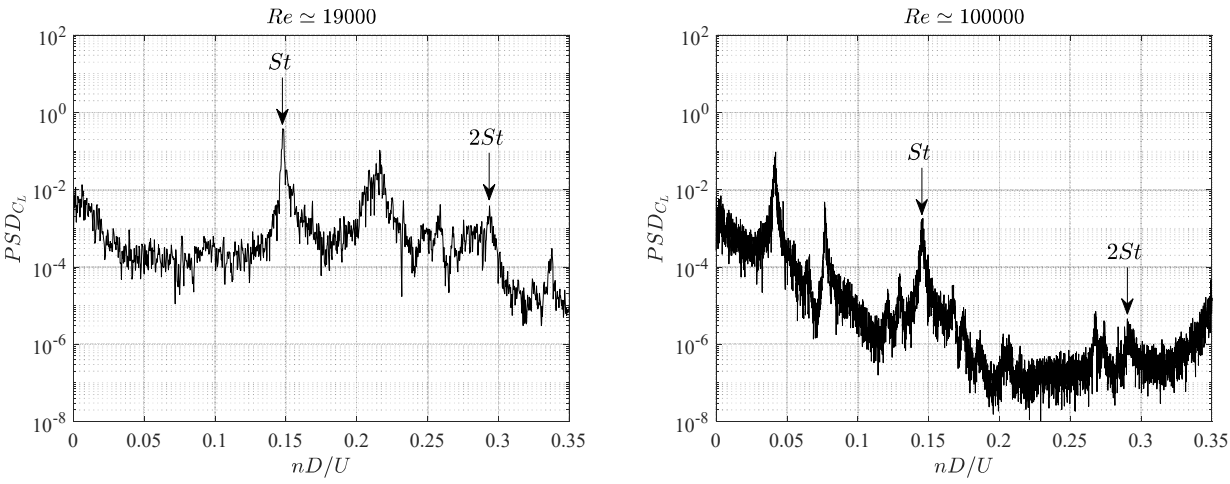

a) b)

Figure 4.10. Power spectral densities of the lift coefficient for bare deck with round corners configuration at zero angle of attack at for two different Reynolds number values. *n* denotes the generic frequency.

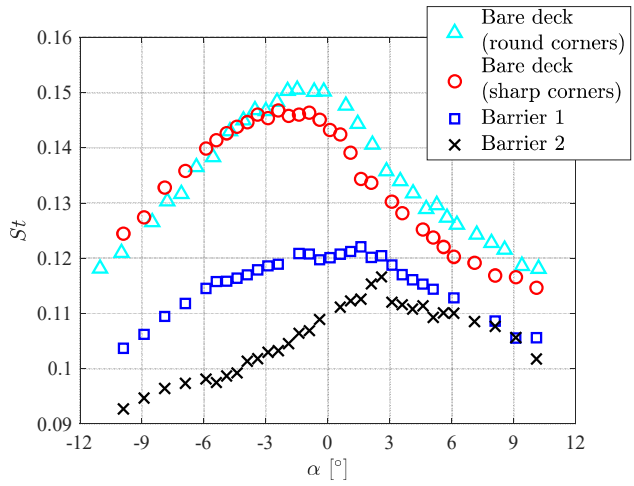

Figure 4.11. Strouhal number values against the flow angle of attack for all the investigated configurations (*Re* ≃ 19000).

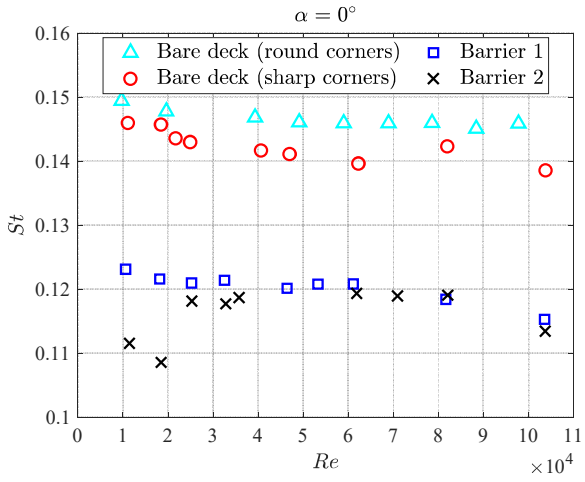

a)

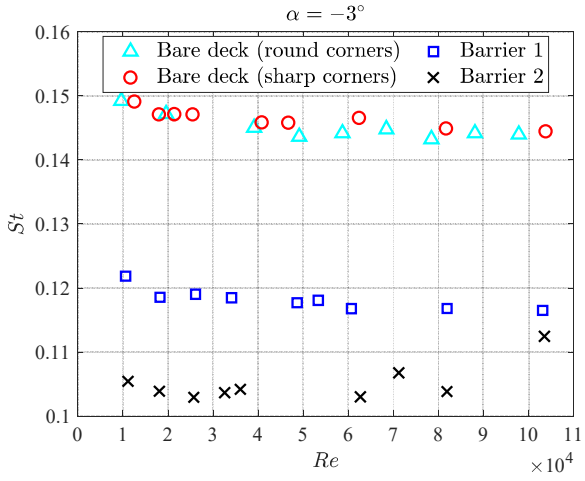

b)

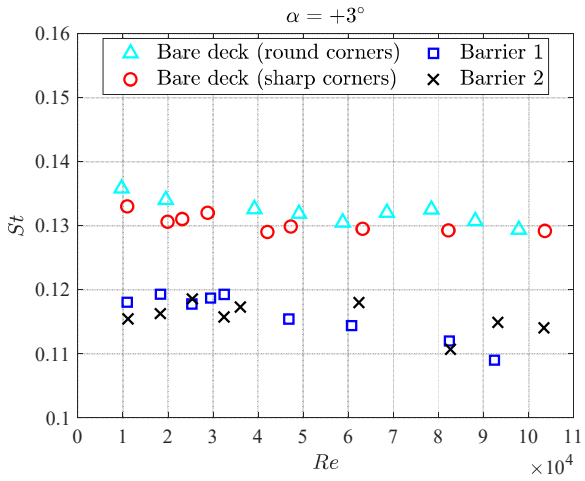

c)

Figure 4.12. Comparison between *St* values for each configuration at three angles of attack (-3°, 0°, 3°) and for different values of Reynolds number.

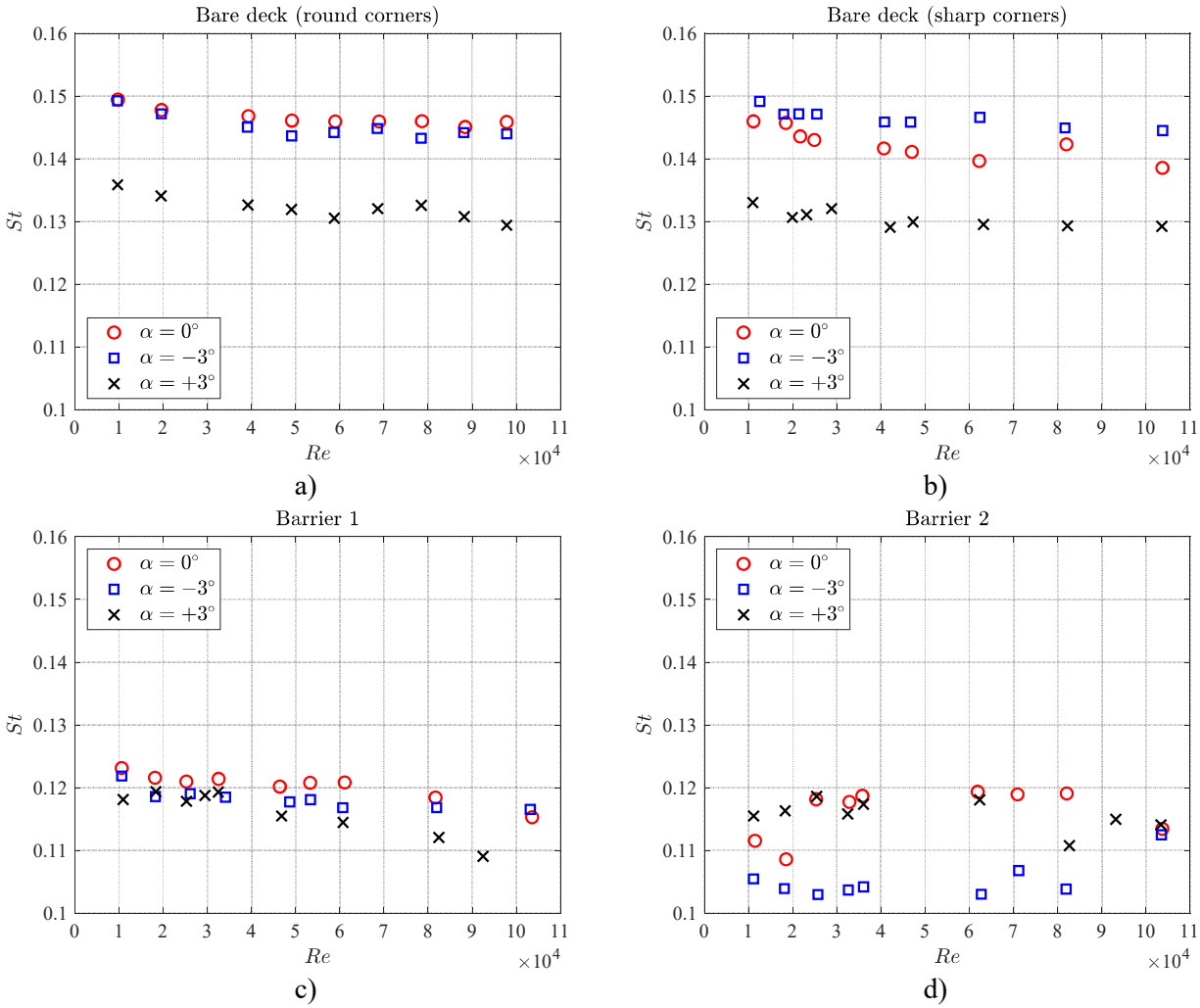

Figure 4.13. Comparison between Strouhal number values at three angles of attack (-3°, 0°, 3°) for each configuration and different values of Reynolds number.

Table 4.2. Summary of Strouhal number values (Re < 20000) for all cross-section geometric layouts at 0°, -3° and +3° angle of attack. For bare deck layouts an additional angle (+8.5°) is specified.

Geometric configuration	α [deg]	St [-]
Bare deck (round corners)	0	0.150
	-3	0.149
	+3	0.134
	+8.5	0.121
Bare deck (sharp corners)	0	0.146
	-3	0.147
	+3	0.133
	+8.5	0.117
Barrier 1	0	0.122
	-3	0.119
	+3	0.121
Barrier 2	0	0.111
	-3	0.104
	+3	0.113

different angles of attack for the same geometry.

Figure 4.12 and Figure 4.13 point out how the Reynolds number variation seems not to produce really remarkable effects on St in most of cases studied, since only with Barrier 2 installed a limited sensitivity of the Strouhal number to Re can be actually observed. A global summary of the main Strouhal number values estimated is reported in Table 4.2. For bare deck with round corners, the angle α = +8.5° is also reported.

4.4. Amplitude of the dimensionless vortex-shedding fluctuating force (C_{L0})

The analysis of the power spectral density of the lift force was also used to estimate the amplitude of the dimensionless transverse fluctuating force on the stationary body (C_{L0}) produced by vortex shedding. This quantity may be interpreted as an indicator of intensity of the investigated force acting on the body and, in addition, it is crucial for several mathematical approaches for VIV response estimation (Section 2.4).

Since vortex shedding in smooth flow is generally a narrow band process, the transverse force generated can be reasonably approximated through a harmonic function with a certain amplitude. The evaluation of this equivalent sinusoidal amplitude was carried out through the integration of the lift coefficient spectrum.

In particular, the variance of the process was evaluated by integrating the power spectral density in a narrow band around the vortex shedding frequency (Figure 4.14), then

the corresponding standard deviation (σ_s) was calculated and multiplied by the square root of two to obtain the equivalent sinusoidal amplitude C_{L0}. The calculation procedure can be expressed as follows:

$$\sqrt{\left(\int_{n_1}^{n_2} PSD_{C_L}(n)\,dn\right)} = \sigma_s \tag{4.4}$$

$$C_{L0} = \sqrt{2} \cdot \sigma_s \tag{4.5}$$

A reliable estimation of C_{L0} is a relatively challenging issue. The main difficulty is represented by taking correctly into account the increasing or reducing amplification effect due to the static wind tunnel setup. In fact, carrying out highly reliable measurements for C_{L0} calculation requires an almost perfectly rigid setup, to avoid any dynamic amplification on the detected fluctuating forces. Even if a perfectly rigid setup is impossible to be realized, a very high natural frequency (n_0) of the system connected to the sectional model usually allows to perform tests sufficiently far from the resonance condition, so that the vortex-shedding force frequency n_s is considerably low compared to the above mentioned natural frequency and dynamics effect are negligible.

In the present experimental work, the whole system composed by the sectional model connected to the setup for static measurements exhibited a natural frequency between 20 Hz and 30 Hz. This range of values was found to be too low to perform tests at a wind speed corresponding to a vortex-shedding frequency sufficiently below n_0. For this reason, a way to take into account the dynamic amplification due to the setup had to be found.

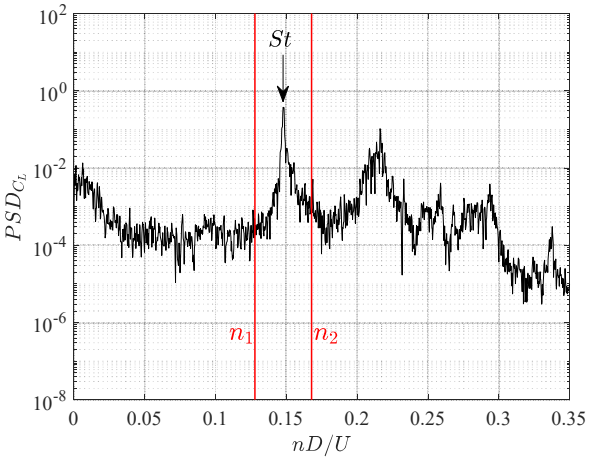

Figure 4.14. Example of power spectral density of the lift coefficient with the integration interval for the evaluation of C_{L0} highlighted.

Given the narrow band process resulting from vortex shedding and the expected linearity of the vibrating system composed by the sectional model fixed to the external holding system, the magnitude of the mechanical admittance function (H) of the setup could be reasonably approximated through the following expression:

$$\left|H(\omega_s)\right| = \frac{1}{\sqrt{\left(1-\frac{\omega_s^2}{\omega_0^2}\right)^2 + 4\zeta_0^2\frac{\omega_s^2}{\omega_0^2}}} = N(\omega_s) \tag{4.6}$$

where ω_s and ω_0 are respectively the angular frequency of the transverse fluctuating force produced by vortex shedding and the natural angular frequency of the system. The latter is a constant value, while the former changes with the mean incoming flow speed according to the Strouhal law and, therefore, it is linearly dependent on the Reynolds number too.

In this way, it was possible to establish a direct relationship between a reasonable estimation of the amplification due to the mechanical admittance of the system and the flow velocity in the wind tunnel. The mechanical damping of the system, named ζ_0, is an unknown quantity, but it was observed that its influence on the dynamic amplification factor is quite limited for all measurements carried out sufficiently far from the resonance condition. As proof of this, Figure 4.15(a) shows dynamic amplification factor curves against angular frequencies ratio for different values of mechanical damping of the system: curves show very marked differences close to resonance condition ($\omega_s/\omega_0 \simeq 1$), while they are closer and closer to each other further from the resonance. Moreover, the considered

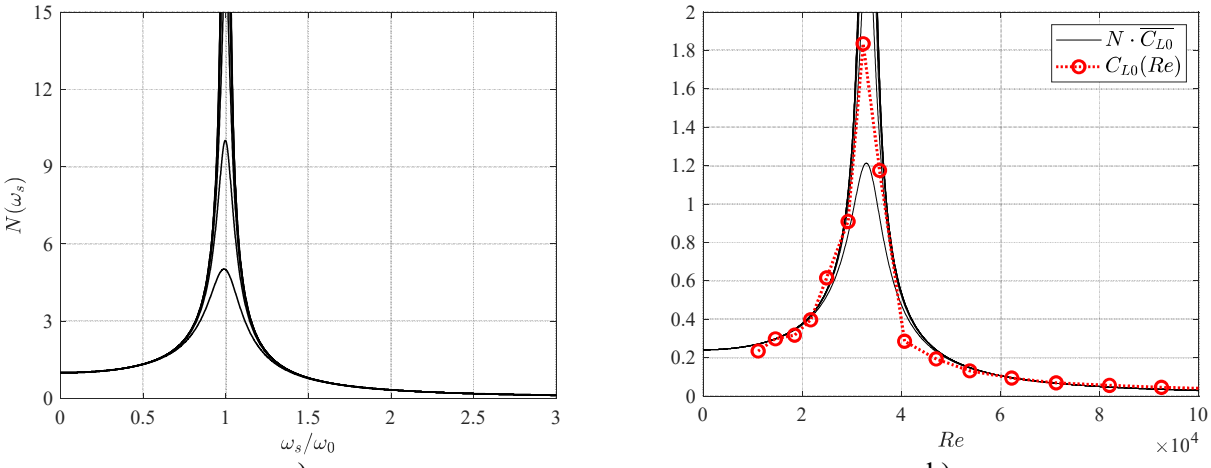

Figure 4.15. Generic magnitude of mechanical admittance function N against ω_s/ω_0 for several damping values (a). Comparison between C_{L0} measured in wind tunnel (red circles) for different Reynolds numbers and N multiplied by scaled C_{L0} value at about Re = 19000, chosen as reference value (b).

range of mechanical damping ratio values goes from 0.1 % to 10 %; the wind tunnel setup, considering how it is realized, is probably characterized by a low damping ratio, much lower than 10 %. Therefore, the estimation of the dynamic amplification factor can be rated sufficiently reliable, provided that the flow speed is not too close to the one corresponding to resonance between the vortex-shedding force and the system. Figure 4.15 emphasizes the scaling procedure carried out on C_{L0} values directly calculated from wind tunnel lift spectrum, which were divided by the estimated mechanical admittance of the setup N. Then, the function $N(\omega_s)$ was multiplied by the scaled value of C_{L0} corresponding to $Re \simeq 19000$, here named $\overline{C_{L0}}$, employed in the following of the work. As observable, a quite good match was found with the C_{L0} directly calculated from wind tunnel lift spectrum (red circles in Figure 4.15(b)) in the range of interest $Re < 20000$, suggesting a reasonably univocal estimation of C_{L0} through this procedure close to Re expected for dynamic tests.

As for Strouhal number, scaled values of C_{L0} are reported for the same angle of attack and different geometric layout (Figure 4.16) and vice versa (Figure 4.17) for several values of Reynolds number. A clear trend is not always easy to identify, nevertheless it can be observed that, generally, C_{L0} values are concentrated around an approximately constant measure for low Re, while for most of cases an increasing trend can be observed for high Re. In particular, in Figure 4.17 increasing trends of C_{L0} with Re, where observed, are highlighted. Table 4.3 reports C_{L0} estimated in each case at $Re \simeq 19000$. Values listed in

Table 4.3. Summary of C_{L0} values ($Re < 20000$) for all geometric cross-section geometric layouts at 0°, -3° and +3° angle of attack. For bare deck layouts an additional angle (+8.5°) is specified.

Geometric configuration	α [deg]	C_{L0} [-]
Bare deck (round corners)	0	0.22
	-3	0.15
	+3	0.20
	+8.5	0.54
Bare deck (sharp corners)	0	0.24
	-3	0.23
	+3	0.19
	+8.5	0.64
Barrier 1	0	0.40
	-3	0.33
	+3	0.30
Barrier 2	0	0.31
	-3	0.42
	+3	0.37

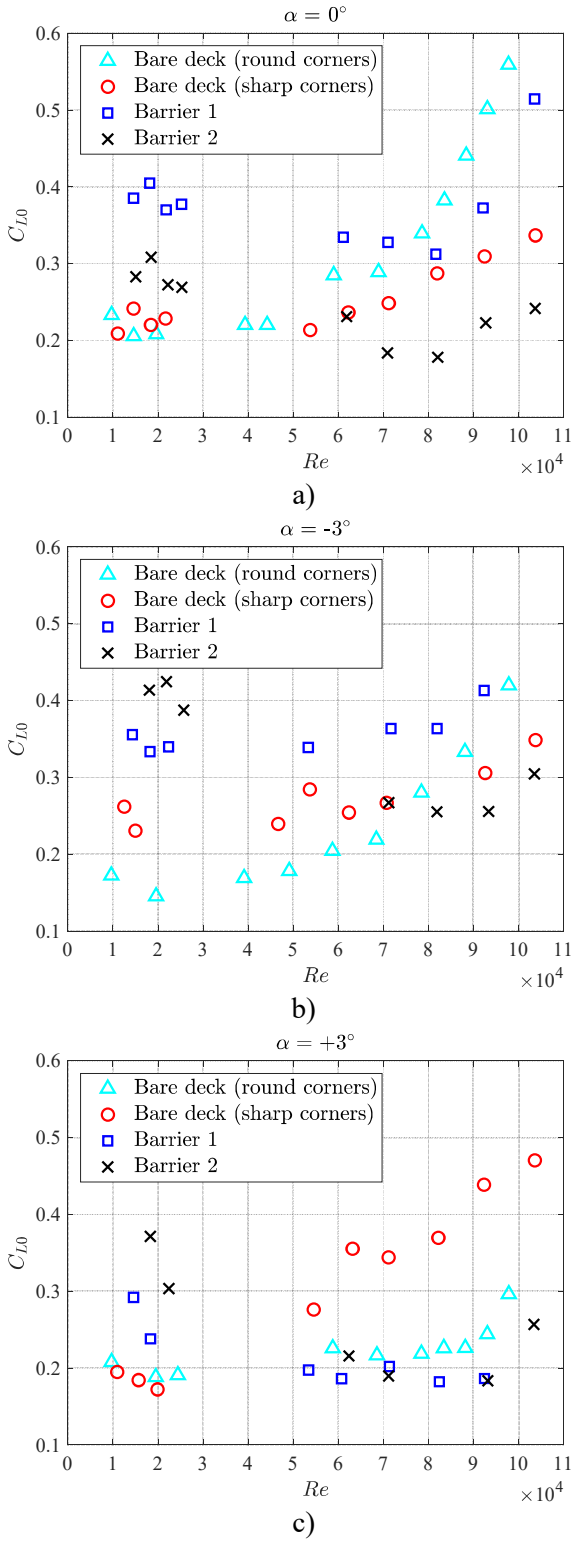

Figure 4.16. Comparison between C_{L0} values for each configuration at three angles of attack (-3°, 0°, 3°) and for different values of Reynolds number.

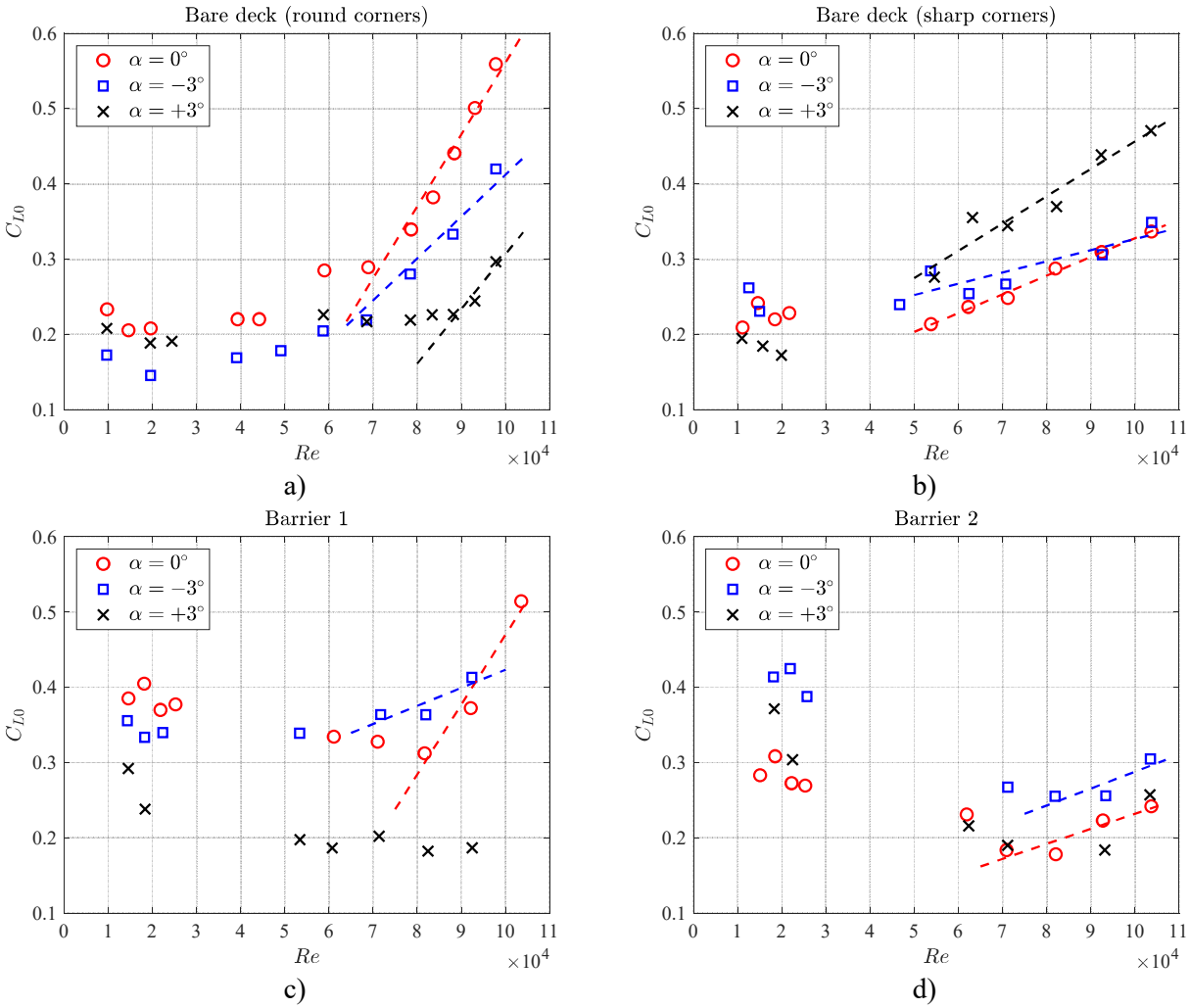

Figure 4.17. Comparison between C_{L0} values at three angles of attack (-3°, 0°, 3°) for each configuration and different values of Reynolds number. Increasing trends at high *Re* are highlighted where observed.

the table are the ones scaled through N and corresponding to $Re \simeq 19000$, above named $\overline{C_{L0}}$, while from now on they will be indicated simply as C_{L0} in the following sections and chapters for simplicity. Such values will be employed for the mathematical models discussed in Chapter 6.

As observable in figures and table, C_{L0} is markedly affected by the presence of lateral barriers, which lead to a general growth of lift coefficient amplitude compared to bare deck configurations. On the other hand, the angle of attack variation in the range between -3° and +3° does not produced a very clear C_{L0} increase or decrease, differently from the case of bare deck at α = +8.5°, where a marked growth up to over 0.5 can be observed.

4.5. Discussion of static test results

4.5.1. Effects of cross-section details and angle of attack

Static force measurements were performed on the sectional model to evaluate aerodynamic force coefficients, Strouhal number and dimensionless lift force fluctuation produced by vortex shedding on the stationary sectional model. Results were compared to each other in terms of cross-section geometric details and flow angle of attack effect and some comments can be made about the aerodynamic influence of such factors.

The modification of lower corner sharpness produced some effects appreciable during force measurements, but certainly limited (Figure 4.2). Force coefficient curves were slightly modified by this kind of detail, as well as St and C_{L0}; nevertheless, no strong differences from the aerodynamic point of view were observed globally.

The installation of lateral barriers, on the contrary, produced clear effects from several points of view (Figure 4.3). The drag coefficient (Figure 4.3(a)) was strongly increased, as expectable, and lift and moment curves changed after barriers addition too. Differences in terms of slope of C_L and C_M curves (Figure 4.3(b, c)) were noticed, but the main effect was probably their global translation towards lower angle of attack values, observed for the transverse force coefficient C_{Fy} too (Figure 4.3(d)). From a quasi-steady point of view, this effect is meaningful in terms of potential stability or instability to transverse and/or torsional oscillations. As regards C_{Fy}, effects due to Reynolds number can also be remarked (Figure 4.4), since C_{Fy} curves were found to be shifted towards lower α values for higher Re comparing to lower Re. It is worth to notice that drag coefficient was influenced in a very similar way by both barriers, regardless the amount and the

distribution of openings, suggesting that total barrier heights, very similar to each other, were mainly decisive for the drag force. On the contrary, lift and moment changed considerably with the opening layout from Barrier 1 to Barrier 2.

As regards the flow angle of attack, the drag curve exhibits a quite flat trend for all the configurations, increasing for strongly negative or positive angles. A particular shape (Figure 4.5) was found between about 0 and +10° and investigated through qualitative flow visualizations by using wool wires, which suggested a possible flow reattachment on the lower side of the model around α = +7°, probably causing the particular curve trend observed. On the other hand, both lift and moment show a growth with the angle of attack up to a peak value and then a decreasing trend. The position of the peak, as said above, is strongly influenced by the geometric layout of the cross section: C_M maximum point varies its location in terms of α between about -7° and +2°, while C_L peak between about -1° and +4°. C_{Fy} curve shows a trend very similar to C_L, but with opposite sign, decreasing and increasing, respectively, before and after a minimum peak.

Strouhal number was found to be sensitive to presence and typology of barrier and to the flow angle of incidence (Figure 4.11). The modification of lower corners was irrelevant in terms of *St* for α < -3°, while for α > -3° a shift was observed, with *St* slightly lower in case of bare deck with sharp corner comparing to round corners. Barriers produced a remarkable reduction of Strouhal number over the whole range of investigated angles, firstly with Barrier 1 installed and even more with Barrier 2 (Figure 4.11 and Figure 4.12). From the point of view of *St* value, the difference in terms of transparency to the flow produced marked effects on results. Starting from bare deck with round corners and passing through configurations to deck with Barrier 2 installed, the body may be supposed to produce a more and more marked separation of the flow, along with a progressive reduction of the Strouhal number.

All *St* curves exhibit their maximum point between -3° and +3°, with a progressive shift of the peak to greater angles starting from bare deck and then adding the first and the second barrier. Strouhal number decreased moving to strongly positive or negative values of α for all configurations. In the range of values between -3° and +3°, considered meaningful for a bridge deck cross section, each geometric layout did not show strong changes in *St* with the variation of α (Figure 4.11 and Figure 4.13). It is also worth to highlight that no particular variations due to Reynolds number were observed for *St*.

Finally, the effects of cross-section details and angle of attack on C_{L0} were observed. In this case too, no strong effects due to lower corners sharpness were noticed. Similarly to

what observed for the drag coefficient, C_{L0} was markedly increased by lateral barriers (Figure 4.16) at low *Re*, but no particular dependence on the transparency to the flow was identified. The addition of barriers led to C_{L0} values almost double compared to the bare deck ones, suggesting a great increase of vortex-shedding force intensity. On the other hand, for high *Re* an increasing trend was observed especially for bare deck configurations, leading to values even higher than the ones achieved with barriers installed (Figure 4.17). Nevertheless, in the present work, C_{L0} values achieved at relatively low Reynolds number (about $Re < 20000$) are specifically considered, due to the closeness to the expected aeroelastic test flow conditions.

The dimensionless amplitude of the lift force was evaluated only at some specific angle of attack values, nevertheless some comments about α influence can be made. At low *Re*, no clear trends related to growth or reduction of α between -3° and +3° were identified, but for bare deck at $\alpha = +8.5°$ a much higher value of C_{L0} was found. On the basis of the latter observation and considering the increase produced by barriers, it can be supposed that a strong increase of the cross-flow size of the body, caused by elements added to the cross section or high values of the angle of attack, may produce a magnification of the vortex-shedding force, with consequent growth of C_{L0}. In this context, conditions leading to lower *St* and higher C_{L0} exhibit a connection with each other.

4.5.2. Suppositions about aeroelastic behavior based on static tests

Results achieved from static force measurements were also used to formulate some suppositions about the expected dynamic behavior of cross-section layouts during aeroelastic tests. The predictions about the expected sensitivity to VIV are only qualitative and based on information achievable from the slope of quasi-steady transverse force coefficient curve ($dC_{Fy}/d\alpha$), Strouhal number and C_{L0}.

As mentioned in Section 4.2.6, the quasi-steady assumption is expected to be more reliable for high values of reduced flow speed. Indeed, this is the reason why this approach is usually considered suitable for galloping addressing, but not really appropriate for VIV. Nevertheless, in this case the quasi-steady assumption was considered to predict qualitatively how a certain configuration is expected to be prone to oscillation. In particular, the slope of the C_{Fy} curve ($dC_{Fy}/d\alpha$) at a certain angle of attack was evaluated (Figure 4.9): by analogy with the quasi-steady approach for galloping, $dC_{Fy}/d\alpha < 0$ was supposed to suggest a certain level of stability to transverse oscillation, greater for more

negative slope, while $dC_{Fy}/d\alpha$ close to zero and even more $dC_{Fy}/d\alpha > 0$ were considered signals of potential stronger proneness to vibration. According to this argument, configurations related to a point on the C_{Fy} curve close to the minimum peak or on the positive slope side were supposed to be more prone to vortex-induced oscillation. In this context, the addition firstly of Barrier 1 and then of Barrier 2 were supposed to increase the VIV response of the cross section, since they produced a marked shift of C_{Fy} curve to lower angles with consequent growth of $dC_{Fy}/d\alpha$ value at a certain angle of attack.

The second quantity observed was the Strouhal number. It was found a general reduction of *St* when addition of barriers or angle of attack caused a marked increasing of the body across-flow size and a less streamlined layout of the cross section was generated. In these cases, stronger flow separation and potential transverse vibration were supposed. This is reasonable, for example, if compared also to mathematical approaches for VIV response prediction available in scientific literature, where a lower *St* is connected to a higher response amplitude.

Finally, C_{L0} values were observed. This quantity is actually an estimation of the fluctuating vortex-shedding force amplitude. It can be seen indeed as indicating the intensity of the vortex-shedding force acting on the body. In line with what observed for Strouhal number reduction, a marked growth of C_{L0} was found with barriers installed and with a strong increase of the angle of attack.

Based on the latter observations, higher values of $dC_{Fy}/d\alpha$ and C_{L0} and lower *St* were assumed as markers of potential greater sensitivity to vortex shedding and VIV response. A global overview of these quantities is reported in Table 4.4 for all cross-section geometric configurations at various angles of attack.

Some cases, therefore, are expected to be particularly prone to VIV and suppositions about the aeroelastic behavior of the studied configurations were formulated:

- The sectional model with barriers installed is expected to be much more prone to VIV than without;
- In the reference range $-3° \leq \alpha \leq +3°$, the most sensitive configurations were supposed to be the ones at +3° with Barrier 1 and Barrier 2;
- Bare deck at +8.5° is expected to be the most sensitive configurations among all those reported in Table 4.4.
- With Barrier 1 installed, an increasing VIV response is suggested with the

Table 4.4. Summary of C_{Fy} slope, Strouhal number and C_{L0} for all cross-section geometric layouts investigated at different angles of attack.

Geometric configuration	α [deg]	$dC_{Fy}/d\alpha$ [-]	St [-]	C_{L0} [-]
Bare deck (round corners)	0	-21.2	0.150	0.22
	-3	-15.8	0.149	0.15
	+3	-28.4	0.134	0.20
	+8.5	+6.4	0.121	0.58
Bare deck (sharp corners)	0	-29.2	0.146	0.24
	-3	-15.9	0.147	0.23
	+3	-18.9	0.133	0.19
	+8.5	+7.5	0.117	0.64
Barrier 1	0	-25.8	0.122	0.40
	-3	-28.2	0.119	0.33
	+3	-4.2	0.121	0.30
Barrier 2	0	-15.3	0.111	0.31
	-3	-40.7	0.104	0.42
	+3	+13.8	0.113	0.37

angle of attack growing from -3° to +3°; with Barrier 2, instead, the +3° case suggests a potentially stronger response, while a clear predominance is not observed between 0° and -3°;

- All the geometric layouts at -3° are expected to be considerably stable from the point of view of transverse vibration and the stability seems even to increase starting from bare deck and installing firstly Barrier 1 and then Barrier 2.

Such list of impressions about possible aeroelastic behavior based on static measurements has been checked through dynamic wind tunnel test, which are described in the following chapter. In this context, the main goal is to assess the level of qualitative information about bridge deck VIV response achievable from relatively simple static wind tunnel tests.

From a quantitative point of view, static test results were employed to apply two mathematical models for VIV response prediction. As introduced in Chapter 2, a certain quantity of aerodynamic parameters have to be determined through wind tunnel tests for mathematical model calibration. Transverse force coefficient curve $C_{Fy}(\alpha)$, its slope $dC_{Fy}/d\alpha$, Strouhal number and C_{L0} are part of the parameters necessary for the two mathematical approaches studied in the present work, analyzed in deep in Chapter 6.

5. Results of aeroelastic wind tunnel tests

5.1. Introduction

In the second phase of the wind tunnel experimental campaign, aeroelastic tests were performed. These experiments were carried out by elastically suspending the sectional model through the setup described in Chapter 3, in smooth flow condition. Aeroelastic tests represent the most usual and reliable way to assess the VIV response of a bridge deck during the design phase of the structure, since they reveal as accurately as possible the response amplitude and the lock-in range. The tests are usually carried out for different values of the wind angle of attack α to assess the deck VIV response for different incoming flow directions. The investigated range of angles is appropriately chosen to cover as well as possible a realistic variety of situations. According to these observations and to the knowledge available about bridge design and consistently with static tests previously described, the three angles of attack 0°, -3° and +3° were selected for the aeroelastic test campaign and studied for all the cross-section geometric layouts.

In this phase of the experimental work, two different typologies of tests were carried out. Firstly, response curves in terms of oscillation amplitude were identified, with the sectional model free to vibrate from rest condition with the wind speed (U) increased gradually. The curves were achieved for all the geometric configurations at the above mentioned angles of attack and for different values of the Scruton number (Sc) of the system. The Scruton number is the key mass-damping parameter for the aeroelastic test performance, here expressed as reported by Eq (2.4) in Chapter 2.

The VIV response of a bridge deck in air depends on this dimensionless parameter and, consequently, it is crucial to compare wind tunnel test results to the full scale structure behavior. Several Sc are usually tested in wind tunnel in order to obtain the Griffin plot of the studied bridge deck. The Griffin plot is a typical and useful tool for bridge design, reporting the maximum non-dimensional oscillation amplitude reached by the deck (Y_{peak}) against the Scruton number of the vibrating system. The value of Y_{peak} is obtained dividing the maximum oscillation amplitude observed by the across-floe bare deck dimension (D). As described below, the Griffin plot was achieved for each cross-section layout and angle of attack, by varying the mechanical damping ζ_0 and, consequently, the Scruton number, through the magnetic damping system described in Chapter 3. Both the damping ratio of

the system and the natural transverse vibration frequency (n_0) were estimated before every set of measures through an appropriate procedure.

In the second phase of the aeroelastic test campaign, free-decay tests were performed, by releasing the model from an initial condition appropriately set, for several values of the wind velocity. This part of the work aimed to estimate the aerodynamic damping (ζ_{aero}) for every layout of the studied cross-section. The main purpose was to achieve a realistic reference value for ζ_{aero} to compare to the values predicted by the quasi-steady theory (Eq. (2.44)), calculated through the aerodynamic parameters coming from static tests. The decay tests were performed for several values of the reduced wind speed, defined as follows:

$$U_{red} = \frac{U}{n_0 \cdot D} \tag{5.1}$$

to achieve a wide set of results both at low and high values of U_{red}, where the quasi-steady prediction is expected to be, respectively, less and more accurate. Special attention was paid to results obtained close to the lock-in condition, with a view to the mathematical modeling of VIV response, as remarked in the discussion section.

Finally, before carrying out all dynamic measurements, some preliminary checks were done. In particular, the exact value of the system mass was evaluated and the linearity of the adopted setup was checked in the range of displacement reached during the tests.

5.2. Frequency and damping identification

The procedure adopted to estimate natural frequency and damping ratio was the Modified Unifying Least-Squares (MULS) method for the mechanical system identification (Bartoli et al., 2009). Free-decay tests in still air were repeated several times for each series of aeroelastic measurements, showing very good repeatability. The effect of still-air resistance was minimized by considering only small vibrations for damping estimation, with a maximum amplitude below 0.5 mm.

An example of the dynamic identification process of the system is reported in Figure 5.1, where the difference in the decay curve for different Scruton numbers can be observed. Both vertical displacement and time were expressed in a non-dimensional way:

the dimensional displacement y was divided by the cross-flow dimension of the bare deck D, while the generic time t was multiplied by the natural frequency of the system n_0.

5.3. Equivalent mass identification

First of all, the total mass related to the transverse degree of freedom (M) had to be estimated accurately. It is worth to remark that a sectional model elastically suspended and able to vibrate along the across-flow direction exhibits a constant mode shape, and the equivalent mass per unit length (m) is equal to M divided by the length of the model L.

The searched mass M is the result of the sectional model mass (M_{model}) plus the mass coming from the suspension system (M_{susp}) that participates to the vertical displacement degree of freedom:

$$M = M_{model} + M_{susp} \tag{5.2}$$

The total mass was estimated in two different ways. Firstly, it was measured by progressively adding different known masses to the system and checking the vertical displacement when the system was perfectly still. The knowledge of the generic mass added (M_{add}) and the displacement obtained (y) allowed to calculate the stiffness in the transverse degree of freedom (k), which was found to be about 17.3 kN/m. Knowing the natural frequency of the system, estimated as explained above, the mass of the system could be evaluated. In addition, this procedure also allowed to check the linearity of the setup employed over a certain range of transverse displacement. As shown in Figure 5.2(a), the behavior is markedly linear up to more than 20% of the bare deck height, a range of values compatible with the greatest oscillation amplitudes reached during the tests. P_{add} indicates the weight added corresponding to M_{add}. Then, another procedure was carried out for the mass identification: several free-vibration tests were performed with different masses added to the system, and different values of the frequency were measured (Figure 5.2(b)). The stiffness k of the setup was calculated through a linear regression starting from known added masses and identified natural frequencies, according to the following expression:

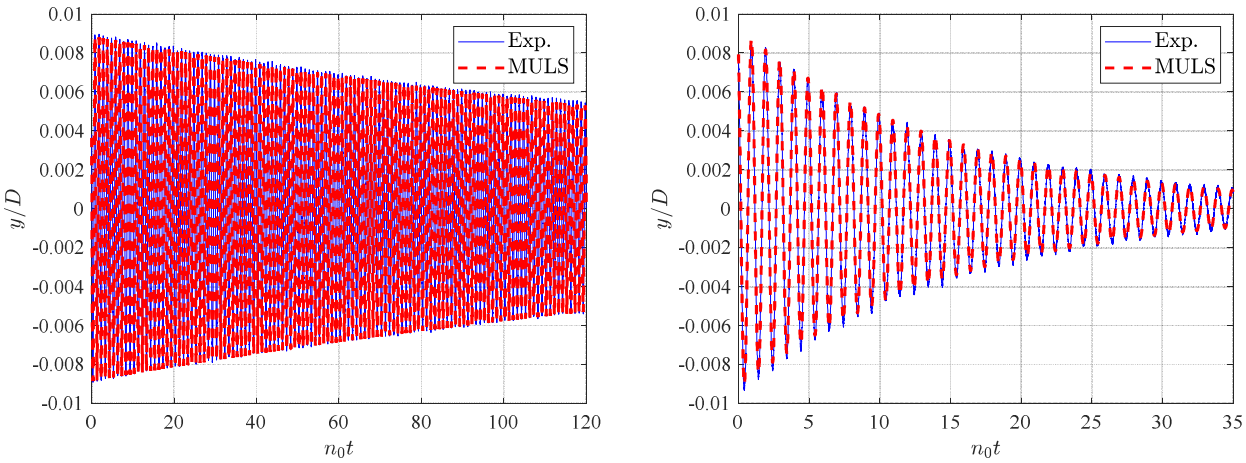

Figure 5.1. Examples of free-decay tests results for identification of natural frequency and damping ratio, at low *Sc* (a) and high *Sc* (b).

$$\omega = 2\pi n_0 = \sqrt{\frac{k}{(M + M_{add})}} \Rightarrow \frac{1}{(2\pi n_0)^2} = \frac{1}{k} \cdot (M + M_{add}) \tag{5.3}$$

The equivalent mass of the oscillating system was calculated through the stiffness obtained as above (k = 17.4 kN/m) and the natural frequency value identified without any additional masses.

The equivalent masses identified through the two procedures were respectively 5.87 kg and 5.92 kg, with a relative error of about 0.8% and, therefore, in very good agreement with each other. The natural frequency of the system composed only by the sectional model fixed to the shear-type frames, without any barriers and without the aluminum plates of the additional damping system, was found to be about n_0 = 8.3 Hz.

5.4. Determination of VIV response oscillation amplitude

After the preliminary checks above described, the first phase of aeroelastic tests was carried out. The response curves in terms of oscillation amplitude were obtained for all the geometric layouts of the cross section at different angle of attack values. To this purpose, the model was let free to vibrate in the transverse degree of freedom, the wind velocity was progressively increased and the time histories of the vertical displacement were recorded. In some cases, measurements were also performed reducing the wind velocity in order to highlight possible hysteresis phenomena.

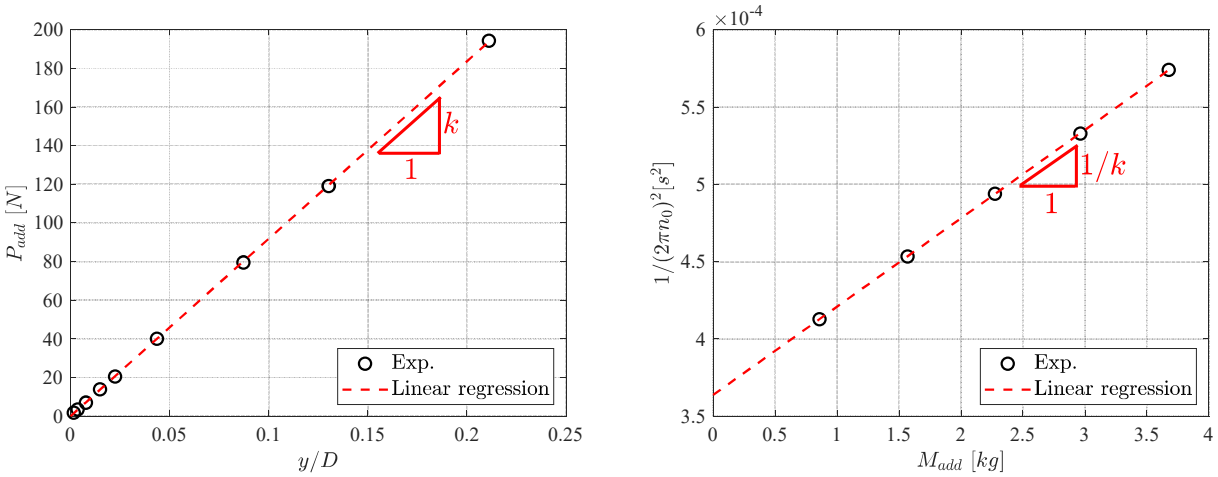

Figure 5.2. Results of the mass identification, through static (a) and dynamic (b) procedure.

The four geometric configurations were tested at 0°, -3° and +3° angle of attack in a similar range of Scruton number of the system. The bare deck layout was also tested for two additional angles, +5° and +8.5°, as described in the following sections. The damping ratio ζ_0 was varied from below 0.1% to about 1%, with a consequent Scruton number approximately ranging from 3 to 60. The natural frequencies identified before each measurement resulted about between 8 Hz and 9 Hz for all tested cases, slightly altered when lateral barriers or aluminum plates for damping system were installed, due to the increase of the mass M.

All the response curves were reported in terms of non-dimensional response amplitude y_{10}/D against reduced wind speed U_{red}. y_{10} indicates the mean value of the 10%-highest peaks in the displacement time history. Nevertheless, the vibration amplitude is usually calculated also as equivalent sinusoidal amplitude, by multiplying the time history standard deviation y' by $\sqrt{2}$, since the lock-in condition usually leads the system to a quasi-harmonic oscillation. According to experimental results, the two ways were found to be in good agreement in almost all of the cases studied. The reduced wind speed U_{red} was defined through the expression indicated by Eq. (5.1), leading to a theoretical vortex-resonance wind speed equal to $1/St$.

The response curves achieved are presented below in two different sections. In the first one, the bare deck configurations with round and sharp lower edges have been compared, while in the second one the bare deck, with sharp corners, has been compared to the two layouts with lateral barriers installed. Such distinction has been chosen consistently with the presentation of static test results.

5.4.1. Bare deck configurations

Firstly, the effect of the lower edge sharpness was observed, by comparing the two bare deck layouts before and after corner modification. As mentioned above, the tests were conducted for the three selected angles of attack 0°, -3° and +3° for different Scruton numbers of the system. For the round corner layout, α = +5° and α = +8.5° were also investigated for different Scruton numbers, while they were tested also after corner modification only for the lowest *Sc*. In Table 5.1 a general overview of all the dynamic parameters identified is reported.

The first information arising from the tests was that the sharpness of the lower corners seems not to change the aeroelastic behavior of the cross section. This was verified for zero, positive and negative angle of attack, as reported in Figure 5.3(a, b, c) for the lowest Scruton number tested. The shape of the curve, the lock-in range and the reached peak amplitude were not affected by the modification of the edges and the onset wind velocity too remained almost the same, in agreement with the very slight variation of the Strouhal number measured during static tests. The very similar behavior of the two layouts was confirmed also for higher *Sc* values. In particular, the Griffin plots obtained for the selected angles are compared in Figure 5.3(d, e, f) and, as observable, no noticeable differences in terms of dimensionless peak response amplitude (Y_{peak}) are observable.

As previously mentioned, two additional cases were tested for the bare deck: α = +5° and α = +8.5°. These values, in particular the second one, are not so typical for studies about bridge deck VIV response. As a matter of fact, a smooth and sufficiently regular flow condition with such a considerable angle of incidence is relatively unusual, except for specific locations with a particular orography. These two angles were tested consequently to the observation of the C_{Fy} curve coming from static tests. In fact, α = +5° and α = +8.5° correspond, respectively, to the minimum peak point, where the C_{Fy} curve changes its slope, and to a part of the curve with a markedly positive slope.

The aeroelastic results obtained in these two particular conditions are shown in Figure 5.4, where both round and sharp corner results are reported for the lowest Scruton number. It is clear that the sharpness of the edges did not affect the VIV response also in these two cases. The onset wind velocity was well related to the Strouhal number determined during static tests and did not change despite a slight variation of *St* value. The lock-in range obtained for both angles of attack was found to be much wider comparing to

Table 5.1. Summary of the system dynamic characteristics for bare deck configurations.

Cross-section geometric layout	α [deg]	ρ [kg/m^3]	n_0 [Hz]	ζ_0 [%]	Sc [-]
Bare deck (round corners)	0	1.16	8.66	0.08	3.9
		1.15	8.34	0.17	9.0
		1.15	8.35	0.25	13.2
		1.15	8.34	0.43	22.6
		1.15	8.34	0.63	33.3
	-3	1.14	8.66	0.09	4.5
		1.15	8.34	0.15	7.9
		1.15	8.34	0.25	13.2
		1.15	8.34	0.41	21.6
		1.15	8.34	0.65	34.3
	+3	1.16	8.66	0.09	4.2
		1.15	8.34	0.16	8.4
		1.15	8.34	0.25	13.3
		1.16	8.35	0.42	22.0
		1.16	8.34	0.63	33.1
	+5	1.15	8.66	0.09	4.2
		1.15	8.34	0.16	8.5
		1.15	8.34	0.35	18.5
		1.15	8.34	0.70	37.1
	+8.5	1.14	8.65	0.09	4.4
		1.15	8.34	0.16	8.4
		1.15	8.34	0.36	19.0
		1.14	8.34	0.69	36.6
Bare deck (sharp corners)	0	1.18	8.65	0.07	3.2
		1.18	8.35	0.15	7.7
		1.17	8.35	0.38	19.6
		1.21	8.34	0.68	34.1
		1.18	8.35	1.04	53.6
	-3	1.22	8.65	0.07	3.0
		1.18	8.35	0.16	8.2
		1.18	8.35	0.38	19.5
		1.22	8.35	0.72	35.7
		1.18	8.35	1.01	51.8
	+3	1.21	8.65	0.07	3.3
		1.22	8.35	0.15	7.5
		1.21	8.34	0.35	17.5
		1.21	8.34	0.67	33.5
		1.21	8.34	1.01	50.6
	+5	1.15	8.65	0.09	4.4
	+8.5	1.15	8.65	0.09	4.5

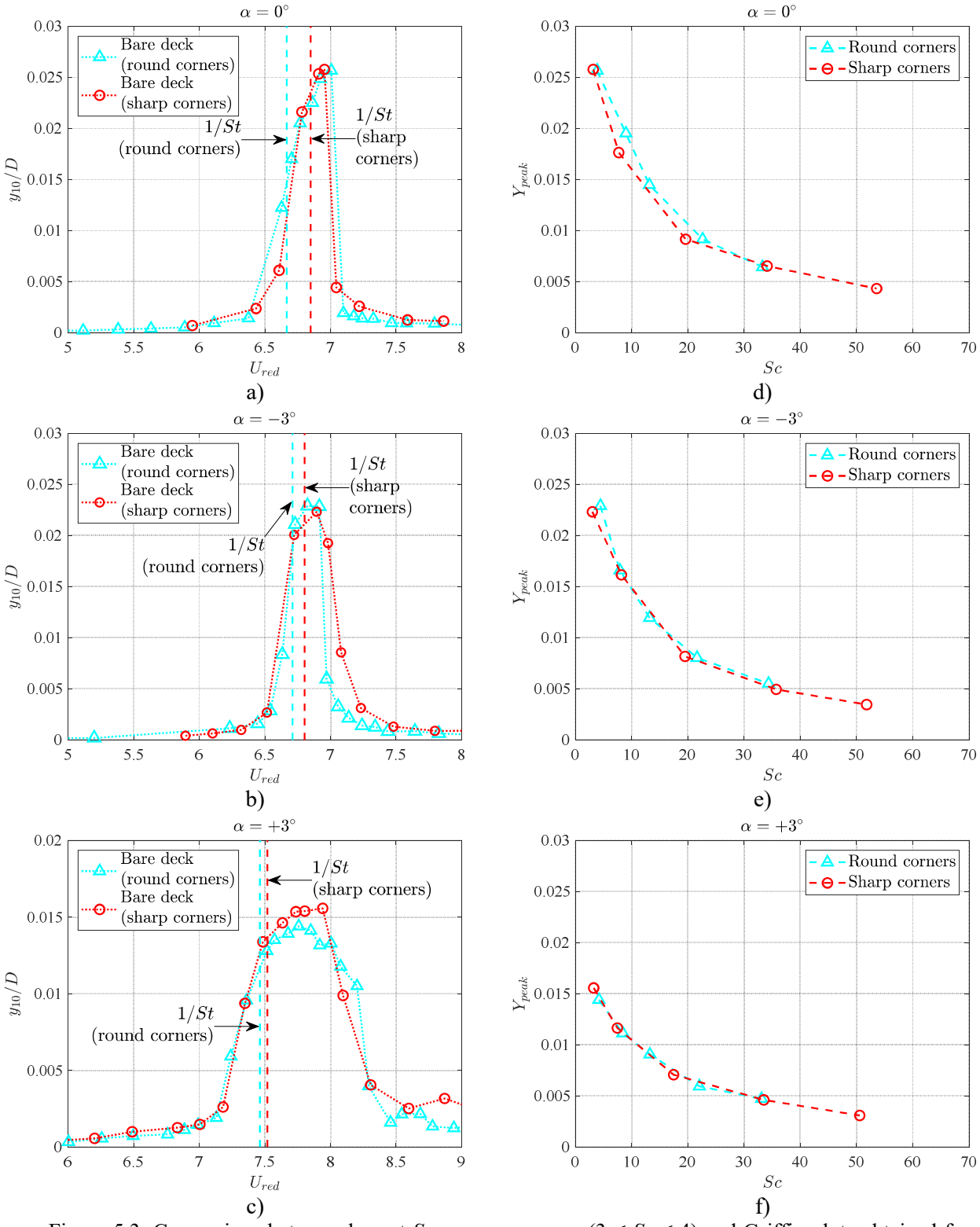

Figure 5.3. Comparison between lowest *Sc* response curves ($3 \leq Sc \leq 4$) and Griffin plots obtained for the bare deck before and after lower corners modification, at 0° (a, d), -3° (b, e) and +3° (c, f).

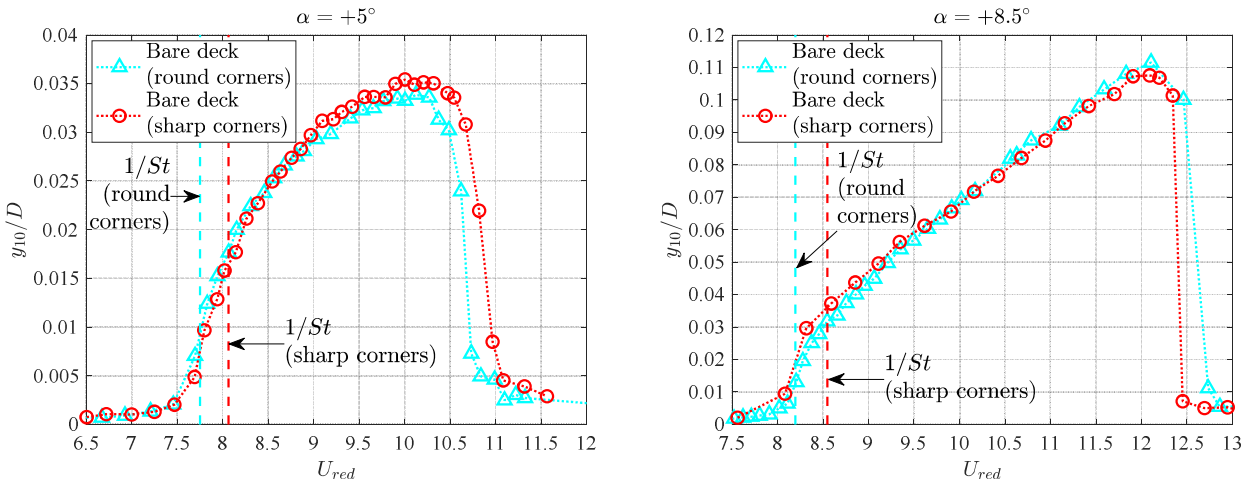

Figure 5.4. Response curves ($3 \leq Sc \leq 4$) obtained for bare deck with original and modified edges at α = +5° (a) and α = +8.5° (b).

the three values of α previously analyzed and, especially in case of α = +8.5°, the peak response amplitude observed was considerably greater, over 10% of D. The shapes of the two curves are different from the previous three found for the bare deck and from each other too. In both cases, the lock-in range is similarly extended; for +5°, nevertheless, the curve is quite rounded and symmetric (Figure 5.4(a)), while at +8.5° it appears strongly asymmetric, approximately triangle-shaped (Figure 5.4(b)). In this context, further observations are proposed in the discussion section.

5.4.2. Bare deck vs lateral barriers

In contrast to what observed for lower corner modification, the differences produced by the addition of both lateral barriers are evident from several points of view. In this section, the marked influence of the flow angle of attack is pointed out too.

As above, a resume of the dynamic parameters related to the aeroelastic tests with barriers installed is reported in Table 5.2. It is worth to note the case of Barrier 2 at -3°: the natural frequency value related to the second Scruton number tested is markedly different from all the other cases. This is because in this specific situation some additional mass was attached to the vibrating system, to obtain an appropriate value of the Scruton number between the lowest one tested and the lowest achievable through the external damping system.

The effect produced by the addition of lateral barriers at the three different angles of

Table 5.2. Summary of the system dynamic characteristics for configurations with lateral barriers.

Cross-section geometric layout	α [deg]	ρ [kg/m^3]	n_0 [Hz]	ζ_0 [%]	Sc [-]
Barrier 1	0	1.21	8.56	0.07	3.5
		1.21	8.26	0.14	7.2
		1.21	8.26	0.23	11.8
		1.21	8.26	0.37	18.9
		1.21	8.26	0.67	34.2
		1.21	8.26	1.16	59.2
	-3	1.20	8.56	0.08	3.8
		1.19	8.26	0.13	6.7
		1.20	8.27	0.25	12.9
		1.19	8.27	0.4	20.7
		1.19	8.27	0.7	36.3
		1.19	8.27	1.13	58.7
	+3	1.22	8.56	0.07	3.4
		1.21	8.26	0.12	6.1
		1.21	8.26	0.24	12.2
		1.21	8.26	0.39	19.9
		1.21	8.26	0.58	29.5
		1.21	8.26	0.8	40.8
		1.22	8.26	0.97	49.2
		1.22	8.26	1.23	62.2
Barrier 2	0	1.19	8.52	0.08	3.8
		1.18	8.23	0.15	7.9
		1.18	8.23	0.23	12.1
		1.18	8.23	0.39	20.5
		1.18	8.23	0.72	38.1
		1.17	8.23	1.23	65.2
	-3	1.18	8.52	0.08	3.9
		1.18	7.80	0.083	4.9
		1.18	8.23	0.12	6.3
		1.17	8.22	0.15	7.9
		1.17	8.22	0.24	12.7
		1.17	8.22	0.40	21.2
		1.17	8.22	0.73	38.7
		1.19	8.22	1.16	60.7
	+3	1.19	8.52	0.07	3.5
		1.19	8.23	0.15	7.8
		1.19	8.23	0.24	12.5
		1.19	8.23	0.38	19.8
		1.21	8.23	0.55	28.2
		1.21	8.23	0.75	38.6
		1.20	8.23	0.91	46.9
		1.20	8.23	1.16	59.9

attack is pointed out in Figure 5.5. The peak response amplitude is generally increased by the presence of barriers comparing to the bare deck and the lock-in range becomes slightly wider with Barrier 1 while it is much more enlarged by Barrier 2. Globally, it seems like the first barrier produced more effects on the peak response, while the second one on the width of the synchronization velocity range. Such an observation is not valid in case of Barrier 2 at -3° (Figure 5.5(b)), which exhibited an unexpected very high amplitude response branch, which will be discussed with particular attention. The vortex-resonance wind velocities ($1/St$) are indicated in the figures. The curves corresponding to bare deck and Barrier 1 show an onset wind velocity in quite good agreement with the theoretical value achieved from static tests, while this does not occur for Barrier 2. In particular, at 0° and -3°, Barrier 2 curves exhibit an onset velocity markedly lower and a particular shape of the curve, with the response amplitude that partially decreases over the first portion of the lock-in range (Figure 5.6(a)).

The effect of the angle of attack variation was also accurately observed and it is well pointed out by Figure 5.5(d, e, f). For the bare deck (Figure 5.5(d)), 0° and -3° curves are really similar to each other, both in terms of curve shape and in terms of peak point, while at +3° the lock-in range increases slightly and the maximum amplitude is lower. In addition, the curve at +3° is shifted towards higher speed values, in agreement with the lower Strouhal number estimated. Globally, the angle of attack variation seems not to affect strongly the bare deck VIV response in this range of values, since both the peak amplitude and the lock-in range extension remain quite limited.

With lateral barriers installed, the situation changes drastically. In presence of Barrier 1 (Figure 5.5(e)), the growth of the flow angle of incidence produces an amplitude increasing up to more than 10% of the cross-flow dimension. In addition, for α = -3° a noticeable hysteresis loop at the lower bound of the lock-in range was found and it is indicated in Figure 5.5(b, e).

The main effects caused by the angle of attack change were exhibited with Barrier 2. First of all, it is worth to point out that a secondary resonance phenomenon was obtained for all the angles reported. In the main lock-in, the curves show an anticipated onset comparing to the theoretical resonance wind velocity. As previously mentioned, at -3° and 0° the response amplitude does not increase continuously, showing a reduction over a portion of the lock-in range indicated in Figure 5.6(a) by the dashed arrows, while at +3° a more regular trend of the response curve is observable. The most critical VIV response

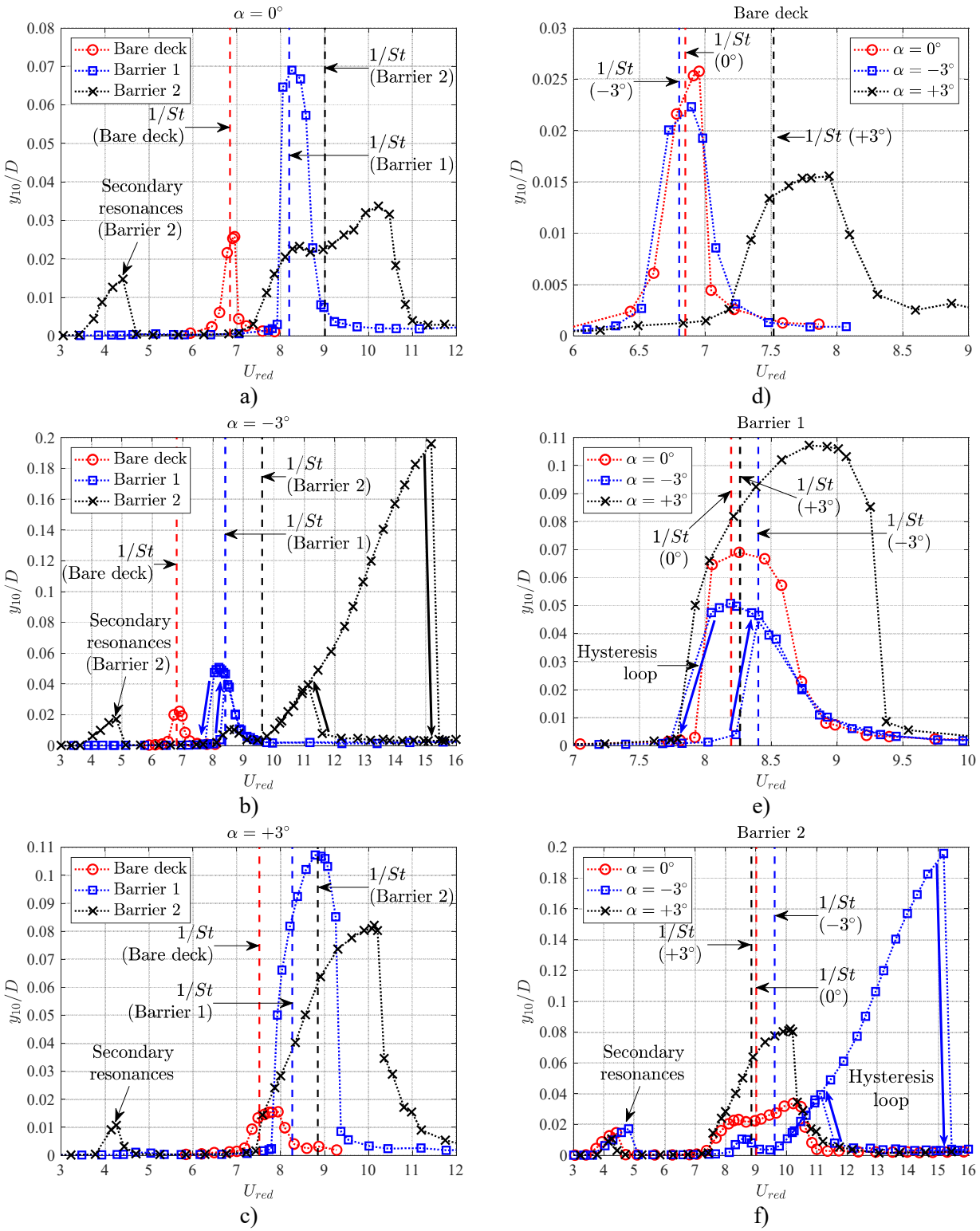

Figure 5.5. Comparison between response curves ($3 \leq Sc \leq 4$) obtained for different geometric configurations, at 0° (a), -3° (b) and +3° (c). The same curves are compared varying the angle of attack for bare deck (d) and deck with Barrier 1 (e) and Barrier 2 (f) installed.

effect was certainly the very high amplitude branch observed at α = -3°. In this case, the vibration amplitude increases almost linearly with the flow speed over an extended range, between U_{red} = 9.5 and U_{red} = 15.5, reaching almost the 20% of the cross-flow dimension for the lowest Scruton number tested. A very large hysteresis loop was found, as indicated by the arrows in Figure 5.5(b, f) and Figure 5.6(b). A significant role played by *Sc* can be also remarked in this case: for the two lowest Scruton numbers tested the high response branch was found, while for about *Sc* = 6 it totally disappeared (Figure 5.6(b)).

After response curve determination, Griffin plots were achieved for each case (Figure 5.7). As mentioned above, the Scruton number of the system was varied approximately from 3 to 60. No unexpected effects due to the Scruton number increase need to be pointed out, except for the case of Barrier 2 at α = -3 ° already described above and remarked in Figure 5.6(b).

The peak values of each response curve were collected for all the Scruton numbers set and they were used to draw the Griffin plots. For Barrier 2 at the lowest Scruton number (Figure 5.7(b)) both Y_{peak} obtained increasing the wind velocity and Y_{peak} corresponding to the jump on the main branch obtained reducing the velocity were indicated, and the difference between each other highlighted. Finally, the envelope of the Griffin plots over the angles of attack was achieved for every cross-section layout, as shown in Figure 5.8.

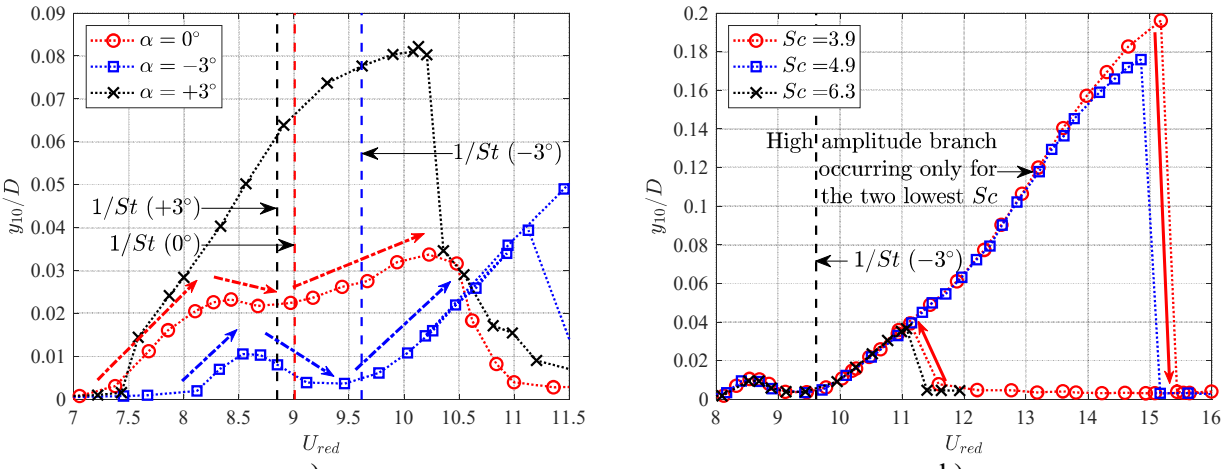

a) b)

Figure 5.6. Close-up of a portion of Barrier 2 response curves (a) for 3 ≤ *Sc* ≤ 4. Comparison between plots obtained with Barrier 2 at α = -3° for different values of the Scruton number (b).

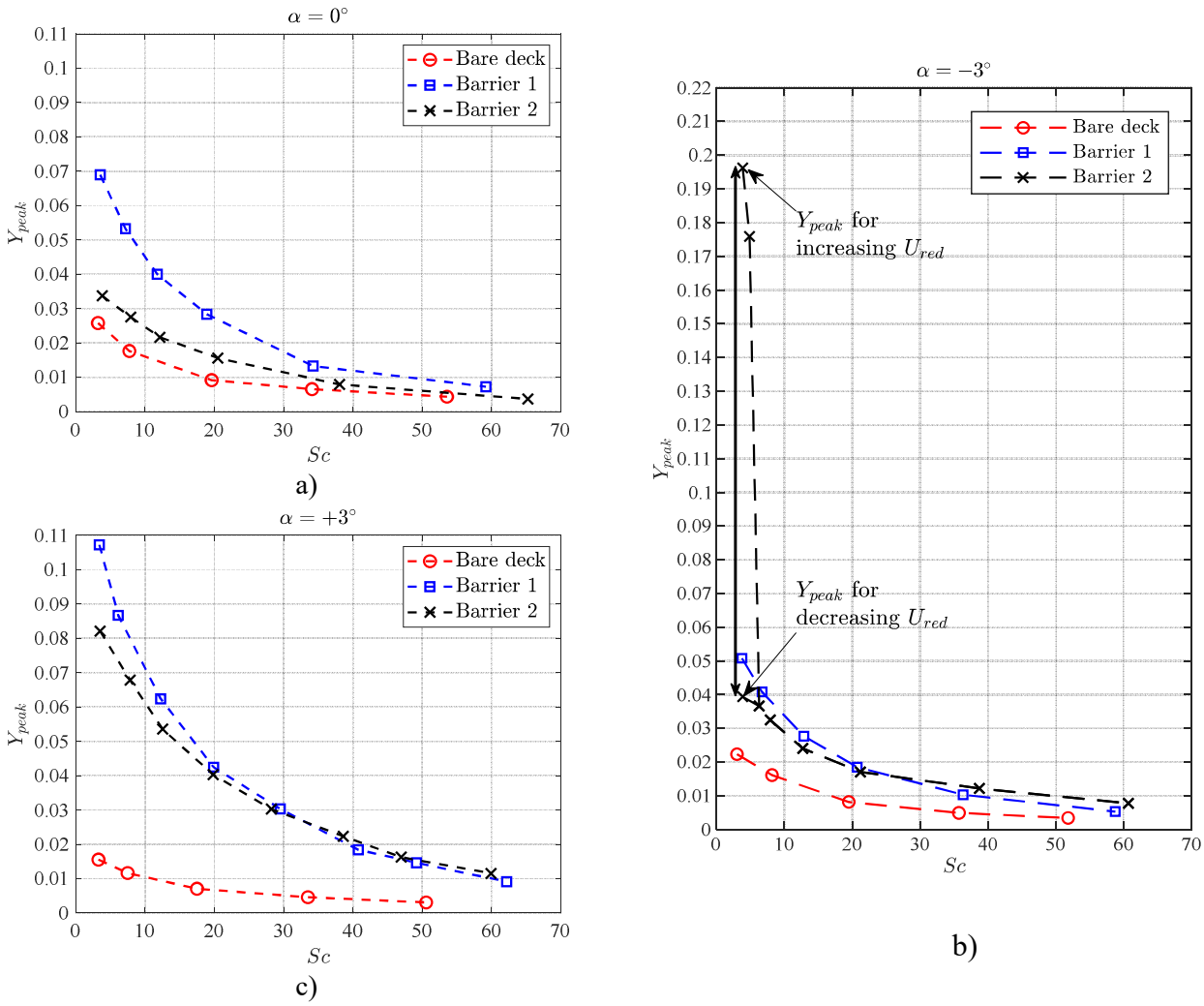

Figure 5.7. Comparison between geometric layouts in terms of Griffin plot at 0° (a), -3° (b) and +3° (c).

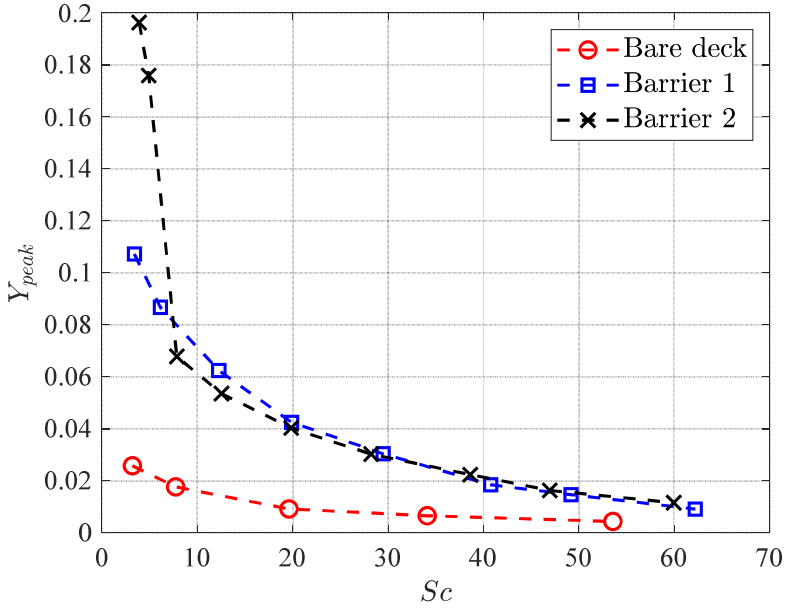

Figure 5.8. Griffin plot envelope over the selected angle of attack values for every geometric layout.

5.5. Free-decay tests

The second part of the aeroelastic wind tunnel tests consisted of free-decay tests from a certain initial condition of transverse displacement. These experiments were mainly carried out with the purpose of estimating the aerodynamic damping (ζ_{aero}) for all the different cases studied, for many flow velocities. As mentioned in the introduction, the main goal was to compare the aerodynamic damping ratio estimated through such measurements to the aerodynamic damping calculated from static tests results, according to the quasi-steady theory (Eq. 2.44), namely ζ_{aero}^{QS} .

The estimation of ζ_{aero}^{QS} is based on the linearization of the transverse force coefficient C_{Fy} and its value is proportional to the curve slope ($dC_{Fy}/d\alpha$). According to scientific literature, the reliability of the quasi-steady definition of aerodynamic damping is expected to increase with the reduced flow speed U_{red}. Free-decay tests were performed both for high U_{red} and low U_{red}, closer to the lock-in condition, to assess the capability of the quasi-steady assumption of predicting, even approximately, the aerodynamic damping over a wide range of wind velocity for several cross-section layouts which exhibited a variety of aerodynamic and aeroelastic behaviors. Reduced wind velocities close to the vortex-resonance speed $1/St$ were investigated with special care, to estimate as well as possible the aerodynamic damping of the cross-section close to lock-in condition.

The theoretical method adopted for the free-decay tests was the same used for the mechanical damping ratio identification, through the MULS method previously mentioned. In this phase too, the dynamic identifications were repeated several times for each case tested, in order to have a suitable level of confidence about the results and to assess the repeatability of the identifications. The still-air mechanical damping ζ_0 was determined before every set of measurements, as for the response curves, and then the total damping of the system ζ_{tot} was evaluated for different values of the reduced wind speed U_{red}. To this purpose, at a certain value of the flow speed, the suspension system was pulled down through two thin and light cables and fixed at a symmetric transverse displacement condition (about 20% of D). Then, the cables were released and the decay of the vibrating system was used to determine ζ_{tot} .The searched aerodynamic damping ζ_{aero} was obtained by difference between the two former damping ratios mentioned:

$$\zeta_{aero} = \zeta_{tot} - \zeta_0 \tag{5.4}$$

The more ζ_0 and ζ_{aero} are comparable to each other, the more ζ_{aero} evaluation by difference is reliable. For this reason, the identifications were always repeated for at least two different values of the mechanical damping, respectively close to 0.1 % and 1 %, in order to obtain more reliable results both at low and high values of detected aerodynamic damping.

Differently from dynamic identification for mechanical damping, the time histories registered during the decay tests at a certain value of flow speed were expressed in terms of apparent wind angle of attack (α_{app}) instead of transverse displacement. By approximating the vibration of the system as a harmonic motion, the fluctuating apparent angle of attack amplitude was evaluated from the transverse oscillation amplitude y as follows:

$$\alpha_{app} \simeq \frac{\omega_0 \cdot y}{U} = \frac{2\pi \cdot n_0 \cdot y}{U_{red} \cdot n_0 \cdot D} = 2\pi \frac{(y/D)}{U_{red}} \tag{5.5}$$

It is worth to highlight that the same dimensionless transverse displacement y/D corresponds to decreasing values of α_{app} for increasing U_{red}.

Such choice came mainly from the will to compare the aerodynamic damping found experimentally and the quasi-steady one, which is a function of the angle of attack through C_{Fy}. In addition, the more the C_{Fy} trend is linear and the variation of the angle of attack is limited during the oscillation, the more the linearization of the curve is theoretically correct and reliable. For this reason, the portion of the decay time history for the damping identification was appropriately selected to keep α_{app} as small and homogeneous as possible over the whole range of reduced flow speed investigated. According to the latter observations, the dynamic identifications were performed for an apparent flow angle of attack lower than about 1°.

Finally, an important specification about the tests have to be done: the procedure described for aerodynamic damping identification could not be carried out inside lock-in range. The linear mechanical model which stands behind the MULS method is not suitable at lock-in, due to the marked non-linearity included in such condition and the free decay leading to a limit cycle of oscillation instead of a quasi-zero amplitude. Examples of decay tests outside and inside lock-in, respectively suitable and not suitable for damping identification, are reported in Figure 5.9. The decay at lock-in in Figure 5.9(b) was obtained, as expected, for U_{red} very close to the vortex-resonance flow speed $1/St$. Given the impossibility of identifying inside lock-in range, the value of ζ_{aero} at lock-in was

approximately deduced from identifications carried out as close as possible to such condition, immediately before and after the synchronization range.

Figure 5.10 and Figure 5.11 report the results obtained from free-decay tests for all configurations. Every figure shows the values of ζ_{aero} achieved from the experiments and the prediction obtained from quasi-steady theory formulation. The slope of the C_{Fy} curve obtained from static tests, as described in Chapter 4, was observed to be sensitive to the Reynolds number, especially in terms of shift exhibited by the minimum peak of the plot. For this reason, two quasi-steady aerodynamic damping values were calculated and reported in the figures: one corresponding to a lower (Re_{min}) and the other one to a higher (Re_{max}) Reynolds number, respectively $Re \simeq 19000$ and $Re \simeq 100000$. In addition, a small box reminding the transverse force coefficient curve was reported in each plot, in order to highlight the slope and the shape of the curve at a certain angle of attack α for low and high velocity values.

In Figure 5.10, the results obtained for the bare deck are shown. The tests were performed on the sectional model with the sharp lower edges. The behavior in terms of aerodynamic damping was assessed for the same three angles of attack selected (0°, -3° and +3°). In this case, the angle +8.5° was also tested and discussed later in the following section. As observable, for α = -3° (Figure 5.10(b)) the damping values estimated experimentally are in good agreement with the quasi-steady prediction along the whole reduced wind velocity range investigated. As expectable, for the highest U_{red} values the experiments were found to be in very good agreement with the damping calculated for high Reynolds number. At 0° and +3° the results are less easy to understand clearly. At 0°

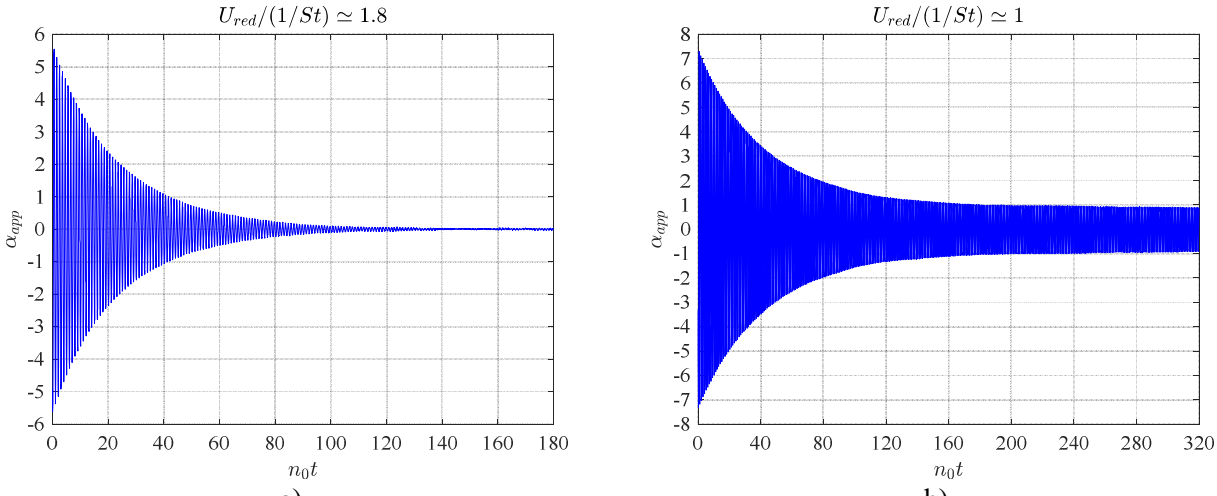

a) b)

Figure 5.9. Examples of free-decay test time history of α_{app} for reduced wind speed after (a) and inside the lock-in range (b).

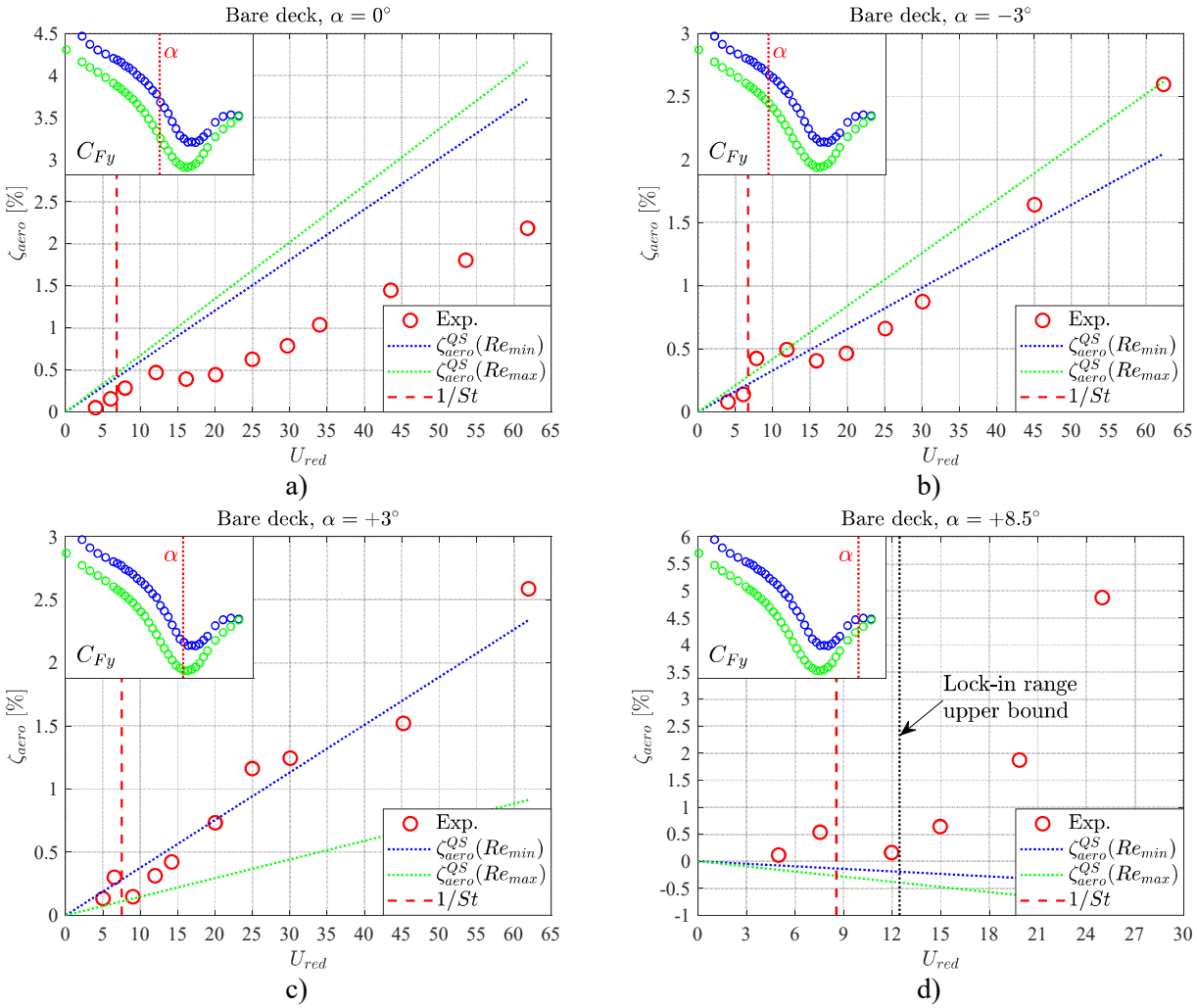

Figure 5.10. Aerodynamic damping identification for bare deck at 0° (a), -3° (b), +3° (c) and +8.5° (d).

(Figure 5.10(a)), the quasi-steady theory seems to match better the measurements at low reduced wind speed, while around U_{red} = 15 a marked shift is generated and after about U_{red} = 30 the damping measured keeps growing with the same slope of the quasi-steady line. At +3° (Figure 5.10(c)), a very good agreement is found, quite surprisingly, between tests and predictions corresponding to low *Re* over the whole velocity range, up to highest U_{red} values where a better agreement with the high *Re* line was presumed. Finally, at +8.5° the result was even more surprising: while quasi-steady theory suggests negative aerodynamic damping, the experiments provide slightly positive values up to about U_{red} = 12 and a very strong growth after it, in marked contrast to what expected at highest U_{red} values according to quasi-steady theory.

Figure 5.11 shows the results obtained with Barrier 1 and some similarities with previous observations about bare deck can be noticed, even if for different flow angles of incidence. At 0° angle of attack (Figure 5.11(a)) the global behavior of measured damping recalls what was observed at -3° for bare deck: a good agreement with the quasi-steady assumption both at low and high reduced wind velocities. For -3° (Figure 5.11(b)), on the other hand, the results are quite similar to the ones obtained for bare deck at 0°: an initial very good agreement, a shift occurring at about U_{red} = 15 and then a continuous growth with a slope leading towards the quasi-steady line. Figure 5.11(c) reports the results obtained for α = +3°, in which case the experiments provide positive damping values considerably greater than ζ_{aero}^{QS} .In particular, for the highest velocities tested a negative aerodynamic damping was predicted, strongly in contrast to the measurements.

In Figure 5.11, results for Barrier 2 are collected too. This configuration provided the most difficult results to interpret. The most regular behavior was found for α = -3° (Figure 5.11(e)) out of the range over which the high amplitude branch was observed for the lowest Scruton numbers (Figure 5.6(b)). Before and after this range the damping ratios measured seem in relatively good agreement with the quasi-steady theory. Inside the this velocity range, the identifications were carried out even if for lower Scruton numbers a lock-in was observed. The measurements were performed setting a mechanical damping ratio sufficiently high to avoid any noticeable lock-in, so that the identification process for ζ_{aero} could be conducted, despite some uncertainties comparing to other measurements. The upper bound of the above mentioned range is indicated in Figure 5.11(e), and Figure 5.12 shows examples of time histories recorded outside (Figure 5.12(a, b)) and inside

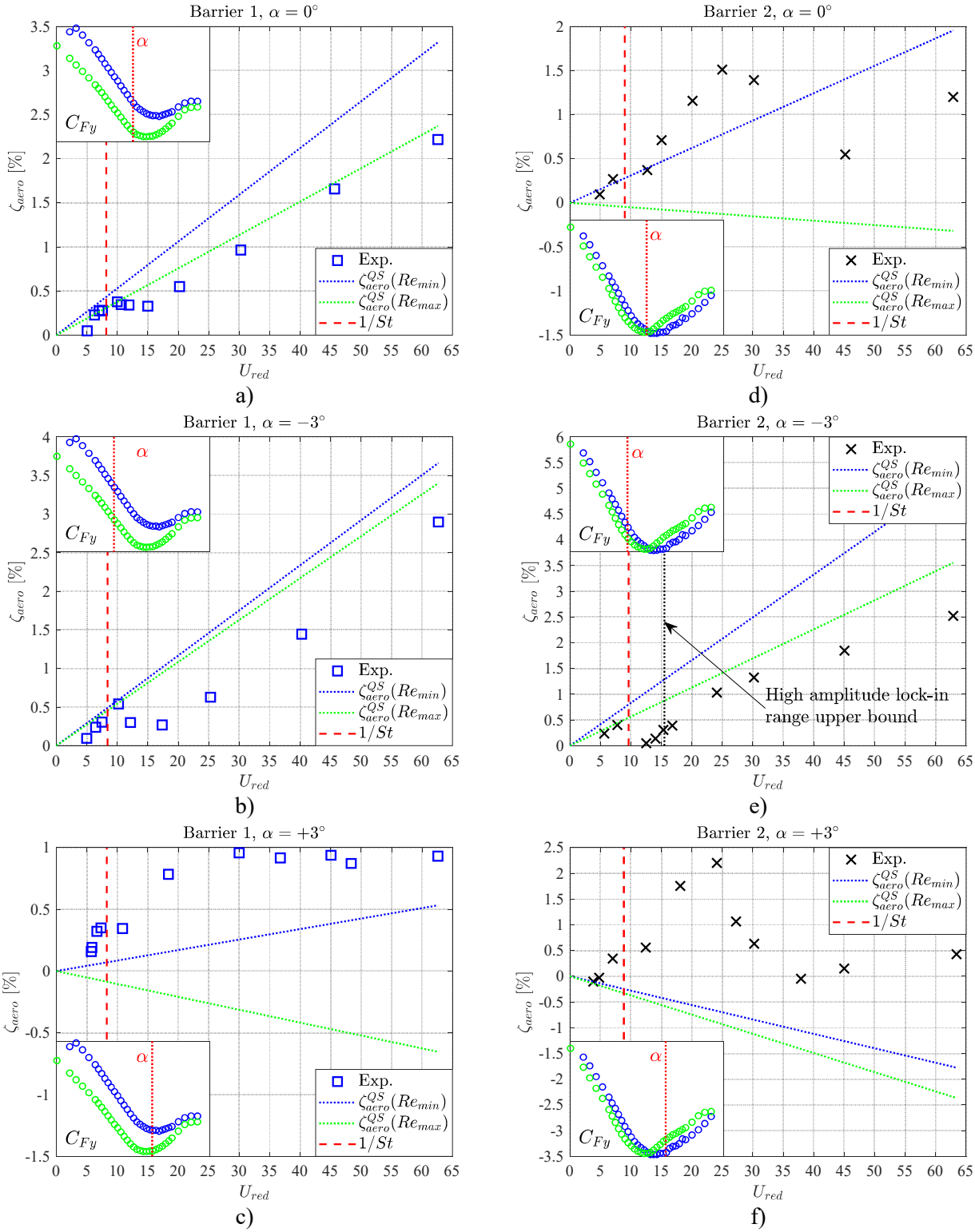

Figure 5.11. Aerodynamic damping identification at 0°, -3° and +3° with Barrier 1 (a, b, c) and with Barrier 2 (d, e, f) installed.

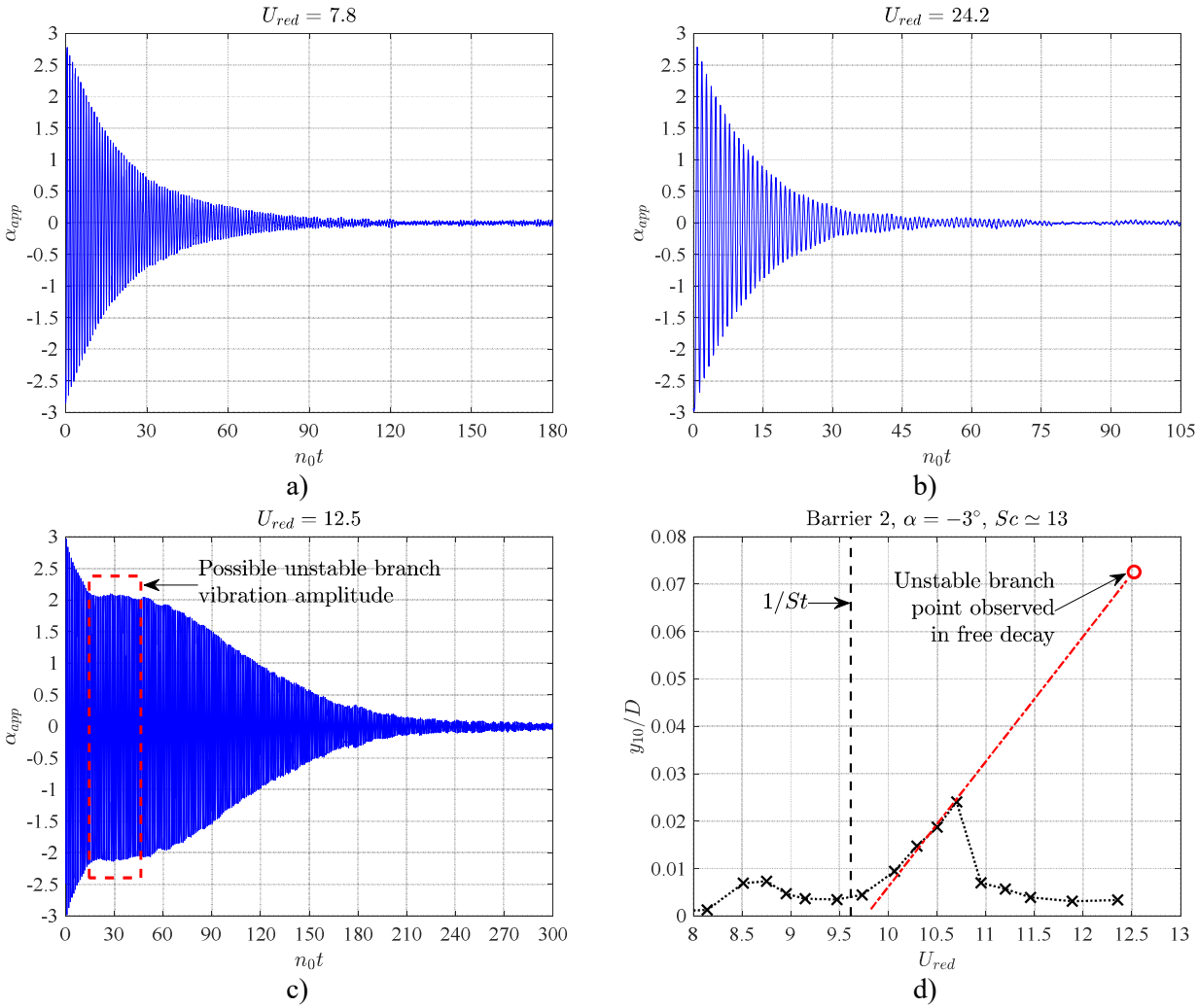

Figure 5.12. Free-decay results with Barrier 2 for α = -3° before (a) and after (b) lock-in range. Free-decay inside the lock-in range related to the high response branch observed only for lowest *Sc* (c).

(Figure 5.12(c)) it. In this latter case, a sort of plateau recalling a limit cycle can be observed in the time history plot, as highlighted in Figure 5.12(c). As said before, the aerodynamic damping identification was anyway performed after this portion of the decay time history. Figure 5.12(d) shows the response curve obtained for the same Scruton number set for decay tests, and the amplitude of this sort of unstable limit cycle is reported, exhibiting a quite good alignment with the increasing branch of the response curve, similarly to what observed for the two lowest *Sc*.

Proceeding with Barrier 2 analysis, at 0° (Figure 5.11(d)), experiments and quasi-steady theory gave very similar results below U_{red} = 15, while after the difference between them increased strongly. In addition, a non-monotonic trend of the aerodynamic damping, which markedly decreases between 25 and 45 reduced wind speed, was suggested. Finally, in Figure 5.11(f) the +3° results are reported. As observable, in this case the mathematical prediction and the experimental data were totally in disagreement, both for low and high U_{red}: calculated ζ_{aero}^{QS} is negative, based both on low and high Reynolds number C_{Fy} curve, while the damping evaluated through decay tests is always positive. As for the 0° case, the measured damping is not monotonic, since it exhibits a growth up to over 2 %, then a reduction to zero and, finally, a new increase.

As previously specified, the main goal of the described free-decay test campaign was an estimation of the aerodynamic damping for every layout of the studied cross-section close to lock-in condition. Given the impossibility to measure it directly inside the lock-in range, an estimation was found through a polynomial approximation over the experimental results. A summary of the obtained values is reported in Table 5.3. In this way, a realistic,

Table 5.3. Aerodynamic damping close to vortex-resonance flow speed (1/*St*), estimated through experimental tests and according to quasi-steady theory based on C_{Fy} curve slope at low and high *Re*.

Cross-section geometric layout	α [deg]	Exp. [%]	$\zeta_{aero}^{QS}(Re_{min})$ [%]	$\zeta_{aero}^{QS}(Re_{max})$ [%]
Bare deck	0	0.22	0.41	0.46
	-3	0.25	0.22	0.28
	+3	0.24	0.28	0.11
	+8.5	0.44	-0.13	-0.27
Barrier 1	0	0.34	0.43	0.31
	-3	0.41	0.49	0.46
	+3	0.33	0.07	-0.09
Barrier 2	0	0.28	0.28	-0.05
	-3	0.44	0.80	0.54
	+3	0.34	-0.25	-0.33

even if approximate, reference value for ζ_{aero} around U_{red} = 1/*St* was achieved. The meaning of the obtained results is discussed in the following section.

5.6. Discussion of aeroelastic test results

5.6.1. Response curves

Dynamic tests gave rise to several observations about the aeroelastic behavior of the studied cross section and the effects of geometric details and angle of attack. From the study of the response curves, a large variability of results was found. The results covered a wide variety of VIV response typologies in terms of curve shape, extension of the lock-in range and peak vibration amplitude. The effects produced by the sharpness of the sectional model lower edges were extremely limited, while the role played by both lateral barriers and flow angle of attack was crucial. This can be generally considered a positive element, since the sharpness of cross-section corners cannot be easy to reproduce correctly in a wind tunnel model.

The synchronization range was found to be quite short for both bare deck and Barrier 1, but in this latter case the peak response amplitude increased strongly, up to more than 10% of *D*. In addition, in all of these configurations the lock-in onset wind velocity is strictly related to the vortex-resonance flow speed obtained from the Strouhal number coming from static tests, as highlighted in Figure 5.3, Figure 5.4 and Figure 5.5.

With Barrier 2 installed, on the other hand, the observed aeroelastic behavior is markedly different. For this geometric layout the lock-in range became wider, about two times the one observed for bare deck and Barrier 1, for all the studied angles of attack. The maximum response amplitude detected also increased with the addition of this barrier, reaching the very high value of almost 20% of *D* at α = -3° for the two lowest Scruton number values tested. It is worth to recall the quite particular shape of the curves related to 0° and -3°, with the non-monotonic trend previously highlighted in Figure 5.6(a) and the onset reduced wind velocity markedly lower than 1/*St*. A possible explanation for this occurrence could be found in impinging shear layer instability, similarly to what observed by Nakamura and Nakashima (1986) for a H cross-section, because of the cavity created by a deck with closed barriers. In this case, such effect could be promoted by the lower continuous closed portion of Barrier 2, while Barrier 1 is much more transparent to the flow. When this condition occurs, the Strouhal number value is often constant and equal to

0.6 approximately, referring to the along-wind dimension *B*, and hence independent of the cavity depth and width (Rockwell and Naudascher, 1978). According to this supposition, a possible interaction between vortex shedding behind the body and impinging shear layer instability is suggested. Figure 5.13(a) shows Barrier 2 and the height of its closed lower portion, while in Figure 5.13(b) the response curves at 0° and -3° are reported and the vortex-resonance and impinging shear layer instability reduced velocities are indicated.

The extreme VIV response sensitivity to the presence of barriers is consistent with the results of previous studies mentioned in Section 2.3.2. Such lateral elements arising vertically from the deck surface may promote lock-in and act on both the extension of synchronization range and on the peak response observed (Figure 2.19, Figure 2.22). In particular, Barrier 1 was found to affect mainly the vibration amplitude at lock-in, while Barrier 2 promoted a markedly larger synchronization range, possibly explainable through the impinging shear layer instability above mentioned. The almost identical height of the barriers, which differ in terms of transparency to the flow, highlights the role played by opening amount and distribution, consistently with what reported by Figure 2.24 (Bai et al., 2020). It can be indeed asserted that the distribution of openings may affect the VIV response even more the barrier dimension.

With regards to the flow angle of attack in the range between -3° and +3°, it showed a very remarkable influence on VIV response in presence of both the barriers. In case of bare deck, the effect produced was indeed almost negligible in the above mentioned range and really noticeable only at +5° and +8.5°. With lateral barriers installed, even a relatively limited change of the angle of attack gave rise to strong variations of VIV response,

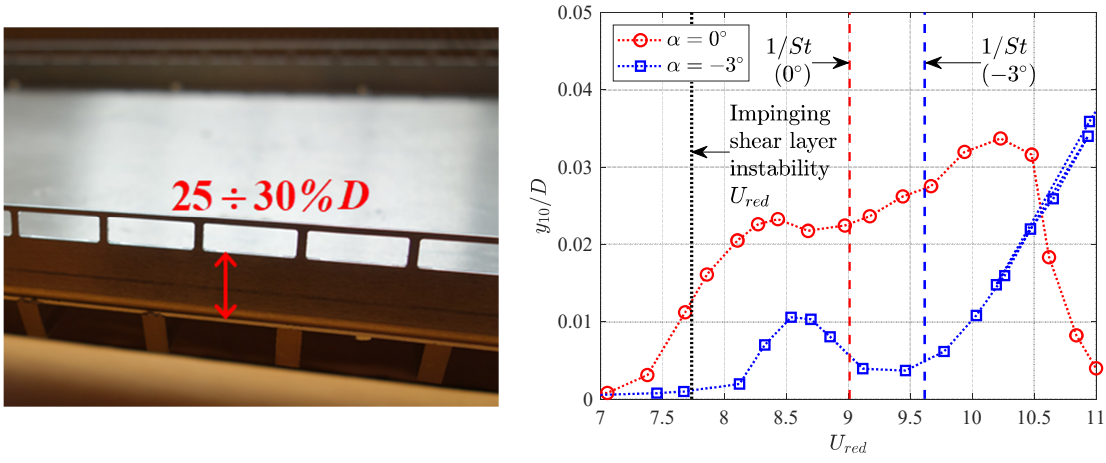

a) b)

Figure 5.13. Picture of Barrier 2 with height of the closed portion indicated (a). Close up of response curves with Barrier 2 at 0° and -3° (b), with significant reduced flow speed values indicated.

especially in terms of maximum vibration amplitude. The dimensionless peak amplitude increased from about 5% to more than 10% with Barrier 1, shifting α from -3° to +3°, but the most valuable effect was observed with Barrier 2. In this case, at -3°, the greatest amplitude all over the experimental campaign was found. The change of the angle of attack value from 0° to -3° produced an almost six-times increasing of the peak response for low *Sc*. This is noticeable, since it occurred for a limited change in flow angle of incidence, quite typical for a bridge deck study. In addition, the transverse force coefficient curve achieved during static tests suggested stability of the cross section to transverse vibration, considering the strongly negative slope of C_{Fy} plot around α = -3° with Barrier 2 installed. For this reason the VIV response observed was really unexpected and, indeed, difficult to explain. It is therefore evident how, during the design phase of a bridge, the selection of angle of attack values to test might be crucial, given the potential extreme sensitivity to the direction of the incoming flow combined with details like barriers.

Proceeding with the discussion about response curves and flow angle of incidence, some observations about the bare deck at +5° and +8.5° are presented. It is interesting to remark that these typologies of curve are available in scientific literature for rectangular cross sections: in fact, +5° and +8.5° response curves recall, respectively, the ones found for a 4:1 (Marra et al., 2015) and 3:2 (Mannini et al., 2018) rectangular cylinders. In Figure 5.14, the curves found for bare deck at +5° and +8.5° are compared to the ones coming from the mentioned rectangular cylinders. As observable, the reduced flow speed and the response amplitude were divided, respectively, by the vortex-resonance speed and the peak response, thereby making the results better comparable. The most remarkable notice concerns α = +8.5°: in this case, according to the quasi-steady assumption, galloping instability was expected. The same consideration can be done also with Barrier 2 installed at α = +3°. In both cases the slope of the C_{Fy} curve is markedly positive for a considerable range around the mean flow angle of attack set, as shown in Figure 5.15. The quasi-steady theory, however, did not work for any of them, since no galloping was observed. Further considerations about these cases are included in free-decay test discussion.

Similarly to what asserted in the discussion about lateral barrier effects, the influence of the flow angle of attack observed in the present study finds confirmation in previous scientific works. The examples reported in Section 2.3 by Figure 2.19 (Honda et al., 1992) and Figure 2.23 (Chen et al., 2017) are particularly meaningful in terms of effects on lock-in generation produced by relatively limited angle of attack variation. In the present work,

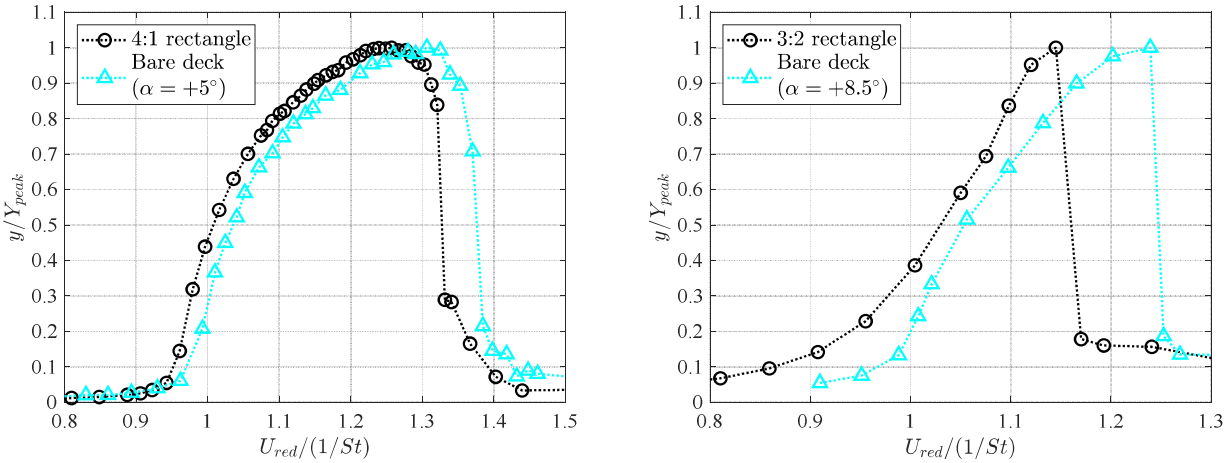

Figure 5.14. Bare deck response curve at +5° (a) and +8.5° (b) compared, respectively, with the ones obtained for 4:1 (Marra et al., 2015) and 3:2 (Mannini et al., 2018) rectangular cylinders.

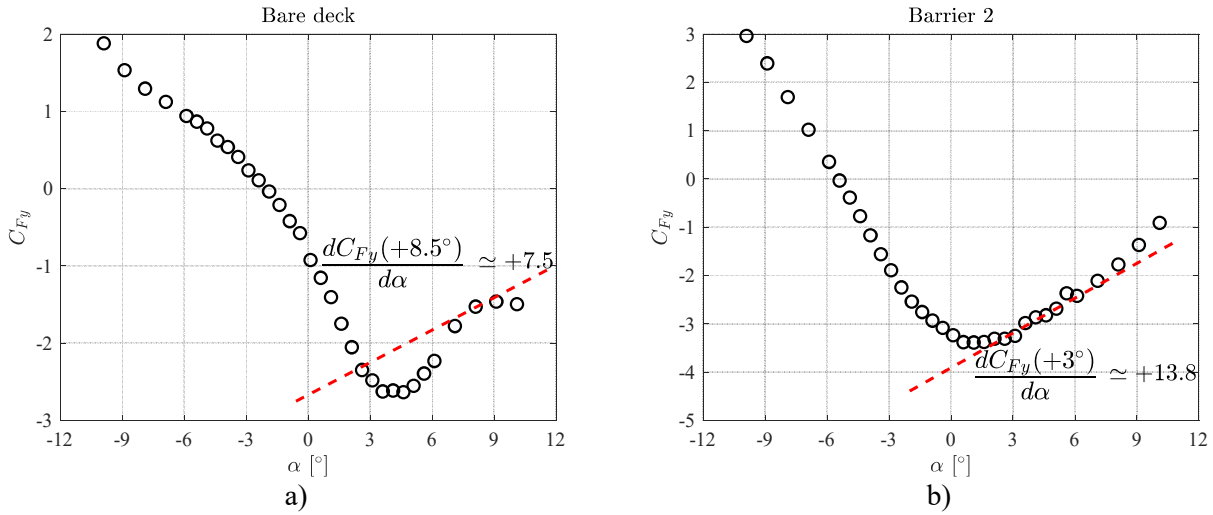

Figure 5.15. Transverse force coefficient curves for bare deck (a) and Barrier 2 (b). C_{Fy} slope was indicated for α = +8.5° and α = +3°, for which galloping was predicted by quasi-steady theory.

this was observed in case of bare deck and even more in presence of barriers, whose contribution may certainly enhance effects promoted by angle of attack variation (Figure 2.24; Bai et al., 2020).

To conclude the response curve analysis, some considerations about the maximum transverse displacements are reported, since the peak vibration amplitude Y_{peak} is probably the most decisive result for bridge deck design and construction. As reported above, a wide range of peak response values was found all over the experimental campaign. It is worth to compare the results obtained from dynamic tests to the qualitative suppositions about the proneness to vortex-induced oscillation based on static measurements. In Chapter 4, some of the configurations were supposed to be particularly prone to transverse oscillation, based on the slope of the C_{Fy} curve ($dC_{Fy}/d\alpha$), the Strouhal number and the C_{L0} value. Considering these aerodynamic parameters, the following assumptions were made:

- The sectional model with barriers installed was expected to be much more prone to VIV than without;
- The most sensitive configurations were supposed to be the ones at +3° with Barrier 1 and Barrier 2;
- With Barrier 1, VIV response increasing with angle of attack growing from -3° to +3° was suggested; instead, with Barrier 2 a clear predominance in terms of potential sensitivity to VIV was not found between 0° and -3°;
- All the geometric layouts at -3° were expected to be considerably stable from the point of view of transverse vibration.

The above listed assumptions found a partial positive qualitative feedback in dynamic tests. In particular, the comparison between bare deck and deck with barriers was very well confirmed. On the other hand, the other suppositions were found to be in quite good agreement with dynamic tests from a qualitative point of view, except for the high response amplitude branch observed with Barrier 2 at -3°. As a matter of fact, this result was neither predicted nor suggested by static test results. To be exact, the only suggestion coming from the static tests about a possible high VIV sensitivity was represented by the lowest and the highest value found, respectively, for St and C_{L0} among all configurations. Nevertheless, the extremely great negative slope of the C_{Fy} did not lead to expect a strong VIV response. Consequently, the assumptions based on force measurements were

contradicted by this specific case. The physical mechanism leading to the high response branch is actually unknown.

5.6.2. Free-decay tests

Further comments arise from the results of the free-decay tests. As previously explained, they were performed with the purpose of estimating the aerodynamic damping for several reduced wind velocities, especially around vortex-resonance flow speed. Measurements were compared to the quasi-steady prediction of the aerodynamic damping (Figure 5.10 and Figure 5.11) and, in this context, the results were qualitatively classified in macro-categories as below:

Geometric layout	Angle of attack [deg]	$dC_{Fy}/d\alpha$		C_{Fy} curve linearity	ζ_{aero} vs ζ_{aero}^{QS}
		Low Re	High Re		
Bare deck	0	-29.2	-32.6	High	B
	-3	-15.9	-20.3	High	A
	+3	-18.9	-7.1	Low	B
	+8.5	+7.5	+15.4	Medium	C
Barrier 1	0	-25.8	-18.4	Medium	A
	-3	-28.2	-26.2	High	A
	+3	-4.2	+5.2	Low	C
Barrier 2	0	-15.3	+2.5	Low	B
	-3	-40.7	-27.7	Medium	A
	+3	+13.8	+18.3	Low	C

In particular, three levels of C_{Fy} curve linearity were proposed. A high C_{Fy} linearity was observed when the curve shows a marked linear trend both before and after the mean angle of attack set, while the medium one refers to cases exhibiting a weaker linear shape. Finally, the low linearity level indicates situations of closeness to the minimum peak of the C_{Fy} or of considerable change of its slope in a limited range of angles. From the point of view of comparison between results and quasi-steady prediction, another rating system was defined. Configurations showing good or quite good agreement between the values were classified with the letter A. Letter B indicates cases that exhibited a clear difference between experimental and predicted results, but with a similar increasing or decreasing

trend and with the same sign. The level C refers to situations providing results in clear contrast to each other, with opposite sign and/or totally different trend.

It was observed a relationship between transverse force coefficient curve and closeness of quasi-steady prediction to experimental results. Globally, configurations corresponding to a negative slope ($dC_{Fy}/d\alpha < 0$) and a quasi-linear or smooth trend of the C_{Fy} curve provided the best results. On the other hand, configurations corresponding to positive C_{Fy} slope or in close proximity to the minimum peak of the transverse force coefficient, where its slope changes considerably in a limited range of angle variation, provided lower or bad agreement between the compared values. In particular, bare deck for α = +8.5° and Barrier 2 for α = +3°, characterized by markedly negative quasi-steady aerodynamic damping, provided experimental results in clear contrast to the predicted values. In both these cases, the measured aerodynamic damping ranged from about zero to strongly positive values, also explaining why galloping was not found. Figure 5.10(d) highlights the upper bound of the wide lock-in range at +8.5°, after which the measured aerodynamic damping increased very quickly.

An additional remark about ζ_{aero} estimation through decay tests can be done. The difference between the total and the mechanical damping ratio provides an aerodynamic damping that includes all the possible contributions coming from the interaction between the flow and the body. In particular, both a quasi-steady contribution and a possible unsteady effect due to the oscillating wake are included, which are impossible to separate. The second one could be substantial and able to influence the decay of the system strongly. This hypothesis could explain the total failure of quasi-steady prediction, at high U_{red} too, in some of the cases studied. It is only a supposition, but the configurations expected to be prone to galloping could be characterized by a large wake able to stabilize the system against transverse oscillation in some cases.

5.6.3. Concluding remarks

The response curves suggested an extreme variability of aeroelastic behavior, obtained by starting from the same cross section and installing different lateral barriers. The angle of attack variation was also found to play a critical role, with effects comparable to those produced by a geometric modification of the cross section, especially when the angle of attack variation is combined with the effect of geometric details like barriers.

Speculations reported in Section 4.5.2 about proneness to VIV were qualitatively confirmed by a significant part of dynamic tests. Nevertheless, the most violent VIV event remained totally unpredicted and unexpected (Barrier 2 at α = -3°)

The free-decay tests suggested a relatively good capability of the quasi-steady theory to estimate, even approximately, the cross-section aerodynamic damping in case of negative slope and quasi-linear trend of C_{Fy} curve. It is interesting to notice that in case of satisfactory match between quasi-steady prediction and measurements at high U_{red}, the same result was found, quite surprisingly, for low U_{red} too, close to the vortex-resonance flow speed. In some cases, the quasi-steady approach provided even better results, in terms of aerodynamic damping estimation, for low reduced velocities than for higher U_{red} values.

On this basis, the interest in the assessment of mathematical approaches for VIV modeling including a quasi-steady dissipative contribution, like Tamura-type wake oscillator model and modified harmonic model introduced in Chapter 2, is promoted. It is also clear that the quasi-steady assumption is expected to fail in some cases, especially when strong unsteady effects occur.

6. Mathematical modeling

6.1. Introduction

Mathematical modeling of VIV response, especially with regard to bridge decks, is still an open and challenging issue. As described in Chapter 2, scientific literature provides several approaches to determine the VIV response for elongated oscillating cylinders with different cross-section geometries.

With regards to bridge design, the aeroelastic behavior in case of vortex-induced oscillations cannot actually be predicted or even guessed without an experimental campaign including accurate dynamic tests, as said in Chapter 5. The amount in terms of money and time of wind tunnel measurements is usually considerable and, even if the experimental investigation could be irreplaceable, a reduction of the quantity and/or of the complexity of the required tests would be certainly attractive. So, the development of a mathematical method to predict as well and easily as possible a bridge deck VIV response, even approximately, is certainly interesting from both a scientific and a practical point of view, especially for the preliminary design phase of the structure.

Regardless of the mathematical model typology, a certain amount of parameters has usually to be determined through wind tunnel tests, which can be generally grouped in three main categories:

- Static force and/or pressure measurements;
- Dynamic free-vibration test;
- Dynamic forced-vibration tests.

The level of difficulty in calibrating the model is important almost as much as the accuracy of the mathematical approach. Static tests are generally easier to perform than dynamic ones. On the other hand, dynamic forced-vibration measurements require an appropriate and particularly articulate setup, usually hardly available compared to a free-vibration system.

Finally, the efficiency of a certain mathematical approach is also affected by its performances in terms of prediction at different Scruton number values. As a matter of fact, *Sc* is considerably difficult to estimate for a bridge deck, because of the large amount of uncertainties about the mechanical damping ratio of the structure. This is indeed the reason why it is usually necessary to investigate an extended range of *Sc* values during

wind tunnel experiments for the bridge preliminary design. Consequently, approaches based on parameters strongly depending on *Sc* may be not particularly efficient for bridges, while a satisfying VIV response prediction for a wide *Sc* range with the same set of parameters would be more attractive. This should be indeed considered as another important feature to evaluate for a mathematical approach for bridge decks.

In the present work, two different approaches, introduced in Chapter 2, were studied carefully and applied. Firstly, a Tamura-type wake oscillator model was considered, in the formulation proposed by Mannini et al. (2018), as reported in Section 2.4.3. This kind of approach provided promising results for cylinders with different cross section (circular, square, rectangular with 3:2 side ratio), from both a qualitative and a quantitative point of view. In addition, model equations of motion and parameters are defined on the basis of clear physical assumptions. Finally, a considerable part of the required parameters are achievable from relatively simple static wind tunnel tests. For all these reasons, this model was rated worthy of a deep investigation and assessment also for bridge decks.

On the other hand, a modified harmonic model (Section 2.4.4) was also studied. The interest in this kind of approach came from its simplicity, in terms of output calculation and estimation of model parameters, potentially attractive for an approximate evaluation of the maximum VIV response amplitude during the bridge deck preliminary design phase. This model provided interesting results for rectangular cross sections (Marra et al., 2017; Mannini et al., 2018) and, as introduced in Section 2.4.4, an apparent relationship between such modified harmonic model and Tamura's model was noticed and discussed

In this chapter, both Tamura-type wake oscillator model and modified harmonic model are applied to a 4:1 rectangular cylinder and to the bridge deck cross section for all its geometric configurations. With regards to the former, the version proposed by Mannini et al. in 2018 was considered and some physical suppositions were formulated about the adaptation of the model to elongated cross sections, like bridge deck ones. The results of numerical experiments are compared to each other and to wind tunnel test results. The models are analyzed and discussed, and their main qualities and limitations are described.

6.2. Adaptation of the wake-oscillator model to an elongated cross section

Modified Tamura's approach proposed by Mannini et al. (2018) was selected to perform numerical experiments on the investigated bridge deck cross section, for each geometric configuration, and on a 4:1 rectangular cylinder. Compared to the 3:2 rectangle

discussed by Mannini et al. in 2018, such rectangular section was considered as a meaningful simplified geometry, characterized by a side ratio between along-wind and cross-flow dimensions closer to the one of bridge deck sections in general and, in particular, to the one of the bridge section studied in the present work.

To this purpose, firstly, static wind tunnel force measurements were performed on a sectional model with a 4:1 rectangular cross section to evaluate model parameters. Tests were carried out through the same static setup described in Chapter 3 and used for the bridge deck sectional model. The rectangular cylinder model tested is made of wood, and it is 986 mm long (L), 300 mm wide (B) and 75 mm deep (D). This sectional model is the same used by Marra et al. (2015) to perform aeroelastic tests, whose results are here considered to compare mathematical prediction to wind tunnel experiments.

Mean aerodynamic force coefficients for drag (C_D) and lift (C_L) were estimated for different angle of attack values, to achieve $C_{Fy}(\alpha)$ (Eq. (2.35)), and the power spectral density of the lift force time history was analyzed to evaluate St and C_{L0}. In Figure 6.1, C_{Fy} curve and a lift force spectrum are shown. As reported in the figure, the slope of the C_{Fy} at zero angle of attack is $dC_{Fy}/d\alpha$ = -25.6, a markedly negative slope suggesting a certain level of stability against transverse vibration. The Strouhal number and the C_{L0} were found to be, respectively, 0.131 and 0.63. These results relate to a Reynolds number value ($Re \simeq$ 27000) close to the one corresponding to the dynamic test results on the 4:1 rectangular cylinder by Marra et al. (2015).

The wake oscillator model was applied to the 4:1 rectangular cross section, by solving numerically Eqs. (2.33) and (2.34) by means of the ODE45 Matlab® function. The

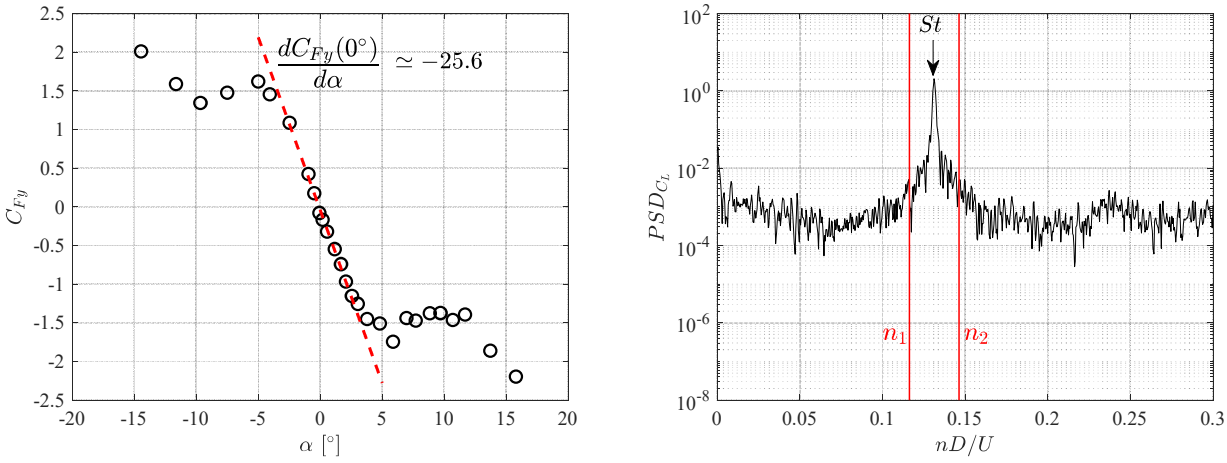

Figure 6.1. Transverse force coefficient curve (a) and power spectral density of the lift force (b) of 4:1 rectangular cylinder (Re ≃ 27000).

parameters C_{Fy}, St and C_{L0} were estimated through static wind tunnel tests, as said above, while the values for f, β and λ were determined to match as well as possible the experimental response curve achieved by Marra et al. (2015). In particular, the experimental curve selected to set the mentioned parameters is the one obtained for the lowest Scruton number of the oscillating system in wind tunnel.

The following values provided a quite satisfying match with the experimental response curve in terms of onset wind speed, lock-in range and curve shape:

- $f = 7.2$;
- $\beta = 0.58$;
- $\lambda = 1.16$.

and the comparison between the curves obtained from wake oscillator model and from experiments, at the lowest Scruton number, is reported in Figure 6.2(a). As observable, the only feature of the experimental curve totally not matched is the dimensionless peak response amplitude Y_{peak}, that was found to be much lower for the mathematical model. Figure 6.2(b) shows the Griffin plot comparison for several Scruton numbers: the peak response gap is clear, especially at low Sc. Nevertheless, the difference between numerical and experimental results decreases with the growth of Sc.

Two main observations about the model parameters have to be remarked:

- The set of values for f, β and λ previously reported is not achievable by assuming the expressions for model parameters defined by Eqs. (2.38), (2.39) and (2.40),

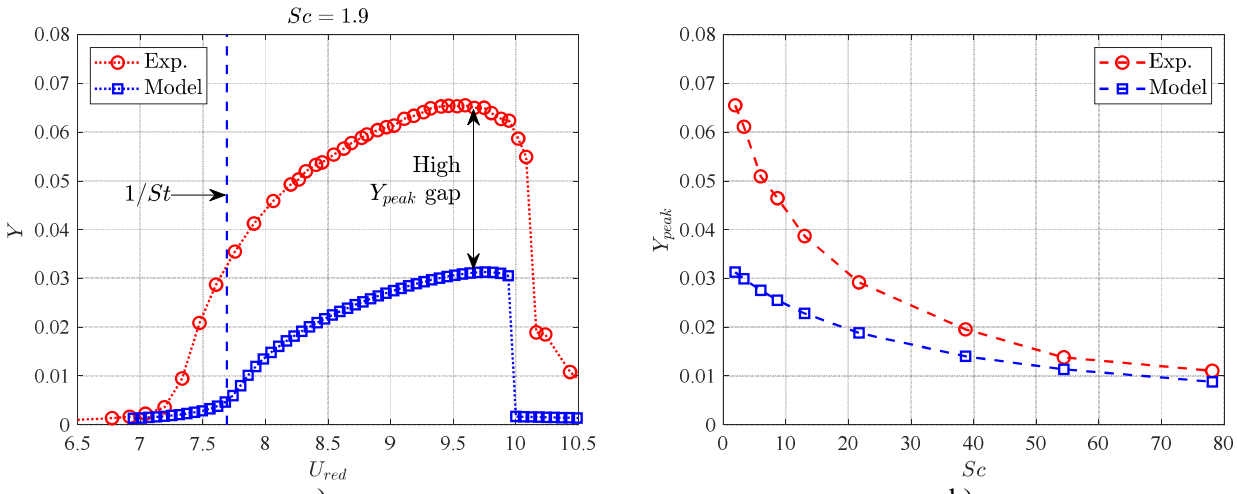

a) b)

Figure 6.2. Comparison between response curves at lowest Sc (a) and Griffin plots (b) obtained from wake oscillator model and from experiments for 4:1 rectangle at zero angle of attack.

adopted by Mannini et al. (2018) for the 3:2 rectangle;

- According to Eqs. (2.38), (2.39) and (2.40), $f = 7.2$ and $\beta = 0.58$ lead to a width and a half-length of the wake lamina equal respectively to $h^* = 2.61$ and $l^* = 0.89$, while $\lambda = 1.16$ leads to $h^* = 2.69$ and $l^* = 0.86$. These two couples of values for h^* and l^* are not realistic if compared to flow visualizations available in the scientific literature, especially concerning the dimension h^*;

The expressions proposed by Mannini et al. (2018) for the model parameters in case of a 3:2 rectangular cylinder are reasonably unsuitable when employed in case of a markedly different cross section like a 4:1 rectangle. The same problem was observed when several first attempts were performed to reproduce experimental response curves for the bridge deck section. This led to consider that a partially different structure of the oscillating wake lamina should be considered for the 4:1 rectangle and for the bridge deck section. Indeed, a 4:1 rectangle is considerably more elongated than a 3:2, a square or a circular cross section, with a remarkable afterbody and differences in the flow separation. The same consideration can be done for the bridge section, which is characterized by a side ratio of about 4.6 for the bare deck configuration.

For this reason, some speculations about possible modifications introduced in the wake oscillator structure were formulated, with the purpose of achieving the searched features of the response curves along with more reasonable dimensions of the wake lamina, without losing completely a physical description for model parameters. Some modifications to the wake oscillator geometry were indeed hypothesized and new expressions for the parameters consequently achieved.

With reference to the modified version of Tamura's model (Eqs. (2.33) and (2.34)) proposed by Mannini et al. in (2018), the values of l^*, h^*, f, β and λ are mutually connected and the expressions defining their relationship depend on the wake oscillator structure. As observable from Eqs. (2.25), (2.30) and (2.32) for original Tamura and Matsui's formulation, such expressions are function of the inertia I and of the restoring moment per unit rotation K, whose definition depends on the size of the equivalent lamina and the location of the pivot point O and of the restoring force F_L.

The equivalent wake lamina aims to reproduce approximately the dynamic behavior of the dead-air region behind the body and, consequently, its structure is necessarily influenced by the flow pattern around the body. This supports the supposition that bodies which differ markedly in terms of side ratio might require different structures for the wake

oscillator. In Figure 6.3, a comparison between flow visualizations provided by Shimada and Ishihara (2002) for a 3:2 and a 4:1 stationary rectangular cylinder is reported to highlight the differences in the flow pattern.

For a very bluff and sharp-edged cross section (Figure 6.3(a)), a large separation of the flow is observable, with the wake oscillator pivot point reasonably coinciding with the upstream end of the lamina and located inside the oscillating body, as assumed by Mannini et al. (2018) for the 3:2 rectangular cylinder. On the other hand, in case of a relatively elongated body like a 4:1 rectangular cylinder (Figure 6.3(b)), it could be reasonable to suppose a wake lamina composed by two different portions: the first one partially superposed to the oscillating body and the second one located downstream and farther away from the cylinder. The two parts of the wake lamina could be reasonably assumed to rotate differently from each other, with the downstream portion of the wake lamina free to oscillate with respect to the upstream part.

This supposition about the fluid lamina structure would lead to add a degree of freedom to the wake oscillator, which would be certainly more complicated to model, with the two parts pivoting around O_1 and O_2 as shown in the qualitative scheme in Figure 6.4(a). With the purpose of maintaining a simpler one-degree-of-freedom rotating wake coupled with the vibrating cylinder, and hence a two-degree-of-freedom wake oscillator

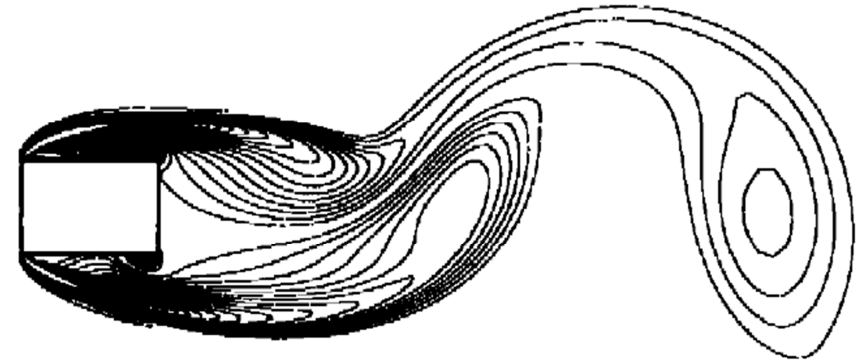

a)

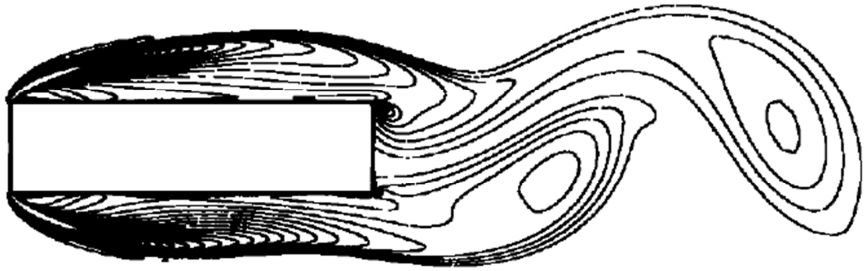

b)

Figure 6.3. Flow visualizations (Shimada and Ishihara, 2002) for 3:2 (a) and 4:1 (b) rectangular cylinders.

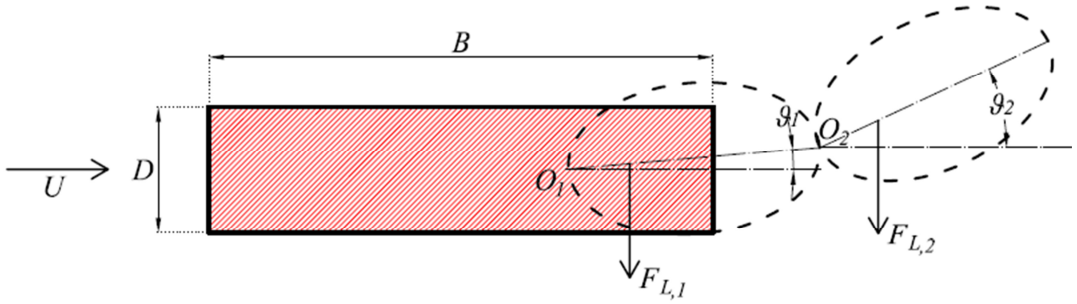

a)

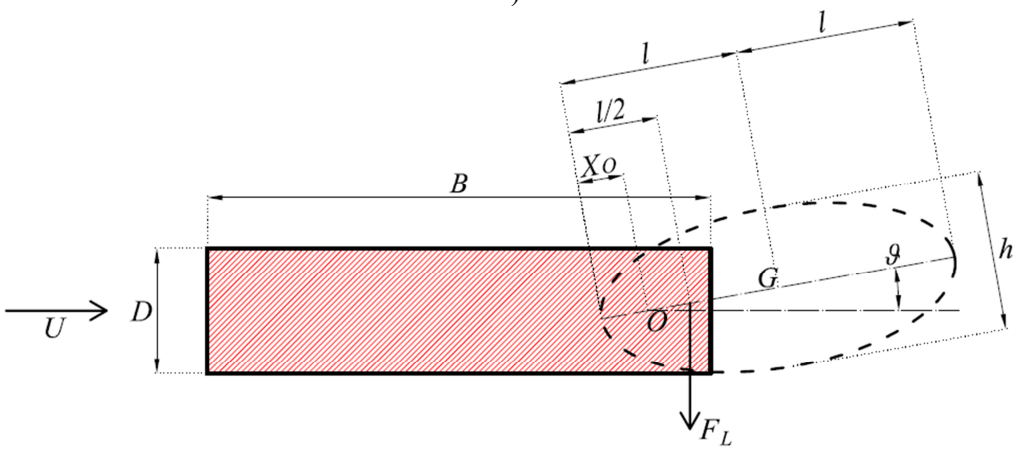

b)

Figure 6.4. Qualitative outline of a three-degree-of-freedom model with a two-degree-of-freedom wake lamina (a). Two-degree-of-freedom wake oscillator model with pivot point O moved inside the fluid lamina (b).

model, it was assumed a unique fluid lamina (Figure 6.4(b)) pivoting around a point placed internally to the lamina itself, in an intermediate position between O_1 and O_2.

Two new quantities were finally introduced, with reference to the outline in Figure 6.4(b):

- X_O is the distance of the pivot point O from the upstream end of the equivalent wake lamina;
- α_I is a global reducing factor applied to the rotational inertia I of the oscillating lamina.

Similarly to what done for the wake lamina dimensions, $l^* = l/D$ and $h^* = h/D$, a normalized expressions of X_O was introduced: $X_O^* = X_O/D$. The inertia reducing factor ($\alpha_I \leq 1$) was introduced to consider the likely substantial portion of afterbody occupying the upstream part of the wake oscillator region and to take into account that the downstream part is free to oscillate with respect to the first one. Finally, the value of the restoring force

F_L was not modified (Eq. (2.22)) as well as the position of the force, applied at one fourth of the lamina length (Figure 6.4(b)).

The introduction of this new wake-oscillator geometry, with, X_O and α_I, dose not modify the model equations of motion (Eqs. (2.33) and (2.34)) or the physical assumptions which the parameters are based on, but leads to new mathematical expressions connecting l^*, h^*, f, β and λ, according to the description of the model in Section 2.4.3. The expressions of the inertia I and of the restoring moment per unit rotation K of the lamina (Eqs. (2.36) and (2.37)) are modified as follows:

$$I = \left[2\rho hl\left(l - X_O\right)^2 + \frac{2\rho hl}{12}\left(4l^2 + h^2\right) \right] \alpha_I \tag{6.1}$$

$$K = 2\pi\rho V^2 l\left(l - X_O\right) \tag{6.2}$$

where I is calculated including the contribution of the polar inertia with respect to G. Such a contribution is neglected in Tamura's model formulation, while in this case it is considered because of the shift of O towards the center of the wake lamina. Consequently, the expressions reported by Eqs (2.38), (2.39) and (2.40) change and new expressions are obtained:

$$St^2 = \frac{3\left(l^*/2 - X_O^*\right)}{\pi h^* \alpha_I \left[12\left(l^* - X_O^*\right)^2 + 4l^{*2} + h^{*2} \right]} \tag{6.3}$$

$$\beta = \frac{f\left(l^* - X_O^*\right)}{2\sqrt{2}\pi^2 l^*\left(l^*/2 - X_O^*\right)} \tag{6.4}$$

$$\lambda = \frac{12\left(l^* - X_O^*\right)}{\alpha_I \left[12\left(l^* - X_O^*\right)^2 + 4l^{*2} + h^{*2} \right]} \tag{6.5}$$

Eqs. (6.3), (6.4) and (6.5) were employed to obtain the searched values f = 9, β = 0.34 and λ = 1.39, which provided the best match with the experimental lock-in curve. The above mentioned values of f, β and λ were achieved by assuming the following values for the wake lamina geometry:

- l^* = 0.95;
- h^* = 0.85;
- X_O^* = 0.35;

- $\alpha_I = 0.60$.

The connection between h^* and l^* is provided by Eq (2.38) according to the work of Mannini et al. (2018) and by Eq (6.3) for the wake oscillator geometry here proposed. In particular, the value obtained for the half-length l^* assuming the wake oscillator structure reported by Figure 6.4 is probably more reasonable compared to the ones previously mentioned. Finally, it is worth to remark that X_O^* and α_I could be theoretically estimated through flow visualizations, although with a certain difficulty.

In the following of the work, numerical experiments were performed on the bridge deck cross-sections for all the configurations tested. The procedure is the same followed for the 4:1 rectangle: C_{Fy}, St and C_{L0} were determined from static test results, while f, β and λ were estimated starting from the experimental response curve at the lowest Sc tested, in absence of flow visualizations. As for the 4:1 rectangular cylinder, the values of the parameters f, β and λ leading to matching the experimental curve, in most of cases, were difficultly achievable from the model configuration adopted by Mannini et al. (2018) for the 3:2 rectangular cylinder. The introduction of X_O^* and α_I could help to reach the searched values of parameters for the bridge section too.

The speculations formulated about the geometry of the equivalent wake lamina (Figure 6.4(b)) do not solve the problem of adapting the model to elongated cross sections. Nevertheless, a further study about the introduction of an additional degree of freedom to the wake oscillator (Figure 6.4(a)) is encouraged by the discussion reported in the present section.

6.3. Sensitivity analysis

The evaluation of the wake oscillator model parameters requires flow visualizations along with force/pressure measurements on the stationary wind tunnel model. In the present work only static force measurements were performed and the values of parameters had to be supposed or at most set by matching an experimental response curve achieved through aeroelastic wind tunnel tests.

At any rate, knowing the sensitivity of results to the variation of model parameters could be useful, especially when their estimation is uncertain and/or incomplete. St and C_{Fy} are probably the simplest parameters to evaluate. Relatively simple wind tunnel force measurements are usually sufficient for their estimation, especially in case of smooth flow

condition. The only remarkable observation has to be done about the effects of Reynolds number (*Re*) variation. For the sections studied in the present work, a 4:1 rectangular cylinder and different configurations of a bridge deck section, *St* was found not to be markedly affected by *Re*. On the other hand, the modification of C_{Fy} curve and its slope at a certain value of the wind angle of attack for different *Re* values were found to be not negligible. For this reason, the C_{Fy} curve included in the Tamura-type model should be achieved for *Re* as close as possible to the one at which aeroelastic tests have been performed. As a matter of fact, the suppositions about VIV response based on static test results were formulated by considering C_{Fy} curve corresponding to the lowest wind velocity tested, that is the closest value to the one corresponding to dynamic test results. As an example, Figure 6.5 shows the response curves predicted by the model, for the 4:1 rectangular cylinder, at the lowest Scruton number tested (Sc = 1.9) by including C_{Fy} evaluated for different *Re* values (Figure 6.5(a)). The importance of considering the transverse force coefficient measured at the appropriate Reynolds number is emphasized by Figure 6.5(b).

The coupling term between the wake oscillator motion and the acceleration of the mechanical oscillator, depending on the parameter λ, was found to influence considerably both the shape and the peak value of the response curve. A higher value of λ seems to cause a slightly lower onset wind velocity and a greater slope of the increasing branch at lock-in, with a rounder and more symmetric shape of the whole lock-in curve, along with a higher value of the peak response amplitude. On the other hand, a lower λ was found to give rise to a more asymmetric triangle-shaped curve and a lower peak amplitude. Effects

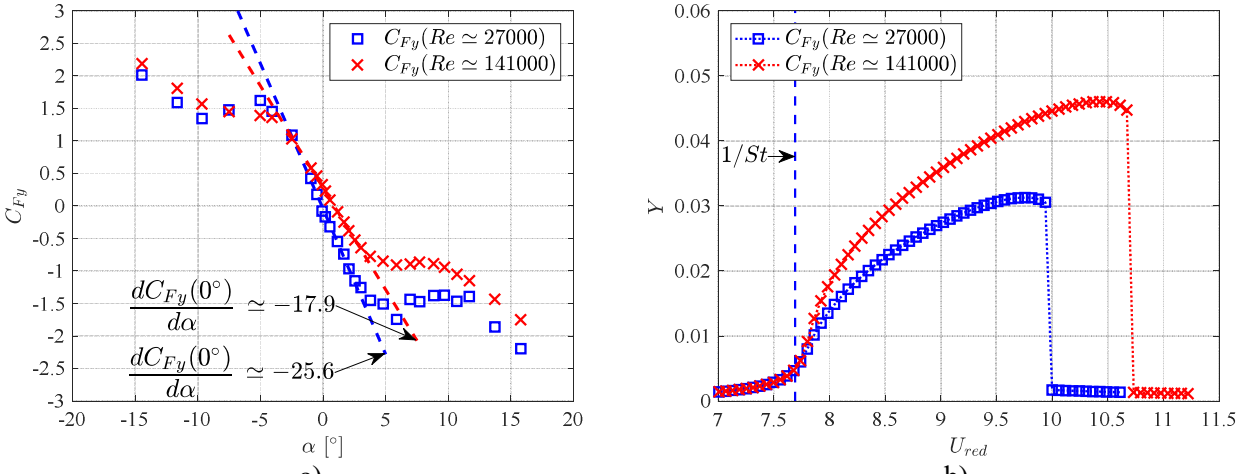

Figure 6.5. C_{Fy} achieved at different *Re* values (a) and corresponding response curves (b). Both figures refer to 4:1 rectangular cylinder.

of λ value on predicted peak vibration amplitude and response curve shape are observable in Figure 6.6 and Figure 6.9.

The peak response amplitude was also observed to be strongly affected by C_{L0}. The greater it is, the higher is the peak response, while the synchronization range is not affected by such parameter. As a consequence, an increase of C_{L0} leads to a higher slope of the lock-in increasing branch, since a higher peak response amplitude is reached over the same range of wind velocity.

The results of a sensitivity study about the influence of C_{L0} and λ on the peak amplitude are shown in Figure 6.6, where both axis report normalized values. The horizontal axis indicates the ratio between several values assumed for the two parameters ($C_{L0,i}$ and λ_i) and their reference values, that are the ones reported in Section 6.2 (C_{L0} = 0.63 and λ = 1.16) for the 4:1 rectangular cylinder. Similarly, the vertical axis reports the ratios between the peak amplitudes obtained with the different values of parameters ($Y_{peak,i}$) and the reference value. Both parameters seem to affect almost linearly the peak oscillation of the system, even if with different slope. It is worth to note that the contribution of C_{L0} to the variation of Y_{peak} is much more influent compared to λ. It is noteworthy, since C_{L0} can be directly measured through wind tunnel tests, even if with some difficulties, while λ depends on the physical model assumed for the equivalent wake lamina, generally more uncertain and difficult to be correctly defined.

The parameter β can be seen as negative linear damping ratio of the fluid oscillator, but it also affects the amount of non-linearity in the wake oscillator equation, acting on the non-linear part of the damping term. The greater is β, the higher is the amount of

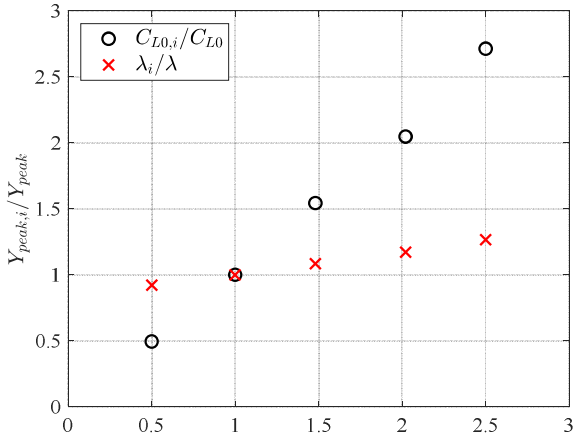

Figure 6.6. Sensitivity study for C_{L0} and λ in terms of influence on peak response amplitude Y_{peak}. Different values of C_{L0} and λ are divided, respectively, by the reference values C_{L0} = 0.63 and λ = 1.16.

nonlinearity in Eq. (2.34). Once the geometry of the equivalent wake lamina is fixed, β depends on the parameter f (Eqs. (2.39) and (6.4)), so that the damping in the wake oscillator equation is actually determined by the value of f, whose role was observed carefully.

From the point of view of the response curve shape, the parameter f was found to play a key role in terms of lock-in range extension: for increasing value of f, the lock-in range extension enlarged progressively. On the other hand, the peak amplitude reached by the response curve seems not to be influenced by f, as shown by Figure 6.7, where response curves obtained for different values of f are reported for the 4:1 rectangular cylinder. It is worth to mention that very similar results in terms of f influence on the peak amplitude were achieved for bridge deck cross section with both barriers installed (Figure 6.12(a, b)). In addition, such results confirm what reported by Mannini et al. in 2018 for the 3:2 rectangular cylinder. The almost complete absence of effects caused by f on the peak response is indeed observed for two different rectangular cross-sections and for more complicated bridge deck geometries.

6.4. Response branches for different initial conditions

Solving model equations was observed to provide different solutions for different initial conditions for the body displacement (Y_0) in a certain range of interest of mechanical oscillator vibration amplitude. In particular, assuming a certain value for the initial transverse displacement may lead to predict response hysteresis branches nonexistent or

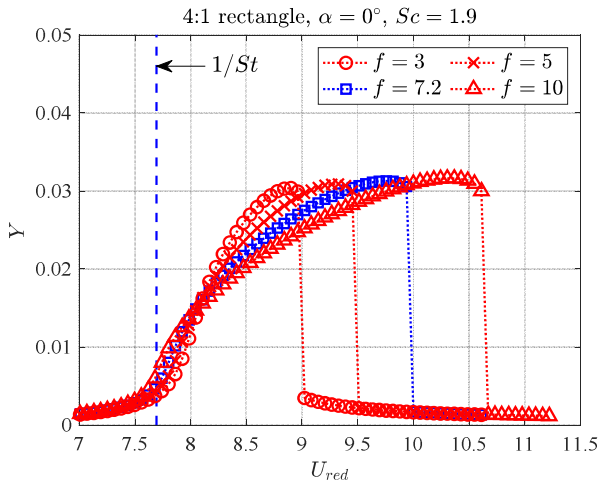

Figure 6.7. Response curves obtained for different f values at zero angle of attack and lowest Sc, for the 4:1 rectangular cylinder.

difficult to observe during wind tunnel tests.

The largest values of Y_0 considered were those corresponding to an apparent angle of attack of about α = 10°, consistent with the results achieved from force measurements for C_{Fy}, since no data are available for larger flow incidences. To this purpose, by approximating the motion of the body as a harmonic process, the initial dimensionless displacement Y_0 is determined in the following way:

$$Y_0 = \frac{\tan(\alpha) \cdot U_{red}}{2\pi} \tag{6.6}$$

As an example, Figure 6.8 reports the response curves obtained for the 4:1 rectangular cylinder at the lowest *Sc* tested, with an initial transverse displacement of about 15% of the section cross-flow dimension *D* and with a very low initial displacement. A marked hysteresis loop can be observed.

6.5. Connection between wake-oscillator model and modified harmonic model

A mathematical connection between the wake oscillator model formulation and the modified harmonic model was introduced in Section 2.4.4. The relationship between the two approaches was explored in light of the results of numerical experiments for the 4:1 rectangular cylinder and for the bridge deck cross section, in terms of peak oscillation amplitude prediction. Such a quantity (Y_{peak}) is indeed the only output of the modified

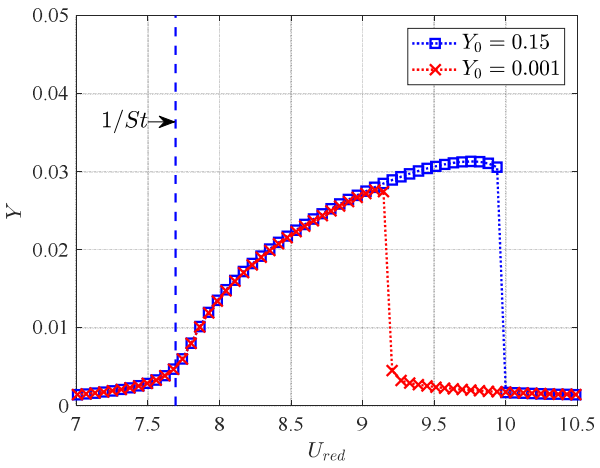

Figure 6.8. Comparison between curves obtained with different initial conditions for the dimensionless transverse displacement, for the 4:1 rectangular cylinder at *Sc* = 1.9. The other initial conditions, for *Y'*, ϑ and ϑ', are equal to zero.

harmonic model and, consequently, the only result appropriate for a comparison between the two models.

The mechanical oscillator equations of the two models were compared to each other in Section 2.4.4 and two very similar formulations were obtained after some simplifications and approximations (Eqs (2.46) and (2.47)). In particular, it was observed that such formulations are actually equivalent except for the presence of $-f$ in the damping term in Eq. (2.46). Nevertheless, the sensitivity analysis reported in Section 6.3 pointed out how the value of f is almost irrelevant in terms of peak oscillation amplitude predicted by the wake oscillator model. This is apparently in contrast with the damping term expression in Eq. (2.46), which would suggest that f is expected not to influence the peak response only when its value is reasonably negligible compared to $dC_{Fy}/d\alpha$. In case of both 4:1 rectangle and investigated bridge deck section this condition is not observed. So, the negligible influence of the parameter f on Y_{peak} value for the wake-oscillator model was systematically observed from numerical experiments, but it is not explained by the mathematical simplifications reported in Section 2.4.4 and leading to Eq. (2.46).

On the other hand, in a Tamura-type approach, the motion of the vibrating body interacts with the wake oscillator through the coupling terms depending on the acceleration (Y'') and on the velocity (Y') of the body. Such terms were considered from the point of view of their effect on the peak response amplitude and it was found that the acceleration coupling $\lambda Y''$ in Eq. (2.34) has a non-negligible effect on Y_{peak}. In particular, the greater is the parameter λ, the greater is the peak response amplitude (Figure 6.6), as described in Section 6.3. Performing numerical experiments with a progressive reduction of λ led to a decrease of the lock-in extension and of the peak response amplitude. It was observed that the value of Y_{peak} obtained by reducing λ value down to $\lambda = 0$ is close to the one predicted by the modified harmonic model for the 4:1 rectangle (Figure 6.9). The same result was found for the bridge deck cross section for different geometric layouts (Figure 6.12(c, d)). Therefore, a progressive reduction of the Y_{peak} predicted by the wake oscillator model to the value predicted by the modified harmonic model was observed for decreasing values of the parameter λ.

According to the numerical experiments performed, the modified harmonic model appears actually as a very simplified way to evaluate Y_{peak} predicted by a Tamura-type approach, provided that the coefficient of the acceleration coupling term is limited. Moreover, a further consideration can be formulated on the basis of the peak response

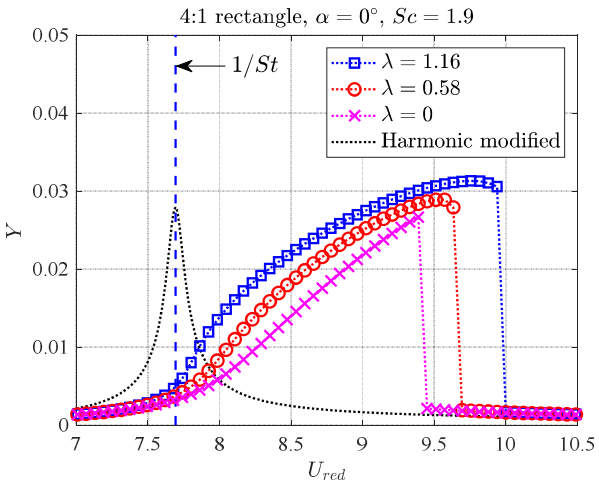

Figure 6.9. Response curves obtained by reducing λ value down to zero at lowest *Sc*, compared with the solution provided by modified harmonic model, for the 4:1 rectangular cylinder.

sensitivity to C_{L0}. The maximum value of the vibration amplitude predicted by the modified harmonic model (Eq. (2.45)) is directly proportional to C_{L0} value. On the other hand, the relationship between Y_{peak} and C_{L0} for the Tamura-type model is almost the same, while the influence of λ is markedly more limited (Figure 6.6). For this reason, the two models predict close results for a large range of acceleration coupling coefficient values, since the most influent parameter in terms of peak amplitude prediction of the models is, by far, C_{L0}. This is particularly meaningful, since the amplitude of the fluctuating lift coefficient is simpler to estimate compared to the acceleration coupling coefficient.

6.6. Spanwise correlation of the vortex-shedding lift force

Knowledge about vortex shedding achievable from scientific literature led to consider the role played by the spanwise correlation length of the fluctuating lift force on an oscillating body. It is known that, with the increase of the oscillation amplitude at lock-in, the spanwise correlation of vortex shedding can increase markedly, becoming much higher than in case of a stationary body. Ruscheweyh (1990) proposed a model based on the correlation length for the estimation of VIV response for slender structures. This approach, whose first presentation was in 1986, considered a linear approximation to evaluate the correlation length over a wide range of non-dimensional oscillation amplitude. The "Approach 1" provided by Eurocode 1 (EN 1991-1-4, 2005) for VIV across-wind amplitude prediction is actually based on Ruscheweyh's model. The potentially important

role played by the vortex-shedding correlation length was taken into account in the present work.

Since the mathematical models under investigation are based on the assumption of a two-dimensional body, the C_{L0} value included in their formulation is a fluctuating dimensionless lift force per unit length. When static measurements were performed, its value was obtained by dividing the one obtained for the whole sectional model by the total length L. This procedure did not take into account the spanwise correlation length of the vortex-shedding lift force along the stationary body, since no pressure measurements were carried out.

According to Holmes (2001), the relationship between the mean-square fluctuating total force on a slender body ($\overline{F'^2}$) and its sectional value ($\overline{f'^2}$) can be considered as function of the force correlation length (L_c). The expression of L_c is defined as follows:

$$L_c = \int_0^{\infty} C_c(z_i - z_j)\, d(z_i - z_j) \tag{6.7}$$

where $z_i - z_j$ is the distance along the longitudinal axis z between two sections of the body, and $C_c(z_i - z_j)$ is the correlation coefficient of the fluctuating sectional forces. C_c is a function of the separation distance ($z_i - z_j$), but not of the individual positions along the body (z_i and z_j). So, the relationship between $\overline{F'^2}$ and $\overline{f'^2}$ is expressed as:

$$\overline{F'^2} = \overline{f'^2} \int_0^L \int_0^L C_c(z_i - z_j)\, dz_i dz_j \tag{6.8}$$

The latter expression can be evaluated in two particular cases:

- Full correlation, with $C_c(z_i - z_j) = 1$ for every separation distance, leading to an infinite value for L_c according to Eq (6.7), while Eq. (6.8) becomes:

$$\overline{F'^2} = \overline{f'^2} L^2 \tag{6.9}$$

- Rapidly decreasing correlation length, with $L_c << L$, leading to the approximate expression:

$$\overline{F'^2} = \overline{f'^2} L \cdot 2L_c \tag{6.10}$$

So, the C_{L0} obtained dividing the total fluctuating force by the length of the body is really close to the sectional C_{L0} only in case of very high correlation. Pressure measurements should be performed to evaluate L_c, both on the stationary body and on the oscillating body. Since generally sectional models used for wind tunnel tests are considerably elongated and the correlation length is at its minimum value for a stationary body, it is reasonable to assume that $L > L_c$ in case of static tests. Consequently, measuring only total load through force balances on a stationary cylinder may lead to assume a C_{L0} value much lower than its sectional value and, above all, to consider a fluctuating lift force considerably lower than the one acting on the vibrating cylinder.

In this part of the work, an approximate supposition about correlation is proposed: in case of limited but non-negligible VIV response amplitudes, for example between about 3% and 10% of D, a marked increase of the correlation length from the stationary to the oscillating cylinder is expected, potentially up to almost full correlation for the largest vibration amplitude observed at lock-in. C_{L0} measured during static tests should be amplified when included in the mathematical models for VIV response prediction, especially at low Sc, where highest oscillation amplitudes are observed. To this purpose, possible spanwise correlation functions were selected from available scientific literature and the hypothesis of full correlation at lock-in was assumed as upper bound condition.

As an example, Ricciardelli and Marra (2008) provided results about pressure spanwise correlation for a stationary 5:1 rectangular cylinder, for two different longitudinal arrays. In particular, the correlation coefficient $C_c(z_i - z_j)$ was approximated for the stationary body with the following decreasing exponential function:

$$C_c = \exp\left[-c\left(\frac{|z_i - z_j|}{D}\right)\right] \tag{6.11}$$

where the decay coefficient c was found to be equal to 0.23 and 0.53 for the two different longitudinal arrays considered, located, respectively, at 0.18 B and 0.82 B downstream the leading edge of the 5:1 rectangular cylinder, where B is the along-wind cross-section dimension. The two values of c correspond, respectively, to the following values of correlation length: $L_{c,1} \simeq 4.4\ D$ and $L_{c,2} \simeq 1.9\ D$.

Assuming the values of c and the expression for C_c above reported, two different values for the non-dimensional amplitude of the sectional lift force, named $C_{L0,sec}$, were calculated, starting from C_{L0} obtained from static tests:

$$C_{L0}{}^2 \cdot L^2 = C_{L0,sec}{}^2 \cdot \int_0^L \int_0^L C_c(z_i - z_j) dz_i dz_j \tag{6.13}$$

$$C_{L0,sec} = C_{L0} \sqrt{\frac{L^2}{\int_0^L \int_0^L C_c(z_i - z_j) dz_i dz_j}} \tag{6.14}$$

where the amplitude of the total vortex-shedding force on the stationary body (Eq. (6.13)) is expressed as function of $C_{L0,sec}$ according to the expressions by Holmes (2001) previously introduced by Eq. (6.8). According to Eq. (6.14), an amplification factor A, multiplied by C_{L0} to obtain $C_{L0,sec}$, can be defined:

$$A = \sqrt{\frac{L^2}{\int_0^L \int_0^L C_c(z_i - z_j) dz_i dz_j}} \tag{6.15}$$

so that:

$$C_{L0,sec} = A \cdot C_{L0} \tag{6.16}$$

The lift correlation length assumed for the stationary body may be included in the wake oscillator model by supposing full correlation at lock-in. In case of full correlation, the sectional value of the lift coefficient amplitude $C_{L0,sec}$ is extended to the whole oscillating body. This is an extreme case and it represents actually a limit condition for the C_{L0} magnification due to correlation increase. The higher the correlation growth due to body oscillation is, the closer the full correlation assumption is to the reality. For this reason, the full correlation assumption is an upper bound for the lift force magnification and, in case of large oscillation amplitude, it can be a reasonably realistic approximation.

As an example, Figure 6.10 shows the Griffin plots obtained for the 4:1 rectangular cylinder assuming the two vortex-shedding force correlation lengths $L_{c,1}$ and $L_{c,2}$ and supposing full correlation for the oscillating body at lock-in. In this way the $C_{L0,sec}$ included in the model formulation is an amplification of the original C_{L0}. The values of

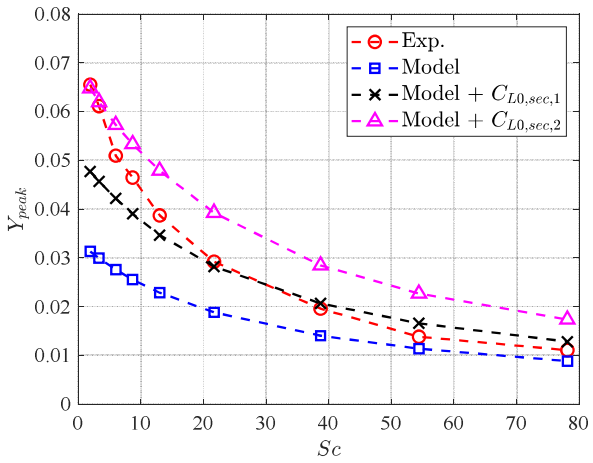

Figure 6.10. Experimental Griffin plot for the 4:1 rectangular cylinder, from Marra et al. (2015), compared to the ones predicted by the model including C_{L0}, $C_{L0,sec,1}$ and $C_{L0,sec,2}$. For the last two cases, the full correlation condition was assumed.

$C_{L0,sec}$ coming from $L_{c,1}$ and $L_{c,2}$ are, respectively, $C_{L0,sec,1}$ = 0.93 and $C_{L0,sec,2}$ = 1.27, calculated according to Eq (6.14) and corresponding, respectively, to A_1 = 1.48 and A_2 = 2.02.

The Griffin plot comparison shows that the experimental curve is closer to the one obtained through $C_{L0,sec,1}$ and $C_{L0,sec,2}$ (black and magenta curves) for low Sc, where amplitudes are greater, while for increasing Sc experimental results are closer to the ones predicted through C_{L0} for the stationary body (blue curve). This is compatible with the supposition about the possible role played by the force correlation, whose effects were reasonably expected to increase with the vibration amplitude. In this context, the apparent dependence of vortex-shedding force correlation with the Scruton number, remarked above, represents actually the dependence on the amplitude of oscillation.

In particular, the Griffin plot obtained without correlation increase (blue curve) and the one obtained by including $C_{L0,sec,2}$ and assuming full correlation condition (magenta curve) define a region where the experimental plot is located, providing a sort of upper and lower bound for the response amplitude at different Sc values. This is also emphasized by the results reported in Figure 6.11, where response curves obtained through stationary body C_{L0} and through $C_{L0,sec,2}$ are reported and compared to experimental curve over a wide range of Sc.

The results do not provide a realistic indication from the quantitative point of view for this cross section, since the assumed correlation length for the stationary body could be

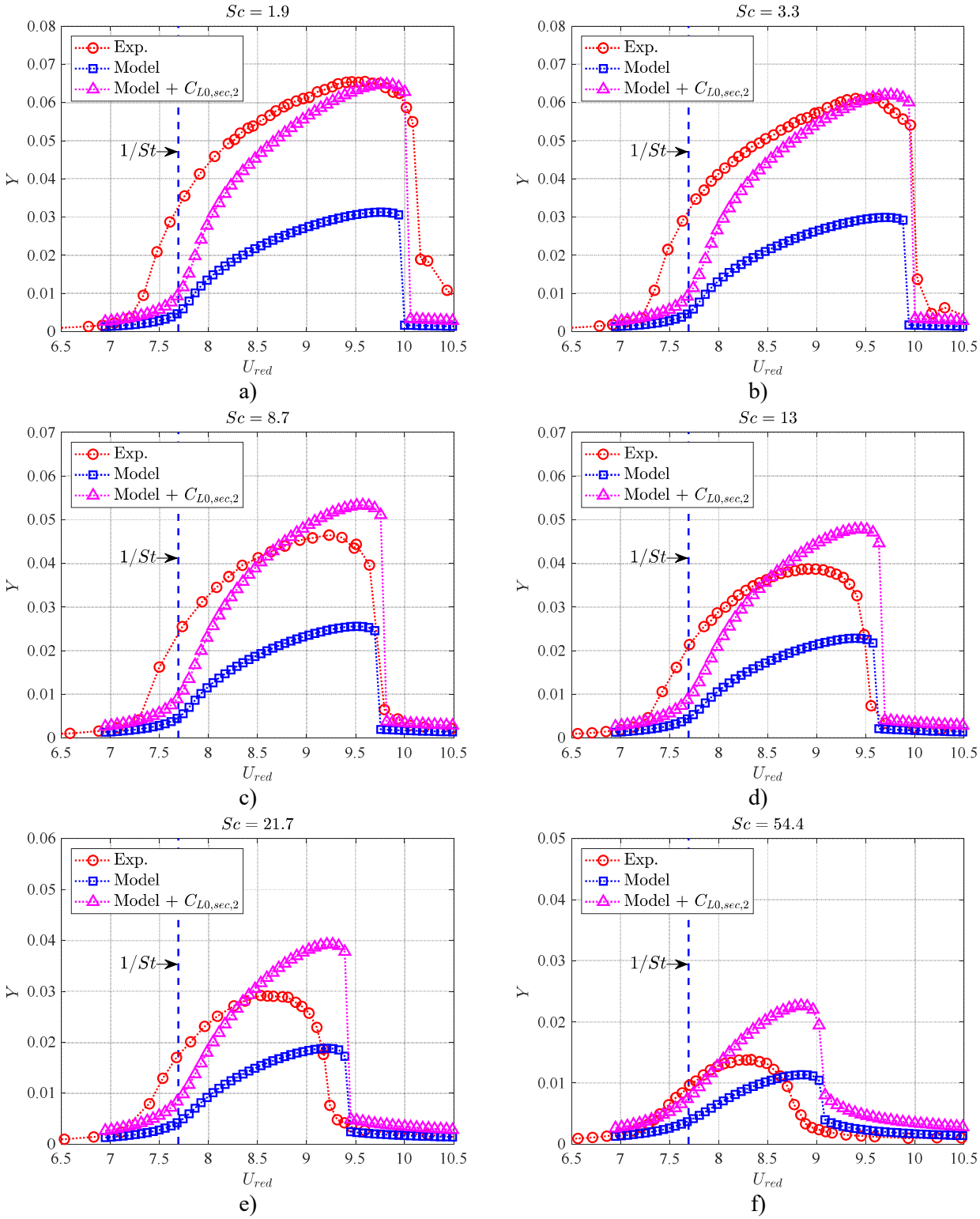

Figure 6.11. Response curves for the 4:1 rectangular cylinder at different values of the Scruton number of the system.

incorrect and the correlation of the oscillating cylinder could be not full, but suggest how taking into account the correlation of the vortex-shedding force may be crucial, especially in terms of peak amplitude.

6.7. Response curves for different Scruton number values

The modified Tamura's wake-oscillator model proposed by Mannini et al. (2018), was found to be able to reproduce the response curve for a 4:1 rectangular cylinder at the lowest *Sc* in a quite satisfying way in terms of onset wind velocity, lock-in extension and curve shape (Figure 6.2), while the incapability of matching the peak response amplitude was attributed to the correlation of the vortex-shedding force (Section 6.6). A part of model parameters (C_{Fy}, St, C_{L0}) were achieved from static wind tunnel tests, while the others (f, β, λ) were set by adjusting their values in order to match as well as possible the experimental response curve at low Scruton number.

It is certainly interesting to evaluate the prediction of the model for increasing *Sc* values, to assess if the virtues and limitations of model results are maintained with the same set of model parameters, determined for the lowest *Sc*, at higher *Sc* too. A substantial independence of model parameters by changing the Scruton number of the system, indeed, would represent a considerable virtue for the mathematical approach.

As observable in Figure 6.11, the onset wind speed, the curve shape and the lock-in range are satisfactorily reproduced in the whole range of Scruton number values with the same set of values of model parameters, compared to the experimental results from Marra et al. (2015).

6.8. Results of numerical experiments

6.8.1. Wake-oscillator model results

The Tamura-type wake oscillator model was applied to perform numerical experiments for the 4:1 rectangular cylinder and for the bridge deck cross section studied in the present work. Configurations with and without barriers were considered for the bridge deck section, at different angles of attack. As previously mentioned, the model was applied by solving numerically Eqs. (2.33) and (2.34) by means of the ODE45 Matlab® function. As for the 4:1 rectangular cylinder and in absence of flow visualizations, the

parameters f, β and λ appearing in the equations of motion were set by matching as well as possible the experimental response curve for the lowest Scruton number tested.

Model predictions were achieved also with the amplification of C_{L0} value determined through force measurements on the stationary body, by including the two correlation lengths $L_{c,1} \simeq 4.4\ D$ and $L_{c,2} \simeq 1.9\ D$ for the stationary model and assuming full correlation at lock-in, following the procedure described in Section 6.6. Even if such values of the correlation length might not be realistic, in absence of further information they were employed for the bridge section too. Two sectional values for the fluctuating lift coefficient amplitude ($C_{L0,sec}$) coming from $L_{c,1}$ and $L_{c,2}$ were calculated and included in the model equations of motion. Identically to what reported in Section 6.6, they were named, respectively, $C_{L0,sec,1}$ and $C_{L0,sec,2}$ to distinguish them from C_{L0}, which indicates the value obtained from static tests. According to this procedure, $C_{L0,sec,1}$ and $C_{L0,sec,2}$ values were found to be equal to C_{L0} multiplied, respectively, by 1.67 and 2.36, which are the values assumed by the amplification factor A, defined by Eq. (6.15), for the bridge deck sectional model. Model parameters and fluctuating sectional lift coefficient amplitudes are reported in Table 6.1, for each cross-section geometry and for different angles of attack.

Firstly, Figure 6.12 reports the results of numerical experiments performed for different values of f and λ for the deck equipped with lateral barriers at zero angle of attack, equivalently to what previously shown by Figure 6.7 and Figure 6.9 for the 4:1 rectangle. Then, Figure 6.13, Figure 6.14 and Figure 6.15 report the response curves for all the cases studied, for Sc value at which the parameters were calibrated. In each figure, the

Table 6.1. Summary of wake-oscillator model parameters adopted for the reported results of numerical experiments for each configuration at different angles of attack.

Cross-section geometric layout	α [deg]	St	C_{L0}	$C_{L0,sec,1}$	$C_{L0,sec,2}$	λ	f	β
4:1 rectangle	0	0.131	0.63	0.93	1.27	1.39	9.0	0.34
Bare deck	0	0.146	0.24	0.40	0.57	1.85	0.8	0.02
	-3	0.147	0.23	0.39	0.54	1.65	1.0	0.02
	+3	0.133	0.19	0.30	0.43	1.00	2.7	0.05
	+8.5	0.121	0.54	0.90	1.27	0.66	11.5	0.55
Barrier 1	0	0.122	0.40	0.68	0.96	1.85	1.5	0.05
	-3	0.119	0.33	0.56	0.79	1.75	1.2	0.03
	+3	0.121	0.30	0.49	0.70	0.75	1.7	0.03
Barrier 2	0	0.111	0.31	0.51	0.73	0.60	5.5	0.12
	-3	0.104	0.42	0.70	0.99	0.55	6.0	0.55
	+3	0.113	0.37	0.62	0.88	0.30	3.0	0.04

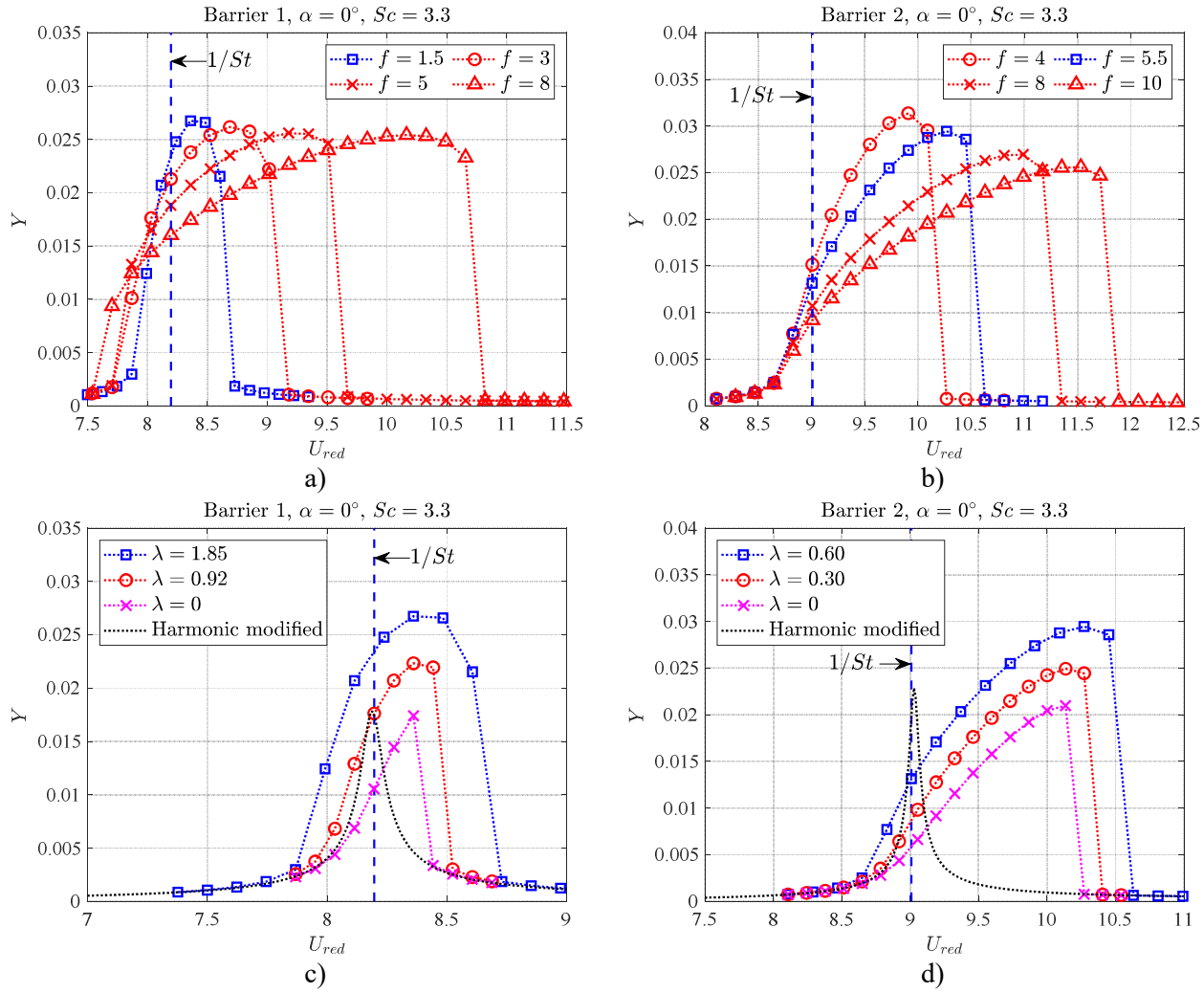

Figure 6.12. Response curves predicted by Tamura-type model for different f values (a, b) and by reducing λ value down to zero (c, d) for the bridge cross-section equipped with barriers at zero angle of attack and lowest Sc. In (c) and (d) the solution provided by modified harmonic model is also reported.

experimental curve is superposed to the results predicted by the Tamura-type model. As observable, from the point of view of peak response amplitude, the curves predicted by using C_{L0} exhibit a good match with experimental ones in some cases, while in other cases the lift coefficient amplitude amplification is necessary to match experimental results more correctly.

Where lower vibration amplitudes are reached, it could be expected that the use of C_{L0} provide better results. This is indeed reasonably confirmed where Y_{peak} is below 3% (Figure 6.14(b, c), Figure 6.15(d, f)), except in case of bare deck at 0° (Figure 6.14(a)). In other cases, where Y_{peak} values higher than about 3% were found (Figure 6.13, Figure 6.14(d), Figure 6.15(a, b, c, e)), the gap between the experimental vibration amplitude and the predicted one is either moderately or markedly greater. It is worth to notice that, where a good match is not found, experimental Y_{peak} is considerably higher than Y_{peak} predicted through C_{L0}. This emphasizes a potential underestimation of the fluctuating lift force, supporting the supposition of spanwise correlation increase from a stationary body to a body oscillating with noticeable vibration amplitude for the bridge section too.

In terms of onset wind velocity, lock-in extension and curve shape, a satisfying agreement between experiments and model prediction was found for bare deck (Figure 6.14) and deck with Barrier 1 (Figure 6.15(a, b, c)) for each investigated angle of attack. In case of Barrier 2, the possible interaction between impinging shear layer instability and vortex shedding, described in Chapter 5, is expected to make a good match between experiments and model results difficult, because of the marked anticipation of lock-in onset velocity compared to the vortex-resonance flow speed $1/St$. This is particularly remarkable for $\alpha = 0°$ and $\alpha = +3°$ (Figure 6.15(d, f)).

An additional remark is needed about Barrier 2 configuration at $\alpha = -3°$ (Figure 6.15(e)): the high response branch observed only for lowest Sc values during aeroelastic tests (see Chapter 5) was not reproduced by the wake oscillator model. The comparison between model and wind tunnel results in Figure 6.15(e) includes the experimental lock-in curve obtained for decreasing wind speed, where the peak point relates to the jump on the increasing branch giving rise to a large hysteresis loop. This part of the lock-in curve is the one observed in the whole range of Scruton number, while the high response branch disappears for about $Sc \geq 6$.

A final clarification is needed: the lock-in curve found for the bare deck at $\alpha = +8.5$ exhibited a marked similarity to the one of the 3:2 rectangular cylinder found by Mannini

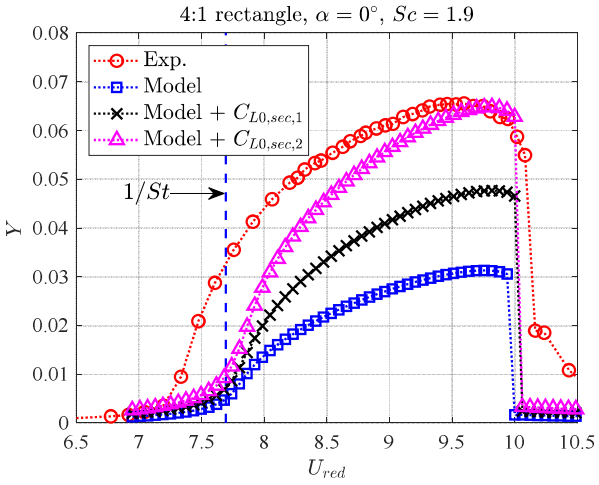

Figure 6.13. Experimental response curves compared to wake oscillator model results, by including C_{L0}, $C_{L0,sec,1}$ and $C_{L0,sec,2}$. Results relate to the 4:1 rectangular cylinder at 0° angle of attack.

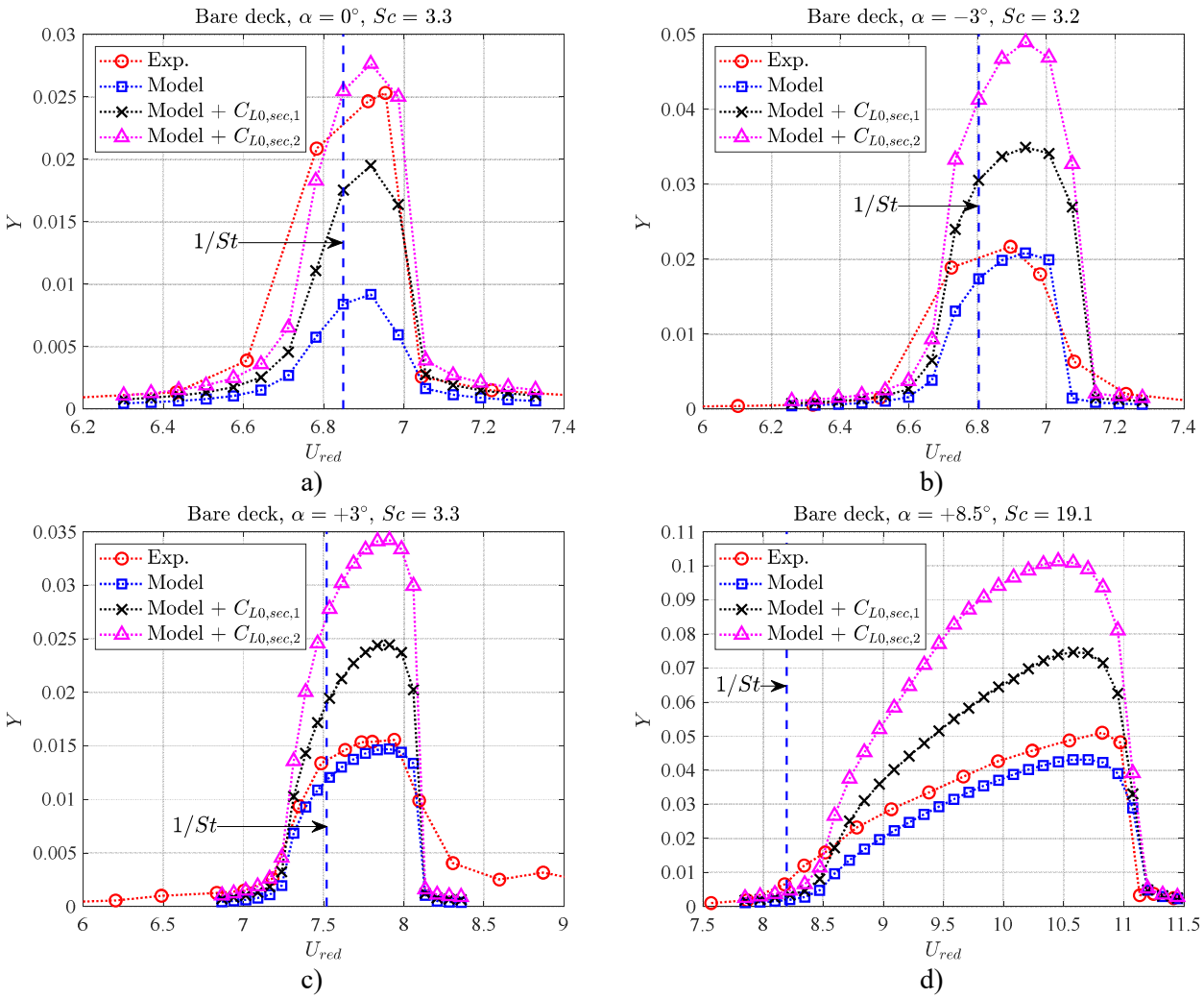

Figure 6.14. Experimental response curves compared to wake oscillator model results, by including C_{L0}, $C_{L0,sec,1}$ and $C_{L0,sec,2}$. Results relate to bare deck at 0° (a), -3° (b), +3°(c) and +8.5° (d) angle of attack.

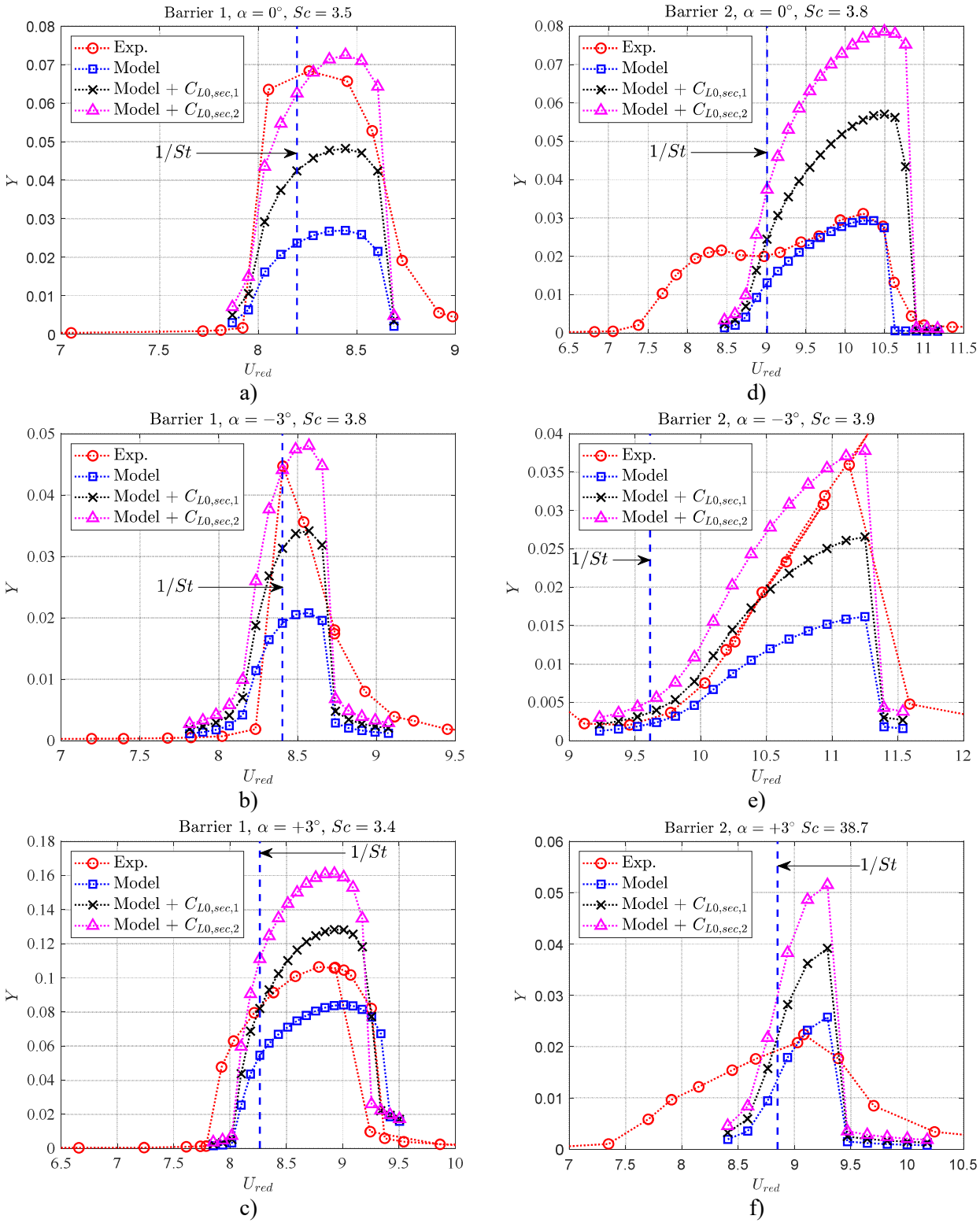

Figure 6.15. Experimental response curves compared to wake oscillator model results, by including C_{L0}, $C_{L0,sec,1}$ and $C_{L0,sec,2}$. Results relate to deck with Barrier 1 (a, b, c) and Barrier 2 (d, e ,f) at 0°, -3° and +3°.

et al. in 2018 (see Chapter 5, Figure 5.14). In this specific case, model parameters allowing to match the experimental curve are achievable by assuming the outline in Figure 2.34, along with wake lamina geometric features identical to the 3:2 rectangle (X_O* = 0, α_I = 1, h* = 1.8, l* = 1.5) and the force F_L applied at one fourth of the chord of the lamina. In other words, the wake oscillator geometry adopted by Mannini et al. (2018) for the 3:2 rectangle was found to be suitable for such bridge deck configuration too. The model was able to reproduce very well the shape of the experimental lock-in curve, with f = 11.5 (Figure 6.14(d)), confirming the similarity in terms of VIV response behavior observed in experimental results between such two cases.

A large part of the observations achievable from the response curves are confirmed and emphasized by the Griffin plots in Figure 6.16, Figure 6.17 and Figure 6.18. In these figures too, a better global agreement between experiments and model prediction based on C_{L0} is observed in case of small Y_{peak}, while larger discrepancies were found where Y_{peak} overcomes 3-4 % of D, leading to an underestimation of the experimental peak amplitude and a better match with model predictions obtained by using $C_{L0,sec,1}$ and $C_{L0,sec,2}$.

The suppositions about spanwise correlation effects are emphasized by Griffin plots: experimental Y_{peak} is higher than the one predicted by using C_{L0} determined for the stationary body, especially at low Sc, where oscillation amplitudes are higher, with the gap between results and prediction progressively reduced for increasing Sc, where vibration is smaller and spanwise correlation is supposed to be weaker and, above all, much closer to the static condition.

Indeed, another relationship between experimental and mathematical Griffin plot curves can be highlighted: in several cases the curve obtained by using $C_{L0,sec,1}$ and $C_{L0,sec,2}$ and the one obtained through C_{L0} demarcate a region in which the experimental curve lays, going from the former curve at low Sc to the latter for increasing Sc, as already pointed out in Section 6.6 with reference to Figure 6.10. This remarks how the knowledge of spanwise correlation and/or sectional C_{L0} for the stationary body, with the full correlation hypothesis, might likely provide a sort of reasonable upper bound for Griffin plot, while the curve obtained by using C_{L0} achieved from static force measurements could be considered a lower bound, defining a region where the experimental curve is expected to be approximately located.

As said for the response curves, the wake oscillator model was not able to reproduce the mechanism leading to the extremely large vibration amplitude observed for the lowest

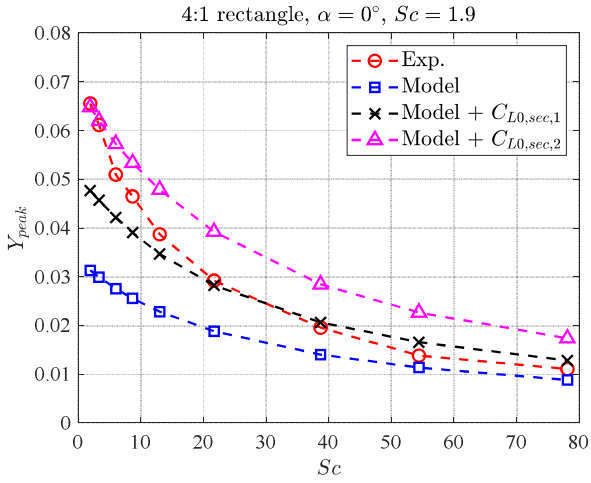

Figure 6.16. Experimental Griffin plots compared to wake oscillator model results, by including C_{L0}, $C_{L0,sec,1}$ and $C_{L0,sec,2}$. Results relate to the 4:1 rectangular cylinder at 0° angle of attack.

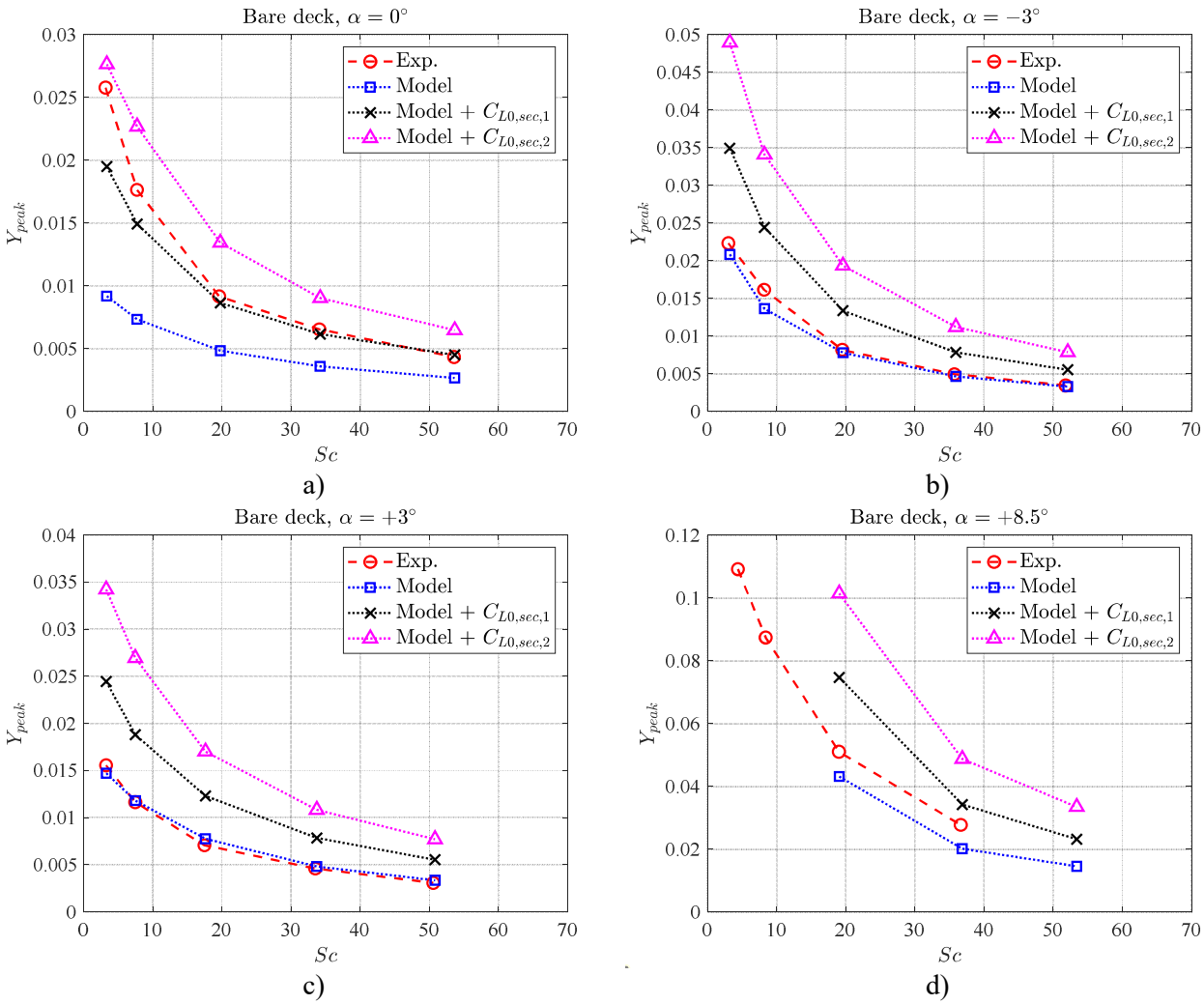

Figure 6.17. Experimental Griffin plots compared to wake oscillator model results, by including C_{L0}, $C_{L0,sec,1}$ and $C_{L0,sec,2}$. Results relate to bare deck at 0° (a), -3° (b), +3°(c) and +8.5° (d) angle of attack.

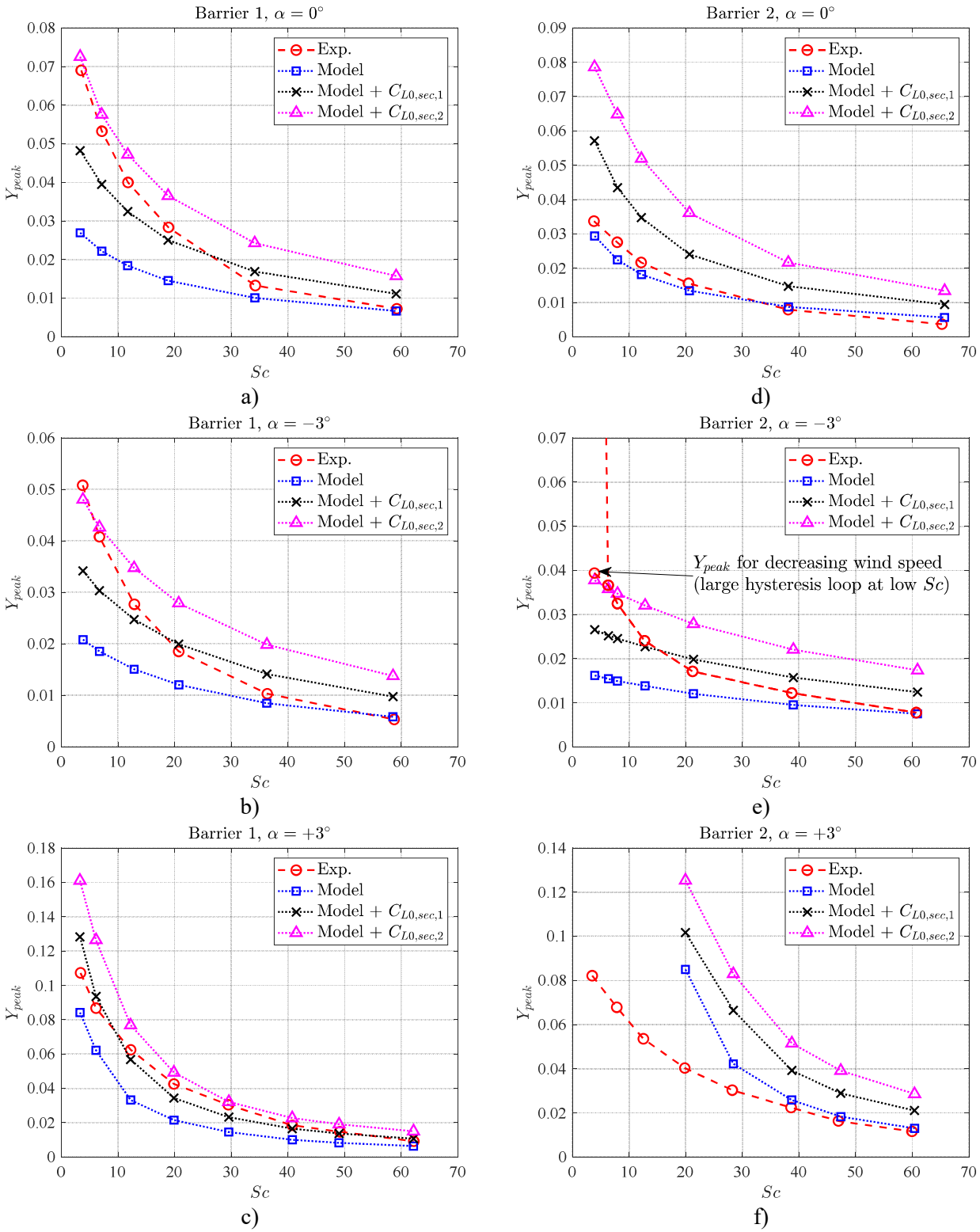

Figure 6.18. Experimental Griffin plots compared with wake oscillator model results, by including C_{L0}, $C_{L0,sec,1}$ and $C_{L0,sec,2}$. Results relate to deck with Barrier 1 (a, b, c) and Barrier 2 (d, e ,f) at 0°, -3° and +3°.

Sc, for increasing wind velocity, in case of Barrier 2 at -3° (Figure 6.18(e)). On the other hand, the configurations characterized by a positive slope of C_{Fy} curve ($dC_{Fy}/d\alpha > 0$), namely bare deck at +8.5° and Barrier 2 at +3° exhibited a similar behavior for the lowest *Sc* values tested: the model predicted a strong interference between VIV and galloping excitation, and no peak VIV response amplitude was achieved and reported in the Griffin plots. With the growth of *Sc*, galloping was no more predicted for bare deck at +8.5° (Figure 6.19(a)), while for Barrier 2 at +3° a clear separation of the two mechanisms was observed (Figure 6.19(b)). Griffin plots (Figure 6.17(d) and Figure 6.18(f)) report only the cases where a peak VIV response amplitude was identified. In these two cases, VIV-galloping interaction was not observed experimentally, while wind tunnel tests and mathematical model exhibited a quite good agreement in terms of maximum response amplitude beyond a certain value of *Sc*, between about 20 and 30. In addition, the assumption of full correlation condition along with the use of $C_{L0,sec,1}$ and $C_{L0,sec,2}$ led to a strong overestimation of the response amplitude, and the best match was found with C_{L0}.

6.8.2. Modified harmonic model results

The modified harmonic model was applied to the 4:1 rectangular cylinder and to the bridge deck section, and the performances of this simplified approach were compared to Tamura-type model results. The comparison was conducted in terms of Griffin plot, since the output of modified harmonic model is represented by the peak response amplitude Y_{peak}. A global overview of results is reported in Figure 6.20, where Griffin plots obtained by using C_{L0} value for the stationary body for both mathematical models are reported. The

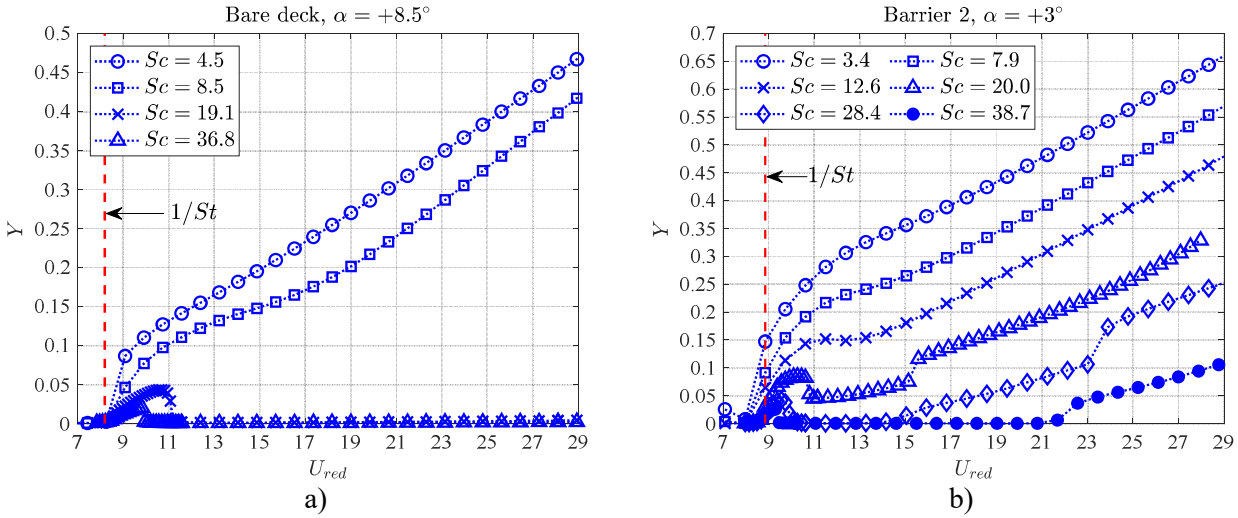

Figure 6.19. Response curves at different *Sc* for bridge deck configurations with positive C_{Fy} slope: bare deck at α = +8.5° (a) and Barrier 2 at α = +3° (b).

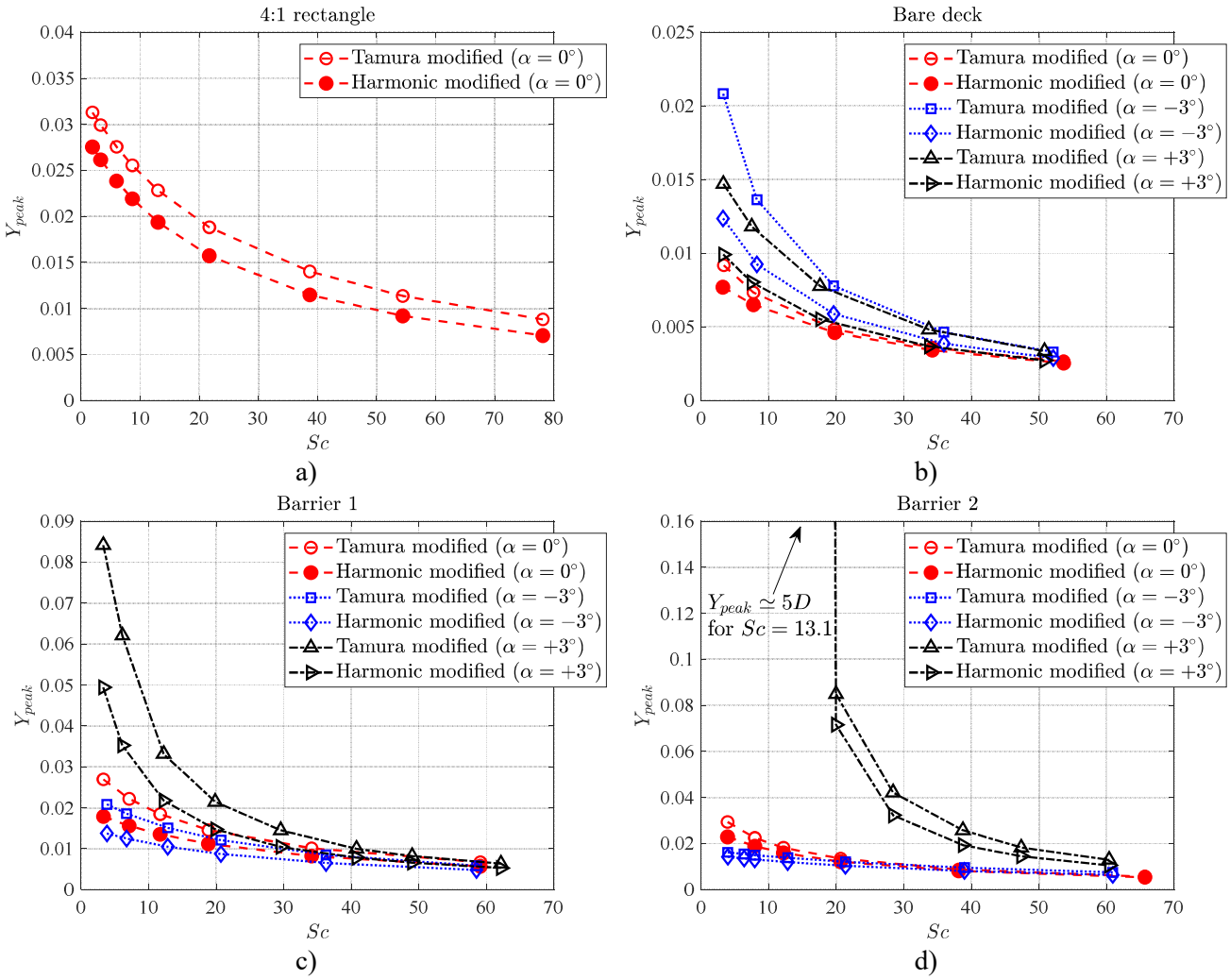

Figure 6.20. Comparison between Tamura-type wake oscillator model and modified harmonic model in terms of Griffin plot, for 4:1 rectangle (a) and bridge model in case of bare deck (b) and in presence of Barrier 1 (c) and Barrier 2 (d).

inclusion of $C_{L0,sec,1}$ and $C_{L0,sec,2}$ would lead to an amplification of Y_{peak} predicted by the two models without modifying the ratio between them, since the relationship between the lift coefficient amplitude and the predicted response amplitude is linear for the modified harmonic model (Eq. (2.45)) and almost linear for the Tamura-type model (Figure 6.6), with a constant of proportionality approximately equal to 1 in both cases.

Clearly, the peak amplitude predicted by the simplified approach was found to be systematically lower than the wake oscillator model one. As said in Section 6.5, this gap was supposed to be mainly caused by the influence on the peak response of the coupling between the wake oscillator motion and the body acceleration, dependent on the parameter λ. Such effect is not incorporated into the single-degree-of-freedom model, according to the comparison between the results of the two models (Figure 6.9, Figure 6.12(c, d)). Even if this contribution is relatively limited comparing to the one given by C_{L0} value (Figure 6.6), it was expected to produce a systematic underestimation of the peak amplitude predicted by the modified harmonic model compared to the Tamura-type formulation, as confirmed by Figure 6.20. On the basis of this and of what reported in Sections 6.6 and 6.8.1, it is reasonable to assert that the modified harmonic model prediction might be possibly affected by a double Y_{peak} underestimation compared to the experimental results: a first one due to neglecting the growth of the lift force spanwise correlation with the response amplitude and a second one given by the impossibility to include the contribution of the wake oscillator coupling with the body acceleration.

It is worth to notice another possible difference between the two models: modified harmonic model is based in the linearization of C_{Fy} curve around the mean wind angle of attack, while the wake oscillator model prediction is based on the actual shape of the C_{Fy} curve. This might cause some differences in quasi-steady aerodynamic force contribution especially where C_{Fy} curve trend is markedly non-linear, while in case of a nearly linear and smooth C_{Fy} trend the two model are expected to work similarly from this point of view.

Finally, some remarks about galloping prediction are necessary. The modified harmonic model is based on the quasi-steady definition of the aerodynamic damping, which is included in a linear harmonic equation of motion. Consequently, in case of galloping condition predicted by the quasi-steady theory ($\zeta_0 + \zeta_{aero}^{QS} < 0$), the model does not provide a VIV peak response amplitude. On the other hand, the Tamura-type wake oscillator model is a non-linear approach and, despite the inclusion of the quasi-steady

transverse force coefficient, it could provide a different result compared to quasi-steady theory in terms of galloping prediction.

As described in Section 6.8.1, the numerical experiments performed by applying the wake oscillator model provided a strong VIV-galloping interaction in case of Barrier 2 at +3° angle of attack (Figure 6.19(b)) for the three lowest *Sc* values tested. On the other hand, for the same three Scruton numbers, modified harmonic model predicted galloping or an extremely high response amplitude of about 5 times *D* (Figure 6.20(d)). In this case, both Tamura-type model and quasi-steady theory provided indeed results in contrast with experiments, where galloping was not observed for any *Sc*.

6.9. Remarks and conclusions

A Tamura-type wake oscillator model, was found able to provide a large variety of results, by appropriately setting the values of model parameters. Such values should be determined through static wind tunnel tests including aerodynamic force and/or pressure measurements and flow visualization. In absence of the flow visualizations, the parameters were set in order to match the response curve behavior at the lowest Scruton number of the system and they were found to be able to follow the curve modification at different *Sc* values (Figure 6.11) quite satisfyingly. This suggested a substantial independence of the model calibration procedure from the vibration amplitude of the oscillating system. Actually, C_{L0} is the only parameter which exhibited a likely dependence on the vibration amplitude and, hence, on *Sc* value.

From the point of view of the lock-in curve shape, two macro-categories were identified: round weakly asymmetric and triangle-shaped strongly asymmetric. The first curve typology was found to be related to a coupling with body acceleration ($\lambda Y''$) dominant over the velocity coupling ($\upsilon^2 2\pi Y'/U_{red}$) in the wake-oscillator equation, while the second one to the opposite condition. As an example, the ratio between the coefficients of body acceleration and velocity at lock-in is:

- $\dfrac{\lambda}{\left(\upsilon^2 2\pi\right)/U_{red}} = 1.4$ for 4:1 rectangular cylinder, derived from what reported in Section 6.2;

- $\frac{\lambda}{\left(\upsilon^2 2\pi\right)/U_{red}} = 0.8$ for 3:2 rectangular cylinder, derived from the work by Mannini et al. (2018).

Actually, the ratio between the two coefficients of the forcing terms depends on the value of the aerodynamic parameter λ, which derives from the equivalent wake lamina geometry according to Tamura's physical concept. Facchinetti et al. (2004), in the work described in Section 2.4.2, proposed an accurate investigation about coupling possibilities between wake and mechanical oscillator, finding results similar to what observed in the present work in terms of curve shape and coupling typology. Facchinetti found the acceleration coupled wake oscillator exhibiting the best global performances. Nevertheless other important examples of VIV response modeling considering a pure velocity coupling are available in literature, such as Hartlen and Currie (1970) and Skop and Griffin (1973) approach (Section 2.4.2). A Tamura-type wake oscillator model includes both coupling terms and this could be an explanation for the variety of response curve typologies achievable.

The adaptation of the model to different cross sections was discussed and some modifications to the wake lamina geometry were supposed (Figure 6.4), in order to achieve the searched parameter values without losing their physical description. The speculations about the geometry of the equivalent wake lamina encourage further study about its structure, possibly leading to the addition of a degree of freedom to the wake oscillator in case of elongated cross sections. At the same time, the capability of reproducing different response curve typologies and the apparent independence of most model parameters from the Scruton number of the system represent promising features of this approach from the point of view of application to bridge decks.

On the other hand, the main limitation of the model was found to be the peak response amplitude prediction, and this was attributed to the increase of the vortex-shedding force spanwise correlation from stationary to vibrating body (Section 6.6), especially in case of considerable oscillation amplitude. In other words, the lift coefficient amplitude per unit length measured for the stationary body (C_{L0}) is supposed to be a lower bound for the dimensionless vortex-shedding force per unit length and to underestimate considerably the force acting on the oscillating cylinder. The problem represented by the lift spanwise correlation should be addressed by means of pressure measurements along the sectional model for each *Sc* tested. A simplified approach was proposed, by assuming full

correlation condition at lock-in, in order to define un upper bound for the vortex-shedding force.

Contextually, the modified harmonic model described in Section 2.4.4 was applied to the 4:1 rectangular cross section and to the bridge deck section for all geometric configurations at different angles of attack. This approach exhibits a very simple mathematical formulation and the required parameters (C_{Fy}, St, C_{L0}) can be determined through relatively simple aerodynamic force measurements on the stationary body. A connection between modified harmonic model and Tamura-type model was suggested by the mathematical formulation of the two approaches and observed during numerical experiments, in terms of peak response amplitude prediction (Section 6.5): the former seems actually a sort of simplified version of the second one. The extreme simplicity and the potential physical origin of the modified harmonic model, coming from such a connection with Tamura's approach, promoted the assessment of its performances.

Compared to experiments, this simplified model exhibited an underestimation of the peak response amplitude, which was substantially attributed to two contributions. The first one is the likely increase of the vortex-shedding force spanwise correlation with the vibration amplitude, equivalently to what said for the wake oscillator model. The second one comes from the effect of the coupling with the body acceleration, included by Tamura's model and not considered by the simplified approach (Figure 6.9 and Figure 6.12(c, d)). In addition, it was observed that the contribution to the peak response amplitude Y_{peak} coming from the lift force increase due to spanwise correlation seems to be markedly higher than the one coming from the acceleration coupling (Figure 6.6). The correlation increase can be taken into account in the same way adopted for the wake oscillator model, by determining an upper bound for the fluctuating lift force based on its dimensionless sectional value measured on the stationary body ($C_{L0,sec}$) and assuming full spanwise correlation.

At the same time, modified harmonic model was found able to provide a satisfying approximation of Tamura-type model in terms of peak response prediction in case of limited acceleration coupling, especially when the acceleration coupling coefficient (λ) is lower than the velocity coupling coefficient ($v^2 2\pi/U_{red}$). As a matter of fact, for the 3:2 rectangle, studied by Mannini et al. (2018), and for the bridge deck with Barrier 2 installed, in the present work, the acceleration coefficient value $\lambda < 1$ led to the best match between the predictions provided by the two models. In addition, 3:2 rectangle and bridge with Barrier 2 exhibit a geometry considerably bluffer than, respectively, the 4:1 rectangle and

the bridge without barriers or even with Barrier 1, more transparent to the flow. This suggested that a limited acceleration coupling might be possibly connected to a bluffer section geometry. Nevertheless, the relatively limited influence of λ on the peak response compared to the lift coefficient amplitude (Figure 6.6) indicates that modified harmonic model could provide a satisfying estimation of the peak response amplitude also in case of greater acceleration coupling if the vortex-shedding force intensity is correctly determined. A reliable estimation of the vortex-shedding force correlation growth with the oscillation amplitude could lead to a more general employment of modified harmonic model to quickly approximate the peak vibration amplitude predicted by a Tamura-type wake oscillator model and, above all, to determine, during bridge deck preliminary design phase, peak response at lock-in in a relatively simple way.

7. General conclusions and remarks

In the present work, the effects on bridge deck response caused by local cross-section details and angle of attack are emphasized and investigated extensively. At the same time, the considerable number of experimental results is employed to point out virtues and limitations of two mathematical approaches for VIV response modeling. The inclusion of the effects produced by realistic geometric details and angle of attack aims to enhance the practical usefulness of the study about mathematical models and further advancements aimed to increase their suitability for bridge deck response prediction are proposed.

The variability of results coming from the combination of lateral barriers and angle of attack variation is noticeable. In particular, the degree of transparency of the barrier and the distribution of the openings were found to be even more critical than the height of the element in terms of effects on the VIV response. According to the experimental tests, a different transparency may dramatically affect both maximum vibration amplitude at lock-in and synchronization range. At the same time, the onset velocity may considerably differ from the vortex-resonance flow speed inferred from static measurements, and the lock-in condition may be even significantly anticipated. The openings of barriers, screens or railings might be studied and adapted to improve deck aerodynamic performances (Bai et al. (2020)), giving to these bridge elements a role in vortex-induced oscillation control even in absence of particular aerodynamic devices installed on them. At the same time, the angle of attack is able to change radically the effect of a certain geometric feature. Even though static force measurements can provide qualitative indications about proneness to VIV for different flow angles of incidence, violent oscillations can occasionally be found even in case of low expected susceptibility to VIV. Response variability to limited angle of attack variations appears enhanced by the presence of barriers. Therefore, the choice of the flow incidence range of interest becomes particularly critical in presence of geometric details markedly affecting section aerodynamics, especially in case of barriers or screens with limited transparency to the flow. Hence, a correct evaluation of the effects produced by geographical features of bridge building area on wind angle of attack is essential.

Free-decay tests shed further light on virtues and limitations of the indications provided by static tests and based on quasi-steady theory. Quasi-steady aerodynamic damping represents a satisfying estimation of the experimental results only in some cases. In this context, the quality of the quasi-steady prediction appears to be much more sensitive to the cross-section layout, in particular to the corresponding trend and slope of

the transverse coefficient curve (C_{Fy}), than to the flow reduced velocity range: a satisfying match between predicted and experimental aerodynamic damping values at high reduced velocity was generally confirmed at lower velocity too. Decay test results also provided further information on those cases where galloping instability predicted by quasi-steady theory was not observed experimentally.

From the point of view of mathematical modeling, a Tamura-type wake-oscillator model seems to be able to reproduce a substantial number of experimental curves, despite the variability of VIV response at lock-in, provided that the estimation of the wake lamina geometry and model parameters is reasonably correct. For this purpose, static force measurements are necessary along with flow visualizations. At the same time, the parameters exhibited a substantial independence of the vibration amplitude, except for the amplitude of the fluctuating lift force (C_{L0}), and, for each cross-section layout, some of them could also be evaluated on the basis of a response curve obtained for a single Scruton number.

On the other hand, a harmonic-type model was found to provide results, in terms of peak response amplitude, similar to the ones exhibited by Tamura-type model, especially where a weak acceleration coupling is observed. This was especially observed for section layouts with limited side ratio due to the presence of the least transparent barrier and/or in case of a positive angle of attack value able to remarkably enlarge the ratio between across-flow and along-wind size of the body, as for bare deck at +8.5° angle of attack. Both models include a quasi-steady contribution, depending on the transverse force coefficient curve, whose correct estimation is critical for the predicted vibration amplitude. At the same time, quasi-steady theory inclusion appeared not to be sufficient for a proper response prediction in some cases as highlighted by decay tests and this was attributed to remarkable unsteady effects related to certain section layouts. Apart from the role played by the quasi-steady contribution, the sensitivity of the peak vibration predicted by both approaches to the C_{L0} value is clear. Therefore, the lower oscillation amplitude generally provided by both models compared to the experimental one was attributed to vortex-shedding correlation increase with the oscillation amplitude, with a magnification of the fluctuating lift force. In this regard, a marked growth of the force spanwise correlation, compared to stationary condition, over a typical range for bridge deck vibration amplitude (about 10% of D) is considered as reasonably expectable (Sun et al., 2019). Assuming full correlation at lock-in may provide an upper bound for the force acting on the body and,

hence, for the predicted Griffin plot, while the lift coefficient amplitude measured through static force measurements may lead to a lower bound.

Pressure measurements to quantify and include in both models the correlation contribution should be the next step to improve the results of the present work. At the same time, a deeper study should be carried out about the wake-oscillator structure for Tamura-type model. The physical speculations formulated about the wake lamina geometry encourage to consider an additional degree of freedom for the model. In this context, an analogy with airfoil flaps could provide useful suggestions for the motion of the two parts of the wake oscillator. The identification of a proper wake lamina geometry for elongated sections is necessary to define model parameters from the physical point of view, equivalently to what previously proposed for circular (Tamura and Matsui, 1979), square (Tamura and Shimada, 1987) and 3:2 rectangular (Mannini et al., 2018) cylinders. The issue is complex and attractive at the same time, especially with the purpose of developing a model suitable for elongated sections like bridge deck ones.

Bibliography

Bai, H., Ji, N., Xu, G., & Li, J. (2020). An alternative aerodynamic mitigation measure for improving bridge flutter and vortex induced vibration (VIV) stability: Sealed traffic barrier. *Journal of Wind Engineering and Industrial Aerodynamics*, 206, 104302.

Baker, B. (1884). *The Forth Bridge.*

Bartoli, G., Contri, S., Mannini, C., & Righi, M. (2009). Toward an improvement in the identification of bridge deck flutter derivatives. *Journal of Engineering Mechanics*, 135 (8), 771-785.

Bearman, P. W. (1984). Vortex shedding from oscillating bluff bodies. *Annual Review of Fluid Mechanics*, 16, 195-222.

Bearman, P. W., & Obasaju, E. D. (1982). An experimental study of pressure fluctuations on fixed and oscillating square section cylinders. *Journal of Fluid Mechanics*, 119, 297-321.

Benaroya, H., & Lepore, J. (1983). Statistical flow-oscillator modeling of vortex-shedding. *Journal of Sound and Vibration*, 86 (2), 159-179.

Berger, E., & Wille, R. (. (1972). Periodic flow phenomena. *Annual Review of Fluid Mechanics*, 4, 313-340.

Bernard, H. (1908). Formation de Centres de Giration a l'Arriere d'un Obstacle en Mouvement. *Comptes Rendus*, 146.

Billah, K. (1989). A study of Vortex Induced Vibration (Ph. D. Thesis). Princeton University, New Jersey.

Birkhoff, G. (1953). Formation of vortex streets. *Journal of Applied Physics*, 24, 209-231.

Bishop, R., & Hassan, A. (1964). The lift and drag forces on a circular cylinder oscillating in a flowing fluid. *Proceedings of the Royal Society of London. Series A, Mathematical and Physical Sciences*, *277*, p. 51-75.

Blevins, R. D. (2001). *Flow-induced Vibration.* Krieger Publishing Company, Malabar, Florida.

Brancaleoni, F., & Diana, G. (1993). The aerodynamic design of the Messina Straits Bridge. *Journal of Wind Engineering and Industrial Aerodynamics*, 48, 395-409.

Bruno, L., & Mancini, G. (2002). Importance of Deck Details in Bridge Aerodynamics. *Structural Engineering International*, 4, 289-294.

Buresti, G. (1998). Vortex shedding from bluff bodies. In J. D. Riera, & A. G. Davenport, *Wind Effects on Buildings and Structures.* Balkema, Rotterdam.

Carassale, L., Freda, A., & Marrè-Brunenghi, M. (2013). Effects of free-stream turbulence and corner shape on the galloping instability of square cylinders. *Journal of Wind Engineering and Industrial Aerodynamics*, 123, 274-280.

Chen, Z., Liu, S., Yu, X., Ma, C., & Liu, L. (2017). Experimental Investigations on VIV of Bridge Deck Sections: A Case Study. *KSCE Journal of Civil Engineering*.

Corriols, A. S., & Morghental, G. (2012). Computational analysis of VIV observed on existing bridges. *The Seventh International Colloquium on Bluff Body Aerodynamics and Applications (BBAA7).* Shangai, China; September 2-6.

Cowdrey, C. F. (1963). A Note on the Use of End Plates to Prevent Three-Dimensional Flow at the Ends of Bluff Cylinders. Aeronautical Research Council, Current Paper No.683, HMSO, London.

D'Asdia, P., Sepe, V., Caracoglia, L., & Noè, S. (2003). A model for vortex-shedding induced oscillations of long-span bridges. *Proceedings of the 2nd International Structural Engineering and Construction Conference (ISEC-02)*, *3*, p. 2331-2336. Univeristy of Rome, Italy.

Den Hartog, J. P. (1956). *Mechanical Vibrations.* 4th ed., McGraw-Hill, New York. Reprinted by Dover, New York, 1984.

Diana, G., Resta, F., Belloli, M., & Rocchi, D. (2006). On the vortex shedding forcing on suspension bridge deck. *Journal of Wind Engineering and Industrial Aerodynamics*, 94, 341-363.

Dowell, E. (1981). Non-linear oscillator models in bluff body aero-elasticity. *Journal of Sound and Vibration*, 75 (2), 251-264.

Ehsan, F., & Scanlan, R. H. (1990). Vortex-induced vibrations of flexible bridges. *Journal of Engineering Mechanics*, 116(6), 1392-1411.

Facchinetti, M. L., de Langre, E., & Biolley, F. (2004). Coupling of structure and wake oscillators in vortex-induced vibrations. *Journal of Fluids and Structures*, 19, 123-140.

Feng, C. C. (1968). The measurements of vortex-induced effects in flow past stationary and oscillatory circular and D-section cylinders. Master's thesis, University of British Columbia, Vancouver.

Frandsen, J. B. (2001). Simultaneous pressures and accelerations measured full-scale on the Great Belt East suspension bridge. *Journal of Wind Engineering and Industrial Aerodynamics*, 89, 95-129.

Fujino, Y., & Yoshida, Y. (2002). Wind-Induced Vibration and Control of Trans-Tokyo Bay Crossing Bridge. *Journal of Structural Engineering*, 128, 1012-1025.

Funakawa, M. (1969). The vibration of a cylinder caused by wake force in a flow. *Bulletin of JSME*, 12, 1003-1010.

Goswami, I. (1991). Vortex-Induced vibration of circular cylinders (Ph. D. Thesis). Johns Hopkins University, Baltimore, Maryland.

Hartlen, R. T., & Currie, I. G. (1970). Lift-oscillator model of vortex-induced vibration. *Journal of Engineering Mechanics Division (ASCE)*, 96 (5), 577-591.

Holmes, J. D. (2001). *Wind Loading of Structures.* Taylor & Francis, London and New York.

Honda, A., Ito, M., & Kimura, H. (1992). Aerodynamic Instability of Prestressed Concrete Cable-stayed Bridge with Noise Barrier. *Journal of Wind Engineering and Industrial Aerodynamics*, 41-44, 1169-1180.

Hu, C., Zhao, L., & Ge, Y. (2018). Time-frequency evolutionary characteristics of aerodynamic forces around a streamlined closed-box girder during vortex-induced vibration. *Journal of Wind Engineering & Industrial Aerodynamics*, 182, 330-343.

Iwan, W., & Blevins, R. D. (1974). A model for vortex induced oscillation of structures. *Journal of Applied Mechanics*, 41 (3), 581-586.

Iwan, W., & Botelho, D. (1985). A model for vortex induced oscillation of structures. *Journal of Applied Mechanics*, 41 (3), 581-586.

Jones, N. P., H., S. R., Sarkar, P. P., & Singh, L. (1995). The effect of section model details on aeroelastic parameters. *Journal of Wind Engineering and Industrial Aerodynamics*, 54/55, 45-53.

Kernot, W. C. (1893). Wind pressure. *Proceedings, Australasian Society for the Advancement of Science*, *V*, p. 573-581.

Knisely, C. W. (1990). Strouhal numbers of rectangular cylinders at incidence: a review and new data. *Journal of Fluids and Structures*, 4, 371-393.

Krenk, S., & Nielsen, S. (1999). Energy balanced double oscillatior model for vortex-induced vibrations. *Journal of Engineering Mechanics*, 125, 263-271.

Kubo, Y., Honda, K., Tasaki, K., & Kato, K. (1993). Improvement of aerodynamic instability of cable-stayed bridge deck by separated flows mutual interference method. *Journal of Wind Engineering and Industrial Aerodynamics*, 49, 553-564.

Kubo, Y., Kimura, K., Sadashima, K., Okamoto, Y., Yamaguchi, E., & Kato, K. (2002). Aerodynamic performance of improved shallow π shape bridge deck. *Journal of Wind Engineering and Industrial Aerodynamics*, 90, 2113-2125.

Laima, S., Li, H., Chen, W., & Li, F. (2013). Investigation and control of vortex-induced vibration of twin box girders. *Journal of Fluids and Structures*, 39, 205-221.

Landl, R. (1975). A mathematical model for vortex-excited vibrations of bluff bodies. *Journal of Sound and Vibration*, 42 (2), 219-234.

Larsen, A. (1993). A generalized model for assessment of vortex-induced vibration of flexible structures. *Proceedings of the First IAWE European and African Regional Conference.*

Larsen, A. (1993). Aerodynamic aspects of the final design of the 1624 m suspension bridge across the Great Belt. *Journal of Wind Engineering and Industrial Aerodynamics*, 48, 261-285.

Larsen, A., & Wall, A. (2012). Shaping of bridge box girders to avoid vortex shedding response. *Journal of Wind Engineering and Industrial Aerodynamics*, 104-106, 159-165.

Larsen, A., Esdahl, S., Andersen, J. E., & Vejrum, T. (2000). Storebælt suspension bridge - vortex shedding excitation and mitigation by guide vanes. *Journal of Wind Engineering and Industrial Aerodynamics*, 88, 283-296.

Lienhard, J. H. (1966). Synopsis of Lift, Drag and Vortex Frequency Data for Rigid Circular Cylinders. Washington State University, College of Engineering, Research Division Bulletin 300.

Lugt, H. J. (1983). *Vortex Flow in Nature and Technology.* Wiley, New York.

Ma, C., Liu, Y., Yeung, N., & Li, Q. (2019). Experimental Study of Across-Wind Aerodynamic Behavior of a Bridge Tower. *Journal of Bridge Engineering*, 24(2), 04018116.

Macdonald, J. H., A., I. P., & Fletcher, M. S. (2002). Vortex-induced vibrations of the Second Severn Crossing cable-stayed bridge - full-scale and wind tunnel measurements. *Proceedings of the Institution of Civil Engineers - Structures and Buildings*, (p. 152, 123-134).

Mannini, C., Massai, T., & Marra, A. M. (2018). Modeling the interference of vortex-induced vibration and galloping for a slender rectangular prism. *Journal of Sound and Vibration*, 419, 493-509.

Marra, A. M. (2011). Risk assessment of bridge decks prone to vortex induced vibrations (Ph. D. Thesis). University of Florence.

Marra, A. M., Mannini, C., & Bartoli, G. (2015). Measurements and improved model of vortex-induced vibration for an elongated rectangular cylinder. *Journal of Wind Engineering and Industrial Aerodynamics*, 145, 358-367.

Marris, A. W. (1964). A review on vortex streets, periodic wakes, and induced vibration phenomena. *Journal of Basic Engineering*, 185-196.

Massai, T., Zhao, J., Lo Jacono, D., Bartoli, G., & Sheridan, J. (2018). The effect of angle of attack on flow-induced vibration of low-side-ratio rectangular cylinders. *Journal of Fluids and Structures*, 82, 375-393.

Matsumoto, M. (1999). Vortex shedding of bluff bodies: a review. *Journal of Fluids and Structures*, 13, 791-811.

Morkovin, M. V. (1964). Flow around circular cylinders - kaleidoscope of challenging fluid phenomena. *Proceedings of ASME Symposium on Fully Separated Flows*, (p. 102-118).

Nakamura, Y. (1969). Vortex excitation of a circular cylinder treated as binary flutter. *Reports of Research Institute for Applied Mechanics, Kyushu University*, 13, 217-234.

Nakamura, Y., & Nakashima, M. (1986). Vortex excitation of prisms with elongated rectangular, H and ⊦ cross-sections. *Journal of Fluid Mechanics*, 163, 149-169.

Obasaju, E. D. (1979). On the effects of end plates on the mean forces on square sectioned cylinders. *Journal of Wind Engineering and Industrial Aerodynamics*, 5 (1-2), 179-186.

Oertel, H. J. (1990). Wake behind blunt bodies. *Annual Review of Fluid Mechanics*, 22, 539-564.

Okajima, A. (1982). Strouhal numbers of rectagular cylinders. *Journal of Fluid Mechanics*, 123, 379-398.

Parkinson, G. V., & Brooks, N. P. (1961). On the Aeroelastic Instability of Bluff Cylinders. *Journal of Applied Mechanics*, 28, 252-258.

Perry, A. E. (1982). The vortex-shedding process behind two-dimensional bluff bodies. *Journal of Fluid Mechanics Digital Archive*, 116, 77-90.

Rayleigh, J. W. (1879). Acoustical Observations II. *Philosphical Magazine*, 7, 149-162. Contained in Scientific Papers, Dover, New York, 1984.

Ricciardelli, F. (2010). Effects of the vibration regime on the spanwise correlation of the aerodynamic forces on a 5:1 rectangular cylinder. *Journal of Wind Engineering and Industrial Aerodynamics*, 98, 215-225.

Ricciardelli, F., & Hangan, H. (2001). Pressure distribution and aerodynamic forces on stationary box bridge sections. *Wind and Structures*, 4 (5), 399-412.

Ricciardelli, F., & Marra, A. M. (2008). Sectional aerodynamic forces and their longitudinal correlation on a vibrating 5:1 rectangular cylinder. *Proceedings of BBAA VI International Colloquium on: Bluff Bodies Aerodynamics & Applications.* Milan, Italy.

Roshko, A. (1993). Perspective on bluff body aerodynamics. *Journal of Wind Engineering and Industrial Aerodynamics*, 49, 79-100.

Ruschweyh, H. (1990). Practical experiences with wind-induced vibrations. *Journal of Wind Engineering and Industrial Aerodynamics*, 33, 211-218.

Sakai, Y., Ogawa, K., Shimodoi, H., & Saitoh, T. (1993). An Experimental Study on Aerodynamic Improvements for Edge Girder Bridges . *Journal of Wind Engineering and Industrial Aerodynamics*, 49, 459-466.

Sarpkaya, T. (1978). Fluid forces on oscillating cylinders. *Journal of Waterway, Port, Coastal, and Ocean Division ASCE*, 104, 275-290.

Sarpkaya, T. (1979). Vortex-induced oscillations: a selective review. *Journal of Applied Mechanics*, 46, 241-258.

Sarwar, M. W., & Ishihara, T. (2010). Numerical study on suppression of vortex-induced vibrations of box girder bridge section by aerodynamic countermeasures. *Journal of Wind Engineering and Industrial Aerodynamics*, 98, 701-711.

Scanlan, R. H. (1981). *On the state-of-the-art methods for calculations of flutter, vortex-induced and buffeting response of bridge structures.* Technical report, FHWA/RD-80/050, National Techincal Information Service, Springfield, Va.

Scanlan, R. H. (1998). Bridge flutter derivatives at vortex lock-in. *Journal of Structural Engineering*, 124 (4), 450-458.

Scruton, C. (1963). On the wind-excited oscillations of stacks, towers and masts. *Proceedings of the International Conference on the Wind Effects on Buildings and Structures*, (p. 798-837). Teddington, Middlesex.

Shimada, K. I. (2012). Predictability of unsteady two-dimensional k-ε model on the aerodynamic instabilities of some rectangular prisms. *Journal of Fluids and Structures*, 28, 20-39.

Shimada, K., & Ishihara, T. (2002). Application of a modified k-ε model to the prediction of aerodynamic characteristics of rectangular cross-section cylinders. *Journal of Fluids and Structures*, 16 (4), 465-485.

Shiraishi, N., & Matsumoto, M. (1983). On classification of vortex-induced oscillation and its application for bridge structures. *Journal of Wind Engineering and Industrial Aerodynamics*, 14, 419-430.

Skop, R., & Griffin, O. (1973). A model for the vortex-excited resonant response of bluff cylinders. *Journal of Sound and Vibration*, 27 (2), 225-233.

Staubli, T. (1983). Calculation of vibration of an elastically mounted cylinder using experimental data from a forced oscillation. *Journal of Fluid Engineering*, 105, 225-229.

Steinman, D. B., & Watson, S. R. (s.d.). *Bridges and Their Builders.* Dover Publications, New York.

Strouhal, V. (1878). Uber eine Besondere Art der Tonerregung. *Annalen der Physik und Chemie* , V, 217-251.

Sun, Y., Li, M., Li, M., & Liao, H. (2019). Spanwise correlation of vortex-induced forces on typical bluff bodies. *Journal of Wind Engineering and Industrial Aerodynamics*, 189, 186-197.

Tamura, Y., & Matsui, G. (1979). Wake-oscillator model of vortex-induced oscillation of circular cylinder. *Proceedings of the Fifth International Conference on Wind Engineering*, (p. 1085-1094). Fort Collins, Colorado, USA.

Tamura, Y., & Shimada, K. (1987). A mathematical model for the transverse oscillations of square cylinders. *Proceedings of the 1st International Conference on Flow Induced Vibrations*, (p. 267-276). Bowness-on-Windermere, UK.

Vickery, B. J., & Basu, R. I. (1983a). Across-wind vibrations of structures of circular cross-section. Part I. Development of a mathematical model for two-dimensional conditions. *Journal of Wind Engineering and Industrial Aerodynamics*, 12, 49-73.

Vickery, B. J., & Basu, R. I. (1983b). Across-wind vibrations of structures of circular cross-section. Part II. Development of a mathematical model for full-scale application. *Journal of Wind Engineering and Industrial Aerodynamics*, 12, 75-97.

von Karman, T. (1912). Uber den Mechanismuss des Widersstandes den ein bewegter Korper in einen Flussigkeit Erfahrt. *Nachrichten der K. Gesellschaft der Wissenschaften zu Gottingen*, 547-556.

Weber, F., Distl, J., & Maślanka, M. (2013). Semi-Active TMD Concept for Volgograd Bridge. *Proceedings of the 31st IMAC, A Conference on Structural Dynamics*, (p. 79-88).

Wille, R. (1960). Karman vortex streets. *Advances Applied Mechanics*, 6, 273-287.

Williamson, C. H. (1996). Vortex dynamics in the cylinder wake. *Annual Review of Fluid Mechanics*, 28, 477-539.

Xu, F., Ying, X., Li, Y., & Zhang, M. (2016). Experimental Explorations of the Torsional Vortex-Induced Vibrations of a Bridge Deck. *Journal of Bridge Engineering*, 21(12), 04016093.

Yang, Y., Wu, T., Ge, Y., & Kareem, A. (2015). Aerodynamic Stabilization Mechanism of a Twin Box Girder with Various Slot Widths. *Journal of Bridge Engineering*.

Yu, Y., Xie, F., Yan, H., Constantinides, Y., Oakley, O., & Karniadakis, G. E. (2015). Suppression of vortex-induced vibrations by fairings: A numerical study. *Journal of Fluids and Structures*, 54, 679-700.

Zdravkovich, M. M. (1996). Different modes of vortex shedding: an overview. *Journal of Fluids and Structures*, 10, 427-437.